FRAGMENTATION AND REACTION OF STRUCTURAL ENERGETIC MATERIALS

A Thesis
Presented to
The Academic Faculty

by

Brady B. Aydelotte

In Partial Fulfillment
of the Requirements for the Degree
Doctor of Philosophy in the
School of Materials Science and Engineering

Georgia Institute of Technology
December 2013

FRAGMENTATION AND REACTION OF STRUCTURAL ENERGETIC MATERIALS

Approved by:

Naresh N. Thadhani, Advisor
School of Materials Science and Engineering
Georgia Institute of Technology

David McDowell
School of Mechanical Engineering
Georgia Institute of Technology

Arun Gokhale
School of Materials Science and Engineering
Georgia Institute of Technology

Min Zhou
School of Mechanical Engineering
Georgia Institute of Technology

Tom Sanders
School of Materials Science and Engineering
Georgia Institute of Technology

Barrie Homan
US Army Research Laboratory
Aberdeen, MD

Date Approved: 1 August 2013

To my wife, Tristyn, and my daughters, Kaia, Katie, and Lizzy, who make it all worth while.

ACKNOWLEDGEMENTS

This work represents efforts and contributions by many people to whom I am indebted. My advisor, Naresh Thadhani has been a great source of support and encouragment. I am very grateful for the support of current and former members of the High Strain Rate Laboratory at the Georgia Institute of Technology including Greg Kennedy, Paul Specht, Brad White, Kit Neel, Michael Tucker, Jennifer Breidenich, Ricky Whelchel, Chris Wehrenburg, Anthony Fredenburg, Alex Bryant, Sean Kelly, Adam Jakus, Stephanie Holguin, René Diaz, Manny Gonzalez, and Parveen Sood.

The mentorship and support of Barrie Homan, Kevin McNesby, Michael Zellner, and Brian Schuster of ARL have been of tremendous value. Matthew Trexler, formerly of ARL, provided the cold sprayed Ni+Al material for this study.

A number of collaborators provided helpful support in conducting experiments. The experimental support of Christopher Braithwaite and Adam Collins at The Cavendish Laboratory, Cambridge University is acknowledged. At ARL valuable assistance was provided by Dawn Saunders, Kevin Bare, Chris Imon, Debbie Pilarski, Gene Summers, Ronnie Thompson, William Sickels, Ray Sparks and Matthew Biss. At Ohio State the assistance of Jason Johnson and Glenn Daehn are gratefully acknowledged. Tim Pryun performed the DTA measurements at Georgia Institute of Technology for which I am grateful.

Kelli Rettew, Sadie Roberts, Sean McGaha, Julien Turner, and Blake Wilckens have been extremely helpful in performing stereological measurements, doing optical and electron microscopy, and building experimental setups.

I am also very grateful for support by Dr. Cliff Bedford as a part of ONR/MURI grant No. N00014-07-1-0740 and support of my PhD by the DOD SMART scholarship

program. The simulations in this work were supported in part by a grant of computer time from the DOD High Performance Computing Modernization Program at the ARL DSRC.

TABLE OF CONTENTS

LIST OF TABLES

LIST OF FIGURES

SUMMARY

Structural energetic materials (SEM) are a class of multicomponent materials which may react under various conditions to release energy. Fragmentation and impact induced reaction are not well characterized phenomena in SEMs. The structural energetic systems under consideration here combine aluminum with one or more of the following: nickel, tantalum, tungsten, and/or zirconium. These metal+Al systems were formulated with powders and consolidated using explosive compaction or the gas dynamic cold spray process.

Fragment size distributions of the indicated metal+Al systems were explored; mean fragment sizes were found to be smaller than those from homogeneous ductile metals at comparable strain rates, posing a reduced risk to innocent bystanders if used in munitions. Extensive interface failure was observed which suggested that the interface density of these systems was an important parameter in their fragmentation. Existing fragmentation models for ductile materials did not adequately capture the fragmentation behavior of the structural energetic materials in question. A correction was suggested to modify an existing fragmentation model to expand its applicability to structural energetic materials. Fragment data demonstrated that the structural energetic materials in question provided a significant mass of combustible fragments. The potential combustion enthalpy of these fragments was shown to be significant.

Impact experiments were utilized to study impact induced reaction in the indicated metal+Al SEM systems. Mesoscale parametric simulations of these experiments indicated that the topology of the microstructure constituents, particularly the stronger phase(s), played a significant role in regulating impact induced reactions. Materials in which the hard phase was topologically connected were more likely to react at a lower

impact velocity due to plastic deformation induced temperature increases. When a compliant matrix surrounded stronger, simply connected particles, the compliant matrix accommodated nearly all of the deformation, which limited plastic deformation induced temperature increases in the stronger particles and reduced reactivity. Decreased difference between the strength of the constituents in the material also increased reactivity. The results presented here demonstrate that the fragmentation and reaction of metal+Al structural energetic materials are influenced by composition, microstructure topology, interface density, and constituent mechanical properties.

CHAPTER I

INTRODUCTION

Rapid deformation and fragmentation of materials has been a subject of practical interest and academic study for centuries. Explosive fragmentation of rock for mining purposes has been employed in various forms from the Renaissance until the present day and will continue to be employed for the foreseeable future. Exploding wires have been studied since Nairne's first publication on the topic in 1774 (referenced in [1]). Bertram Hopkinson published work on spall fracture as early as 1910 [2]. Pioneering work on dynamic fracture and fragmentation has been done by Hopkinson, Lineau, Mott, Gurney, and Taylor (cf. [2–6]).

The advent of time resolved measurement capabilities heralded a new era in these studies, where transient states could be captured as well as end states. These newer studies, such as that by Winter and Harding [7] provided a wealth of new information to test existing theories and develop new ones. Similarly, the introduction and proliferation of numerical methods provided new insights into the failure of materials. Despite all these advances, fragmentation remains a rich and challenging phenomena to study because it can occur on length scales ranging from a few atoms to multiple galaxies [8]. Even in common materials, fracture and fragmentation are truly multi-scale events.

The vast majority of the considerable body of literature on fragmentation has been dedicated to homogeneous metal alloys. Gurney [5] and Mott [4] and their collaborators worked during WWII on understanding explosive fragmentation of munitions, and munitions work has continued to the present day. Later work, such as that done by Shockey et al. [9] and Grady and Kipp [10] are typical of efforts to understand the

fragmentation of geomaterials, a topic relating to the extraction of shale oil which was of great interest during the 1970s and early 1980s due to concerns about energy supply and stability. Like other fields of research, the study of fragmentation is often driven by needs of one form or another.

One need that has prompted research on fragmentation is the desire to reduce the hazards of modern munitions to innocent bystanders. Modern warfare, with its use of powerful ordinance, takes a significant toll on innocent life, particularly women and children when it takes place near densely populated areas [11]. Many explosive devices produce high velocity fragments which are able to penetrate walls, as seen in Figure 1.1a, and kill or injure those outside the line of site. Fragments can be dangerous at much greater ranges than blast. This is illustrated in Figure 1.1b, where it can be seen that the distance at which blast is 50 % lethal is almost 200x less than the distance at which different sizes of fragments have kinetic energy comparable to a bullet fired from a large caliber handgun. This understanding has prompted research on reducing the hazards of fragments to innocent bystanders.

One avenue that is being explored to reduce collateral damage is to replace inert munition casings with a *structural energetic material*. In this context structural energetic materials (SEMs), are generally composed of two or more solids which are able to react and release energy during a violent impact [14]. Structural energetic materials are a subset of reactive materials (RMs), which are also composed of reactive mixtures, and are distinguished from reactive materials only by their much greater strength which is usually designed to be roughly equivalent to that of ordinary aluminum alloys. Structural energetic materials are generally designed only to liberate energy during violent impact and are incapable of self-sustaining detonation; when they are subjected to normal handling and storage they are inert and classifiable as USDOT 4.1 flammable solids [15]. This is quite distinct from explosives which are able to undergo a self-sustaining detonation when subjected to an adequate insult.

(a)

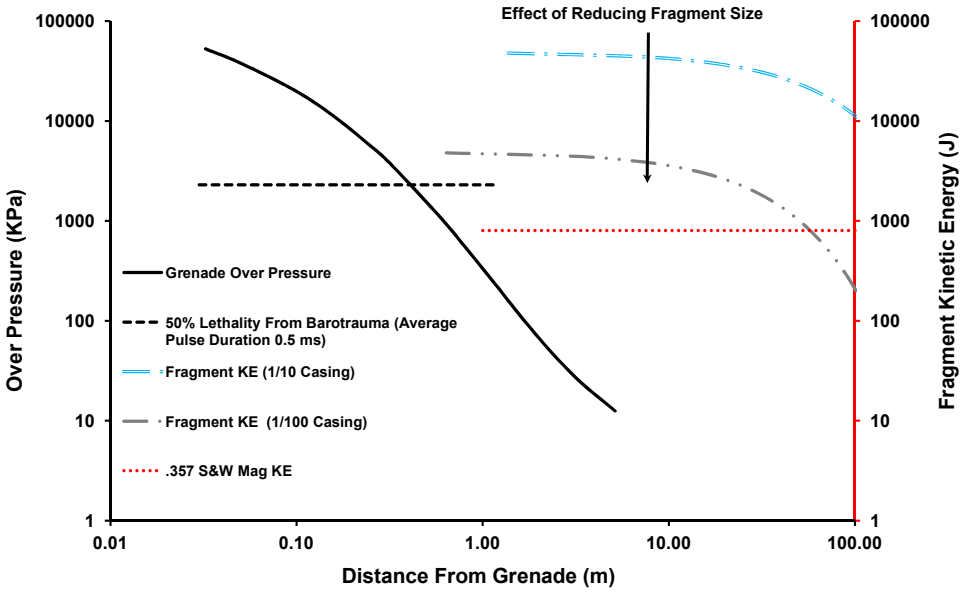

(b)

Figure 1.1: The hazards of fragments to innocent bystanders.[1] (a) Masonry panels perforated by mortar fragments. The mortar fragments may retain significant velocity after penetration [12]. (b) The distance from a grenade over which the pressure is lethal to 50% of people is around 0.3 meters. The distance over which fragments retain greater kinetic energy than a typical 125 grain .357 magnum bullet is almost 100 meters. Fragments are dangerous over a greater distance than blast pressure, which decays rapidly. Notice that as fragment size diminshes, the range over which they remain dangerous also diminishes. The grenade was assumed to be 0.2 Kg of steel containing 0.2 Kg of composition B. The distances and pressures were calculated using data from Cooper [13].

Once motionless, structural energetic materials pose very little hazard to people finding them later. There is also considerable interest in formulating these materials to have biocidal properties or properties suitable for destruction of chemical agents. This unique combination of properties make structural energetic materials suitable for use in certain types of munitions.

Structural energetic materials have also been shown to significantly improve performance of conventional munitions [14]. Blast enhancement has been demonstrated as well as reaction of fragments with target materials as seen in Figure 1.2. A reactive material fragment interacting with a target may transfer both chemical and kinetic energy to the target [14, 16]. The potential effectiveness of reactive fragments is shown in Figure 1.2. The chemical energy that may be transferred is far greater than the kinetic energy alone, sometimes approaching 500% more energy [16]. This staggering increase in the amount of energy coupled into the target potentially makes for a far more effective munition [14, 16].

Serendipitously, the reaction of an energetic fragment may partially or totally consume the fragment according to Aydelotte et al. [17], limiting the lethality of the fragment to people and objects outside of the target zone. Thus structural energetic materials offer a potential path to increased lethality to the target and reduced hazard to the surroundings.

Structural energetic materials have three potential energy release paths: as previously discussed, (i) energy may be released by impact induced reaction of fragments; (ii) energy may be released when a reactive material casing is subjected to the initial shock wave from the high explosives contained in the warhead; and (iii) energy may also be released after reactive material fragments are dispersed into the cloud of hot

[1]Reprinted from *International Journal of Impact Engineering*, vol 35., pp. 1043-1052, 2008, "Standoff-mortar fragment velocity characterization before and after perforating conventional building walls,"' de L.A. de Béjar, L. Simmons, and J.L. Davis, Figure 2, Copyright 2008, with permission from Elsevier.

(a) Damage done to a missile body by inert warhead fragments

(b) Damage done to a missile body by reactive warhead fragments

Figure 1.2: The Effects of reactive fragments on missile components compared with the effects of non-reactive fragments [14].

detonation products to react or combust. Energy release during the propagation of the shock wave through the structural energetic material is termed shock-induced reaction [18].

Shock-induced reactions have been a topic of research in the shock physics community for several decades, and much is known about them and how they proceed. Important contributions have been made by Horie et al. [19], Dunbar et al. [20], and Eakins and Thadhani [21, 22] among many others. Uniaxial strain shock loading in reactive systems has been extensively studied, but uniaxial stress initiation of structural energetic materials has received less scrutiny. Because much attention has already been devoted to shock-induced reactions, they will not be explored in this work except during the literature review to elucidate some important trends.

Little has been done to put combustion behavior of structural energetic materials onto firm footing. Homan et al. [23] and Homan et al. [24] observed fragmentation, impact induced reaction and combustion of structural energetic materials in vented chamber calorimetry tests, as did Ames [15, 25] and Ames and Waggener [16]. However, the focus of these works was global energy output of structural energetic materials, rather than the combustion behavior of reactive material fragments or fragment

forming mechanisms.

Zhang and Wilson [26] observed significant improvement in the amount of energy released during closed chamber tests of an unspecified reactive casing. The authors attributed this to impact induced reaction of fragments, but Zhang and Wilson [26] made no effort to detail the fragment formation mechanisms nor did they suggest a mechanism for the energy release of the fragments. Their focus was also on the global energy output improvement. The fragmentation process and the state of the fragments that are formed from structural energetic materials are poorly understood. There is also a lack of confidence in the ignition of reactive fragments [14] due to uncertainty about the underlying physical properties of the fragments.

The work presented in this thesis focuses on addressing some of the questions that have been raised with regard to the fragmentation of structural energetic materials. Do they fragment in the same manner as homogeneous structural materials such as metals, or are there features unique to structural energetic materials. What role do the properties of the constituents and the microstructure play? What size and size distributions of fragments do structural energetic materials produce? Furthermore, what state of *activation* will the fragments be in, that is, will their condition after formation enhance or detract from fragment reactivity? Lastly, what factors contribute to impact induced reactions of fragments?

The work presented in this dissertation is laid out as follows: Chapter 2 is a detailed review of literature related to structural energetic materials along with a brief description of the systems considered in this work, loading scenarios, shock loading of homogeneous reactive system, and fragmentation. Chapter 3 is a detailed discussion of the structural energetic materials systems described in this work and the experimental and numerical efforts made to characterize them. Chapter 4 provides detailed descriptions of the different fragmentation methods employed to study reactive material systems and the results of those efforts. Chapter 5 discusses experimental and

numerical efforts to study fragment behavior both in terms of the possibility of fragment combustion and impact induced fragment reaction. Chapter 6 is a detailed summary of the conclusions drawn from this body of work and recommendations for future work.

CHAPTER II

BACKGROUND

2.1 Reactive Materials Systems

A considerable body of research exists on reactive material systems. This particular area of research draws a great deal on shock wave propagation studies, especially work on shock loading of porous and reactive mixtures, fragmentation, combustion, and related fields. Reactive materials are distinguished from structural energetic materials by their strength, though they may be identical in composition. The high porosity powder mixtures studied in the shock loading literature have no appreciable structural value. The following literature review is a detailed examination of literature relevant to structural energetic materials, a brief description of the systems considered in this work, loading scenarios, shock loading of homogeneous reactive system, and fragmentation with some limited discussion of metal particle combustion. From the literature review, some pertinent themes will emerge and provide the impetus for the rest of this thesis.

Reactive materials based on metal-polymer composites [15, 16], thermites [27–29], and intermetallic-forming mixtures [30–33] have been studied extensively. Quite a number of different formulations of thermites, intermetallic forming mixtures, and polymer composite systems are potentially available with different densities, reaction temperatures, and other properties [34].

Structural energetic materials (SEMs) systems based on aluminum or boron mixed with higher density metals such as nickel, tantalum, tungsten, etc. are one popular branch of SEM research. They have high densities and good strength as will be shown. They are also quite flexible in actual use in terms of their exact composition,

Table 2.1: Selected reaction or detonation enthalpies for intermetallic systems, high explosives, and aluminum. † taken from Meshel and Kleppa [69], ‡ taken from Chrifi-Alaoui et al. [70], ∗ taken from Dreizin [60], ⋆ from [71].

System	Enthalpy (KJ/g)
WAl_4	0.048†
Ta_2Al	0.051†
NiAl	0.74‡
Cl-20	6.3 ∗
RDX	6.32 ⋆
PETN	6.23 ⋆
HMX	6.19 ⋆
TNT	4.56 ⋆
Al_20_3	31.0 ∗

fabrication methods, and densities. Intermetallic formation reactions do not require oxygen and may initiate at lower temperatures than metal combustion; intermetallic forming reactions release less energy on a per mass basis than high explosives, as seen in Table 2.1. Aluminum and boron combustion are very energetic and greatly exceed the specific energy of common C-N-O high explosives as seen in Table 2.1. It has been postulated that an intermetallic formation reaction may be a catalyst for the more energetic Al or B combustion reaction, and there is some experimental support for this [35, 36]. In the present work, several different structural energetic materials are studied: binary systems which were formed via the explosive compaction of mixtures of Ni+Al, W+Al, and Ta+Al; a binary system formed via gas dynamic cold spray of nickel coated aluminum powder; a ternary system composed of W+Ni+Al formed via explosive compaction; and a quaternary system composed of W+Ni+Zr+Al which was also formed via explosive compaction.

Polymeric systems that oxidize a metal component are widely studied SEMs, but are not germane to the present research. Hence, a detailed discussion of these systems is not included here. The reader is urged to consult the following references for more information [15, 16, 25, 37–44]. Likewise, for information on thermite systems the interested reader is directed toward the included citations [27–29, 45–68].

2.2 Possible Loading Scenarios for Structural Energetic Materials

Several different loading scenarios are relevant to the use and study of SEMs. Certain munitions are designed to explode before impact with a target to disperse fragments or cause a large blast. This would be a scenario in which the structural energetic components would be subjected to shock waves (uniaxial strain loading) as the warhead detonates. As the hot gases expand within the casing, a condition of extreme hoop stress develops which leads to tensile failure and fragmentation. Fragments may strike nearby targets and react, but in a fashion more akin to uniaxial stress loading because of the traction free sides of the fragment. In either case, it is anticipated that structural energetic materials would experience extensive deformation and fragmentation in ordinary service conditions. Existing literature has focused on several areas: shock initiation of reactive materials, uniaxial stress initiation of structural energetic materials, fragmentation, and reaction modeling. Each area will be addressed individually.

2.3 Shock Physics Fundamentals

A few essential concepts of the shock compression of solids and powders will be reviewed in order to expose essential underlying physics and make the literature review more transparent. The following treatment is similar to that by Asay and Shahinpoor [72] and Meyers [73] and derives much from both.

A shock wave, a type of longitudinal wave, is considered to be a discontinuity between thermodynamic variables such as pressure, temperature, and density. Shock waves form due to the attraction and repulsion behavior of atoms. Atoms are surrounded by electron clouds which largely determine the mechanical properties of materials. When subjected to a volumetric compression, these clouds approach one another and begin to interpenetrate. This leads to enormous short range repulsive

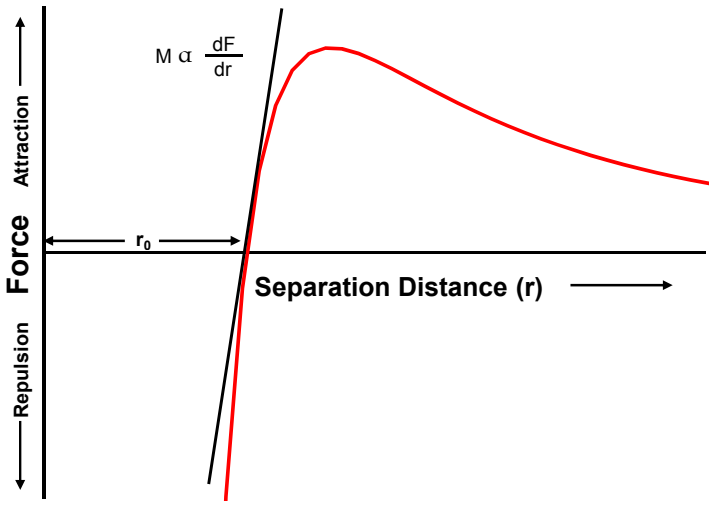

Figure 2.1: Condon-Morse force curve for an elastic material

forces. The Condon-Morse curve, shown schematically in Figure 2.1, illustrates the effect on the interatomic forces of either lengthening or shortening the average bond length between atoms. As compression increases, the repulsive forces increase by approximately r^4 [73]. The bulk modulus, denoted M in Figure 2.1, is required to be positive and proportional to the tangent of the force curve. Therefore, the bulk modulus also increases with increasing compression. Wave speed in an ordinary elastic medium is $C = \sqrt{\frac{M}{\rho}}$, and is a function of the density and the modulus which implies that wave speed increases with increasing pressure. This feature is an essential requirement for a material to be able to support shock waves.

When a uniaxial strain condition is rapidly applied to a real material, the sound speed at peak pressure is higher than at ambient pressure. This allows the peak of the wave to overtake the base of the wave, forming a moving, discontinuous boundary between the higher pressure, temperature, and density region and the ambient pressure region. This discontinuity is the shock wave.

To derive the governing equations for shock waves, a piston with a cross section area A_c, initially at rest, is imagined moving into a compressible, inviscid fluid. A discontinuity moves ahead of the piston. Between the discontinuity and the piston,

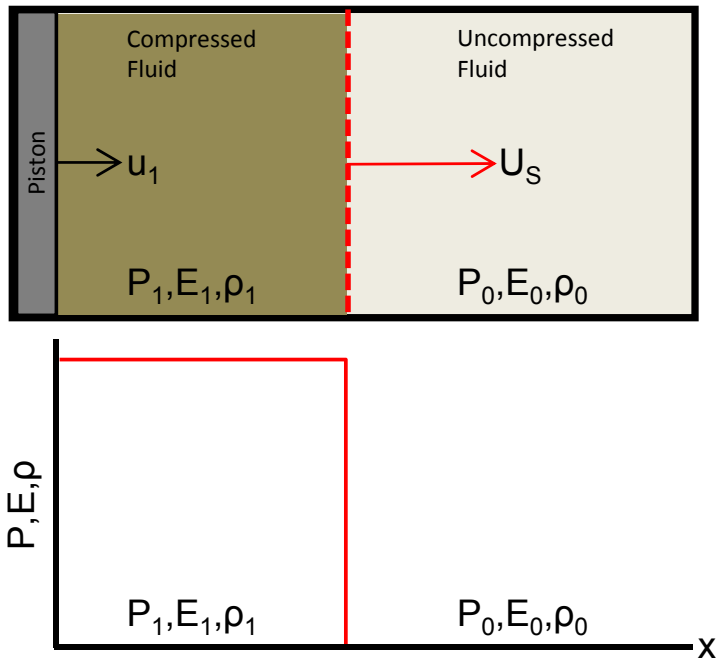

Figure 2.2: A schematic of shock compression of an inviscid fluid.

the fluid is compressed to a higher pressure P_1, density ρ_1, and energy E_1. The piston, and the compressed fluid, move at u_1. Ahead of the discontinuity (the shock wave) the fluid is at rest, $u_0 = 0$, with pressure P_0, density ρ_0, and energy E_0. This is shown schematically in Figure 2.2 The shock wave moves at a velocity of U_S. The mass enveloped by the shock wave in a time increment Δt is $A_c\rho_0 U_s \Delta t$, as only uniaxial deformation is allowed. The mass is conserved behind the shock, its density is increased and its volume decreased so that the mass between the piston and the shock wave is $A_c\rho_1(U_s - u_1)\Delta t$. Equating the two yields

$$\rho_0 U_s = \rho(U_s - u_1). \tag{2.1}$$

This is a statement of the conservation of mass across a shock wave in a Lagrangian reference frame. The net force within the piston-fluid system is $A_C(P - P_0)$ and it is balanced by the time rate of change in momentum of the shocked fluid, which is $\frac{\Delta(mv)}{\Delta t} = \frac{\rho_0 U_S \Delta t A_C(u_1)}{\Delta t}$. Combining these terms and simplifying them results in Eq. 2.2,

the conservation of momentum.

$$P_1 - P_0 = \rho_1 U_s u_1. \tag{2.2}$$

The kinetic energy of the material accelerated to u_1 is $\frac{1}{2}(\rho_0 U_S \Delta t) u_1^2$. The increase in internal energy is $(E_1 - E_0)\rho_0 U_s \Delta t$. The work performed on the system is $(P - P_0)u_1$. Equating the work done by the piston to the kinetic energy of the fluid and the change in internal energy of the fluid yield the conservation of energy, Eq. 2.3.

$$(P - P_0)u_1 = \frac{1}{2}(\rho_0 U_S)u_1^2 + (E_1 - E_0)\rho_0 U_s \tag{2.3}$$

Combining Eq. 2.1, Eq. 2.2, and Eq. 2.3 eliminates the velocity terms and yields Eq. 2.4.

$$(E_1 - E_0) = \frac{1}{2}(V_1 - V_0)(P_1 + P_0) \tag{2.4}$$

The specific volume is defined as $V = 1/\rho$. Eq. 2.1, Eq. 2.2 and Eq. 2.4 are often called the jump conditions because they describe how the system variables change discontinuously across a shock front. These equations need to be combined with the Hugoniot, a subset of the full equation of state, in order to provide enough equations to solve for all of the variables in 1D steady shock propagation of an inviscid fluid. A Hugoniot is a relationship between any two of five equation of state variables P, V, U_S, u, E, though relationships between $P - V$, $P - u$, or $U_S - u$ are particularly useful. In $U_S - u$ space the Hugoniot is often a linear relationship for solids and liquids of the form $U_S = C_0 + Su$. A Hugoniot in $P - V$ space is shown schematically in Figure 2.3. The Hugoniot is considered a material property; it is most often determined through experiments that measure shock wave speed, U_S, and particle velocity, u, or pressure, P, and particle velocity, u. A Hugoniot is not a loading path; it is a locus of end states. The loading path is the Rayleigh line shown in Figure 2.3.

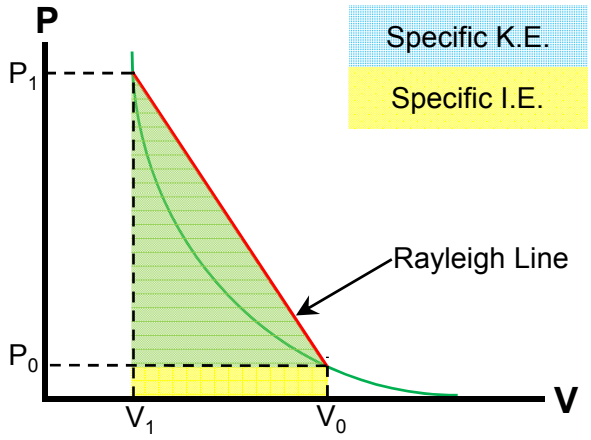

Figure 2.3: A schematic of a Hugoniot in $P-V$ space. The Rayleigh line is indicated as well as the areas representing the specific kinetic energy and specific internal energy increase of the shocked material.

The material *jumps* from ambient conditions to an end state that lies on the Hugoniot following the Rayleigh line.

It was assumed in the treatment above that the shocked material is an inviscid fluid and the shock wave is a true discontinuity, but these assumptions can be relaxed provided P is replaced with σ_x and the wave profile, whether it is discontinuous or not, is time invariant. Obviously, in a solid that can support shear stresses, σ_y and σ_z are not equal to σ_x and are not described by the jump conditions. However, shock pressures quickly exceed the shear strength of most materials by a large margin and the strength of the shocked material can be neglected in many instances. The jump conditions turn out to be an excellent approximation even for unsteady shocks that exist in porous materials and are widely applied to such problems. [72].

As indicated, the Hugoniot is not a complete equation of state, merely a portion of it. It is advantageous to combine the experimentally derived Hugoniot with an equation of state model to yield a complete equation of state for a material. Apparently, the most popular model is the Mie-Grüneisen equation of state. The detailed

development of this model is beyond the scope of this work; the reader is urged to consult McQueen et al. [74] or Meyers [73] for more information. The Mie-Grüneisen equation of state takes the form

$$P - P_{ref} = \frac{\gamma}{V}(E - E_{ref}) \tag{2.5}$$

with P_{ref} and E_{ref} coming from a reference state. The reference state can be determined from an experimentally determined Hugoniot or isentrope. Essentially, the pressure and internal energy off the reference state are related to the pressure and internal energy on the reference state. The difference between the reference and the off-reference states is due to thermal effects which are accounted for by γ, which is termed the Grüneisen coefficient. It is defined as

$$\gamma = V\frac{dP}{dE}\Big|_V \tag{2.6}$$

and is a measure of the change in pressure for a change in internal energy. It can be estimated using the Maxwell's relations to derive

$$\frac{\gamma}{V} = \frac{3\alpha}{C_V K} \tag{2.7}$$

where α is the isobaric coefficient of thermal expansion, C_V is the constant volume heat capacity, and K is the isothermal bulk modulus. The change in γ with pressure is usually estimated using the expression $\frac{\gamma_0}{V_0} = \frac{\gamma}{V}$.

Given the cost and complexity of shock wave experiments, it is not practical to test every real substance to determine its Hugoniot. It is often desirable to estimate the Hugoniot of a material that has not been tested based on existing Hugoniot data for its constituents, for which a number of different schemes have been proposed. The simplest, and perhaps most unrealistic, is the mass averaging or additivity method which has been attributed to Dremin and Karpukin [75, 76]. It assumes that the

specific volume of mixture shocked to a certain pressure is the same as the mass averaged volume of the constituents shocked to the same pressure. This approach does not account for differences in the thermal behavior of the solids under compression which can lead to significant errors; however, it is convenient. This mixture model takes the form $V(P) = \Sigma\chi_i V_i(P)$ where χ_i is the mass fraction and $V_i(P)$ comes from the $P - V$ Hugoniot. The same mixture model can also be applied to predict the Hugoniot in other spaces. The linear $U_S - u$ relationship for mixtures or alloys is sometimes approximated in this manner by mass averaging the bulk sound speed C_0 and S [73].

McQueen et al. [74] improved upon this method by accounting for the effect of shock heating on the constituents. The McQueen mixture theory relies upon constructing the zero kelvin isotherms (or isentrope since at zero kelvin the isentrope and the isotherm are equal) of each material. The isotherms are then mass averaged in the manner described above and then the mixture zero kelvin isotherm is converted to a Hugoniot. The process is somewhat involved and is described in [73, 74]. The resulting mixture Hugoniot is generally a significant improvement upon that obtained by mass averaging alone.

Other mixture theories have been developed, such as that by Baer et al. [77, 78] which estimates the sound speed in a homogeneous mixture using the densities, volume fractions, and sound speeds of the mixture constituents. Grady et al. [79] developed the P-λ model by considering a mixture in which the softer mixture component is supported by a lattice of the stronger component. The shock compression response of the material at low pressures transitions from iso-strain to iso-stress conditions in the P-λ model. It is also possible to construct the Hugoniot of a mixture by using a hydrocode or a finite element code [64, 80]. A representative or notional material microstructure is constructed with a finite element mesh or other computational domain as appropriate and each phase is assigned appropriate constitutive relationships

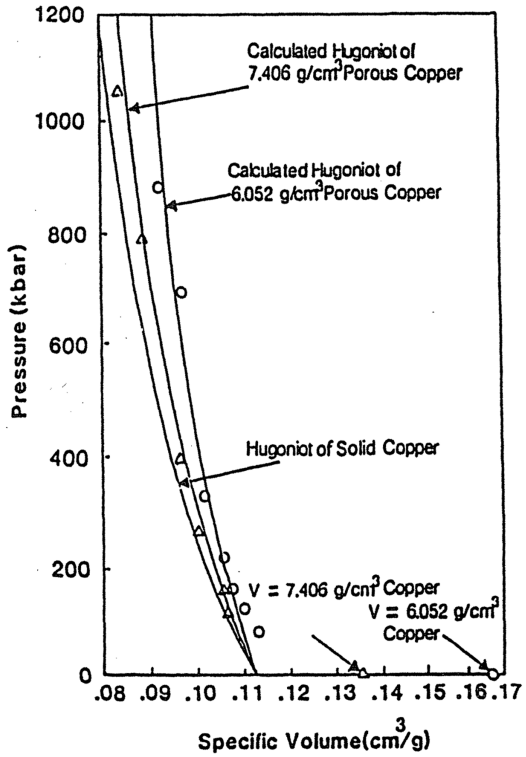

Figure 2.4: Hugoniot of Porous and Solid Copper by Boade [81] [2]

and equations of state. A shock wave is induced in the material, perhaps through a simulated impact or appropriate choice of a boundary condition, and pressure, stress, strain, temperature, and other parameters induced by the shock wave are tabulated. The Hugoniot or a complete equation of state can be determined in this fashion. Obviously, this method is as good or as bad as the models used in the hydrocode or finite element package but can provide very accurate results because it accounts for microstructure properties and material properties in ways that are too complex to be tractable in an analytical model.

Shock compression studies have also been conducted on porous materials such as sintered bodies and powder compacts. Hugoniots of copper at several densities in the $P - V$ space are shown in Figure 2.4. It is impractical to perform shock experiments

[2]Reprinted from *Journal of Applied Physics*, vol 39., pp. 5693-5702, 1968, "Compression of Porous Copper by Shock Waves,"' R.R. Boade, Figure 4, Copyright 1968, with permission from the American Institute of Physics.

on every porous material that might be of interest, a problem similar in scope to that earlier mentioned with alloys and mixtures. Models have been developed to construct the Hugoniot of a porous material (at a given density) from the known Hugoniots of its solid constituents.

The simple mass averaging model can be used, by simply including air as one of the constituents. A porous model may also be formulated using the Mie-Grüneisen EOS model previously defined in Eq. 2.5. In this case, the reference state in the Mie-Grüneisen EOS model becomes the Hugoniot of the solid. The Rankine-Hugoniot jump conditions for a porous material can be written

$$\rho(U_S - u) = \rho_{00} U_S \tag{2.8}$$

$$(P - P_0) = \rho_{00} U_S u \tag{2.9}$$

$$(E - E_0) = \frac{1}{2} P(V_{00} - V) \tag{2.10}$$

where the specific volume is defined as $V_{00} = \frac{\rho_{solid}}{\rho_{porous}} V_0$ and $\rho_{00} = \frac{1}{V_{00}}$. By combining Eq. 2.4, Eq. 2.2, Eq. 2.1, Eq. 2.10, and the Mie-Grüneisen EOS model, Eq. 2.5, it can be shown that

$$P = \frac{[2V - \gamma(V_0 - V)]C_0^2(V_0 - V)}{[2V - \gamma(V_{00} - V)][V_0 - S(V_0 - V)]^2}. \tag{2.11}$$

This expression provides a model for a porous material based on the Hugoniot of the related solid, but it does not address compaction behavior. As seen in Figure 2.4, the calculated powder Hugoniots are reasonably close to the experimental data for the two porous Cu samples except at low pressures. Essentially, the model assumes that compaction takes place at zero pressure. In cases where the crush-up behavior, as compaction is often termed, is important or when the powders have very high strength then the Mie-Grüneisen powder model shown here must be augmented or replaced with a more sophisticated model to address the compaction process. Models

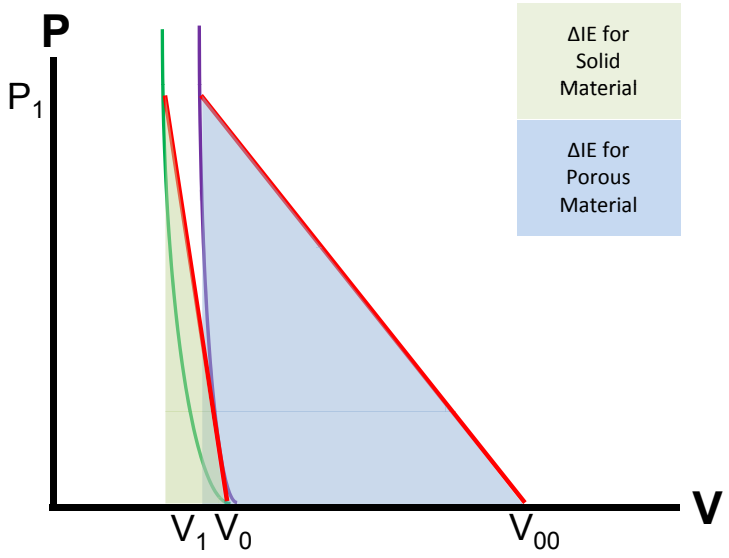

Figure 2.5: A comparison of a Hugoniot in $P - V$ space for a solid material and a porous material. Notice the significantly greater change in internal energy for the porous material. The reference Hugoniots are slightly different due to the temperature increase in the compacted solid due to energy dissipated during compaction.

like Herrmann's [82] P-α or Grady et al.'s [79] P-λ model, with an added porosity phase, are among the more popular models for augmenting an equation of state to address the compaction process in distended materials.

Consider the schematic of a solid and a related porous Hugoniot in $P - V$ space, shown in Figure 2.3, and Eq. 2.4. The triangular area under the Rayleigh line is equal to the change in specific energy of the shocked material. This is true for solids, liquids, gases, porous materials, etc. In the case of $P = 0$, the change in specific kinetic energy is equal to the change in specific internal energy in a shocked material [72]. As shown in Figure 2.5, the change in internal energy for a shocked powder is much larger than that for a solid at a given pressure. The corresponding change in temperature for a shocked powder can be estimated as

$$\Delta T = \frac{(P - P_0)(V_{00} - V)}{2C_p}. \tag{2.12}$$

It is clear from Figure 2.5 and Eq. 2.12 that the temperature change in shocked porous

materials are much higher at a given pressure than for the corresponding solid. This is due to the extensive deformation necessary to close voids in a shocked porous material and the intense adiabatic heating resulting from the densification process. As initial porosity increases, for a given end state shock pressure, the temperature of the shocked material also increases.

2.4 Shock Initiation of Reactive Materials

One possible scenario for the use of SEMs involves releasing energy when subjected to a shock wave produced by the detonation of a high explosive warhead. This would be termed a *shock-induced* reaction if the reaction takes place during loading before the reactive material returns to ambient pressure [18]. It may also be desirable for impact induced reaction to occur, for example in fragment interaction with a target or a structure. Impact of fragments may also lead to shock propagation. Considerable research has been directed toward determining what intrinsic and extrinsic factors influence reaction in intermetallic-forming systems. This research is reviewed below.

The first intentional explosive consolidation of powders leading to the formation of an intermetallic phase that the author is aware of is that of tungsten and aluminum carbides by Horiguchi [83] via explosive compaction in 1966. In the field of intermetallic reactions S, C, and Si are treated as metals. Horie et al. [19] were the first to report synthesizing nickel aluminides via explosive shock compaction of nickel and aluminum powder mixtures. Horie et al. [19] theorized that reaction was induced by plastic deformation and aided by mechanical cleansing of interfaces. Horie et al. [84] also shock compacted two different powder morphologies with the same initial volume fraction of constituents and packing density, and found they possessed different susceptibilities to reaction. During shock compaction powders primarily mix on the surface, thus nickel coated aluminum powder was found to mechanically mix Al and Ni very little since the particle surfaces in contact were all nickel coated. Very little

nickel aluminide was formed. Under the same loading conditions a mixture of Ni and Al powders proved far more reactive, again due to surface mixing. Horie et al. [84] found evidence of fine scale mass mixing at micron length scales that could not be explained by ordinary bulk diffusion processes. Yu and Meyers [85] demonstrated consolidation of Nb+Si, Mo+Si, and Ti+Si silicides as well as reactive consolidation of Nb+Si+$NbSi_2$, Mo+Si+$MoSi_2$, and Ti+Si+Ti_5Si_3. Kelly et al. [86] observed wave like mixing in recovered multi-layer foil samples which were subject to planar impact.

Batsanov et al. [87] reported time-resolved, in situ shock measurements on reactive Sn+S mixtures. Above a certain impact threshold, the Sn+S mixtures deviated from the inert mixture Hugoniot and followed a trend seemingly parallel to the inert Hugoniot but displaced in pressure. Batsanov et al. [87] suggested that velocity gradients between Sn and S due to shock impedance mismatches are responsible for mass mixing and reaction behavior. Dunbar et al. [88] and Thadhani et al. [89] conducted recovery and instrumented plate impact experiments on mixtures of Ti+Si powders. By measuring pressure and shock speed using PVDF gages, they found a large shift in the Hugoniot above a certain pressure threshold indicating a large increase in internal energy which suggests a shock-induced reaction in the mixture of titanium and silicon powders in the medium mixtures (10-45 μm Ti and Si). Coarse (105-149 μm Ti and 45-149 μm Si) and fine (1-3 μm Ti and ¡10 μm Si) mixtures did not show evidence of reaction under similar loading conditions. Similar time resolved data showing shifts in the Hugoniot due to shock induced reactions were published by Yoshida and Thadhani [90], Xu and Thadhani [91, 92], and Eakins and Thadhani [21, 22].

Boslough [93] measured temperature changes in 38% TMD Ni powder and 43% TMD Ni+Al powder impacted at 1.2 km/s by a Cu flyer and backed by LiF windows with a four channel radiation pyrometer. Reasonable agreement was found between P-α model predictions and temperature measurements in the shocked Ni powder.

Temperature measurements in the shock compressed Ni+Al powder mixture showed an average temperature 600 K above the measured temperature in the Ni powder. If the entire sample had reacted, the theoretical energy release can be used to identify an upper bound on the temperature change: the adiabatic reaction temperature. Comparing the measured temperature to the adiabatic reaction temperature, roughly 45% of the powder reacted during shock compression. Next, Boslough [94] measured temperatures for shock induced reaction in Al/Fe_20_3 thermite backed with LiF at impact velocities of 1.2 and 1.3 km/s. At full density, the thermite mixture has a lower shock impedance than the LiF window, therefore the experiment generated two shock waves in the sample, a shock-reshock, which yield two distinct temperature peaks. This suggests that the reaction is shock initiated and then the material begins to cool as diffusion limited reaction takes over. When the remaining reactants are reshocked the reaction drastically speeds up as evidenced by a large temperature increase. Jetté et al. [95] used a two channel pyrometer and thermocouples to make temperature measurements in a large variety of different powder mixtures. They found that, in mixtures that initiated, strong light emission and temperature changes were observed [95]. The light emissions during shock compression were consistent with initiation at hot spots which grew into bulk reactions slowly, long after the shockwave passage [95].

The picture that emerges is that reactive materials react during shock compression above a threshold, though they may not react in their entirety; rather they react initially at hot spots during the passage of the shock wave. That reaction may be quenched if more heat is lost to conduction than is generated or it may become self-sustaining, spreading to unconsumed material after the sample material returns to ambient pressure.

2.4.1 Mechanical Activation of Reactive Materials

2.4.1.1 The Role of Plastic Deformation

It is well known that plastic deformation in metals dissipates energy through formation of defects such as dislocations and twins and through heating of the deformed metal [96–99]. The energy stored as defects is often termed the stored energy of cold work, and it is frequently estimated to be ≈10%. The remaining energy is dissipated through heating of the plastically deformed material [100, 101]. In fact, the amount of energy deposited as cold work or heat is a function of strain and strain rate. It has been shown by Ravichandran et al. [101] in the case of aluminum that the amount of cold work saturates at strains near 1 and that futher deformation only contributes to adiabatically heating the material . Adiabatic heating via plastic deformation may lead to phenomena such as the formation of shear bands which have been experimentally shown to produce temperature increases on the order of 500 C^o [102]. Several researchers [103–105] have noted that plastic deformation plays a role in the reaction initiation of reactive, powder mixtures.

2.4.1.2 Shock Induced Deformation and its Effects

Shock processes are unique because of the high pressures, elevated temperatures, and large levels of shear that are applied rapidly, but exist only for a brief period of time. These conditions lead to significant alteration of the shocked material which can influence subsequent reaction behavior.

Trueb [106] observed extremely high dislocation densities in shocked nickel. The dislocation densities were comparable, though somewhat different in character, to those found in extensively cold rolled Ni. Morosin and Graham [107] found that shocked rutile and alumina powders showed dislocation densities consistent with heavily cold worked metals. Such high dislocation densities contribute to high strength.

Hammetter et al. [108] performed differential thermal analysis (DTA) on Ni+Al

samples from Horie et al.'s [19] experiments. As shown in Figure 2.6, the shocked but unreacted (shock-modified) samples of Ni+Al powder mixtures exhibited a large exotherm at around 450 C^o for Ni+Al, well below the expected reaction exotherm at 660 C^o (the melting point of aluminum). This was attributed to fine scale mechanical mixing of the reactants. The shock-modified composite particles, that proved unreactive in Horie et al.'s [19] experiments, showed much less of the solid state reaction exotherm. Thadhani et al. [109] conducted explosive shock consolidation experiments on five different Ni+Al powder mixtures packed to approximately 60 % density. DTA measurements performed on unreacted regions taken from four samples (the fine mixture reacted completely as did one of the flake Ni+ coarse spherical Al mixtures) showed that the area under the exotherms for all shocked samples are much larger than their respective exotherm in the unshocked state and all are comparable to the largest pre-shock exotherm which occured in the flake Ni+coarse spherical Al mixture. After shock compaction, all of the compacted powders showed large exotherms at temperatures below the pre-shock exotherms consistent with the results of Hammetter et al. [108]. The results suggest that the shock-modified powders were far more reactive and were more likely to react at lower temperatures due to the shock modification. This is attributed to fine scale mixing, extensive deformation, and intimate contact through cleansing oxide layers from interfaces. Similar results were found for the Ti+Si system by Frost et al. [110].

Dunbar et al. [20] studied fine round Ni+Al mixtures, flake Ni+ coarse round Al, and course round Ni+Al mixtures mixed in 3 Ni:1 Al, 1 Ni:1 Al, and 1 Ni:3 Al mole ratios subjected to shock loading. They found that flake Ni mixtures were the most reactive and the coarse mixtures the least. Dunbar et al. [20] also conducted DTA studies and found that unreacted, shock processed mixtures all showed evidence of exotherms below the Al melting point, but the flake Ni mixture showed the largest low temperature exotherm and the coarse powder mixture the smallest. Thadhani

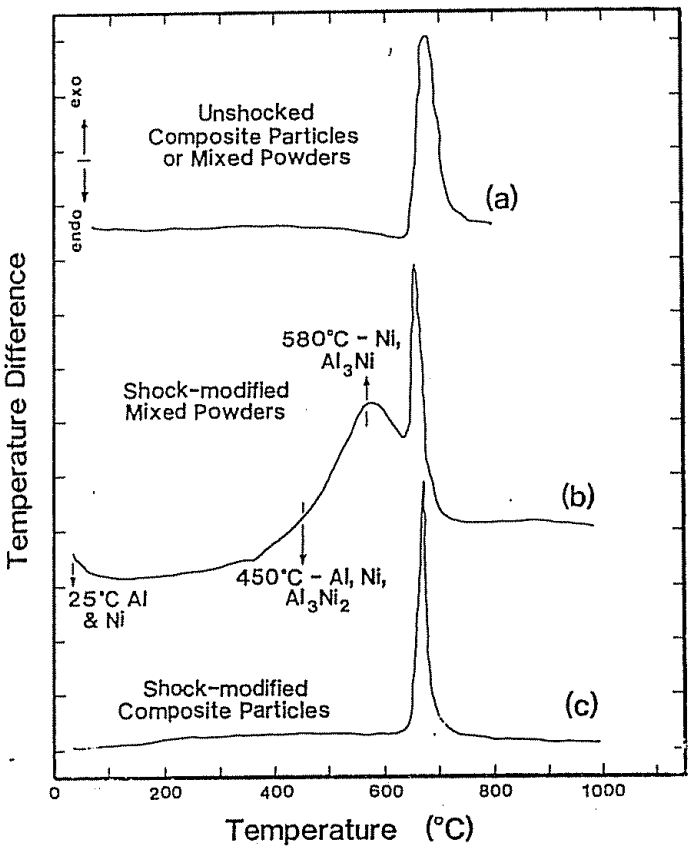

Figure 2.6: Differential Thermal Analysis Traces of Three Different Ni+Al Mixtures from Hammetter et al. [108]. The trace marked (a) is from an unshocked powder mixture and shows no exothermic reaction below the melting point of Al. The trace marked (b) is from a shock compressed mixture of Ni and Al powders. The extensive deformation and intimate mixing provide conditions such that a solid state intermetallic forming reaction can take place below the melting point of Al. Trace (c) is from shock compacted Ni coated Al powders. Shock compacted powders are most extensively deformed on their boundaries. All the boundaries in contact are Ni thus little intimate mixing is achieved despite the significant increase in dislocation density. No solid state reaction is noted.

and Namjoshi [111] found that reaction in shock densified Ti+Si mixtures took place at lower temperatures (beginning in the solid state)than ordinary pressed Ti+Si mixtures and without porosity formation that is typical of self-sustaining reactions. This was attributed to defect enhanced solid state diffusion.

Even when a reaction is not initiated in a shocked powder, pre-processing the material by shock wave leads to enormous increases in dislocation density and fine scale mixing of reactants. Diffusion along dislocations, often called pipe diffusion, can dominate the apparent diffusivity constant of a metal at low temperatures [112]. Extensive plastic deformation, like that experienced by metals subjected to shock waves, provides a dense network of dislocations. Because of this, it is possible to infer that dislocation assisted diffusion can play an important role in shock compacted powders. This leads to enhanced reactivity upon subsequent thermal or physical stimulus and can assist a reaction taking place in the solid state.

2.4.2 Microstructure Effects on Shock Induced Reaction

Microstructure morphology can have a strong effect on shock induced reaction. Morphology is taken to be the collection of metric and topological properties that uniquely quantify a microstructure, such as volume fraction, surface area per unit volume, connectivity, curvature, and others. The following review is closely related to the preceding review; many of the microstructural features that promote shock induced reaction do so by promoting deformation, and mechanical activation is also strongly dependent on deformation.

Song and Thadhani [113] conducted shock loading experiments on a flake Ni + round Al powder mixture and a round Ni + round Al powder mixture at four different impact velocities. They found that Ni flake powder mixtures were more likely to react under shock loading. Song and Thadhani [113] attributed this to increased interface area between constituents in the powder mixture. Eakins and

Thadhani [21, 22, 104, 105] studied shock loading of spherical Ni+spherical Al and flake Ni+spherical Al mixtures using time resolved plate impact experiments and 2D simulations using CTH, an Eulerian hydrocode. They found that flake Ni+spherical Al tended to deviate from inert behavior, evidence of intermetallic formation reaction, but the spherical Ni+spherical Al did not deviate up to the maximum tested pressure [21,22]. Eakins and Thadhani [104] also conducted mesoscale studies using real, imported microstructures of different Ni+Al powder mixtures and found that they were able to reproduce inert shock data. They also observed focused flow and jetting of particles on the mesoscale that may be important mechanisms for promoting shock induced reactions. In computational studies of spherical Ni+spherical Al and flake Ni+spherical Al mixtures, they found that Al in spherical mixtures tended to deform more than spherical Ni particles, while similar levels of strain were observed in Ni and Al in the flake mixtures [105]. They also found that the density of interfaces between Ni and Al increased for all shocked samples, with interface density in the flake mixtures increasing the most [105]. Simulations and limited experimental data were found to be in good agreement for surface area per unit volume measurements [105].

Specht et al. [114] studied shock propagation in Ni+Al laminates and found that the orientation and spacing of the layers can significantly alter the amount of energy dissipated into the material. If the orientation of the layers was parallel with the direction of shock propagation then plastic deformation at the interfaces between Ni/Al increased, leading to more energy dissipation. Such localization of strain can promote interface mixing and reaction.

Xu and Thadhani [91, 92] studied the effect of ball milling Ni+Ti powders on their shock compaction behavior. They found that as ball milling time increased, the pressure required to cause full densification from an initial density of 50% TMD (so called *crush-up strength*) increased, and the change in the Hugoniot from the reaction diminished. The diminishing reaction output was partly from pre-reaction during ball

milling. Work hardening of the powders also inhibited plastic flow and the resulting deformation induced heating.

Reeves et al. [115] conducted DTA on samples of Ni+Al powders ball-milled for different periods of time, Ni+Al nano-powders, and Ni coated Al powder. They found that the ball-milled powders exhibited large exotherms below the Al melting point [115]. The Ni coated Al powder exhibited an exotherm right around the melting point of Al which is expected in undeformed powders. The nano-powder reacted at 562 C^o but this appears to be the result of a lower melting point in the nano-Al, rather than a solid state reaction [115]. Nanometer size powder particles have depressed melting points due to the significant surface energy present. Shear-impact tests were conducted on select powder mixtures. The ball milled powders did not exhibit bulk reactions when impacted [115]; this may be due to extensive work hardening as seen by Xu and Thadhani [91, 92], but this was not addressed by Reeves et al. [115]. The nano-powder mixture was more susceptible to impact induced reaction [115]. Reeves et al. [116] found similar results comparing ball milled powders with nano-scale features to mixtures of Ni+Al powders that were individually nanoscale, though again work hardening was not addressed. The authors attribute the observed effect to small scale, well distributed porosity in the nanoscale powder mixtures.

Yoshida and Thadhani [90] found evidence of melting of Si during shock compaction of the Nb+Si system. Vandersall and Thadhani [117] found evidence of melting of Si during shock compaction of the Mo+Si system. They observed that with increasing shock pressure, the Mo+Si mixture actually deviated strongly toward the liquid Si Hugoniot. Both papers show evidence that premature melting of only one phase can actually hinder reaction. According to Thadhani et al. [89] melting reduces interphase shear stresses, limiting mixing. The formation of a more compliant liquid phase tends to drastically limit deformation in the stiffer unmelted phase, limiting the subsequent induced heating. Tamura and Horie [118] conducted discrete

element simulations of shear band formation and evolution in idealized Nb+Si and Ni+Al systems. They found that melting and the resultant loss of strength in a phase may actually inhibit mixing and subsequent reaction [118].

Nesterenko et al. [103, 119] studied cylindrical powder compaction in Ni+Si and Mo+Si+$MoSi_2$ mixtures. The mixtures were first shocked to compact them and then shocked again to generate shear bands in the compacted mixtures. They observed that reaction only occurred in shear bands that form naturally as a result of the cylindrical compaction geometry. Within the shear bands they observed fine scale mixing and extensive deformation. Yano and Horie [120] studied particle velocity dispersion in the same systems and its possible role in reactant mixing using both an analytical model and a discrete element model. They found that velocity dispersion was greatest in the shock front and was a strong function of the density difference of the constituents. Velocity dispersions between Ni and Al particles separated by a 2 μ m interparticle distance lead to strain rates of approximately 10^7 which is comparable to estimates of strain rates found by Nesterenko et al. [119]. Tamura and Horie's [118] simulations predicted fine scale mass mixing that would lead to reaction if a certain shear strain rate threshold was exceeded. Mass mixing was found sensitive to porosity, which improved it, and constituent ductility, which can facilitate mixing up to a point. Song and Thadhani [113] found that the tendency for reaction at a constant pressure decreases as the initial density increases; this is consistent with the understanding that less energy is deposited in the shocked powder as porosity decreases.

Thadhani et al. [121] found that reaction in the Ti+Si system showed evidence of pulse duration dependence. Longer pulses initiated reactions at higher initial densities. Additional energy from longer pulses deposits more energy into a shocked powder as well as provides increased time at higher temperature and increased time for shock induced mixing to take place, leading to reaction at higher initial powder

densities.

The volume fraction of reactive mixture constituents has been shown to have a significant impact on reaction behavior. Dunbar et al. [20] studied fine, spherical Ni+Al mixtures; flake Ni+ coarse, spherical Al; and coarse, spherical Ni+Al mixtures. The sizes were as follows: the flaky Ni was 44 μm, the fine Ni was 3-7 μm, the coarse Ni was 45-70 μm, the fine Al was 10-20 μm, and the coarse Al was 45-150 μm. These powders were mixed in 3 Ni:1 Al, 1 Ni:1 Al, and 1 Ni:3 Al mole ratios and subjected to shock loading, and it was found that reactivity diminished as the nickel ratio decreased from 3 Ni:1 Al to 1 Ni:3 Al [20]. As the molar ratio of Al increased, the volume fraction of Al increased relative to Ni. With reductions in volume fraction, nickel became increasingly well dispersed in Al, thus the Al deformed preferentially during compaction. The reduction in Ni deformation with increases in Al volume fraction limited the chance of mixing Ni and Al resulting in a diminished likelihood of reaction.

Surface area per unit volume of reactive interfaces is another microstructure property that can strongly influence reaction behavior. Dunbar et al.'s [88] recovery experiments, conducted at approximate loading pressures between 5 and 7.5 GPa, showed that the medium powder (-325 mesh for Si and Ti) was more reactive than either the fine ($\leq$ 10 μm Si and 3 μm Ti) or coarse (45-149 μm Si and 105-149 μm Ti) mixtures. Microstructures of recovered samples showed that the fine powder mixtures had agglomerated, impairing effective mixing of the constituents [89, 122]. Coarse mixtures showed evidence of Si particle fracture rather than plastic deformation of the Si, therefore mixing was limited in the coarse mixture [89, 122]. The medium size powder mixture of 5 Ti+3 Si showed evidence of deformation and fine scale mixing of both phases [89, 122]. Thadhani et al. [109] conducted explosive shock consolidation experiments on five different Ni+Al powder mixtures packed at approximately 60 % density to explore the effects of powder morphology on reaction behavior. The

finest spherical powder mixture and the flake Ni+coarse Al mixture both reacted completely under planar loading. Here the finest spherical powder mixture showed no tendency toward agglomeration. Frost et al. [110] studied the Ti+Si system and found that coarse, 90 μm Ti+15 μm Si particles did not react under tested shock conditions, but 37 μm Ti+15 μm Si and 40 μm Ti+15 μm Si mixtures did. The coarser microstructure of the 90 μm Ti+15 μm Si mixture limited contact between the constituents and mixing.

In summary, a number of microstructure features can affect reaction behavior in shock impact scenarios. Microstructure morphologies that promote plastic deformation in both constituents generally lead to reaction at lower shock pressure inputs. Morphologies that cause deformation in only one of the constituents, require much larger shock energy inputs to cause reaction. Extensively work hardened microstructure constituents do not deform as readily and thus do not lead to the adiabatic heating necessary to cause reaction. Premature melting of one component in a mixture can also limit reactivity; this is due to the increased compliance of the molten phase limiting deformation in the other phase. Porosity enhances reactivity by leading to more intense and localized deformation and mixing. Increasing interface density between the reactants can also enhance reactivity. Solid state reactions in the shocked state are driven by short range mass mixing processes. Increasing the number of interfaces enhances the opportunity for such mixing, making reactions faster and more likely.

2.5 Uniaxial Stress Initiation

Shock initiation is characterized by an initial state of 1D strain and 3D stress. This state of stress is well suited to dynamic experiment and analysis. Uniaxial stress experiments are characterized by a 1D state of stress and 3D state of strain. These experiments may be of longer duration and they are a useful complement to uniaxial

strain data. Much less effort has been made to study this scenario.

The vented chamber calorimetry, or Pig, tests as conducted by Homan et al. [23] and Ames [25] provide a very useful global measure of the amount of energy that can be extracted from an SEM. It does so at the price of confounding combustion and intermetallic formation as well as ignoring details of the fragmentation process and fragment impact. To this end, Du and Thadhani [123] and Du et al. [124] utilized a simplified variation of this test, the rod-on-anvil impact experiment. It simulates fragment impact against a rigid surface. Small samples of structural energetic materials were mounted on metal or plastic rods and then propelled into a rigid anvil in an experiment chamber with a controllable atmosphere. High speed photography captured evidence of reaction and small samples of deformed material were recovered for characterization from the rigid anvil. Du and Thadhani [123] studied the reaction initiation of samples of Ni+Al, Ta+Al, Nb+Al, Mo+Al, and W+Al pressed to 90% of theoretical density attached to Cu, Al, and polycarbonate rods. They observed that samples did not react upon impact, but only after severe deformation against the anvil. They developed a relationship between volumetric strain and equilibrated sample pressure, and found that each sample showed a unique reaction threshold in that space. This suggests that plastic deformation is a key element of reaction in the uniaxial stress impact of these intermetallic forming systems, just as it was in the uniaxial strain shock compression scenario.

Du et al. [124] performed double tube explosive compaction of Ni+Al, Ta+Al, Nb+Al, Mo+Al, and W+Al powder mixtures to get dense, unreacted samples at or above 94% of theoretical density. Samples were cut from these and mounted on copper rods for rod on anvil experiments. The experiments were conducted at a variety of different impact velocities in vacuum held around 50 mtorr. It was determined that Ta+Al had the lowest reaction threshold of all of these materials, then Nb+Al, Mo+Al, and W+Al in order. Ni+Al did not react under the tested conditions. These

results will be explored more fully in Chapter 5.

Hunt and Pantoya [125] conducted drop weight impact tests on Ti+Al, Ni+Al, Zn+Al, Hf+Al, and W+Al mixtures while varying powder compact density and Al particle size between 10 μm and 50 nm. The other powders were nanometer scale except W, which was 1μm average size. They found that increasing the density of the samples increased sensitivity to impact [125], the opposite trend than is expected for uni-axial strain deformation of reactive powders. They also found that reducing Al particle size improved sensitivity to reaction in Ti+Al, Ni+Al, and Zn+Al, but not in W+Al and Hf+Al [125]. Herbold et al. [126] compared the effects of ball milling time and powder packing density for 50μm Al+5-15μm Ni and 2 μm Al+100 μm Ni. They found that there is an optimal sample packing density versus ball milling time that gives the lowest reaction threshold; the optimal percentage of theoretical mass density found was the highest tested, so it is possible a higher density would have been still more reactive. For any fixed milling time, it was found that increasing the percentage of theoretical mass density reduced the impact velocity for reaction. However, excessive ball milling leads to deleterious amounts of work hardening and processing induced reaction and so the ball milling process becomes a competition between microstructure refinement, hardening, and pre-reaction. Chiu and Nesterenko [127], Chiu et al. [128], Olney et al. [129], Chiu et al. [130], and Olney et al. [131] studied the strength and deformation of cold isostatically pressed and hot isostatically pressed W+Al composites. Simulations on several different microstructure instantiations reveal that shear bands form more readily in samples with no porosity that are well bonded. Porosity allows particles to rearrange, limiting shear band formation and shear cracking [129]. Olney et al. [129] also found that shear bands tend to kink around W particles, rather than deforming them . Chiu et al. [130] observed shear cracking and failure that is consistent with the simulated results of Olney et al. [129]. These results are consistent with Hunt and Pantoya [125] and Herbold et al. [126].

Porosity in a uniaxial stress configuration provides deformation paths that result in little plastic strain.

Wei et al. [132] studied static and dynamic compression of Ni+Al, W+Al, Mo+Al, Nb+Al, and Ta+Al. They found that materials in which Al appeared to be the matrix or binder phase, such as Ni+Al and W+Al, have much lower strength and lower rate sensitivity than Mo+Al, Nb+Al, and Ta+Al where the non-Al phase appears to be the matrix phase [132].

Spey [133] in studying mechanically induced ignition in nanoscale reactive foils via a rotating metal arm found that, ceteris paribus, impact energy leading to reaction was proportional to the spacing of the layers. Similar results were found for thermal initiation of reactive foils by Adams et al. [134].

As with shock induced reaction in structural energetic materials, plastic deformation plays a key role in uniaxial stress initiation of structural energetic materials. Rod-on-anvil tests demonstrate that samples with a higher packing density are more likely to react. Computational and experimental studies show that porosity limits plastic deformation in this impact scenario by providing alternate means of deformation that does not dissipate energy into the material as heat. Increasing interface density shows a tendency to reduce the energy necessary to initiate reaction. It was also seen that the matrix material strongly influences the mechanical properties of metal based structural energetic materials. This will be explored in more detail later.

2.6 Complex Loading Experiments

Shock initiation is characterized by an initial state of 1D strain and 3D stress. This state of stress is analytically tractable and the information gained from it is straightforward to use in an equation of state model. Uniaxial stress is similarly straightforward. Considerable work has been done with more complex loading conditions. Most notable are the vented chamber calorimetry experiments done by researchers

at the Navy and Army laboratories. These experiments involve complex loading and provide a global measure of energy output from SEMs.

Ames [15, 25] and Ames and Waggener [16] first published work on the vented chamber calorimetry experiments using an experimental chamber they termed the Blue Pig. Their work on fluorinated polymer+metal systems was designed to study the reaction behavior of structural energetic material . This was done by shooting an SEM sample through a thin steel sheet, causing it to fragment, into an experiment chamber where the subsequent reaction and energy release of the fragments after they impact a rigid anvil was monitored via pressure gages [25]. This test provided a measure of the total energy output of the SEM fragments based on energy deposited by the reacting and combusting fragments into the air of the chamber [15, 25].

Homan et al. [23], Homan et al. [24], and Densmore et al. [135] conducted tests similar to those described in Ames [25] with the addition of high brightness imaging to view the fragments and shock waves in the ambient air more clearly, X-ray images to view the fragments, and two camera spatial pyrometry to measure temperature in the combusting cloud. Their experiment was dubbed the Green Pig test [23]. Ni+Al samples made by pressing with various metal additives and a pure Ni+Al sample made by gas dynamic cold spray were propelled through a thin sheet to cause fragmentation and then subsequent impact on a rigid anvil and reaction was monitored. They found that the heavier fragments impact first, react, and then ignite the trailing cloud of smaller fragments. This picture is quite consistent for different structural energetic materials. They also found that adding Cu powder, which may depress the melting point of aluminum, had a significant impact on the late time combustion behavior and increased the combustion temperature.

2.7 Fragmentation

2.7.1 Influence of Fragment Size and Composition on Combustion Behavior

The combustion of aluminum is of great technical interest. It has been common practice to include aluminum in some explosive formulations since World War II when the British developed Torpex, a mixture of RDX, TNT, and Al powder, in mid-1942 for use in mines and torpedoes [136]. Tritonal, a mixture of TNT and Al powder, was developed and used as a bomb filler [136]. It was found that Al significantly improved the energy output and the pressure pulse duration of explosives due to the reaction of Al with the surrounding air. Aluminum has also been added to propellants at least as early as the 1950s, because it was realized that large amounts of Al powder increase the specific impulse of solid fuel boosters [137]. It will be seen in Chapter 4 that fragmentation of structural energetic materials yield small fragments which often consist of a great deal of exposed Al. It is reasonable to consider aluminum combustion as a starting point for combustion behavior of structural energetic material fragments.

As aluminum is more finely divided, it becomes more reactive. It is generally believed that this is a result of decreased particle sizes giving a larger surface area to mass ratio and providing more surface area for oxygen diffusion to take place [138]. As particle size decreases, the ignition energy also decreases [139]. The ignition temperature requirements are found to be nearly the melting point of aluminum oxide for particles larger than 100μm and between 1300 and 2300 K for particles between 1μm and 100μm. The ignition temperature for Al particles between 10 and 60 μm is 1700 - 2200 K as reported by Brooks and Beckstead [140]. The ignition temperature goes down to 900 K for nanometer scale Al particles [141].

There remains healthy debate and uncertainty concerning many aspects of aluminum combustion, especially the ignition process [140,142]. Difficulties stem in part from applying experiments in ambient conditions to the high pressure, hot, turbulent

environment of a rocket motor or explosive fireball and in part from a wide variety of different techniques that have been used to study Al combustion [140, 142]. Some researchers have contended that Al combustion cannot take place until the oxide shell has melted, while other work has shown that the oxide layer may fail by mechanical means, and still others contend that self-heating of the particle takes place when oxygen diffuses through the oxide shell to react [140,142]. Research seems to indicate that the destruction of the oxide coating, rather than melting, is what precedes combustion [140, 142]. This destruction can apparently take place via thermal mismatch causing fracture in the alumina layer upon rapid heating of the particle or some other mechanical loading [140,142]. Mechanical loading leading to fracture of oxide surfaces is expected to be important to the combustion of structural energetic materials .

Once ignited, the aluminum combusts in the vapor phase. The combustion time is proportional to D^2 [142], where D is the original particle diameter, for a wide variety of different kinds of test methodologies and particle sizes, though there is considerable scatter in the data as evident in Figure 2.7b. Once combustion begins, a flame zone develops around the particle where the vaporized Al and the oxidizer mix and combust [140]. The aluminum oxide product can form a particulate smoke or condense on the Al particle, contributing to the growth of an oxide cap which can function as a heat sink. The oxide cap may also inhibit combustion underneath the cap [140]. These effects increasingly tend to impede combustion as the burning of the Al particle proceeds.

Reducing particle size in closed pressure vessel powder combustion experiments increases both the peak pressure and reduces the rise time of the pressure pulse, both of which tend to increase the violence of an explosion [139, 143]. Iron particle combustion data shown in Figure 2.7a illustrates this effect. Reduced aluminum particle sizes also increase the flame speed of the combustion reaction [141].

Particle agglomeration effects can play an important role in combustion behavior.

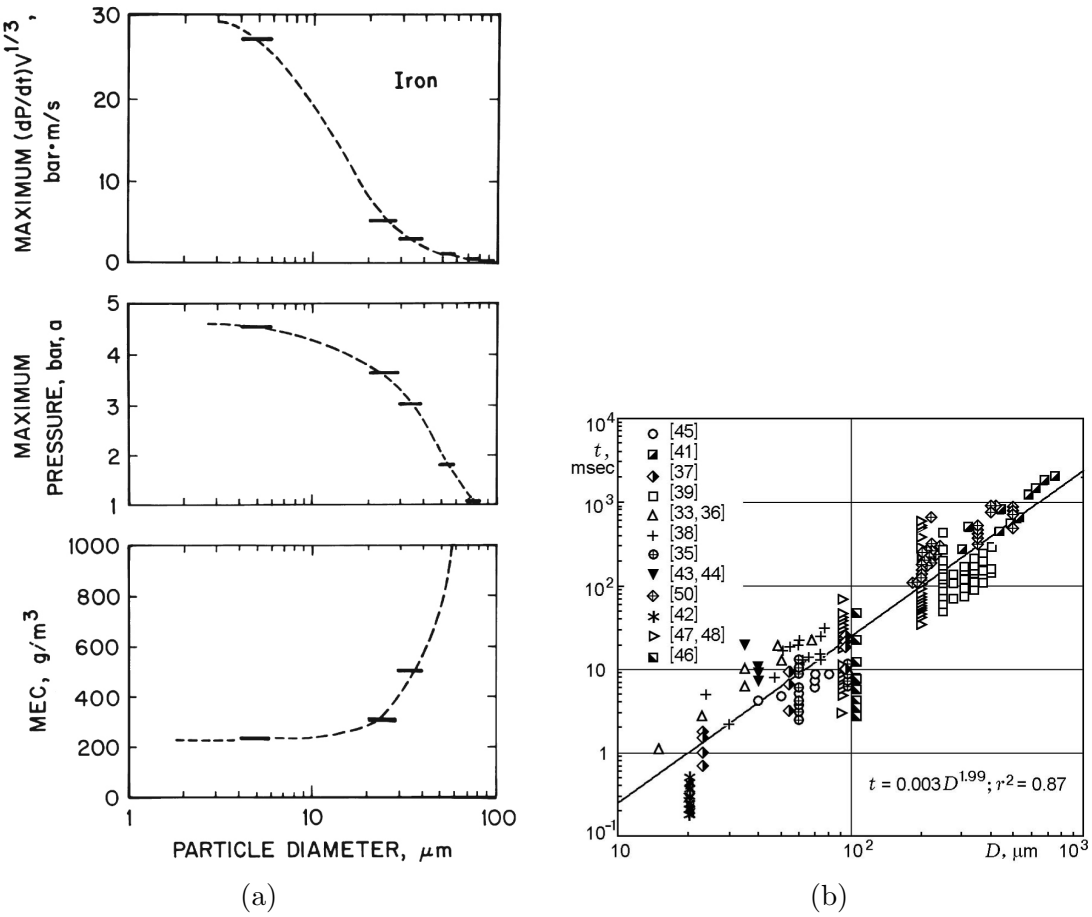

(a) (b)

Figure 2.7: (a)The effect of iron particle size on the volume normalized maximum rate of pressure rise $\left(\frac{dP}{dt}|_{max}V^{1/3}\right)$, the maximum pressure ($P$), and the minimum explosible concentration (MEC).[3] This data shows trends typical of metals. (b) Aluminum combustion time versus particle size.[4] The trends here are also typical of metals and demonstrate that combustion times decline dramatically as particle size is reduced.

In a study of the combustion of spherical versus plate-shaped particles, the spherical particles actually provided faster pressure rise times than flake powders notwithstanding the fact that the flake powders which were considered possessed a specific surface area several times greater than the spherical powders [144]. This result, which initially appears inconsistent with the D^2 law, was believed to be the result of particle agglomeration in the flake powders [144]. Frost et al. [145] studied the critical conditions for ignition of packed beds of Al particles from 3-114 μm in size saturated with Nitromethane sensitized with 10% Triethylamine. They found that that 54 μm size Al particles allowed the smallest critical diameter for complete detonation [145], though they tested particles as large as 114 μm. This result, which also appears to be inconsistent with the D^2 law, is likely a result of particle agglomeration.

According to the D^2 law, a 50% reduction in particle size leads to a 400% reduction in burn time. Fragment size will be critical to combustion behavior and an essential fragment property to characterize.

2.7.1.1 Combustion of Composite Particles

Al combustion is the most widely researched topic in metal combustion. However, coated particles and combustion behavior of other metals have also been studied. The structural energetic materials in this work are composite materials and their combustion behavior is likely to be influenced by their constituents.

There exists a limited body of work on the combustion of Ni coated Al particles, with thin coatings. Brieter et al. [146] found that coating Al particles $\leq 50\mu$m with 0.01 to 0.1μm of Fe, Cu, or Ni significantly improves combustion front velocity in the aluminum+perchlorate system. Fe, Cu, and Ni all have higher melting points than

[3]Reprinted from *Journal of Loss Prevention in the Process Industries*, vol 13., pp. 183-199, 2000, "Overview of dust explosibility characteristics," K.L. Cashdollar, Figure 12, Copyright 2000, with permission from Elsevier.

[4]Reprinted from *Combustion, Explosion and Shock Waves*, vol. 41, pp.533-546, 2005, "Correlating Aluminum Burn Times," M.W. Beckstead, Figure 1, Copyright 2005, with permission from Springer Science and Business Media.

the combustion temperature of the aluminum+perchlorate fuel system. Metals with lower melting points do not help the agglomeration problem or do so very little as in the case of Mg and Bi [146]. Yagodnikov and Voronetskii [147] studied the combustion of aerosolized Ni coated Al particles with different coating thicknesses. For coating thicknesses of 57 angstroms, the combustion flame speed was up to four times faster than in pure aluminum [147]. This was determined to be a result of the thermal mismatch between the Ni and Al, leading to fracture and peeling of the Ni coating after a very brief initial latency period and exposing the unoxidized Al for rapid combustion [147]. Increasing coating thickness tended to reduce the flame speed [147]. Vummidi et al. [148] studied combustion of uncoated and Ni coated Al powders. The coating in this case was very thin and discontinuous and the particles consisted of 5 wt.% Ni [148]. They found that the total overpressure of constant volume explosion experiments was essentially similar for both powders, but the latency period before combustion for the uncoated Al was much longer [148]. They also found the ignition temperature of Ni coated powders was lower than that of uncoated Al powder [148].

Mukayasyan et al. [149] studied reaction fronts in different packing densities of Ni coated Al particles. Here the coating thickness was 7μm or 67.7 wt % Ni. They found that reaction begins at the melting point of Al. The reaction rate of Ni coated Al columns increased dramatically above 68% packing density due to the change from gas phase heat transfer to solid state heat conduction. Furthermore, it was found that the Ni coating prevents particle agglomeration. They also demonstrated self propagating combustion of aerosol clouds of Ni coated Al particles in an inert atmosphere, obviously the product of an intermetallic forming reaction. Shafirovich et al. [150] conducted a detailed study of levitated, single particle combustion in Ni coated Al particles as well as careful bulk sample heating studies [150]. They found that Ni coated Al particles react in all tested atmospheres, whether pure O_2 or in Argon, though with differing reaction temperatures after an initial latency period

that was required to break through the Ni coating [150]. They also found that the reaction of the particles began at the melting point of Al, suggesting an intermetallic forming reaction. Based on their bulk pressed sample studies and photography of individual reacting particles, they concluded that the reaction path of Ni coated Al particles in air begins with intermetallic reaction initiation at the melting point of Al, then the Ni shell cracks, and the molten Al spreads over the particle leading to greatly increased rate of intermetallic formation reaction and ignition of Al combustion [150]. Al has a lower adiabatic flame temperature in air and the Ni vapor pressure is an order of magnitude lower than that of Al; this means that the Al is combusting by itself initially [150]. The Ni begins to combust and continues after the Al is consumed. Shoshin et al. [151], in work on Ti+Al mechanical mixtures, showed convincing evidence of an intermetallic reaction fostering Al combustion which is consistent in principle with the results of Shafirovich et al. [150].

Particles formed purely from metals other than Al are not likely to contribute much to the explosibility of the debris cloud from the structural energetic material. When subjected to closed vessel explosibility tests , Nickel particles above 6μm in size and tungsten particles above 10μm in size did not combust under any condition when tested [143]. Combusting tantalum particles produce a pressure wave rise time that is an order of magnitude slower than that from equivalent aluminum particles [152]. Tungsten and tantalum require higher minimum concentrations of particles per unit volume to ignite than aluminum and have lower combustion temperatures [143].

Composite particles can possess superior properties to uncoated Al particles. Thin coatings of Ni on Al particles lead to shorter latency periods and equal or greater pressure changes and flame speeds in Ni coated Al particles when compared with uncoated Al particles. Thicker Ni coatings can lead to intermetallic reactions and can sustain a reaction even in an inert atmosphere. Furthermore, there is evidence that intermetallic forming reactions can assist combustion [35, 36].

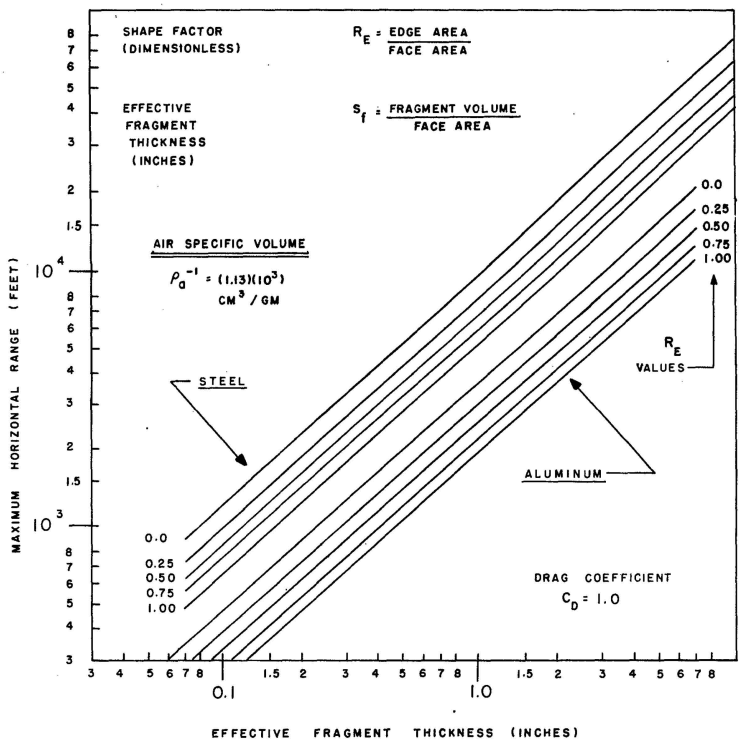

Figure 2.8: Maximum distance for flight of aluminum and steel fragments [155]

2.7.2 Influence of Fragment Size on Fragment Flight Distance

In the scenario where reaction would occur when reactive fragments impact a target surface, the likelihood of reaction increases with velocity. Fragments moving through a fluid are subject to drag, or resistance to motion, from the shear stress of the fluid on the object (generally low for non-streamlined objects), pressure drag due to the pressure on the fragment due to the applied dynamic fluid pressure, and drag due to turbulence behind the fragment [153, 154].

For high Reynolds number flows, like those expected at high fragment velocities, it is known that object shape contributes to pressure drag or form drag [153]. Pressure drag depends primarily on the shape and size of the object [153, 154]. The drag coefficient of a cylinder may be as much as a factor of two larger than that of a sphere [154]. The drag coefficient of a cube may also be two times as large as that of a sphere [154].

Size and mass are also important for pressure drag [154]. Small fragments slow down rapidly in air. This is shown graphically in Figure 2.8 which is a plot of maximum flight distance of aluminum and steel fragments versus their size. Clearly fragment size and fragment density drastically alter the distance a fragment may travel. Bishop [155] found that fragment size is the single most important factor in determining the maximum range of a fragment. Given that one possible application of reactive fragments is to mitigate hazards to innocent bystanders, it is desirable to quantify, and if possible control, the size distribution of fragments to mitigate hazards to by standers and as well as to control how the reactive material's energy is deposited and what effect it will have. The fragmentation process in structural energetic materials will be addressed in some detail in Chapter 4.

2.7.3 Review of Fragmentation Experiment and Theory

A number of experimental techniques have been utilized to study fragmentation including explosive fragmentation, fragmentation using an induced current, and fragmentation using gas guns. A review of the fragmentation literature is presented to cover the most relevant contributions to experimental and theoretical fragmentation studies.

Explosive fragmentation of metallic rings and shells has been a common ordinance test for decades . Mott [4,156] utilized ring bombs and other larger bombs to study the fragmentation process during his time working in the UK for the Ministry of Supply during WWII. The efforts of Gurney and Sarmousakis [5, 157] are representative of efforts in the US during WWII to study fragmentation. The early studies are characterized by the volume of testing and by the absence of time resolved diagnostics. Explosive ring and shell fragmentation is less popular due to the costs and hazards associated with handling explosives as well as the large arenas used for testing, but it remains the premier way to access the highest strain rates. Perrone [158] adapted

the explosive expansion test to measure the constitutive properties of metals at high strain rates by using high speed photography to capture ring motion. Ring velocity is related to its internal stress when the ring is traction-free. By containing the explosive within a metal tube and placing sample rings on the tube, the sample ring is buffered somewhat and contains the explosive gases, for a time at least, which lends itself better to using optical diagnostic tools such as VISAR, PDV, or high speed photography. Forrestal et al. [159] used a cleaver initiation technique to give uniform expansion of 304 Stainless cylinders for studies of plasticity and fracture. More recently, Hiroe et al. [160] and Hiroe et al. [161] adapted Perrone's [158] technique for fragmentation of multiple rings.

Niordsen [162] pioneered the expanding electromagnetic ring technique, which relies on inducing a current in a conductive test ring to cause expansion. A capacitor is discharged into a coil wound without pitch. The coil induces a current in a conductive ring that is mounted on the coil, separated by an insulating layer, and the resulting repulsion pushes the ring outward away from the coil, loading it to fragmentation at strain rates up to 10^4. This technique has several advantages: no explosive handling required (though the high current power supplies may be just as dangerous if not more so), no shock preconditioning of the material to be fragmented, and fine control of strain and strain rate. The temperature change in the sample ring due to the high currents has not been measured and may be an issue. Niordsen [162] showed the capability of this scheme of loading but only made some preliminary observations, showing that fracture occurred after shear localization in cylindrical aluminum samples. Walling and Forrestal [163] used the same technique to study constitutive behavior in aluminum rings.

Grady and Benson [164] utilized the same technique to fragment thin rings of aluminum 1100-0 and OFHC copper. Their data has been the most referenced in the ductile ring fragmentation literature. Grady and Benson [164] observed that the

fractures in the rings were always preceded by necking. They also noted that fragments contained necks that did not lead to failure providing important experimental evidence of Mott's essential idea that fragmentation is a competition between release waves and fractures [164]. Grady and Benson [164] also developed a measure of strain at failure that was based simply on the total length of the fragments from any test. Based on this measure of strain, an apparent increase in the strain to fracture was noted.

Zhang and Ravi-Chandar [165–167] published a series of papers on expanding ring fragmentation from 2006 to 2009. They utilized the electromagnetic expanding ring technique of Niordsen in conjunction with high quality, high speed imaging to capture very detailed, time resolved information for expanding ring fragmentation experiments in 1100 aluminum, 6061 aluminum, and OFHC copper. Zhang and Ravi-Chandar [165–167] made a number of important observations and were able to show that the apparent increase in failure strain that other authors have observed is simply the result of averaging strain over necked regions which form in greater number with increasing strain rate [165–167]. The uniformly strained regions of the rings were found to strain to a nearly constant value prior to necking that is well predicted by the Considére criterion regardless of the strain rate [165–167]. They also showed that necking begins at numerous locations independently of each other, with a statistical distribution of distances between necks [165–167]. However, rings wide enough for sheet necking or shear banding did show strain rate dependence for the onset of nucleation that was related to the time required for the strain localization to traverse the specimen [165–167]. The distance between necks versus the number of necks was found to be well fit by a Rayleigh distribution, a result also found for brittle materials by Zhou et al. [168, 169] suggesting that fragmentation is influenced by pre-existing flaws or defects of some kind in both cases.

Winter [170] and later Vogler et al. [171] utilized a laboratory gas gun to study

fragmentation in metal cylinders. The gas gun was utilized to drive a projectile into a tube partially filled with an elastomer, polymer, or soft metal. The tube, the sample material of interest, was fragmented by the pressure exerted by the fill material as it was deformed by the projectile, due to volume conservation. Winter's [170] technique was convenient because it utilized a gas gun, was readily instrumented with techniques like VISAR and high speed photography, the experiment could be readily contained, and the strain rate was easily and repeatably varied. The drawback is that the sample, a cylinder, is not uniformly strained. Winter [170] was the first to verify Mott's supposition about fractures appearing at different times during the fragmentation event experimentally. Vogler et al. [171] published fragmentation data for Aermet and Uranium alloy cylinders as well as VISAR traces for the experiments.

2.7.4 Analytical Fragmentation Modeling Approaches

Along with the decades of testing that has taken place in the study of fragmentation, there has been a corresponding effort to develop analytical models of the fragmentation process. Many researchers have made contributions here as well, and several models are documented below.

2.7.4.1 Energetic Fragmentation Models

The fragmentation model of Grady [172] was developed by considering an equilibrium balance between the local kinetic energy density of a fragment relative to the center of mass of the fragment, $T = \frac{3\dot{\rho}}{10A^2\rho}$, and the surface energy density of the fragment, $\Gamma = A\gamma$ (see Figure 2.9a); The kinetic energy of the center of mass of the fragment remains unchanged. The strength of the unfragmented body is neglected. It is assumed that the fragmentation process seeks to minimize the total energy

$$E = \frac{3\dot{\rho}^2}{10\rho A^2} + \gamma A \tag{2.13}$$

where $A = \frac{3}{r_{sphere}}$ and is the fragment surface to volume ratio. Given that $\dot{\epsilon} = \frac{\dot{\rho}}{3\rho}$, from

the definition of logarithmic strain, $\dot{r} = \frac{\dot{\rho}}{3\rho} r$ which comes from the time derivative of mass and the conservation of mass, and surface energy $\gamma = \frac{K_{IC}}{2\rho C}$ which comes from fracture mechanics $K_C = \sqrt{\kappa 2\gamma}$, and that change in energy with respect to the change in area gives an average spherical particle diameter of

$$d = \left(\frac{\sqrt{20} K_{IC}}{C \dot{\epsilon} \rho} \right)^{\frac{2}{3}} \tag{2.14}$$

where C is the sound speed, κ is the appropriate elastic modulus, T is kinetic energy density, ρ is density, K_{IC} is the mode I critical fracture toughness, Γ is the total fracture surface energy, γ is the fracture surface energy per unit area, ϵ is the strain, and time derivatives are denoted by a dot $(\dot{\cdot})$.

The Grady [172] model is straightforward but provides only an average fragment size and neglects many of the details of the fracture process. Use of K_{IC} in this fashion is also not strictly correct; K_{IC} depends on a fully developed stress field which is certainly not the case in a fragmenting body. However, it does give reasonable agreement with fragment data and is easy to use [172].

Glenn and Chudnovsky [173] revised Grady's [172] model to include stored strain energy and correct an error in the kinetic energy term. For the case of no strength that Grady considered, Glenn and Chudnovsky found that the average spherical fragment diameter for the no strength case (the same as that considered by Grady) is

$$d = \left(\frac{\sqrt{40} K_{IC}}{C \dot{\epsilon} \rho} \right)^{\frac{2}{3}} \tag{2.15}$$

which is $2^{1/3}$ greater than Grady [172] (all the variables have the same meaning as before). For the more general case where strain energy is included and fracture happens at some critical stress σ_c, Glenn and Chudnovsky found that

$$d = 4\sqrt{\frac{\alpha}{3}} \sinh \frac{\phi}{3} \tag{2.16}$$

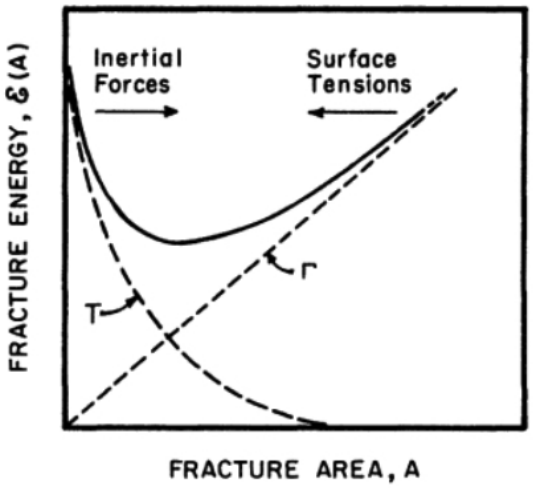

(a)

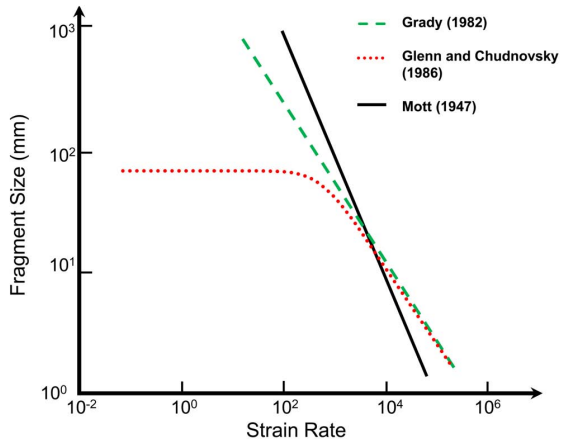

(b)

Figure 2.9: (a)Fracture energy versus fracture area showing the competing influences of surface energy, Γ, and kinetic energy, T [172]. Grady's model minimizes their sum to find a fragment size. (b) Grady's energy model and Glenn and Chudnovsky's model give converging predictions at high strain rates, but at low strain rates Glenn and Chudnovsky's model approaches rate independence.

$$\phi = \sinh^{-1}\left(\beta(\frac{3}{\alpha})^{\frac{3}{2}}\right) \tag{2.17}$$

$$\beta = \frac{5K_{IC}^2}{2\rho^2 C_{long}^2 \dot{\epsilon}^2} \tag{2.18}$$

$$\alpha = \frac{2\beta}{R} + \frac{5\sigma_c^2}{3\rho^2 C_{long}^2 \dot{\epsilon}^2} h \tag{2.19}$$

where R is the original radius of the body and the rest of the variables have their usual meaning.

At low strain rates, Glenn and Chudnovsky's [173] model predicts an average fragment size that is nearly independent of strain rate; this is sensible given that for quasi-static loading one dominant fracture occurs. At high strain rates this model converges to the same fragment size predictions as the Grady energy model (see Figure 2.9b) [174].

Energetic models still serve as the basis of comparison for new fragmentation models, but they have important limitations. They are derived based on a balance of kinetic energy in a material and the surface energy from new surfaces created by fracture. This is obviously part of the physical picture of fragmentation, but not a complete picture. Models based solely on this kind of energy balance approach tend to over predict fragment sizes, sometimes by an order of magnitude [175,176]. Energetic model predictions tend to degrade as problem dimensionality increases [177].

2.7.4.2 Micromechanical Models

In 1947, Mott [156] published a study of fragmentation based on the study of an explosively driven, rigid-plastic expanding ring. He considered the fragmentation process as a competition between the formation of new fractures and the release of elastic strain energy spreading out from each complete fracture to relieve strain in the surrounding material, preventing further fractures in those regions. This process is illustrated in Figure 2.10a and 2.10b, which is a part of the physical picture of fragmentation that is not contained within energetic models. For a rigid-plastic

material the release wave speed is

$$\frac{dx}{dt} = \sqrt{\frac{\sigma_{uts}}{2\rho\dot{\epsilon}t}} \tag{2.20}$$

where σ_y is the yield strength and the other variables are defined previously. Mott showed that fragmentation is a competition between the nucleation of cracks and the action of release waves. The resulting average fragment size is

$$d = \frac{\kappa}{\dot{\epsilon}}\sqrt{\frac{2\sigma_y}{\rho\gamma}} \tag{2.21}$$

where γ is related scatter in fracture strain and κ is a constant around 1.5 [156, 167]. Mott's theory indicates that fragment size should scale $d \propto \dot{\epsilon}^{-1}$ as compared with Grady's and Glenn and Chudnovsky's energy models which scale $d \propto \dot{\epsilon}^{-2/3}$.

There are a few drawbacks to Mott's original model. His treatment requires an estimate of statistical variation in failure strains, which is not usually recorded, and it also does not address energy dissipated in fracture; Mott's model assumes that energy dissipated in fracture is not significant. Shear banding, fractures, and other failure mechanisms were not well understood during the 1940's, and Mott also assumed that the material was rigid-plastic. This assumption introduces a pathology in the Mott wave speed: it is initially infinite though it quickly converges to reasonable values. The Mott release wave is not truly wavelike, but it is termed so for historical reasons. The velocity of the interface decays with time due to the necessity of accelerating the growing stress relieved segment of the ring.

However, Mott correctly saw fragmentation as a competition between growing areas of strain release, where fracture cannot continue, and fracture nucleation. Mott also correctly deduced that fractures do not appear simultaneously, but they nucleate at different times during the fragmentation process; this was later experimentally confirmed by Winter [7]. Mott also correctly apprehended that as strain rate increased, more fractures would reach completion. Zhang and Ravi-Chandar [167] in a recent

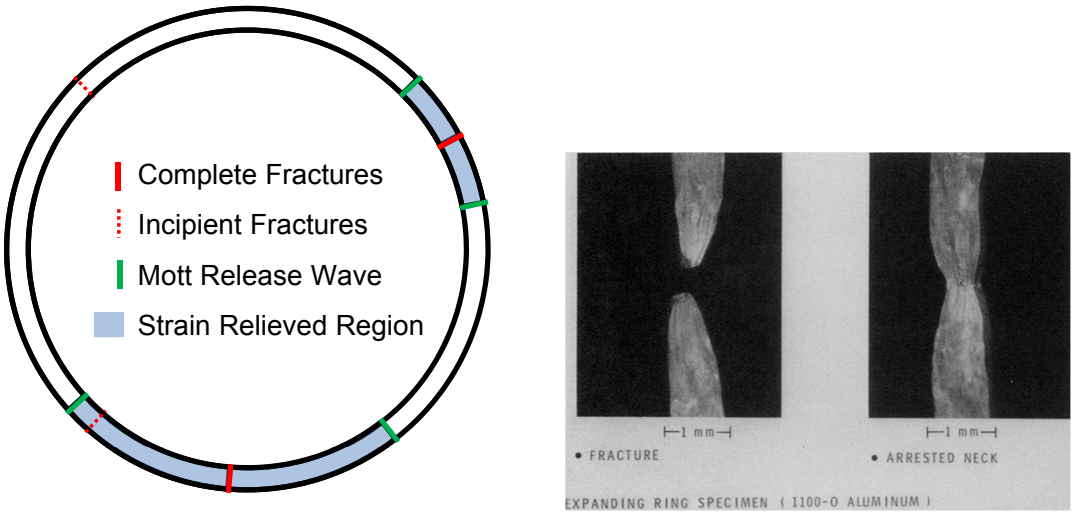

(a) (b)

Figure 2.10: (a) A schematic of Mott fragmentation shows that completed fractures emit release waves that unload the surrounding material. Incipient fractures that are enveloped by the release wave do not continue developing. No further cracking takes place in the strain relieved regions. (b) Images of completed fracture and incipient fracture that was prevented from completing due to the passage of a Mott release wave. [5]

review of expanding ring fragmentation results for ductile metals including aluminum alloys and copper found that fragment sizes in ductile metals scale with $d \propto \dot{\epsilon}^{-1}$ following Mott's model.

In 1967, E.H. Lee, W. Mueller, and M. Shaw [178] published their work expanding Mott's ring problem to an elastic-plastic material. They found that the release wave decays to zero at a distance $d = \frac{2\sigma_y}{\rho C \dot{\epsilon}}$ with the release wave position $x = \sqrt{\frac{2\sigma_y t}{\rho \dot{\epsilon}}}$ for fractures within a rigid-plastic deforming body and $x = \sqrt{\frac{E}{\rho}} t$ with initial velocity $C = \sqrt{\frac{E}{\rho}}$ for an elastic plastic body. Subsequent reflected elastic waves lead to changes in the segment velocity. The variables have the same meaning as above. In either case, the Mott release wave velocity decays as the release wave is robbed of its energy by imparting a tangential velocity to the stress relieved material. Lee et

[5]Reprinted from *Experimental Mechanics*, vol. 23, pp. 393-400, 1983, "Fragmentation of Metal Rings by Electromagnetic Loading," D. Grady and D. Benson, Figure 5, Copyright 1983, with permission from Springer Science and Business Media

al.'s solution for the motion of the release wave and Mott's solution agree with Mott's solution functioning as a sort of bound on Lee's solution.

Grady and Kipp [179] also expanded on Mott's work. They treated cracks in the 1D expanding ring as having a Dugdale-Barenblatt type of traction separation law to investigate the effect of the energy dissipated by a fracture on the overall fragmentation process. By developing analytical solutions as well as conducting 1D simulations, they demonstrated that the energy dissipated in the crack via the traction-separation law significantly reduced the speed of the Mott unloading waves [179]. Energy dissipated in a crack, or in the crack stress field, leads to the formation of larger fragments. Grady and Kipp's [179] treatment of the traction-separation law introduces a time scale into the crack opening. By equating their expression for velocity of the Mott unloading wave to the time scale, they developed an estimate of fragment size

$$d = \left(\frac{\sqrt{12} K_f}{\rho c \dot{\epsilon}} \right)^{2/3}. \tag{2.22}$$

It is interesting to note that this is very similar to the energetic model developed by Grady [172] and has the same $\dot{\epsilon}^{-2/3}$ scaling. Later, Grady [180] generalized this model to the case of biaxial fragmentation. The resulting model has a different strain rate scaling as shown in Eq.2.23.

$$a = \left(\frac{\sqrt{12} K_f}{\rho c \dot{\epsilon}} \right)^{4/3} \tag{2.23}$$

Fragment size, a, is now the average fragment area and the other model parameters have the same meaning as before.

Drugan [174] modeled a brittle, elastic 1D bar that was rapidly strained to fragmentation, essentially the same case as the expanding ring. He considered both an initially unflawed material subjected to a dynamic instability analysis and an array of regularly spaced defects. Drugan's model converges with Grady's energy model [172] and Glenn and Chudnovsky's model [173] at high strain rates $\dot{\epsilon} > 10^7$.

In 2006, Zhou, Molinari, and Ramesh [168, 169] built upon work done by Mott [156], Drugan [174], and Shenoy and Kim [181] in their study of an elastic ring. They included irreversible cohesive crack behavior, time and stress dependent crack loading behavior, random defect placement, and random defect intensity. Combining an analytical model of the Mott [156] ring problem and simulation, they investigated two loading cases: a forced expansion consisting of a constant radial velocity induced by a pressure (rather like the expanding ring of Niordsen or Grady and Benson) and a free expansion case consisting of a non-zero initial velocity but no external pressure. Zhou et al. [168, 169] demonstrated that both loading cases quickly converge, though the forced case does initially show less fragment size dependence on ring size and forms finer fragments due to the additional energy input. The cases converge as the initial kinetic energy input becomes adequate to force fragmentation and additional energy input in the forced expansion case becomes less important.

The ZMR model [168,169] consistently predicts smaller fragment sizes than Grady [172] or Glenn and Chudnovsky's [173] models, though the trends are similar. Zhou et al. [168, 169] justified this by indicating that the constant radial velocity case requires continuous additional energy input –this is sensible given that the only case where this actually happens is with inductive ring expansion like that of Niordsen's experiment [162] where the ring is continuously loaded until fracture rather than being impulsively loaded– and thus finer fragmentation is required to dissipate the extra energy. The additional energy input was not considered by Grady [172], Glenn and Chudnovsky [173], or Drugan [174].

Fragment models that developed based on consideration of the competition between fracture and stress relief seem to offer the best results in terms of fragment sizes and many researchers seem to prefer some derivative of Mott's approach. Grady and Benson [164] and Grady [180] found that for fragmenting rings of 1100-Al and Cu, Mott's prediction of fragment scaling $d \propto \dot{\epsilon}^{-1}$ was more appropriate. Grady [180]

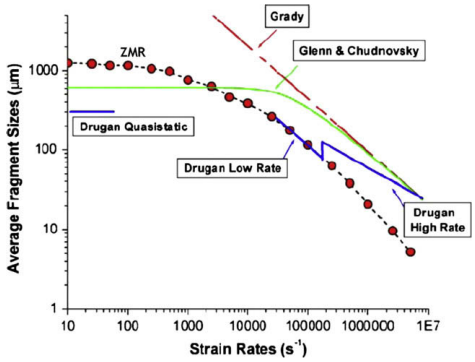

Figure 2.11: The ZMR model predicts smaller fragment sizes at all strain rates than either the Grady energy model or Glenn and Chudnovsky models.[6]

found that for ductile U-Nb6 alloy rings, the fragment scaling $d \propto \dot{\epsilon}^{-2/3}$ was more appropriate.

These models are not without their difficulties. It is challenging to efficiently capture defect distributions or microstructure variations. Prediction of internal damage is not addressed. Jaeger, Englman, and Sprecher [182] developed a simple geometric simulation based on random line placement which indicated that including incomplete internal cracks increased the total fracture surface area from 1.6 to 2 times, though their approach did not contain provision for strain release in surrounding material. Meyers [183] reported that in quartz fragmentation experiments, the surface area added by incomplete cracks is the vast majority of the total surface area. Correctly accounting for the total amount of surface area is necessary for understanding the amount of energy consumed in fragmentation.

2.7.5 Fragmentation in the Presence of Multiple Fragmentation Mechanisms

The fragmentation models reviewed up to this point have been for a single fragmentation mechanism. Experimentally, multiple fragmentation mechanisms have been

[6]Reprinted from *International Journal of Impact Engineering*, vol. 35, iss. 12, pp. 1661-1665, 2008, "CTH Simulations of an Expanding Ring to Study Fragmentation,"' J.P. Meulbroek, K.T. Ramesh, P.K. Swaminthan and A.M. Lennon, Figure 11, Copyright 2008, with permission from Elsevier.

observed. This leads to fragment size distributions which are multi-modal.

Bimodal fragment distributions were observed by Odintsov [184] who studied fragmentation in explosively driven steel cylinders with varying carbon contents. Odintsov found that the fragment populations from a low carbon steel cylinder showed a distinctly bimodal character, whereas the fragment population for the high carbon steel was unimodal in character [184]. Odintsov observed that some of the fragments formed via fracture intersections near the inner (shear dominated fractures) or outer (tension dominated fractures) surface of the cylinder while still others contained both the inner and outer surfaces of the cylinder [184]. The high carbon steel sample, which was more brittle, was dominated by the fragments containing both inner and outer surfaces of the tube while the experiment on the more ductile low carbon steel generated a significant number of fragments of all types [184].

Hooper [185] studied fragmentation of pressed Al spheres which were propelled through a thin metal sheet. He inferred the existence of bulk fracture and smaller scale crack branching leading to two different fragment populations, one on the scale of a few multiples of the original aluminum particle size and the other millimeters in size. The fragment distributions had a multi-modal character which, at high impact velocities, converged on a small fragment size becoming unimodal.

2.7.6 Fragmentation of Structural Energetic Materials

Fragmentation of structural energetic materials has received comparatively little attention in the literature. This is puzzling because fragment size and character will strongly influence how energy is released. Ames [15, 25] and Ames and Waggener [16] designed the Blue Pig test to cause extensive fragmentation of the SEM samples. A sample is propelled into a thin sheet, leading to shock waves that form and reflect off of the free surface boundaries around the sample, placing the sample into tension and

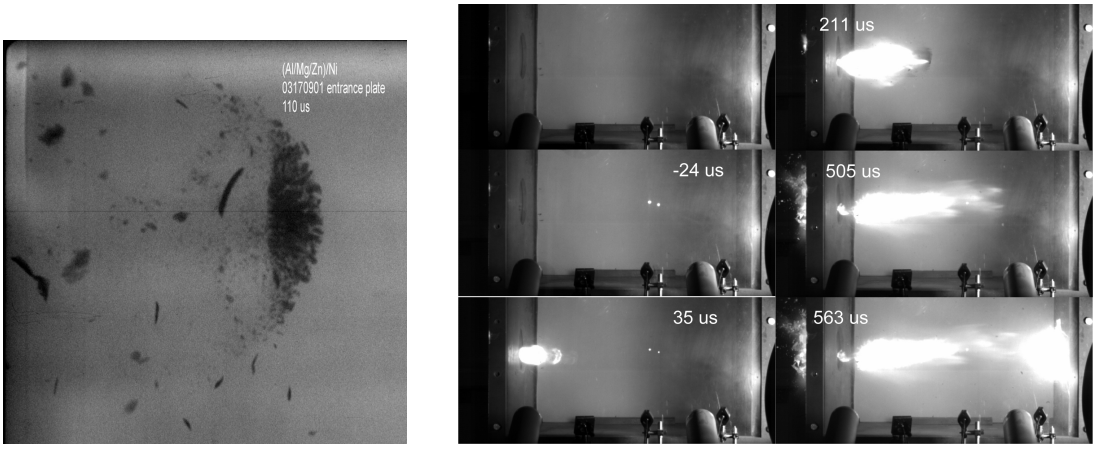

(a) (b)

Figure 2.12: (a)Impact Induced Fragmentation in a (Al+Mg)+Ni sample undergoing testing in the Green Pig from Homan et al. [24] (b) A sequence of images showing partial reaction during perforation of the steel plate in front of the impact chamber, impact induced reaction of the largest fragments, and subsequent ignition and reaction of smaller fragments [24].

tearing it into a cloud of fragments as seen in Figure 2.12a. Homan et al. [23,24] captured images of these fragments. The largest fragments react on impact and release energy, and the smaller fragments begin combustion/reaction before impact as shown in Figure 2.12b. It is clear that fragment size will influence the role that fragments play in energy release. Small fragments may combust while larger ones are more likely to impact and ignite.

Zhang and Wilson [26] tested an unspecified reactive casing in a closed chamber. They found that pressure output of an explosive+reactive casing showed a stepped character, which they interpreted as impact induced reaction in fragments and then the pressure spike due to the HE charge. They also found that a reactive case/charge ratio of 1.75:1 yielded the same quasistatic over-pressure as a charge 2.5 times larger than the one used with the reactive case. This suggests that the case is being consumed and contributing energy to the blast pressure [26], though whether this is from impact induced reaction of fragments or fragment combustion is not clear.

Nesterenko et al. [186] and Olney et al. [187] studied the process of fragmentation in ring samples of Al+W composites when subjected to explosive fragmentation. Modeling of explosive fragmentation of Al+W composites showed that at high expansion velocities, the Al+W composite was first densified, then the Al jetted around the W particles, forming small Al particles [186]. Based on the simulations, Nesterenko et al. [186] claimed that the fragment size was primarily determined by the spacing of W particles though no stereology data and very little fragment size data was presented. Olney et al. [187] conducted a more detailed series of computational investigations of fragmentation in Al+W composites. They observed four possible mechanisms that assist the fragmentation process: macroscopic fragmentation due to hoop stress (called Grady-Kipp fragmentation by the Olney et al.), mesoscale void opening at Al/W interfaces (essentially the same Grady-Kipp mechanism, just at the local scale), Al jetting off of the ring surface due to impedance mismatches between Al and W, and penetration of explosive gases into cracks causing additional loading on the crack faces and additional fragmentation. Based on the simulation data, Olney et al. [187] believed that the placement of W particles determined the size of jetted Al particles as well as the spacing of cracks which explosive product gases may penetrate into, suggesting that the fragment size may be tunable.

Much remains in doubt about the fragmentation of structural energetic materials. Very little experimental fragment data is available, at least in peer reviewed literature, for structural energetic materials. Simulations suggest that mesoscale size features will influence the fragmentation process, but little or no experimental data exists to verify or refute these claims. Little is known about how the microstructure influences the fragmentation process in structural energetic materials or how the fragments themselves behave in terms of their reaction response.

2.8 Conceptual Models of Shock-Induced Reaction

Developing a reaction model for structural energetic materials is not a goal of this work. However, two significant conceptual models are mentioned to draw out useful insights into important mesoscale features that contribute to reaction behavior.

As indicated by the wealth of relevant literature, great interest exists in the fundamental questions surrounding shock wave propagation in reactive material systems. Concomitant interest has been directed toward understanding and modeling shock and impact synthesis phenomena. Dremin et al. [188], commenting on shock synthesis and decomposition mechanisms, proposed a qualitative *Roller* mechanism: A velocity gradient across a material interface leads to significant shear and relative displacement. The shearing and resulting deformation leads to reaction as a nucleus forms of a new phase and, as the surfaces move by it, the nucleus collects atoms from both surfaces. Rearrangement of an atom's electron cloud to form a new bond is required but is rapid. Mass transport is governed by the shock wave and the relative surface displacement which is faster than ordinary mass diffusion.

Graham [189] postulated a general framework of requirements for shock induced reaction, which he called CONMAH from CONfiguration change, Mixing, shock Activation, and Heating. According to this framework, a reactive material system undergoing reaction experiences configuration change due to crush up of pores to full density, mass mixing, extensive deformation related to the crush up and shock wave propagation, and large increases in temperature from the deposition of shock energy. Graham [189] believed that the mass mixing during deformation is the most critical process affecting subsequent reaction behavior.

In both of these models, there is significant emphasis on deformation. Graham's [189] conceptual framework strongly emphasizes both mass mixing and extensive deformation. These behaviors are believed to be generally relevant to the reaction of structural energetic materials.

2.9 Summary of the Literature Review

It is evident that there are several mesoscale features which are important to consider in a reaction that is induced during either the uni-axial strain loading configuration (shock loading) or uni-axial stress loading. Plastic deformation of the reactive material seems to be the primary means by which energy is deposited into the reactants; thus factors that influence plastic deformation will also influence reaction behavior:

- Porosity assists reaction in shocked materials by assisting plastic deformation and in uni-axial stress loading porosity generally limits plastic deformation and thus is negatively correlated with reaction.

- Hard constituents, such as those processed via extensive ball milling, resist deformation and consequently are often not as reactive in deformation induced reaction scenarios.

- Premature melting or softening in one constituent can impede deformation in the other and thus impede reaction initiation.

- Constituent shape has been shown to influence the plastic deformation; Particle or constituent shapes that are more prone to deformation are also more prone to react.

- Increasing the relative amount of a soft phase in a material limits deformation in the harder phase.

- Fine powders, with greater interface area per unit volume, are generally more prone to react when shocked unless they agglomerate. Reactive foils with greater interface density have been shown to require less energy input to react. Ball milling can produce greater amounts of interface density and may contribute to enhanced reactivity if increases in strength do not reduce the tendency to plastically deform too much.

With regard to fragmentation of structural energetic materials and their subsequent reaction, two observations can be made from the literature review:

- Experimental evidence suggests that large fragments may react upon impact with a solid surface.
- Experimental evidence suggests small fragments may combust if properly stimulated.

There are a few topics related to reactive materials where little or nothing is known. The effect of topology on the reaction behavior of fragments, and the fragmentation process of SEMs is not well understood. Mesoscale features that regulate fragmentation have received only a little attention. Fragment sizes and distributions of structural energetic materials have not been explored.

This work will begin to address some of these shortcomings. Fragmentation of structural energetic materials will be addressed in detail. The effect of topology on deformation induced reaction will be addressed in a uniaxial stress loading scenario.

CHAPTER III

STRUCTURAL ENERGETIC MATERIALS SYSTEMS AND PROPERTIES

The materials discussed in this work are all metal-metal mixture systems with constituents chosen to react exothermically to form intermetallics and liberate energy. The microstructural characteristics and the physical and mechanical properties of these reactive mixtures are of great interest as they influence the fragmentation and reaction behavior. It is therefore essential to characterize these properties and establish their effects.

3.1 Structural Energetic Material Systems Explored

Structural energetic materials come in many forms as mentioned previously. Those studied in this work are systems which are composed solely of metal powder components that may react to form an intermetallic compound. There are no polymeric binders or additives, which allows them to achieve significantly greater density than polymer based systems. Many different constituents and different powder morphologies are available for tailoring mechanical properties, reaction behaviors, and product phases. The drawback is that it is very difficult to form fully dense materials from powdered metals without sintering; sintering is not possible with these systems as it may lead to reaction. The materials systems considered here were either formulated via explosive compaction of powder mixtures or gas dynamic cold spray of Ni coated Al particles.

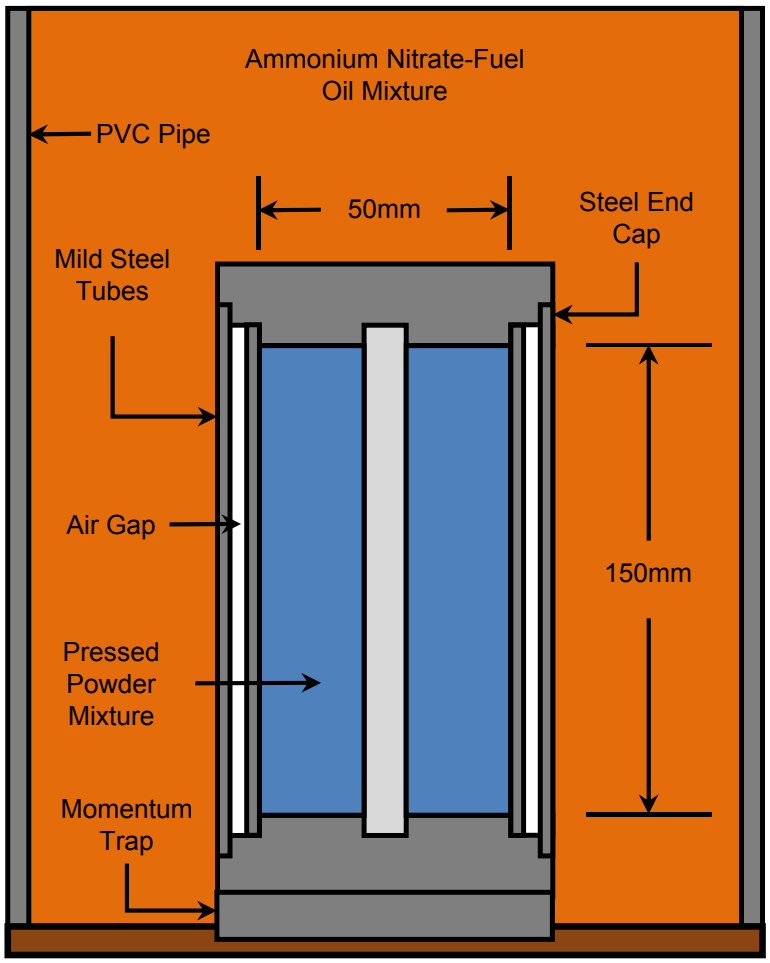

Figure 3.1: The double tube explosive compaction setup is depicted. Detonation initiated in the ANFO mixture causes the outer tube to impact the inner tube in an axi-symmetric analogue to the parallel plate impact experiment. The resulting shock wave compacts the pressed powder mixture contained within the inner tube into a dense solid.

3.2 Explosively Compacted Structural Energetic Material Systems

Three binary intermetallic-forming powder mixture systems, Ni+Al, Ta+Al, and W+Al, were explosively compacted into near full density solid compacts [124]. Explosive compaction of the intermetallic forming systems was performed using a double-tube explosive-compaction fixture [190]. A schematic of the experimental setup required for explosive compaction is shown in Figure 3.1. Explosive compaction allows the controlled application of pressures above those available with typical uniaxial powder compaction methods without the complex machinery required for hot or cold isostatic pressing. The process is also quite scalable, allowing the production of large cylindrical compacted pieces. In the present work, it was desired to form a fully dense structural energetic materials with the potential to react subsequently to form an intermetallic compound.

Explosive compaction is relatively straightforward. It is explained in detail by Meyers and Wang [190]. When the explosive is initiated, the detonation wave moving through the explosive mixture drives the outer tube into the inner tube. This is an axi-symmetric analog to a parallel plate impact experiment. The impact of the steel tubes drives a shock wave into the powder mixture, compacting it. An aluminum rod placed at the axis of the powder compaction assembly contains the mach stem that forms as the pressure front from the detonating explosive marches down the powder column. This prevents the mach stem from spreading into the powder where it may lead to extreme deformation and premature reaction [190]. To avoid reaction initiation in the powder mixtures, a low detonation velocity explosive was used to yield a lower shock pressure and reduce the amount of plastic deformation during consolidation. The ammonium nitrate+fuel oil mixture, diluted with perlite, achieves a detonation velocity of approximately 2.6 km/s. The explosive accelerates the outer compaction tube to a calculated impact velocity of 300 m/s [124]. The peak pressure

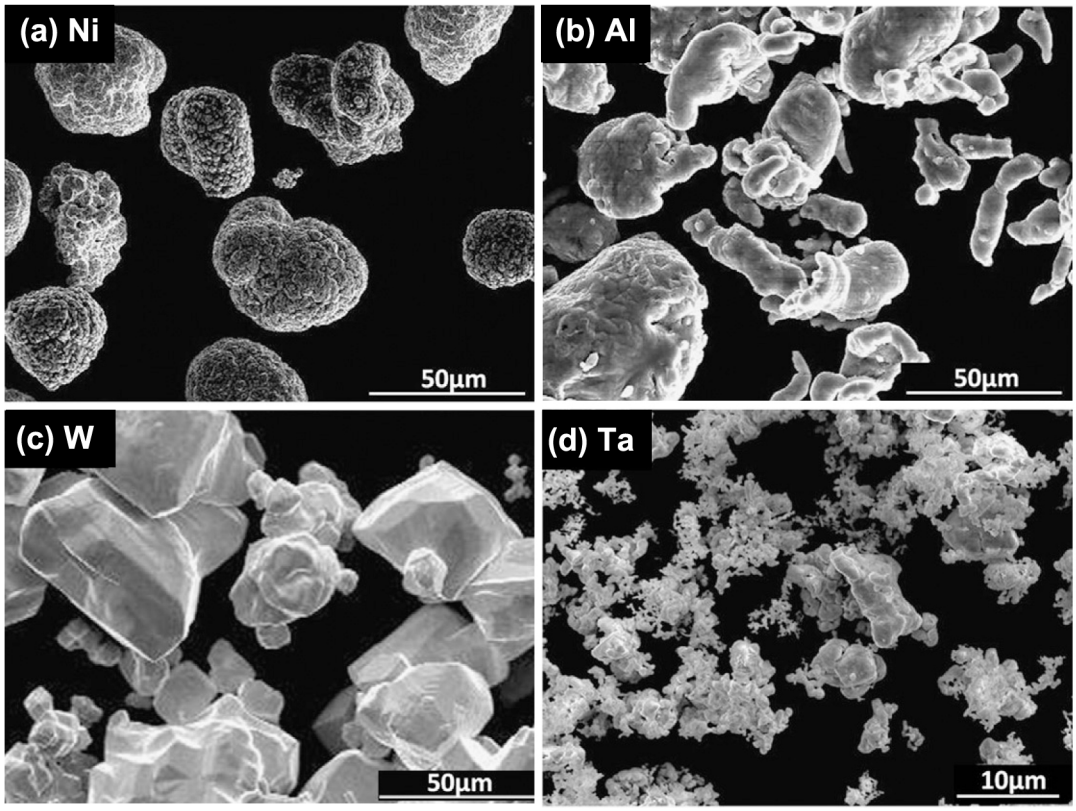

Figure 3.2: (a) Ni powder (b) Al powder (c) W powder (d) Ta powder. Notice the spongy, connected nature of the Ta particles. The Ni and W particles are essentially convex, simply connected particles. The morphology of the aluminum powder is not terribly significant in this case. It deforms so extensively during compaction that there is no trace of the original morphology that remains.[7]

Table 3.1: Selected Properties of Explosively Compacted Ni+Al, W+Al, Ta+Al. † data from [124]

	EC Ni+Al	EC W+Al	EC Ta+Al
V_v	0.51±0.018 Ni	0.54±0.02 W	0.61±0.02 Ta
S_v	68.5±1.8 mm^{-1}	56.0±1.8 mm^{-1}	117±2.7 mm^{-1}
M_v	0.00144±0.0004 $\mu m/\mu m^3$	0.00175±0.001 $\mu m/\mu m^3$	-0.0139±0.010 $\mu m/\mu m^3$
Measured Density (g/cm^3)	5.7±0.1 †	10.90±0.05 †	9.18±0.09 †
Theoretical Density (g/cm^3)	5.80 †	11.0 †	9.70 †
Percent Theoretical Density	98	99.1	94.6

variation during compaction was estimated (using AUTODYN-2D) to be in the range of 4-7 GPa throughout the entire material during the compaction process [124].

Commercially available -325 mesh, 99.8% high purity elemental powders were mixed in an equivolumetric ratio for the binary mixtures for explosive compaction [124]. For the ternary mixture and quaternary mixture, the desired volume fraction Al remained around 50% and the rest of the components were divided among the other 50%. Given that the disparity between the densities and mechanical properties of the powders can be quite large, equivolumetric mixtures provide the greatest opportunity for the constituents of a mixture to mix and react. The morphology of the Ni, W, Al, and Ta powders are shown in Figure 3.2. It is important to note the simply connected nature of the tungsten and nickel particles as contrasted with the spongy appearance of the tantalum particles. This leads to important differences in the microstructures of the explosively compacted materials, and their subsequent behavior, that will be addressed in detail later in this chapter, as well as in Chapter 5.

Following compaction, the ends of the compacted tube assembly were removed, the aluminum mandrel was cut out, and the steel tubes were removed. The cylindrical billet of compressed powder was recovered with good structural integrity and no obvious macro-cracking [124]. It was cut into various experimental samples via

[7]Reprinted in part from *Acta Materialia*, vol. 60, iss. 3, pp. 1418-1432, 2012, "Quasi-static and dynamic response of explosively consolidated metal-aluminum powder mixtures," C.T. Wei, E. Vitali, F. Jiang, S.W. Du, D.J. Benson, K.S. Vecchio, N.N. Thadhani, and M.A. Meyers, Figure 2 and 3, Copyright 2012, with permission from Elsevier.

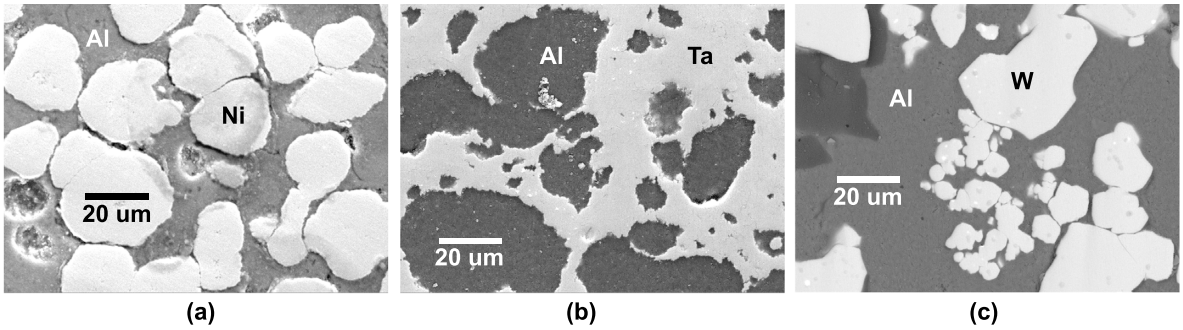

Figure 3.3: (a) Ni+Al microstructure. (b) Ta+Al microstructure. (c) W+Al microstructure.

wire Electrical Discharge Machining (EDM). The microstructures of the explosively compacted binary systems can be seen in Figure 3.3.

Volume fraction is an important characteristic of a structural energetic material not only for estimating elastic properties and theoretical density, but in Ni+Al mixtures increasing the volume fraction of Ni relative to Al improved the reactivity of this system (c.f. Dunbar et al. [20]). Volume fractions of different constituents were characterized using point counting. The method of Karlsson and Gokhale [191] was used to locate vertical sections in samples of the structural energetic materials. Standard metallographic polishing techniques and optical microscopy were used to prepare the samples and generate images of each material system's microstructure. Two measurements were made on each of 25 to 50 different microstructure images which were obtained via uniform random sampling. Volume fractions for the binary systems under consideration are shown in Table 3.1.

Surface area per unit volume is another important metric microstructure property. Investigations of composite Ni/Al foils have shown that reaction ignition energy is proportional to bilayer spacing for electrical [133, 192], mechanical [133, 192], or thermal [192, 193] ignition. It may also be the case that surface area per unit volume influences fragmentation behavior in structural energetic materials. Reactant spacing is proportional to surface area per unit volume. Surface area per unit volume was

characterized on the same images utilized for volume fraction, using the line intercept method. Surface area per unit volume measurements for the explosively compacted mixtures are shown in Table 3.1.

The integral mean curvature was determined following the method of tangent counting described by Russ and DeHoff [194]. Later, the integral mean curvature will be utilized as a two dimensional analog of the Euler characteristic to interpret two dimensional mesoscale simulations of rod-on-anvil impact simulations. In the strictest sense, topological connectivity can only be correctly determined using serial sectioning, however for the purposes of characterizing making topological comparisons among two dimensional simulations this is reasonable.

Differential Thermal Analysis (DTA) was performed on the explosively compacted binary mixtures. As previously indicated, using shock waves to compact powders can lead to extensive deformation and fine scale mixing of the reactant constituents and promote solid state reaction [20, 108–110]. The DTA traces in Figure 3.4 reveal no significant exotherms below the melting point of aluminum, unlike those observed in previous work on shock consolidated nickel+aluminum powder mixtures which showed exotherms from solid state reactions in Ni+Al samples [108, 109].

3.2.1 Ternary and Quaternary Mixtures

One ternary and one quaternary mixture were also compacted in a similar fashion. The W, Ni, Ta, Al, and Zr powders used are shown in Figure 3.2 and Figure 3.5. A ternary mixture of 1:1 molar ratio Ni+Al was combined with a 1:1 molar ratio of W+Al in nominally 50% by volume ratios. This mixture was termed Mixture A. The other mixture, Mixture B, was formed from nominally 20% by volume 1:1 molar ratio mixture of Ni+Al with Al, Zr, and W. These mixtures both contain tungsten as an additive to increase density. Though the tungsten may also react with aluminum, the Al, Zr, and Ni are thought to be the primary reactants in the mixture.

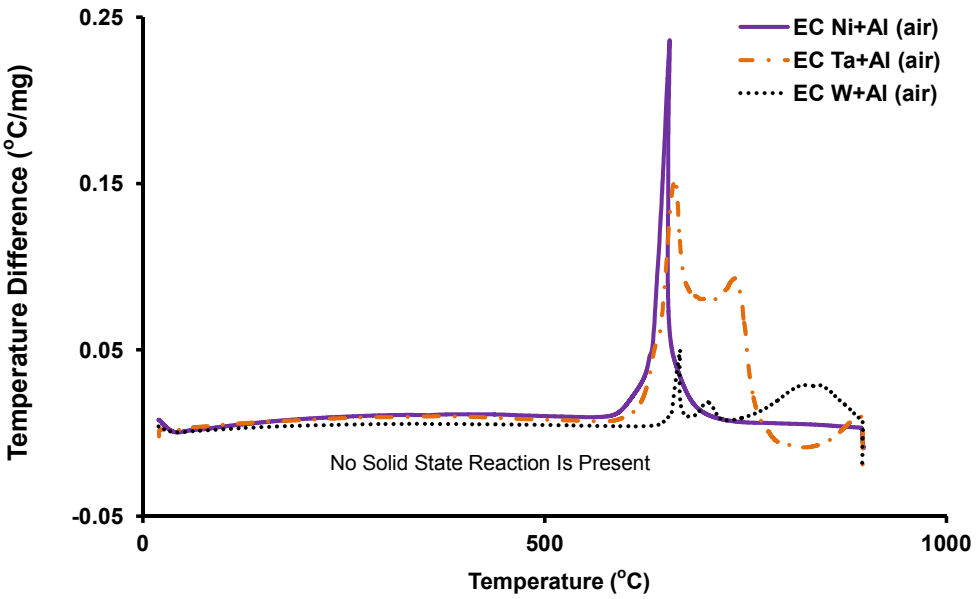

Figure 3.4: Differential Thermal Analysis Data for Three Explosively Compacted Binary Mixtures. The absence of solid state reactions is evidence that little fine scale mixing took place in these samples.

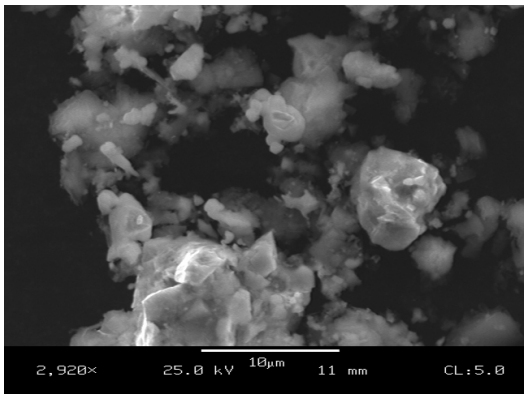

Figure 3.5: Zirconium powder used in explosively compacted Mixture B

Table 3.2: Selected Properties of Explosively Compacted Mixture A and Mixture B. These systems appear to possess essentially similar topology to explosively compacted Ni+Al. Volume fractions were computed from the masses of powders explosively compacted. They represent global averages. *During the compaction process, the lower flow strength of Al may have led to some regions of higher density than expected.

	Mixture A	Mixture B
V_v	0.20 Ni	0.08 Ni
	0.24 W	0.25 W
	0.56 Al	0.13 Zr
		0.55 Al
S_v (Al interfaces only)	73±6 mm^{-1}	91±9 mm^{-1}
S_v (all interfaces)	97±7 mm^{-1}	143±13 mm^{-1}
Measured Density (g/cm^3)	7.65±0.01	*7.89±0.03
Theoretical Density (g/cm^3)	8.0	7.7
Percent Theoretical Density	95	*102
Elastic Modulus (GPa)	17.0±5	20.7±9
Yield Strength (MPa)	240±30	240±30

The microstructures of Mixture A and Mixture B can be seen in Figure 3.6a and 3.6b. They are very similar to those of the explosively compacted binary Ni+Al and W+Al mixtures since all of these systems were made from simply connected particles of higher strength mixed with lower strength aluminum and fabricated in the same way, via explosive compaction. They have an apparently continuous aluminum phase surrounding islands of the harder components.

Volume fraction for Mixture A and Mixture B was determined from the masses of powders utilized to form each mixture and are tabulated in Table 3.2. Density was determined using the Archimedes's method. Each sample's dry and submerged mass were measured and the density was calculated according to $\rho_{sample} = \frac{M_{Dry}}{M_{Dry}-M_{Submerged}}\rho_{H_20}(T)$.

DTA data for virgin samples of Mixture A and Mixture B are shown in Figure 3.7. Notice the presence of solid state reactions in both samples, though not to the same degree.

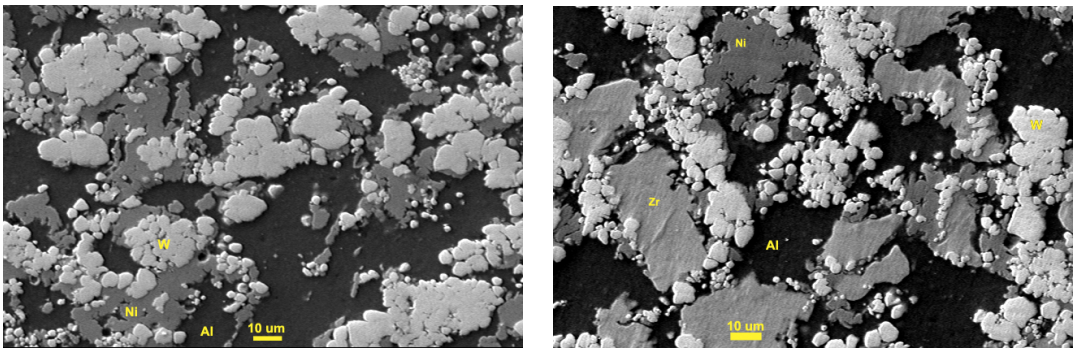

(a) (b)

Figure 3.6: (a) Explosively compacted Mixture A (b) Explosively compacted Mixture B

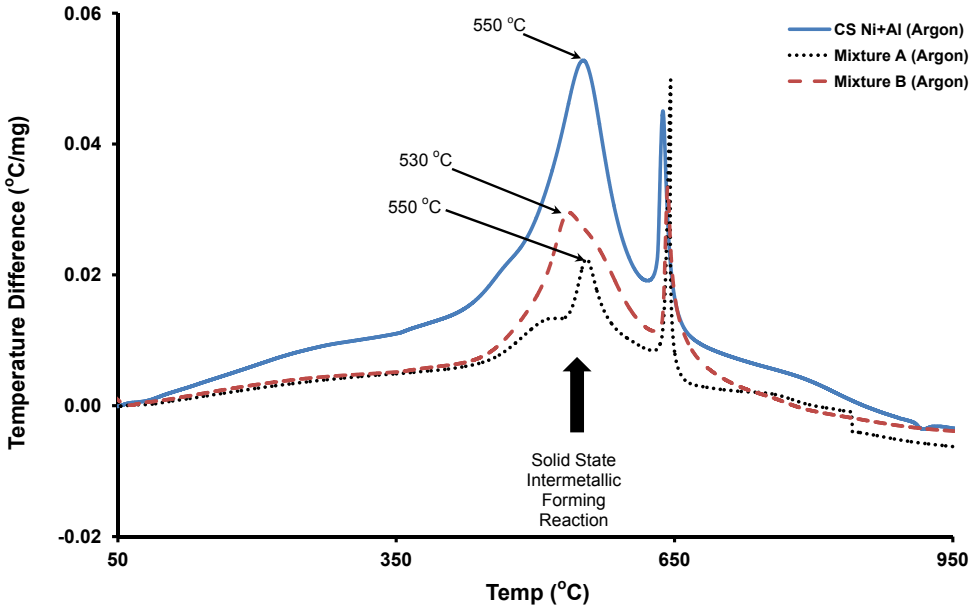

Figure 3.7: Differential Thermal Analysis Data for virgin CS Ni+Al, Mixture A, and Mixture B samples. In contrast to Figure 3.4, there is evidence of solid state reactions in all three samples indicative of extensive deformation and fine scale mixing due to the deposition or explosive compaction processes.

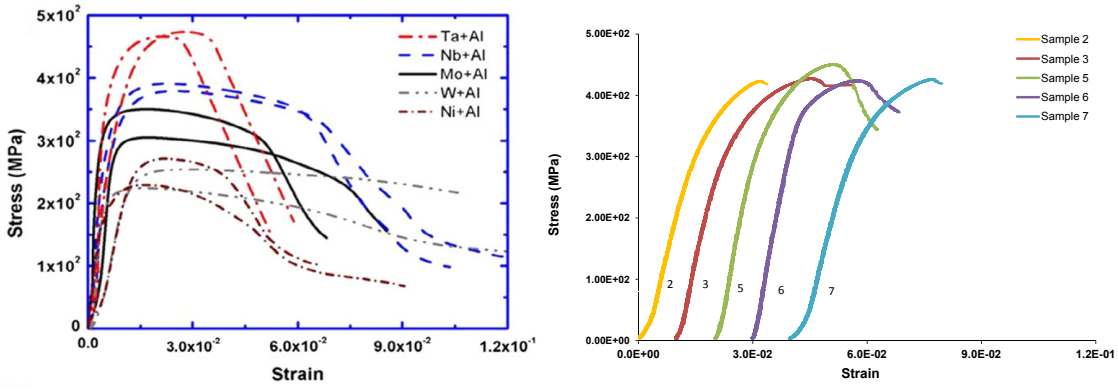

(a) (b)

Figure 3.8: (a) Quasi-static compression data for explosively compacted Ni+Al, W+Al, and Ta+Al. [8] (b) Compression data for cold sprayed Ni+Al. Notice the significantly higher strengths for the cold sprayed Ni+Al vs. the explosively compacted Ni+Al in (a). The stress strain curves are displaced arbitrarily in strain to make details of the curves easier to see.

3.2.2 Quasi-static Compression Testing of Explosively Compacted Structural Energetic Materials

Wei et al. [132] performed quasi-static compression tests on the explosively compacted Ni+Al, W+Al, and Ta+Al using an Instron 3370 machine and cylindrical samples 4 mm long x 3 mm diameter for their tests. They corrected the machine displacement to obtain the actual platen displacement values. The results are shown in Figure 3.8a.

It appears that the Ta+Al is the strongest explosively compacted system. This is somewhat surprising, but examining Figure 3.3 shows that Ta+Al appears to form a matrix around the Al, while in Ni+Al and W+Al, essentially convex Ni or W particles are suspended within Al. In the case of Ta+Al, the stronger phase is also more topologically connected. It was also found by Wei et al. [132] and Aydelotte and Thadhani [195] that Ni and W were poorly bonded with the surrounding aluminum matrix. This poor adhesion further diminishes the mechanical properties of

the explosively compacted Ni+Al and W+Al samples.

Samples of Mixture A and Mixture B were also tested in compression for comparison with the other materials. The method of compression testing was exactly similar to that conducted on the cold sprayed Ni+Al material listed above. The sole difference was the geometry of the available material, which were cylindrical samples ranging from 4.6 mm in diameter up to 6.14 mm in diameter with a nominal length of 9.0 mm. These samples were lapped flat and parallel for testing. Typical results are shown in Figure 3.9. The maximum strengths for both Mixture A and Mixture B samples are comparable to the explosively compacted Ni+Al and W+Al tested by Wei et al. [132] with more apparent ductility, presumably due to the lower porosity. The strength is higher than Al 1100-H18 (159 MPa) but is comparable to ECAPed 1100 Al (159-225 MPa) [196, 197]. No large fractures were observed during testing. The samples plastically deformed uniformly with only a hint of the axial splitting seen by Wei et al. [132] in the explosively compacted Ni+Al and W+Al.

3.2.3 Split-Hopkinson Bar Pressure Testing of Explosively Compacted Structural Energetic Materials

Wei et al. [132] used a Split Hopkinson Pressure Bar to measure dynamic compressive strength for explosively compacted Ni+Al, W+Al, and Ta+Al. An aluminum pulse shaper with a high work hardening rate was used to generate a longer rise time and roughly constant strain rates during the tests. The samples utilized were 4 mm diameter x 5 mm in length, cut via wire EDM from the explosive compact.

Hopkinson Bar data for explosively compacted Ni+Al and W+Al from Wei et al. [132] are shown in Figure 3.10. The dynamic Ni+Al and W+Al exhibit similar

[8]Reprinted in part from *Acta Materialia*, vol. 60, iss. 3, pp. 1418-1432, 2012, "Quasi-static and dynamic response of explosively consolidated metal+aluminum powder mixtures," C.T. Wei, E. Vitali, F. Jiang, S.W. Du, D.J. Benson, K.S. Vecchio, N.N. Thadhani, and M.A. Meyers, Figure 2 and 3, Copyright 2012, with permission from Elsevier.

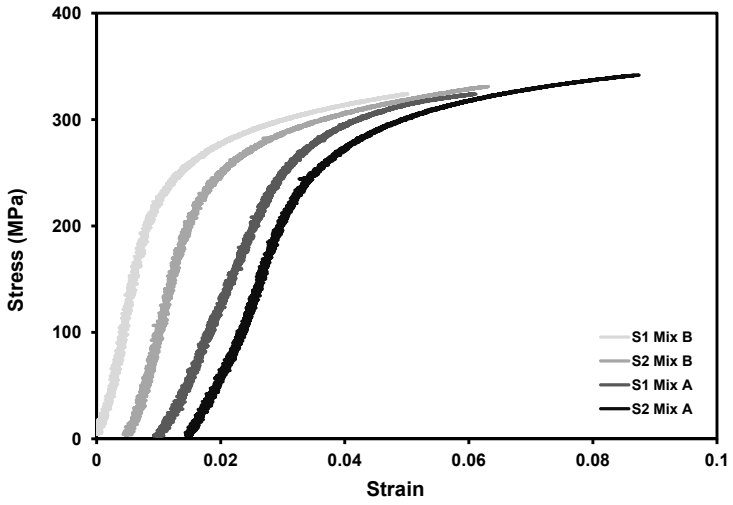

Figure 3.9: Typical compression data for explosively compacted Mixture A and Mixture B. The stress strain curves are displaced arbitrarily on the abscissa to make details of the curves easier to see.

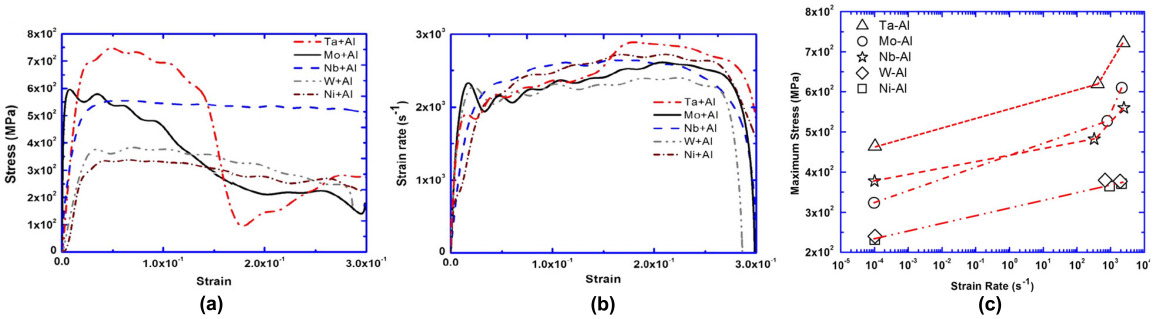

Figure 3.10: (a)Typical stress-strain curves of Ta+Al, Ni+Al, and W+Al from Split-Hopkinson Pressure Bar Tests. (b) Strain rate vs strain for the test data shown in (a). (c) Compiled strength data for Ni+Al, W+Al, and Ta+Al at different strain rates. Notice the rate sensitivity which shows up for Ta+Al vs Ni+Al and W+Al.[9]

strength, suggesting their strength is dominated by the Al matrix and the weak adhesion between phases, rather than the Ni or W particles. Figure 3.8a and Figure 3.10 clearly show that Ta+Al is much stronger than either Ni+Al or W+Al and more rate sensitive. This is due to the topology of the material. The more topologically connected phase in Ta+Al, Ta, is much stronger and more rate sensitive than Al which is the topologically connected phase in Ni+Al and W+Al.

3.3 Cold Sprayed Nickel Aluminum

One other system that was explored was a nickel+aluminum structural energetic material fabricated via gas dynamic cold spray. Gas Dynamic Cold Spray, was first developed by Alkhimov et al. [198–200] and patented by Alkhimov et al. [201]. Since then, many other investigators have studied it including Assidi et al. [202], Novoselova et al. [203], Champagne [204], and Leyman and Champagne [205]. Cold spray has been studied for the application of protective coatings [205], repair of parts on aircraft [205], and as an energetic material [23, 206].

Unlike typical thermal spray processes, where the coating material is heated to near or above its melting point, the cold spray process may use a warm gas but the feed stock is never melted. As shown in Figure 3.11, the powder feed stock is injected into the unheated gas stream. Heating a portion of the gas stream is done to increase velocity through the Laval nozzle. The particles are in the solid state when they impinge on the base material and bonding takes place entirely through processes associated with the dynamic impact: extensive localized deformation, cleansing of oxide surfaces, and similar processes. These processes are felt to be similar in character to those that take place in explosive welding and dynamic powder compaction [202]. Cold spray is a very versatile process. It is capable of producing many different types of novel single and multi-component coatings as well as building up parts with uniform properties or functional gradients. The powders themselves may be pre-processed to provide a number of different constituents, morphologies, etc. Bacciochini et al. [206] ball milled Ni and Al powders to create powders with fine laminate structures and then cold sprayed them to form a structural energetic material of high density with sub-micron scale features.

[9]Reprinted in part from *Acta Materialia*, vol. 60, iss. 3, pp. 1418-1432, 2012, "Quasi-static and dynamic response of explosively consolidated metal-aluminum powder mixtures," C.T. Wei, E. Vitali, F. Jiang, S.W. Du, D.J. Benson, K.S. Vecchio, N.N. Thadhani, and M.A. Meyers, Figure 2 and 3, Copyright 2012, with permission from Elsevier.

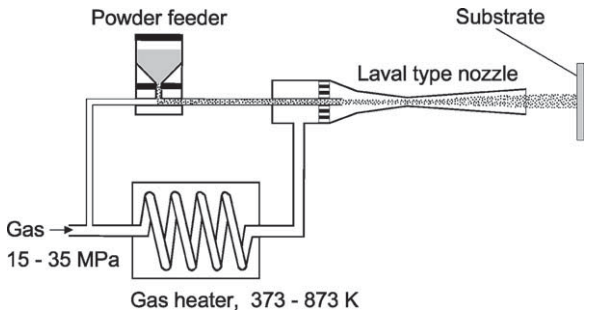

Figure 3.11: Gas dynamic cold spray apparatus. [10]

The cold sprayed Ni+Al studied in this work was derived from a nickel coated aluminum powder sprayed onto a metallic substrate in an argon atmosphere. The powder morphology is shown in Figure 3.12a. The powder was produced for the Army Research Laboratory by Federal Technology Group of Bozeman, MT USA as part of Army SBIR A062-083-0214 contract W911QX-08-C-0072. Samples of the Ni coated Al powder and cold sprayed parts in the form of rings and small rods were obtained through the Army Research Laboratory for the present work.

EDS point scans were performed on a Zeiss Ultra60 FE-SEM using an Oxford Instruments INCA EDS system at accelerating potentials between 5kV and 20kV to characterize the composition of the Ni coating on the Al particles. EDS scans revealed the presence of phosphorous. Scans revealed varying amounts of phosphorous, from 0 to 0.3 weight %, though readings were inconsistent. An example of an EDS spectrum, taken at an accelerating potential of 5 kV, is shown in Figure 3.12b. The aluminum content is due to the sampling volume of the electron beam at 5 kV including some of the aluminum under the nickel coating. The presence of oxygen is likely from oxides. The carbon is believed to be a contaminant due to sample mounting preparations. The presence of phosphorous suggests that the coating is in fact an electroless nickel coating, though ordinary electroless nickel coatings generally contain more than a

[10]Reprinted from *Acta Materialia*, vol 51., pp. 4379-4394, 2003, "Bonding Mechanism in Cold Gas Spraying,"' H. Assidi, F. Gärter, T. Stoltenhoff, and H. Kreye, Figure 1, Copyright 2003, with permission from Elsevier

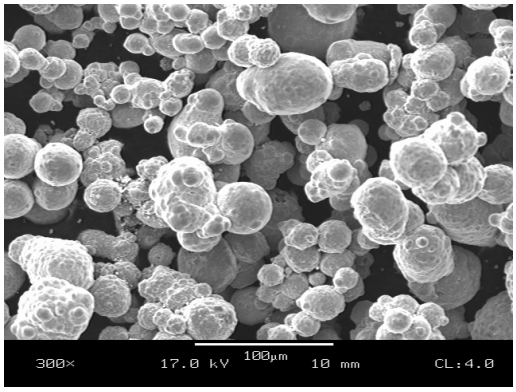

(a)

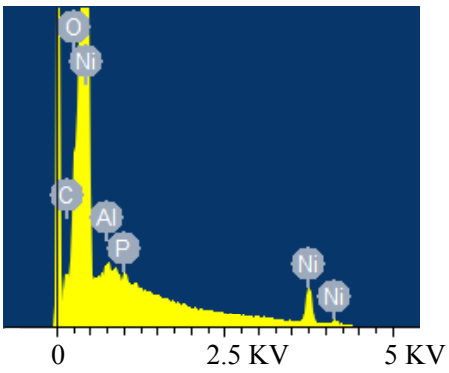

(b)

Figure 3.12: (a)Nickel coated Aluminum powder feedstock for cold sprayed Ni+Al samples tested in this work. The nickel shell is visible on the particles. (b) A typical EDS point scan of a nickel coated aluminum particle at 5 kV showing trace amounts of phosphorous. The Ni shell composition in this scan was 1.32 % C, 1.26% O, 0.27 % Al, 0.29 % P, and 96.9 % Ni (all values are weight percents).

trace amount of phosphorous, up to 11 wt. is common [207]. Phosphorous comes from the use of a sodium hypophosphite reducing agent during the coating process [207]. The electron microscope images of the Ni coated Al powder also show that the surface has a slighly nodular appearance as evident in Figure 3.12a. This is consistent with what is known of the actual deposition of electroless nickel. Nodules or islands of Ni metal form in various locations across the surface to be coated and then gradually spread out, covering the surface [207]. An electroless nickel coating has important implications for the mechanical behavior and physical properties of these particles.

As deposited, electroless nickel is a metastable supersaturated solution of phosphorous in nickel [207]. Low alloy deposits have very small grain sizes (values between 2-6 nm have been reported) due to rapid deposition preventing the coordinated motion of large numbers of atoms [207]. Phosphorous content above 7% by mass leads to Ni-P layers that are amorphous in the as deposited state, though not always uniformly so [207]. Electrolessly deposited nickel is hard, strong, and typically brittle [207]. The modulus of elasticity reported for alloys with 1 to 3 weight percent phosphorous is

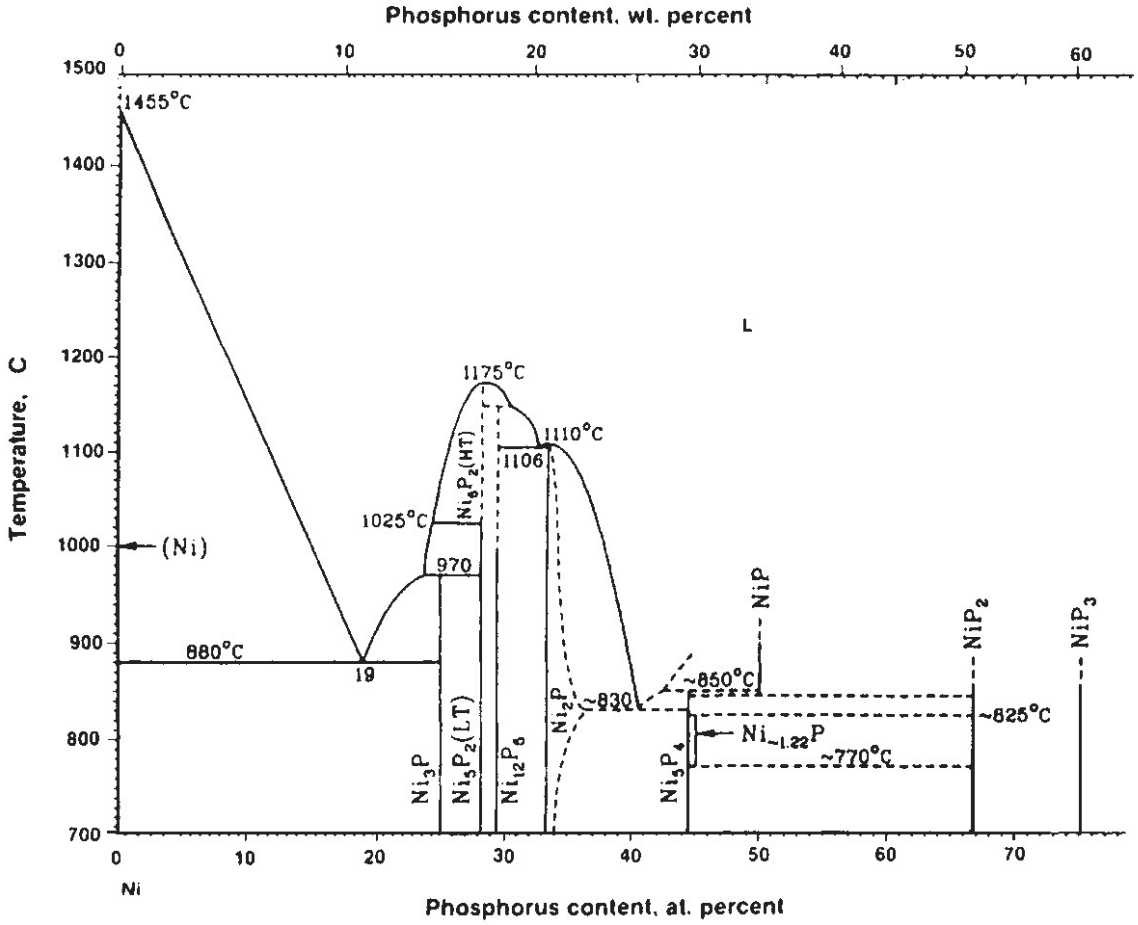

Figure 3.13: Nickel-Phosphorous Phase Diagram. Additions of phosphorous diminish the melting point of Ni as well as increasing its hardness and making it more brittle [207].

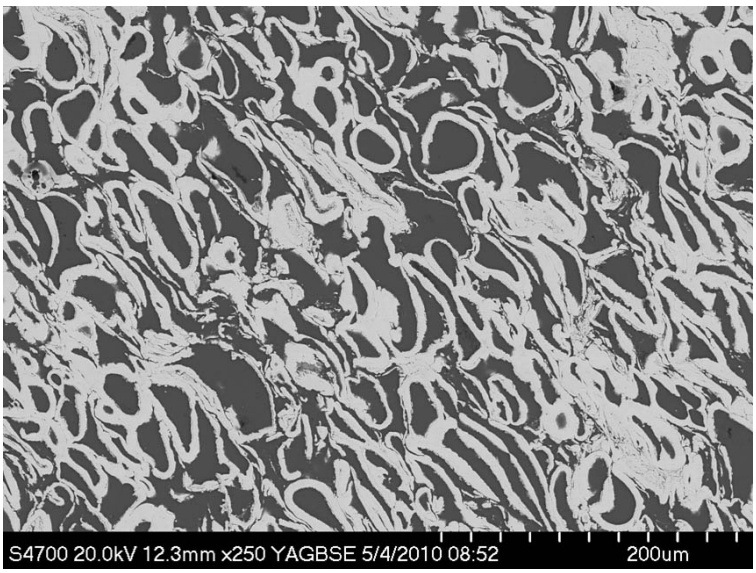

Figure 3.14: Typical cold sprayed Ni+Al microstructure [208]. Nickel is the lighter colored phase.

50-60 GPa a tensile strength of 150-200 MPa and <1% elongation at fracture [207]. Phosphorous in solution with Ni reduces the density and melting point of the solution (see Figure 3.13).

A typical cold sprayed Ni+Al microstructure appears in Figure 3.14. Notice the regions of aluminum surrounded by nickel. Nickel appears to form a matrix in which aluminum particles are suspended, which is sensible given that the feedstock used to create the material is Ni coated Al powder.

Volume fraction, surface area per unit volume, and density were measured using methods already described. These values are tabulated in Table 3.3. The density of the feedstock powder was determined directly using the Archimedes density method. A pycnometer was used to make precise measurements of the dry and submerged density of nickel coated powder and a thermocouple was used to determine the distilled water temperature. The method is described in detail in ASTM C135-96 "Standard Test Method for True Specific Gravity of Refractory Materials by Water Immersion". Sound speed for each sample was determined using Tektronix DPO5104 oscilloscope with an Optimus pulse generator operated at 100 Hz through an Ultran VSP-200

transducer for longitudinal sound speed with glycerin used as a coupling medium. Shear wave speed was measured using an Ultran SRD-50-5 transducer with honey as a coupling medium. The transducers were used in pulse-echo mode to record 10 to 20 peaks which were averaged for each measurement.

DTA data for a virgin sample of cold sprayed Ni+Al appears in Figure 3.7. It is interesting to compare this DTA trace with that of Hammetter et al. [108] (shown in Figure 2.6). Similar solid state reaction exotherms are present, suggesting extensive deformation and some component mixing. Hammetter et al. [108] studied shock compacted Ni+Al mixtures and Ni coated Al powders. Interestingly, they found that Ni coated Al powders did not exhibit much mixing [108]. This is because energy deposited during the shock process is primarily directed on the surface of powders due to the shear between powder particles as they move [209]. Therefore powders mix primarily on the surfaces during shock compaction; Ni/Ni surface mixing is of little utility to promoting a reaction. During the cold spray process, the deformations of the impacting particles are not constrained to the same extent as in a uniaxial strain shock compression experiment. For this reason, it seems likely that mesoscale constituent mixing is easier between the Al particle and its Ni coating during the cold spray process. Similar to shock-consolidation of powders, the cold spray process leads to extensive work hardening in the impacting particles. Champagne et al. [210] reported the average hardness of cold sprayed commercially pure aluminum deposits as 57 Brinell, with some as high as 70 Brinell, while that of fully wrought commercially pure aluminum was reported to be 45 Brinell. This illustrates the notion that the cold spray process introduces a very significant population of dislocations.

3.3.1 Quasi-static Compression Testing of Cold Sprayed Ni+Al Structural Energetic Materials

Cold Sprayed Ni+Al samples were cut into nominally 7 mm x 7 mm x 4 mm rectangular solids via wire EDM and lapped flat and parallel. A screw-driven STI Phoenix

Table 3.3: Selected Properties of Cold Sprayed Nickel+Aluminum

	CS Ni+Al
V_v	0.51±0.02 Ni
S_v	186±6 mm^{-1}
Density (g/cm^3)	5.27±0.04
Theoretical Density (g/cm^3)	5.55±0.01
Percent Theoretical Density	95
C_{long} ($mm/\mu s$)	5.03±0.05
C_{shear} ($mm/\mu s$)	2.72±0.05
Elastic Modulus (GPa)	30±10
Yield Strength (MPa)	310±4

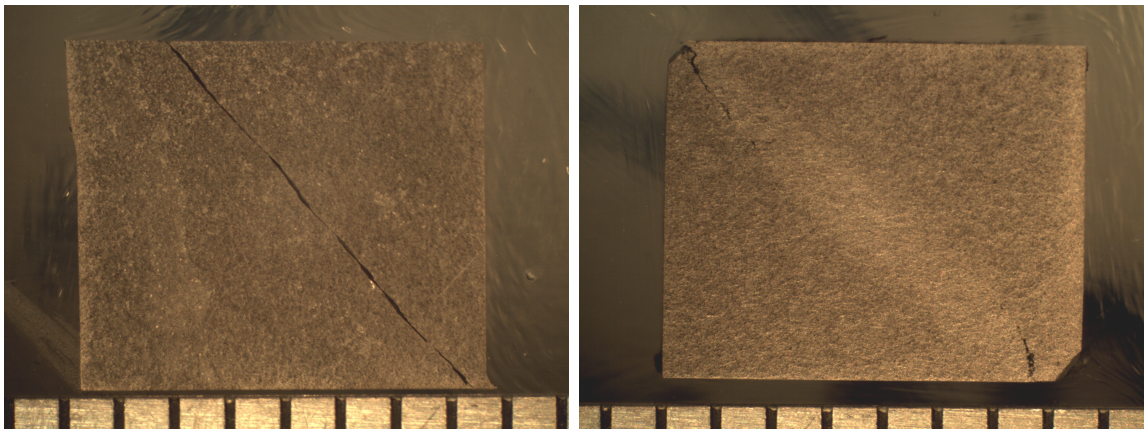

(a) (b)

Figure 3.15: (a) Compression sample which formed a shear crack without a cracked band of material. (b) Compression sample which formed with a *shear band* of cracked material prior to complete failure. The scale is in millimeters.

D30-20 load frame was utilized for compression testing with a 20,000 lb. load cell. The data was captured with a proprietary STI data acquisition card. The loading rate was 0.0013 inches per minute. The hardened steel platens were ground and lapped flat. A fine layer of molybdenum disulphide applied to both compression platens was sufficient to prevent sample barreling. Displacement was measured using a capacitance gage with a displacement range of 0.200 inches and a resolution of 0.0005 inches and a Satec model # AK3 signal amplifier unit through a proprietary STI data acquisition card.

As revealed by the stress strain curves in Figure 3.8b, the cold sprayed nickel+aluminum samples exhibited some apparent ductility in compression. Though there appears to be less inelastic deformation than that in the explosively compacted Ni+Al or W+Al, the high speed images of Hopkinson Bar data from Wei et al. [132] of Ni+Al and W+Al show extensive fracture rather than plastic deformation. Such is likely the case in quasi-static compression as well. The initial non-linear portion of the stress strain curves in the cold sprayed Ni+Al at low strains, seen in Figure 3.8b may be a result of the densification of the cold sprayed Ni+Al. The trace labeled Sample 6 was cycled above its yield point before being tested to failure. It exhibits less of the initial non-linearity as well as increase in yield strength which supports the notion of the non-linear portion being related to porosity. It is interesting to note that the cold sprayed Ni+Al, like explosively compacted Ta+Al, is much stronger than the explosively compacted Ni+Al, W+Al, Mixture A, and Mixture B. This is reasonable if the Ni network dominates the stress strain response of the cold sprayed material. Cold worked Ni may attain strengths above 400 MPa and the Ni coated Al particles are extensively work-hardened during fabrication.

All cold sprayed Ni+Al samples failed via the formation of a dominant shear crack. Some of the samples exhibited the formation of a macroscopic band in the plane of maximum shear, which is actually a region of microcracked material, while others simply formed one dominant crack with no obvious shear band structure. This can be seen in Figure 3.15a, 3.15b. It is also interesting to note that the yield strength of the cold sprayed Ni+Al material, 310 MPa, is higher than the yield strength of the explosively compacted W+Al, 240 MPa, with the explosively compacted Ni+Al being similar as between shown in Figure 3.8a and 3.8b. Young's Modulus was determined by fitting the linear portion of the initial stress-strain curves. Yield strength was determined by the 0.02 offset method ignoring the non-linear foot of each curve.

The static mechanical dynamic properties of three batches of cold sprayed Ni+Al

were also investigated by Pan et al. [211]. They tested cold sprayed Ni+Al made from two batches of Ni coated Al powders, termed H15 and H40, which where sprayed into two different geometries termed *Block* and *Washer*. The H15 and H40 designations are derived from the Valimet size designation for the aluminum powders to which Ni coatings were applied. The *Block* designation refers to powder sprayed onto a flat substrate. Samples were machined out of the dense powder compact via wire EDM. The CS Ni+Al compression samples tested in this work were Block samples. The *Washer* designation refers to powder deposited onto a rotating mandrel. Again the samples were machined from the powder compact. The data for all sets is shown in Figure 3.16a, 3.16b, and 3.16c. Pan et al. used an MTS 810 load frame for quasi-static compression testing [211]. The compression samples were nominally 5.0 mm x 2.5 mm x 2.5 mm for quasi-static tests [211]. The applied strain rates in the quasi-static tests were 10^{-3} in these tests which were conducted at room temperature [211].

The quasi-static test samples all fractured through shear failure [211]. The fracture was reported to form an angle with the surface of the sample of approximately 40 degrees [211] . This description is very similar to the failure mechanism observed in the samples tested in the present work and seen in Figure 3.15a. Comparing stress-strain curves in Figure 3.8b and Figure 3.16a-3.16c the strength levels for the samples tested in this work and those tested by Wei et al. [132] are reasonably comparable.

3.3.2 Split-Hopkinson Bar Pressure Tests of Cold Sprayed Ni+Al Structural Energetic Materials

The dynamic properties of cold sprayed Ni+Al were investigated by Pan et al. [211] and are shown in Figure 3.17a-3.17c. A miniature Split Hopkinson Pressure Bar system was utilized for this purpose. The samples were nominally 2.0 mm x 2.5 mm x 2.5 mm for the dynamic tests [211]. These tests were also performed at ambient temperature. Pan et al. [211] reported that the samples in the dynamic tests showed

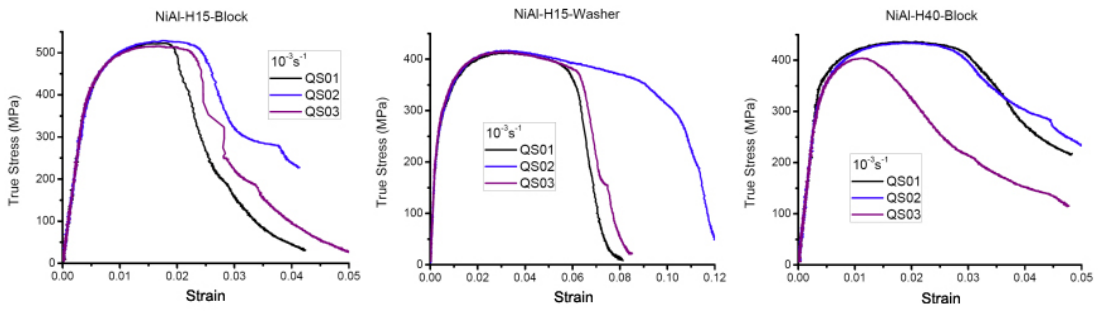

(a) (b) (c)

Figure 3.16: Cold Sprayed Ni+Al Quasi-Static Compression Data from Pan et al. [211]. (a) Compression data for powder H15 sprayed onto flat substrate [211]. (b) Compression data for powder H15 sprayed onto a rotating mandrel [211]. (c) Compression data for powder H40 sprayed onto flat substrate [211]. Figures reprinted by permission.

evidence of shear banding, and when fracture occurred it did so through shear cracking. This description is very similar to the failure mechanism seen in Figure 3.15b, which suggests that the failure mechanisms are reasonably consistent between Pan et. al's data and the results presented for cold sprayed Ni+Al samples in the present work.

For this work, it will be assumed that all of the structural energetic materials are isotropic. This assumption is not strictly true given the anisotropy that is likely to be created by plastic flow in the explosive compaction or cold spray process. However, the amount of available material precluded testing any other assumption and the material variability inherent in these composite materials, which manifests as differences in sound speed, density, and strength (likely due to manufacturing and powder feed stock variability) are considered to be as significant as differences due to anisotropy.

3.3.3 Shock Compression Testing of Cold Sprayed Ni+Al Structural Energetic Materials

Shock propagation properties of the structural energetic materials considered here are of great interest. Modern hydrocodes are widely used in the study of materials at different length scales for topics ranging from theories about the formation of Earth's

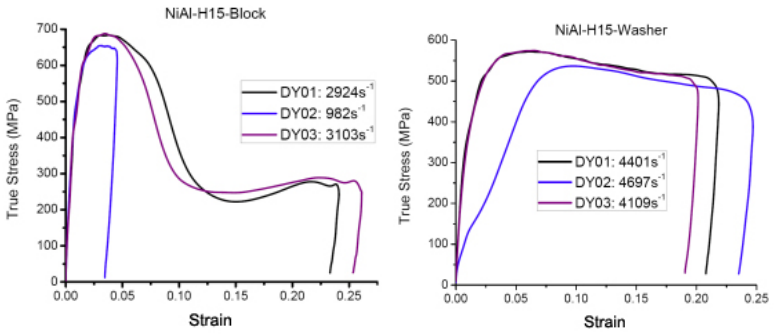

(a)

(b)

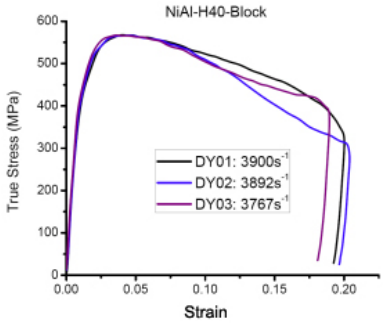

(c)

Figure 3.17: (a) Dynamic compression data for powder H15 sprayed onto flat substrate. Sample DY02 did not fracture during testing [211]. (b) Dynamic compression data for powder H15 sprayed onto a rotating mandrel. The data for sample DY02 is believed to be in error due to poor contact with the input bar face [211]. (c) Dynamic compression data for powder H40 sprayed onto flat substrate [211]. Figures reprinted by permission.

moon [212] to the formation of explosively formed penetrators [213]. In this study, CTH, a multi-material Eulerian hydrocode will be utilized to study the behavior of cold sprayed Ni+Al for comparison with a full scale cased charge experiment which will be described later. Hydrocodes require an equation of state and a constitutive relationship as inputs. The Hugoniot is a relationship between two of the five following variables: pressure P, specific volume v, internal energy E, U_S and U_P. It is a slice of the equation of state. At high pressures, the Hugoniot is often procured through parallel plate impact testing. An experimentally determined Hugoniot is often extrapolated to form the rest of the equation of state via the Mie-Grüneisen approximation as discussed earlier.

It is not practical to conduct a complete set of parallel plate impact experiments on all real or notional systems. Mixture theories have been proposed to develop an equation of state for a mixture from the equation of state of its constituents, the most widely used being that of McQueen and Marsh [214]. Mixture theories play an important role, but neglect the microstructural details of the material in question. Eakins and Thadhani [30, 31], Jordan et al. [80] and Thadhani and Specht [114] have demonstrated that mesoscale simulations of highly heterogeneous structural energetic materials can provide accurate estimates of the shock Hugoniot for non-reacting systems. A similar approach will be taken with cold sprayed Ni+Al.

Parallel plate impact tests were conducted on cold sprayed Ni+Al. In all, five plate impact experiments were conducted and each experiment was conducted on two cold sprayed Ni+Al samples, labeled 1 and 2. The samples were taken from two batches of cold sprayed Ni+Al manufactured under the same conditions. This was done in an effort to understand variability in shock response due to differences in the material. Sample size was limited by the available material. The largest samples available for these experiments were 10 mm diameter. This limited sample thickness to under 2 mm to retain the uniaxial strain state of deformation within the timescale

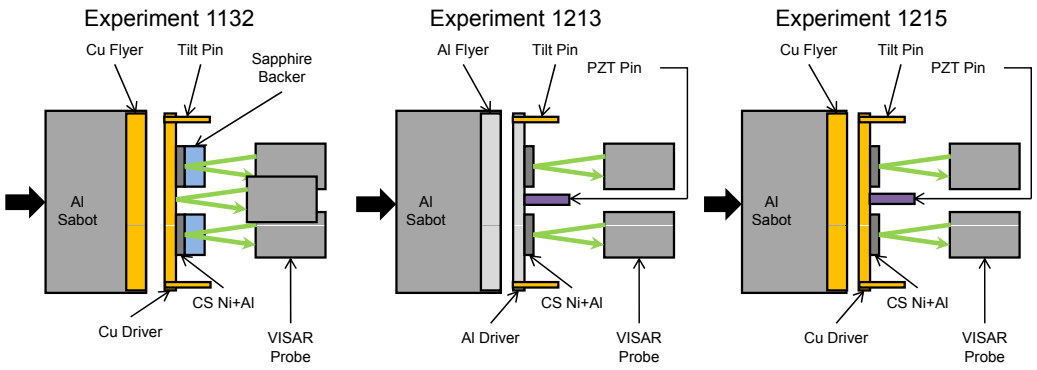

Figure 3.18: Shock Compression Experimental Configurations for Experiments 1132, 1213, and 1215

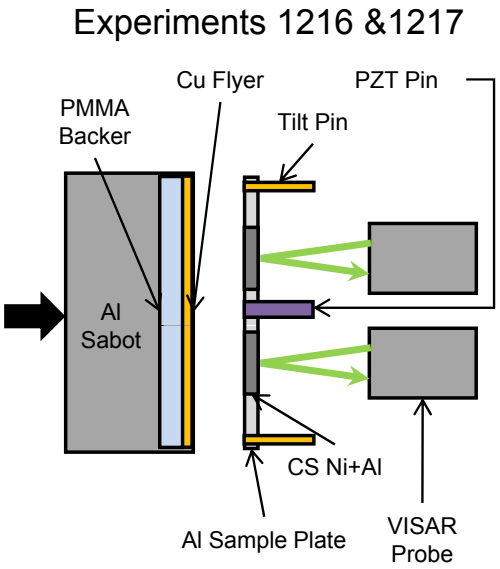

Figure 3.19: Shock Compression Experimental Configurations for Experiments 1216 and 1217

of the experiment.

Three experiments, 1132, 1213, and 1215, were conducted using an OFHC 101 or Aluminum 6061 flier plate mounted on an aluminum sabot, and an OFHC 101 or 6061 aluminum driver plate on the back of which the sample discs were mounted. Matched flier and driver plates were used to create symmetric impacts which simplifies impedance matching in the event of an experiment malfunction.

The driver plate was placed within a polymethylmethacrylate (PMMA) target ring, nominally 1/2 inch in thickness, which was bolted directly to the muzzle of

Table 3.4: Shock Compression Experimental Data for Cold Sprayed Ni+Al.* Shot 1132 utilized sapphire backers which, due to their high impedance, led to a lower particle velocity. Utilizing the p-α model and CTH, simulations of Experiment 1132 were conducted to obtain simulated values of the free surface velocity under the same conditions. $C_{bulk} = \sqrt{C_{long}^2 - \frac{4}{3}C_{shear}^2}$

Experiment	Impact Velocity (mm/μs)	$U_{fs}/2$ (mm/μs)	U_S (mm/μs)	Density (g/cm^3)	C_{bulk}
Sample 1 (avg)				5.26±0.06	4.0±0.2
1132	0.430±0.01	0.19(0.24*)±0.01	3.4±0.3	5.26±0.06	4.0±0.2
1213	0.390±0.005	0.148±0.003	–	5.31±0.01	3.96±0.02
1215	0.575±0.003	0.33 ±0.02	4.2±0.8	5.31±0.01	4.18±0.02
1216	1.22±0.01	0.71 ±0.01	4.95±0.08	5.258±0.004	3.92±0.02
1217	0.81±0.03	0.47 ±0.01	3.75±0.07	5.308±0.009	3.96±0.02
Sample 2 (avg)				5.27±0.01	4.0±0.2
1132	0.430±0.01	0.19(0.24*)±0.01	4.0±0.2	5.27±0.01	4.0±0.2
1213	0.390±0.005	0.145±0.003	–	5.281±0.008	4.11±0.03
1215	0.575±0.003	0.32 ±0.02	4.8±0.9	5.271±0.005	3.90±0.02
1216	1.22±0.01	0.71 ±0.01	5.03±0.09	5.272±0.008	3.86±0.03
1217	0.81±0.03	0.47 ±0.01	3.95±0.08	5.265±0.008	4.10±0.01

the Georgia Institute of Technology High Strain Rate Lab 80 mm single stage gas gun. The PMMA target rings had copper wires or brass screws glued into them and lapped flat at precisely located points; these served to measure the tilt of the flier plate during impact by completing an electrical circuit. Tilt measured right around one milliradian for all experiments. The experimental setups are depicted schematically in Figure 3.18.

Projectile velocity for all shots was determined using an electrical pin contact method. Four pins make successive electrical contact with the side of the aluminum sabot as it emerges from the muzzle prior to contact with the target assembly. The pin voltages were recorded on an oscilloscope and the pin spacing was measured precisely with a micrometer accurate to 0.0001 inches before each experiment.

Experiment 1132 also utilized two C-axis sapphire windows from Meller Optics, which were 2mm thick, as window materials. The rest of the experiments used no windows. Experimental results such as impact velocity, measured free surface velocity, and shock speed as well as density and bulk sound speed of the samples are listed in Table 3.4.

It was ultimately determined that it was unnecessary to use a driver or buffer

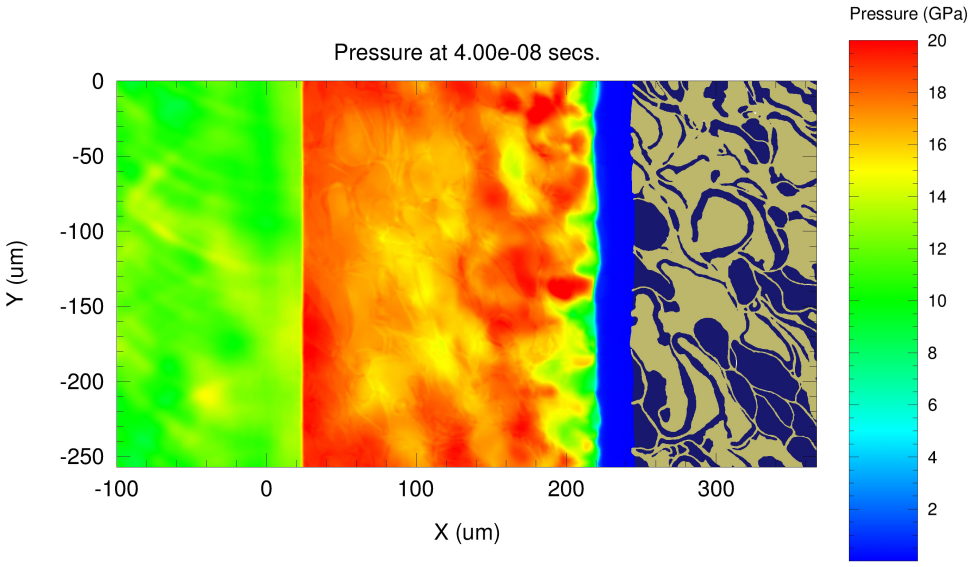

Figure 3.20: Simulated shock wave propagation in cold sprayed Ni+Al impacted at 1000 m/s by a copper projectile after 40 ns. Notice the spatially heterogeneous response.

on the cold sprayed Ni+Al samples, which proved adequately robust for ordinary handling and machining. The experiment design was altered such that the cold sprayed Ni+Al samples were impacted directly by the flier plate. The tilt pins and the PZT pin all became time of arrival detectors and were used in conjunction with the VISAR data to calculate shock velocity. A thinner flier plate was used as well. The altered setup for experiments 1216 and 1217 is shown in Figure 3.19.

Aydelotte et al. [208] utilized CTH [215], an Eulerian Hydrocode, to determine the shock Hugoniot for the cold sprayed nickel+aluminum. To develop a U_S-U_{fs} equation cold sprayed Ni+Al, the microstructure shown in Figure 3.14 was binarized and filtered and then incorporated into a 2D rectangular mesh in CTH using a MATLAB script. The simulation involved impacting the reconstructed microstructure with a rigid copper driver to initiate the propagation of a shock wave through the microstructure. Periodic boundary conditions were used along the edges parallel to the propagating shock wave, while the other boundaries were modeled as sound speed absorbing, simulating an infinite material. The rectangular computational mesh was

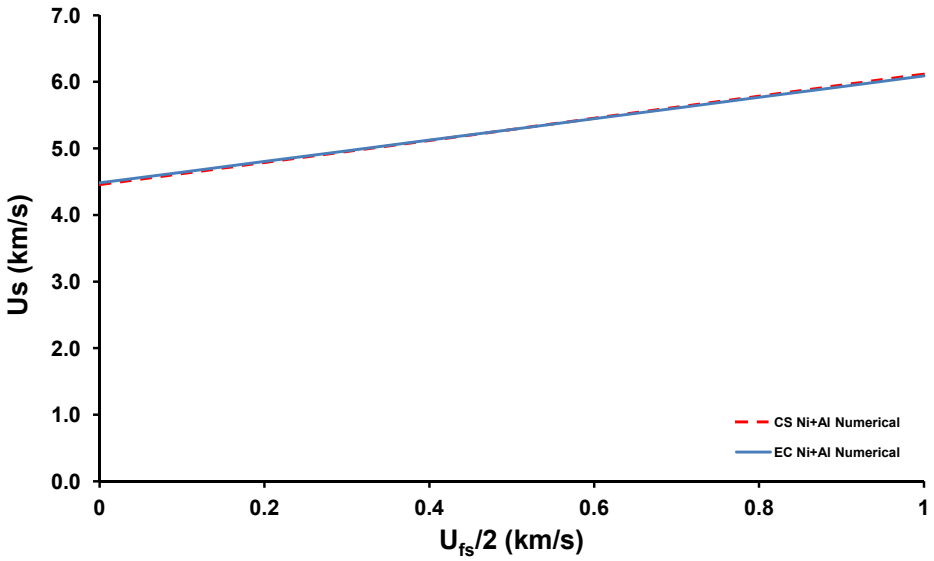

Figure 3.21: Numerically derived Hugoniots for the cold sprayed and explosively compacted Ni+Al Systems

found to converge at a resolution of 0.4 microns per cell. Simulations were run at impact velocities of 500, 750, 1000, 1250, and 1500 m/s. The pressure responses in each simulation were recorded at 5 ns intervals. The pressure response was averaged along the direction perpendicular to the propagating wave at each cell center to obtain a one-dimensional, average pressure trace. A point corresponding to 50% of the steady state pressure was tracked for each impact velocity to obtain the corresponding shock speed. The particle velocity was determined by measuring the velocity of Lagrangian tracers near the driver-sample interface. An example of the simulation is shown in Figure 3.20 where the microstructure was shown 40 ns after impact.

The Mie-Grüneisen equation of state was utilized for all materials. The Steinberg, Cochran, and Guinan [216] constitutive model with no rate dependence was used for both nickel and aluminum with appropriate constants taken from the CTH library. The results of these simulations produced a Hugoniot given by $U_S = 4.46 + 1.66U_P$ km/s. A similar computational setup was used by Specht [217] to estimate the Hugoniot of the explosively compacted Ni+Al mixture. This Hugoniot was found to be

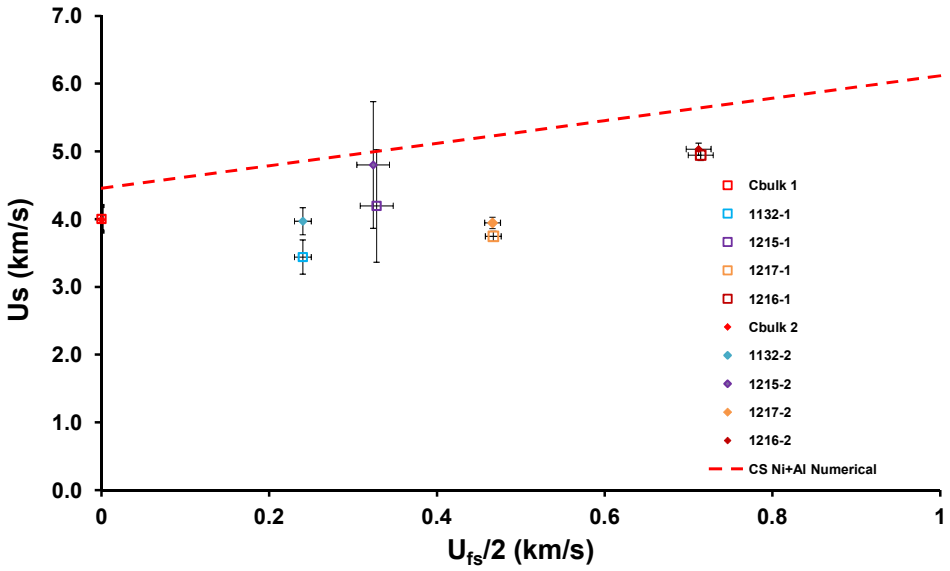

Figure 3.22: Shock wave propagation data for cold sprayed Ni+Al compared with the Hugoniot generated using mesoscale simulations. The Hugoniot derived from mesoscale simulations on a full density microstructure is shown as a dashed red line.

$U_S = 4.48 + 1.61 U_P$ km/s. They are very similar despite their different microstructure morphologies and are compared in Figure 3.21

The shock data that was measured is tabulated in Table 3.4 and plotted in Figure 3.22. The data is also compared with the Hugoniot derived from numerical simulations in Figure 3.22. The Hugoniot derived from simulations, shown as a dashed red line, lies above the data. As indicated in Table 3.3, the cold sprayed material is 95% dense. The intense localized plastic deformation that takes place around voids absorbs significant amounts of energy as was indicated in Chapter 2. The energy absorbed by the localized deformation around porosity energy leads to increases in the post shock sample temperature, but the shock speed is reduced as a consequence. The discrepancy lies in the fact that the micrograph used for the simulations, shown in Figure 3.14 did not contain significant amounts of porosity. This may be due to random sampling or perhaps the polishing process filled the porosity. In either case, the numerically estimated Hugoniot amounts to an estimate of the Hugoniot for full

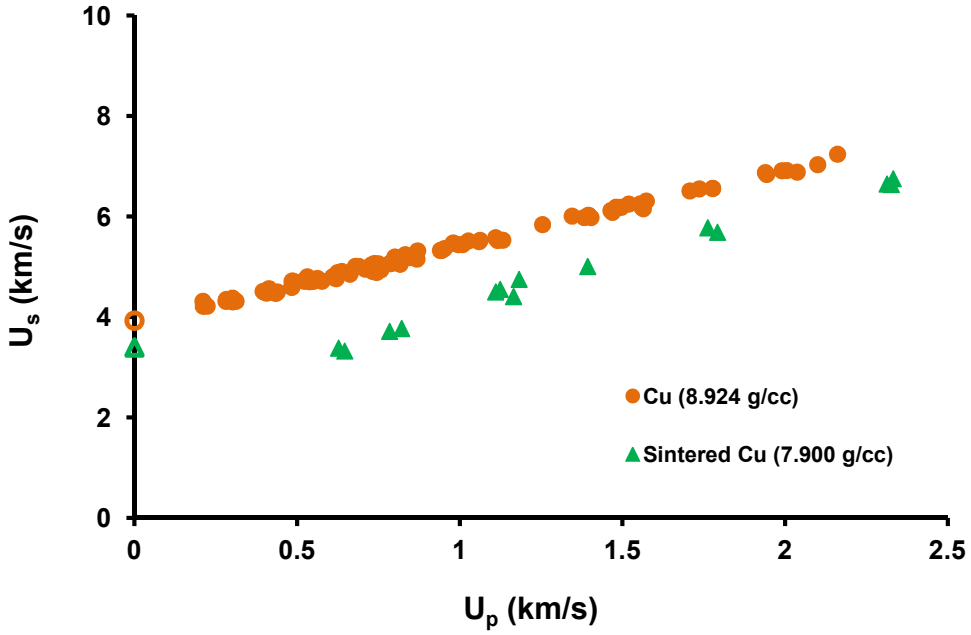

Figure 3.23: Shock wave data for porous and full density copper from Marsh [218]. Notice the significant difference in shock wave speed for a given particle velocity. Propagation of a shock wave through a porous material leads to densification, which requires tremendous local deformation and absorbs a great deal of energy which reduces shock velocity.

density cold sprayed Ni+Al.

Consider data on 11.5% porous copper shown in Fig 3.23 from the LASL shock hugoniot data [218]. The same trend is evident in the porous copper vis-á-vis the full density copper as that observed in Figure 3.22 in the experimental data versus the computationally derived cold spray Ni+Al Hugoniot. The lower density copper has significantly reduced shock speeds for a given particle velocity.

If a simple Mie-Grüneisen porosity model, like that described in Sec. 2.3, is employed in conjunction with the numerically derived Hugoniot, then much more reasonable agreement with the experimental shock wave propagation data is obtained as seen in Figure 3.24. By accounting for the small amount of porosity, a dramatic improvement in model agreement with the data is obtained.

Significant scatter exists in the data. The observed variation in the data is the result of scatter in the physical properties of the cold sprayed samples which were

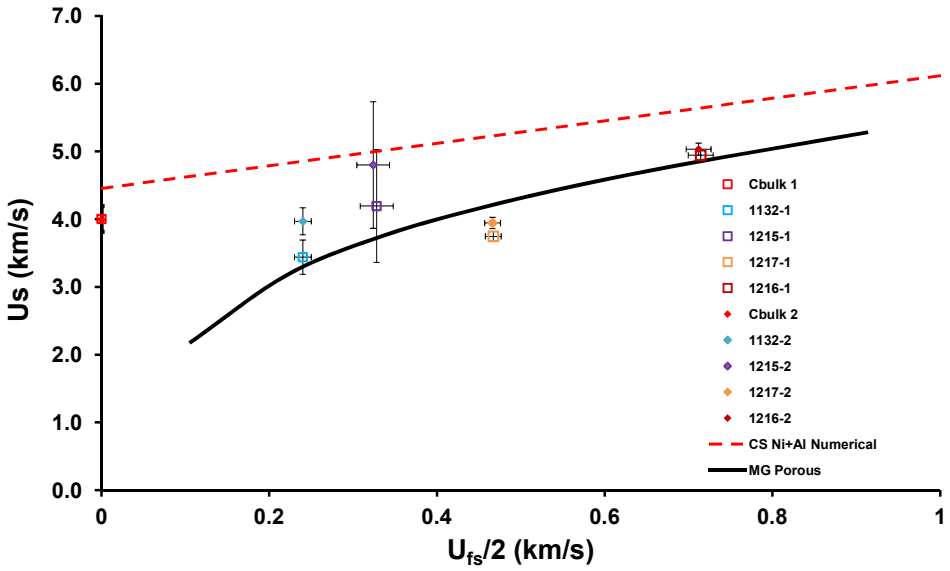

Figure 3.24: Shock wave Hugoniot data for cold sprayed Ni+Al compared with the numerically derived Hugoniot and simplified porosity model. The Hugoniot derived from mesoscale simulations on a full density microstructure is shown as a dashed red line. A simplified porosity model combined with the numerically generated Hugoniot is shown as a thick black line.

tested. Density and bulk sound speed are tabulated for the tested cold sprayed samples in Table 3.4. These physical properties show measurable and significant variation due to natural variations in composition and the amount of porosity. Stochastic variation in materials properties is expected in any material, particularly any highly heterogeneous, research grade composite. These variations naturally influence shock propagation behavior.

3.4 Summary of the Characterization of the Materials Systems

A few key points from this chapter are repeated for emphasis:

- Most of the materials in question have some porosity, but the amount of porosity is similar between materials. The porosity will exert an influence over shock wave propagation behavior as shown.

- The mechanical behavior of the structural energetic materials in question is heavily influenced by their topology. Explosively compacted Ta+Al and the cold sprayed Ni+Al show higher strengths in part due to the topological connectivity of their stronger phases. Explosively compacted Ni+Al, W+Al, Mixture A, and Mixture B also appear to be dominated by their aluminum component rather than their other, stronger components. It remains to be seen if there will also be an effect on the fragmentation behavior.

- All of the binary systems have roughly comparable volume fractions of the Al.

- The Mixture A, Mixture B, and the cold sprayed material have roughly similar interface densities.

- The Hugoniot of 5% porous cold sprayed Ni+Al can be accurately modeled by combining simulation data from a fully dense microstructure with a simple Mie-Grüneisen porosity model.

CHAPTER IV

FRAGMENTATION EXPERIMENTS AND RESULTS OF STRUCTURAL ENERGETIC MATERIALS

The literature on fragmentation of structural energetic materials is surprisingly limited. As indicated previously, fragments may combust if sufficiently small, liberating energy. However, larger fragments will not effectively combust, but can react upon subsequent impact with a target. It is desired to understand the fragmentation response of the explosively compacted and cold sprayed structural energetic materials investigated in this work.

4.1 Experimental Fragmentation Methods

A number of experimental techniques have been utilized to study fragmentation including explosives, an induced current, and gas guns. A brief overview of the experimental fragmentation literature reveals the strengths and weaknesses of the most popular methods of studying fragmentation.

Explosive fragmentation of metallic rings and shells has been performed by Mott [4, 156] and Gurney and Sarmousakis [5, 157]. Variations on explosive fragmentation were conducted by Perrone [158], Forrestal et al. [159], and Hiroe et al. [160, 161]. Explosives are quite versatile, but make fragment recovery more difficult. Furthermore, the cloud of explosive product gases interfere with optical diagnostics, do not give uniform expansion velocities nor, in cylinders, is the entire cylinder accelerated at the same time without careful initiation. Explosives pre-condition the sample material to varying degrees leading to plastic working in metals, possible damage accumulation in brittle materials, and temperature increases. However, at present they remain the

best way to access the highest strain rates for large samples.

Niordsen [162] pioneered the expanding electromagnetic ring technique, using a large capacitor charged by a high voltage powder supply to dump a large current into a solenoid to induce expansion in the ring-shaped metal samples. Walling and Forrestal [163], Grady and Benson [164], Zhang and Ravi-Chandar [165–167] also utilized this technique to study the fragmentation problem. Fyfe and Rajendran [219] used an exploding wire to study dynamic deformation of thin walled metal cylinders. The electromagnetic technique pioneered by Niordsen [162] seems very versatile and works quite well for ductile metals. It provides a constant expansion velocity and constant strain rate. For materials that are poorly conductive it is problematic. It can be adapted but due to the high induced current in the sample ring, when a ring fractures electrical arcs form, as observed by Niordsen [162] and Zhang and Ravi-Chandar [165–167]. This is problematic in any reactive material which might potentially be initiated by a high current electrical discharge. There is also the question of ohmic heating of the samples, which may lead to greater ductility and the formation of fewer fragments. The exploding wire, which uses the same type of capacitor power supply to turn a wire into high pressure plasma, addresses some of these issues, but at the price of a non-uniform expansion velocity much like an explosive.

Winter [170] and later Vogler et al. [171] utilized a laboratory gas gun to cause fragmentation in metal cylinders. Laboratory gas guns are easy to use and instrument, though not without difficulties, as a method of studying fragmentation. Vogler et al. [171] had problems with lateral translation of the sample during the experiment. This could lead to VISAR or PDV probes coming out of alignment with the sample. Winter [170] and Vogler et al. [171] both used tubular samples, which were subject to non-uniform loading.

In the present work, explosives and exploding wires were the primary techniques

used to provide loading to the samples for fragmentation studies. The various experimental set-ups utilized are described below.

4.2 Fragmentation Testing

4.2.1 Cambridge Explosive Ring Fragmentation Experiment Description

Several different experimental setups were utilized to produce fragmentation of structural energetic materials. The experimental setup used at Cambridge to study fragmentation in 6082 Al, cold sprayed Ni+Al, Mixture A, and Mixture B rings employed explosives. As reported in Aydelotte et al. [208], the aluminum and cold sprayed Ni+Al rings tested were 30 mm O.D. x 22 mm I.D. x 4 mm tall. The Mixture A and Mixture B rings were 25 mm O.D. x 19 mm I.D. x 3 mm tall and were fabricated via wire EDM machining. The aluminum rings were manufactured via conventional means. The CS Ni+Al rings were wire EDM'd and turned to final dimensions from Block CS Ni+Al material. The Al and CS Ni+Al samples were mounted on a UPVC tube as shown in Figure 4.1a, and Primasheet 1000 charges (65% PETN, 8% Nitrocellulose and 27% inert binder) were placed inside the UPVC tube as indicated in the figure. The size of the explosive charges for the various experiments is noted in Table 4.1; in all cases 15mm long confined columns of explosive were used in an effort to ensure steady detonation and even sample loading, and Nobel No. 6 hollow-ended type detonators were used to initiate the Primasheet. The entire explosive assembly was placed within a steel tube 200mm in diameter which was lined with a 10mm thick layer of paraffin wax for fragment recovery. The experimental assembly was placed inside a steel box approximately 305 mm on a side, and composed of nominally 12.5 mm thick mild steel plates. The lid was fastened using six steel 12.5 mm diameter bolts of unspecified grade. The port holes in the box were covered either with steel plates or with three 10mm thick PMMA plates when viewing was required.

Photon Doppler Velocimetry, also known as PDV or Het-V, was utilized to monitor

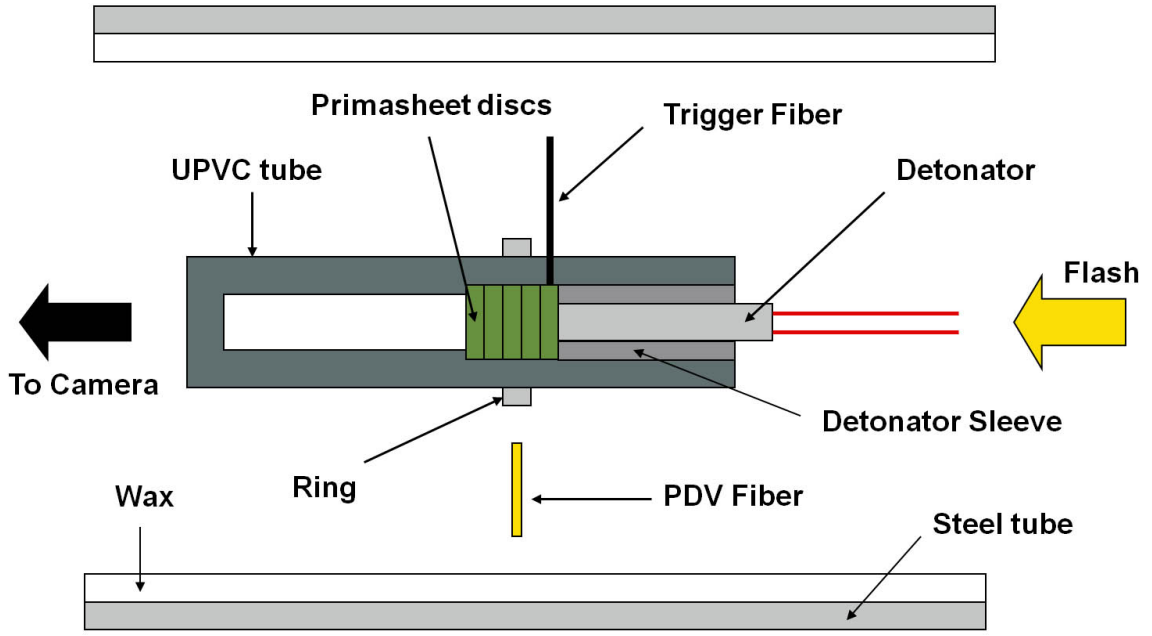

(a)

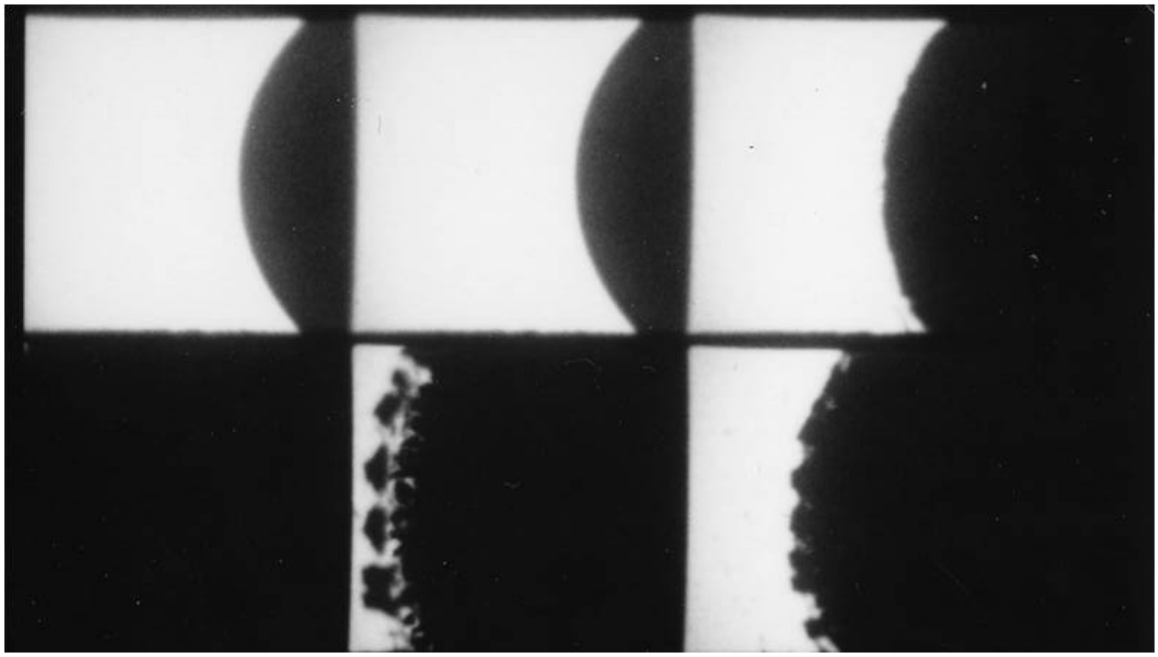

(b)

Figure 4.1: (a)Diagram of the explosive setup employed for the expanding ring tests. (b)Fragmenting UPVC tube obscuring the fragmentation of the cold sprayed Ni+Al ring.

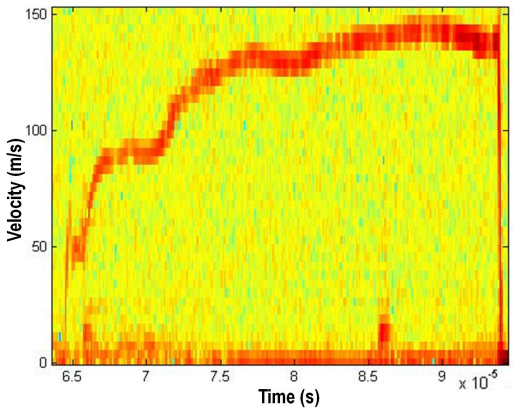

Figure 4.2: Cold sprayed Ni+Al ring free surface velocity data for experiment E101014A.

the rings free surface velocity. The PDV setup, built by AWE Aldermaston, was used with a fiber coupled IR laser with a frequency of 1550 nm and a nominal laser power output of 140mW. Bare fiber probes were mounted normal to the ring surface in small PMMA blocks. The PDV setup was triggered via light emission from the explosive due to considerable variation in the trigger-to-detonation times. Unfortunately, the only experimental PDV trace for a Ni+Al ring captured was that for experiment E101014A, and is shown in Figure 4.2. Further analysis was conducted using CTH to generate estimates of free surface velocities where PDV data was not available.

This experimental setup was successful in causing ring fragmentation but suffered from some deficiencies. Triggering the PDV and high speed camera off of explosive light emission proved unreliable. In addition, efforts to observe the fragmentation process were hampered by the rapid expansion and fragmentation of the UPVC tube which blocked the view from the high speed camera as seen in Figure 4.1b. This setup also does not allow the camera to effectively see the formation of cracks in the sample rings, rather, the completed fractures are only visible when sufficient space opens up between them to allow light through.

The experimental setup was redesigned slightly. The sample ring was front lighted to improve visibility of the nascent fractures. The UPVC tube was replaced with a

Table 4.1: Parameters for Cambridge ring fragmentation experiments. * are estimated from published density.

Test	Sample	Tube	Charge ⌀ (mm)	Charge (g)	Detonator	Ring (g)	Rec. Mass (g)
E100930A	6082 T6 Al	UPVC	7.2	0.980	Nobel #6	3.53*	3.38
E101004A	6082 T6 Al	UPVC	7.2	0.980	Nobel #6	3.55	3.55
E101012A	6082 T6 Al	UPVC	8.2	1.25	Nobel #6	3.53*	3.12
E110117A	6082 T6 Al	Cu	16.0	5.0	Teledyne RP-80	3.53*	3.44
E101020A	CS Ni+Al	UPVC	3.7	0.226	Nobel #6	7.2436	6.1709
E101014A	CS Ni+Al	UPVC	7.2	0.97	Nobel #6	6.3686	5.0350
E101022A	CS Ni+Al	UPVC	9.9	1.887	Nobel #6	6.860	5.555
E121023A	Mix 2	Cu	NA	NA	Teledyne RP-80	4.705	4.648
E120820A	Mix 2	Cu	8.0	1.209	Teledyne RP-80	4.705	4.499
E120816A	Mix 2	Cu	15.0	3.978	Teledyne RP-80	4.702	3.643
E121023B	Mix 5	Cu	NA	NA	Teledyne RP-80	4.856	4.651
E121021A	Mix 5	Cu	8.0	1.173	Teledyne RP-80	4.860	4.449
E120824A	Mix 5	Cu	15.0	4.111	Teledyne RP-80	4.85	4.33

copper tube to better contain the explosive products and prevent the tube from occluding the ring. The Nobel hollow-ended detonator was replaced with a Teledyne RISI RP-80 exploding bridge wire detonator which triggers with much greater temporal consistency. The resulting setup, is shown in Figure 4.3a. This setup was used to test the Mixture A and Mixture B rings.

The updated fragmentation experiment design proved far more effective. Timing proved to be less problematic with the RP-80 detonator. Front lighting the ring made detection of nascent fractures possible, as shown in Figure 4.3b. The copper tube did not fragment and it delayed detonation products from obscuring the sample ring. The copper tube was darkened with black permanent marker or paint in order to improve contrast between the ring and the copper tube. Paint was found to spall off of the tube and was visible as a diffuse, black arc in Figure 4.3b, but the permanent marker provided much less contrast.

4.2.2 Army Research Laboratory Explosive Ring Fragmentation Experiment Description

Cold sprayed Ni+Al rings, machined from from Washer CS Ni+Al material using wire EDM and conventional machining techniques, were also tested at the Army Research Laboratory at Aberdeen Proving Ground (ARL). Similar conceptually to

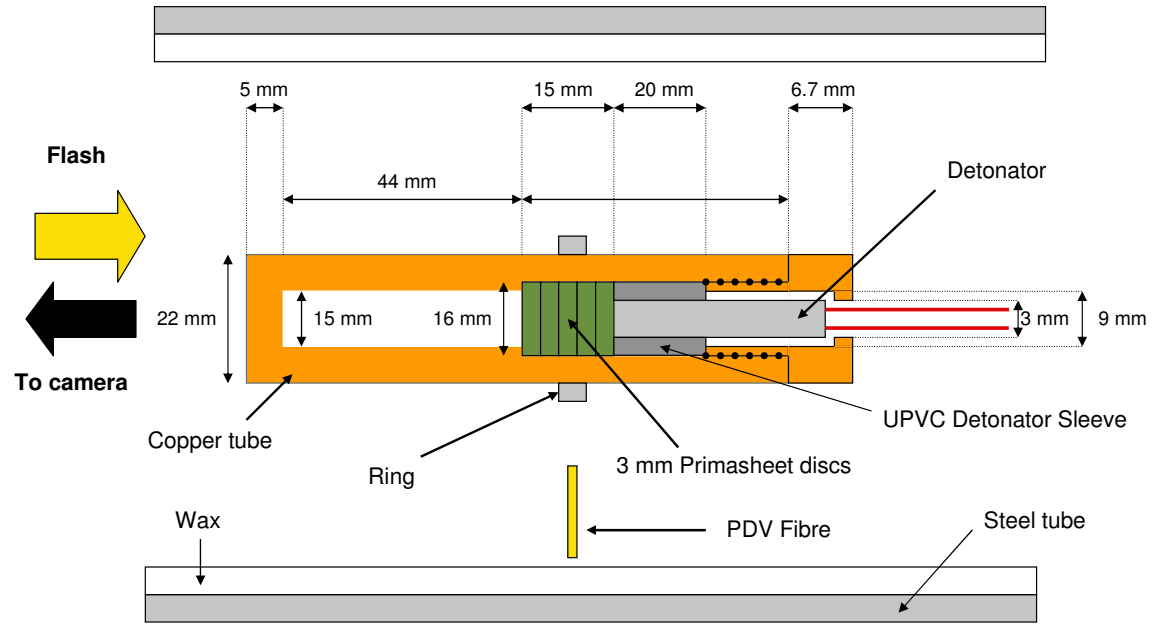

(a)

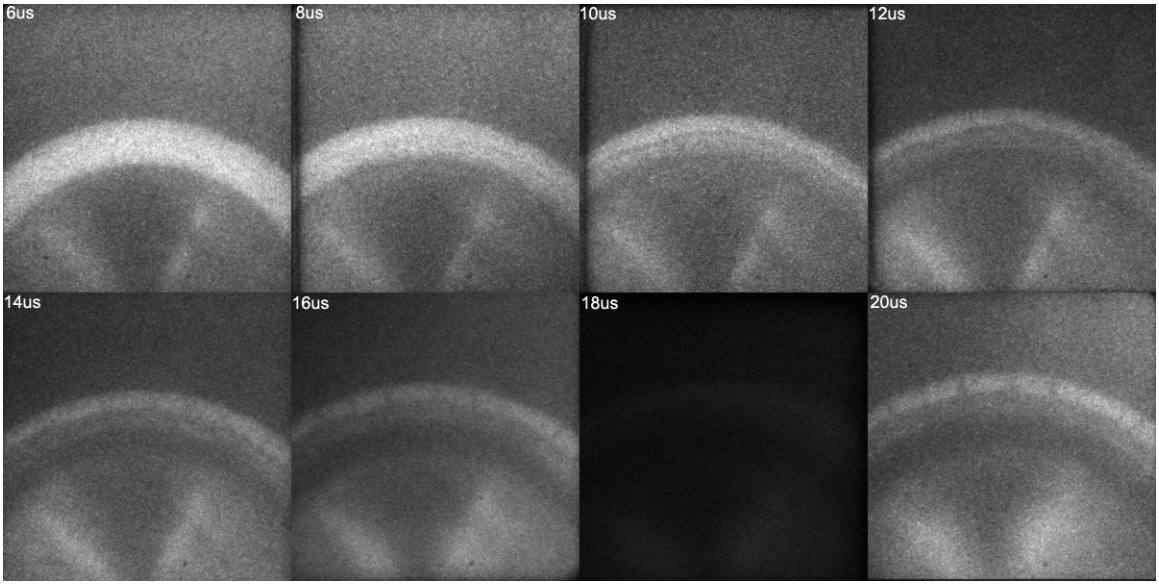

(b)

Figure 4.3: (a) Updated ring fragmentation experimental design [220]. (b) Expanding ring test E120820A during expansion and fracture. Notice the radially oriented cracks that become visible as they form and paint which spalls off of the tube to form an arc that is perpendicular to the radially oriented cracks

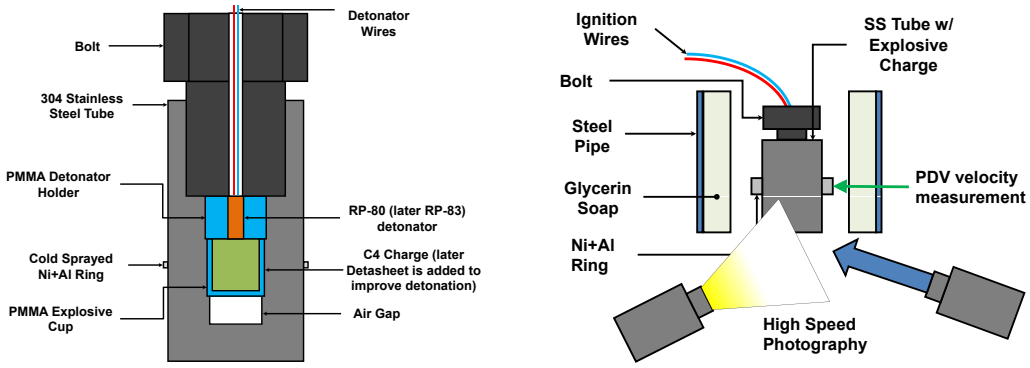

(a) (b)

Figure 4.4: (a) Detailed view of the assembly containing the composition C4 charge and the detonator for rapid fragmentation of the cold sprayed Ni+Al ring. (b) Experimental setup used for explosive fragmentation of cold sprayed Ni+Al Rings at the Army Research Laboratory.

the Cambridge setup illustrated in Figure 4.3a, the ARL setup utilized a thick stainless steel tube which contained a small charge of C4 with a large bolt in one end to contain the detonation products. The sample rings were nominally 71.8 mm outer diameter x 67.2 mm inner diameter x 2.5 mm tall. A hole in the bolt allowed access to the detonator. A plastic ring held an RP-83 detonator in the center of a small charge of Composition C4. Later, due to problems initiating the C4 charge, a small charge of 6mm thick Detasheet was added between the detonator and the C4 to yield better initiation. Charge sizes for the various experiments performed at ARL are indicated in Table 4.2.

A Cordin model 570 high speed framing camera with a helium gas drive was used to film the ARL fragmentation experiments. This camera uses a rotating mirror assembly to sequentially expose 74 digital color cameras arranged in an arc. The camera was operated at its maximum frame rate of 2.5 million frames per second [221]. Minimum exposure time per frame is 300 ns [221]. The camera is capable of 4 megapixels of data per frame. A 30 cm wide square mirror was used to reflect the image of the expanding ring into the telephoto lens mounted on the Cordin, which

was equipped with a Nikon 70-300 telephoto lens.

An argon candle was used to light each experiment. The argon candles consisted of a roughly 4 inch diameter x 1 inch thick charge of composition C4 at the back of a tube filled with flowing argon gas and initiated with an RP-83 detonator. Upon detonation, the argon is compressed by the shock wave from the charge and emits brilliant white light sufficient to provide illumination for the Cordin camera.

Photon doppler velocimetry (PDV) was also utilized with four PDV probes placed in a 180 degree arc around the ring per shot. These probes were purchased from AC Photonics (1CL15A070LSD01) and consisted of a GRIN lens attached to a fiber pigtail. The lens collimated the light over a working distance of 300 mm and had 0.8 mm spot size. The PDV system (from Third Millennium Engineering of Plano, TX, with 2G177PDV1A 4-Channel PDV receiver) was driven with a 2 Watt CW, single mode, Erbium fiber laser centered at $\lambda = 1550.5$ nm (IPG Photonics ELR-2-1550-LP-SF). FC-APC optical connectors were used to connect optical components of the PDV system. The output of the PDV's photodiode was recorded on an Agilent DSXO9000 oscilloscope with a bandwidth 16 GHz and a sampling rate of 1 GHz.

Large blocks of glycerin soap at least one inch thick were used to soft capture fragments. The soap was then melted in a double boiler or dissolved in boiling water and the fragments were sieved out.

Table 4.2: Parameters for the Army Research Lab ring fragmentation experiments.

Test	Sample	Charge ⌀ (mm)/mass (g)	Booster ⌀ (mm)/mass (g)	Ring (g)	Rec. Mass (g)
11201-1	CS Ni+Al	7.5/1.01	NA	6.25	0.233
11203-1	CS Ni+Al	20/7.42	NA	6.27	4.72
11207-3	CS Ni+Al	23/9.18	25.4/4.56	6.39	4.62
11209-1	CS Ni+Al	10/1.85	22.5/3.44	6.46	5.47
11209-2	CS Ni+Al	13/2.04	22.5/3.44	6.47	5.66

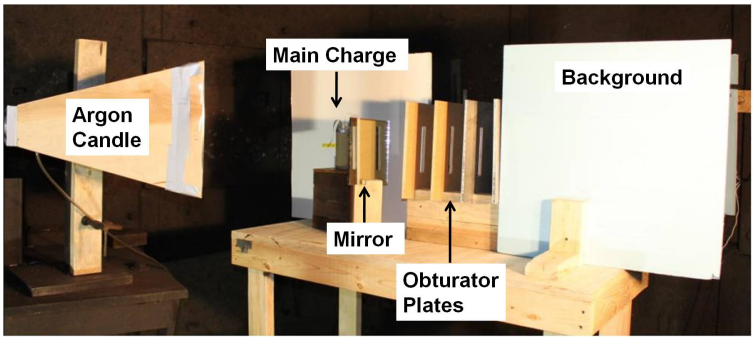

Figure 4.5: Photograph of a cased charge experiment from [222]. This setup is virtually identical to the one used in the Ni+Al expanding case experiment. The cameras and the flashbulbs do not appear in the image. The cameras were outside of the experiment chamber and the flashbulbs were behind the white photographic background.

4.2.3 Army Research Laboratory Explosive Case Fragmentation Experimental Description

In addition to the ring experiments, fragmentation experiment on a CS Ni+Al casing was conducted. A cold-sprayed Ni+Al case, machined via conventional techniques from Washer CS Ni+Al, was filled with TNT and top detonated in order to study fragment formation in a more realistic setting. Fragment motion and reaction were recorded via high speed camera. Further study of the impact of the Ni+Al fragments on a foam sheet was conducted in CTH.

The cold sprayed Ni+Al cylinder was 147 mm long x 66.8 mm ID x 72.4 mm OD. The mass of the Ni+Al cylinder was 360 g. It was formed via gas dynamic cold spray deposition onto a rotating mandrel. The casing was turned to the final diameter using ordinary machine tools.

The main charge consisted of a cast TNT charge 147 mm long x 66.8 mm OD with a mass of 809 g. A pentolite booster 50.8 mm thick x 50.8 mm OD with a mass of 106.9 g was used to ignite the TNT charge. An RP-80 exploding bridgewire detonator from Teledyne RISI Inc. was used to initiate the pentolite booster.

A Cordin 570 camera (2.167 million fps and 400 ns exposure) was used to image the detonation and subsequent case expansion. A Photron SA.1 high speed video

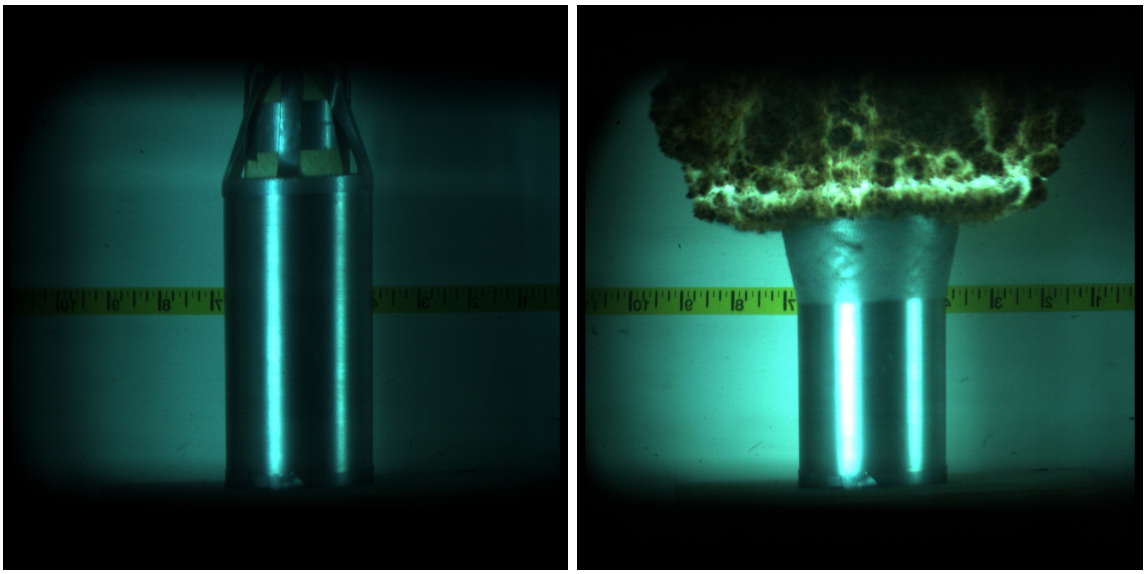

(a) (b)

Figure 4.6: Cold sprayed nickel+aluminum case with detonating TNT charge (a) before detonation (b)8.306 μs post detonation

camera (67,500 fps and 1 μs exposure) captured images of the case fragments as they moved across a white background centered 61 cm from the initial position of the main charge [222]. These images were used to determine the average velocities of the Ni+Al fragments and look for signs of fragment reaction. Images of the explosively driven expansion of the cold sprayed Ni+Al casing are shown in Figure 4.6.

An argon candle, in this case a rectangular wooden baffle filled with argon gas and initiated with a small composition C4 charge, provided light to illuminate the Ni+Al case for 100 μsec. Additional mirrors were placed as needed to ensure uniform illumination [222]. Megga-flash PF300 flashbulbs provided light for the fragment photography.

Four obturator plates were placed between the charge and the white background and aligned so that only fragments lying in the Photron camera's focal plane are allowed to pass through. The two plates closest to the charge were fiberboard and the last two plates were fabricated from aluminum. All the plates were 152 mm wide

Table 4.3: Selected parameters for the Ohio State ring fragmentation experiments.

Test	Sample	Capacitor Charging Voltage (KV)	Ring (g)	Rec. Mass (g)
OSU Ring 1	1100 Al	8	2.95	2.95
OSU Ring 9	1100 Al	16	2.94	2.94
OSU Ring 2	CS Ni+Al	4	7.50	7.49
OSU Ring 3	CS Ni+Al	8	7.51	6.82
OSU Ring 4	CS Ni+Al	6	7.53	7.46
OSU Ring 5	CS Ni+Al	10	7.56	6.91
OSU Ring 6	CS Ni+Al	12	7.52	7.07
OSU Ring 7	CS Ni+Al	14	7.49	7.18
OSU Ring 8	CS Ni+Al	16	7.54	6.85
OSU Small Ring 1	CS Ni+Al	4	2.48	2.01
OSU Small Ring 2	CS Ni+Al	8	2.44	2.32
OSU Small Ring 3	CS Ni+Al	12	2.48	2.01

$\times$ 305 mm tall $\times$ 9.5 mm thick with a 25.4 mm wide $\times$ 203 mm tall slot machined into the center of each plate [222]. The photographic background was constructed from foam and masked with white paper to provide better image contrast to the fragments.

4.2.4 Ohio State University Exploding Wire Ring Fragmentation Experiment Description

Fragmentation experiments were also conducted at Ohio State University (OSU). Two sizes of cold sprayed Ni+Al rings were studied: Rings 72.0 mm outer diameter x 69.5 mm inner diameter x 2.5 mm tall fabricated using wire EDM and conventional machining methods from Washer CS Ni+Al and rings 26.0 mm outer diameter x 22.0 mm inner diameter x 3.0 mm tall fabricated from Block CS Ni+Al. Sample masses and the capacitor charging voltages for each experiment in the series are noted in Table 4.3.

The ring fragmentation experiments were conducted using an RC circuit containing a 480 μF capacitor [223] which was charged with a high voltage power supply with energies up to 20 KJ. The capacitors were discharged into an aluminum wire 0.031 inches in diameter embedded in a block of extruded polyurethane having a Shore durometer hardness of 80A (McMaster-Carr item number 8784K771 or similar). The urethane block was machined so that the sample ring fit tightly. When the capacitor

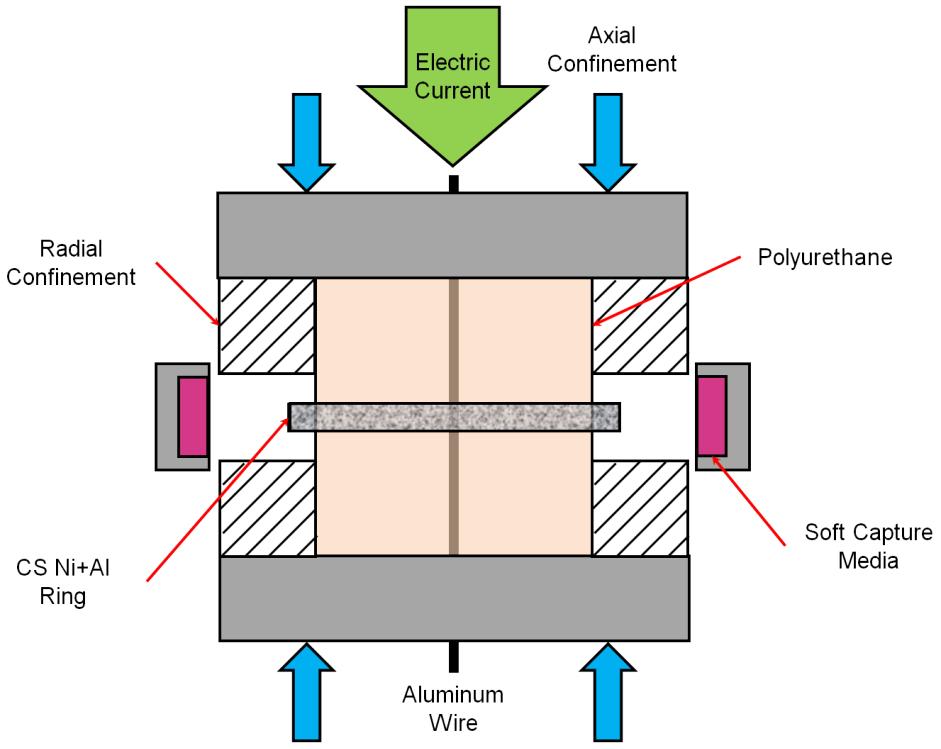

Figure 4.7: The Ohio State ring fragmentation experimental setup.

was discharged into the aluminum wire, ohmic heating transformed the wire into high pressure plasma, not unlike high explosive product gases. This high pressure plasma drove a shock wave into the polyurethane block which coupled the shock wave into the ring. The experimental setup is shown in Figure 4.7. Unfortunately, no high speed photography was available for these experiments.

The PDV system at OSU consists of an NP Photonics 1 Watt CW erbium fiber laser with λ=1550 nm [224]. Data from the PDV is recorded using a LeCroy 4 channel Wavesurfer oscilloscope with a bandwidth of 1 GHz and a sampling rate of 5 GHz and 10 MPts of storage [224].

4.2.5 Preparation and Tabulation of Fragments

Once the fragments were removed from the soft capture media for each of the experiments, the fragments were sieved through ASTM sieves #14, #18, #35, #60, #100, #200, and #400 which correspond to sieve openings of 1.4 mm, 1.0 mm, 0.5 mm, 0.25

mm, 0.15 mm, .075 mm, and 0.038 mm. The fragments were placed on top of a stack of three inch diameter sieves, and then sieved using a Dual Manufacturing Co. model D-4325 motorized sieve shaker for 30 minutes. This choice of sieves was determined through trial and error; it provided a combination of sieves such that fragments were separated into different size groups without yielding samples that were too small to effectively weigh. Fine particles were washed off of the sieves with methanol. The methanol was evaporated off and the fine particles were weighed. Despite these efforts, a small quantity of fine particles was lost due to static adherence to the sieves and weigh boats during the fragment sieving and weighing process.

After sieving, the fragments were weighed. All fragments that were too large to fit through a 0.5 mm mesh opening were weighed individually. Fragments smaller than 0.5 mm mesh size were often weighed together or in groups unless the number of fragments was under a hundred. A spherical equivalent mass was determined according to Eq. 4.1, where $mass_{i_n - i_{n-1}}$ refers to the sphere equivalent mass between two adjacent mesh sizes, ρ_{sample} refers to the sample density, and $\bar{d}_{i_n - i_{n-1}}$ is the average size of two adjacent meshes (for instance meshes #35 and #60 would yield an average size of 0.375 mm). The total mass between two sieves was divided by the spherical equivalent mass to estimate the number of fragments where counting was impractical due to the large numbers of very small particles.

$$mass_{i_n - i_{i-1}} = \rho_{sample} \frac{\pi}{6} \bar{d}^3_{i_n - i_{n-1}} \tag{4.1}$$

The overall results of the experiments performed on different explosively consolidated and cold sprayed structural energetic materials will be presented in the next section and discussed in the context of the average fragment mass –or fragment volume if comparing samples of different densities– as a function of strain rate corresponding with the different experimental techniques.

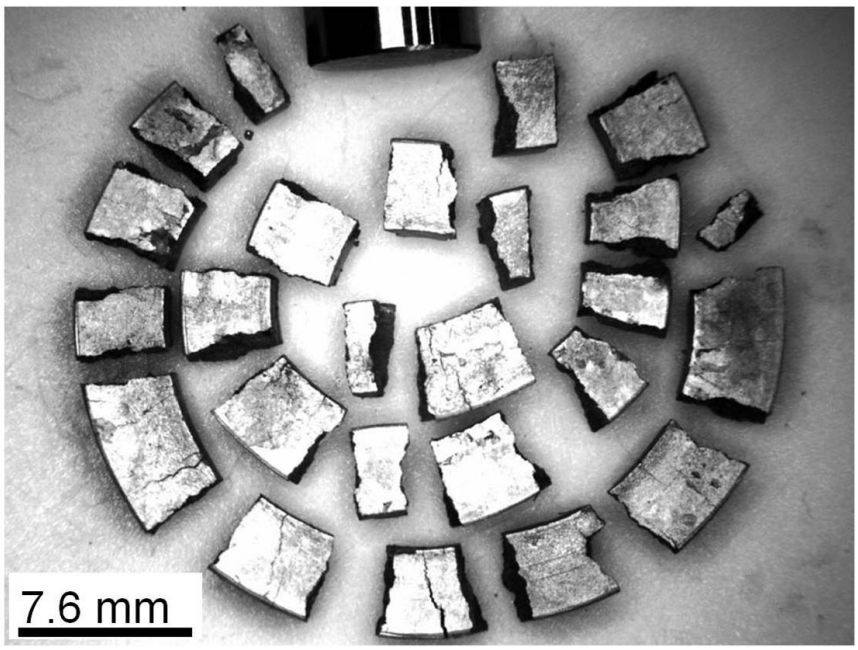

Figure 4.8: Fragments from Cambridge Ring Fragmentation Experiment E101020A. Note the numerous incomplete cracks present. This is unambiguous evidence of Mott-type fragmentation with Mott release waves spreading out from completed fractures and halting the growth of nearby fractures.

4.3 Experimental Fragmentation Results

4.3.1 Cold Sprayed Nickel+Aluminum

4.3.1.1 Cambridge Tests on Cold Sprayed Ni+Al

The first three experiments on cold sprayed nickel+aluminum rings were performed with the setup using the UPVC tube shown in Figure 4.1a. Fragments from experiment E101020A are shown in Figure 4.8. Note the numerous incomplete fractures present in some of the fragments. This is clear evidence of the fragmentation process originally described by Mott [4]: release waves spreading out from completed fractures and halting the growth of nearby fractures. It is interesting to note that there is no necking around fractures as is typically seen in ductile metals (see for example Grady and Benson [164]) in these fragments, nor in any other fragments that were recovered from these experiments.

In the Cambridge experiments, nearly all of the fragments have fracture surfaces

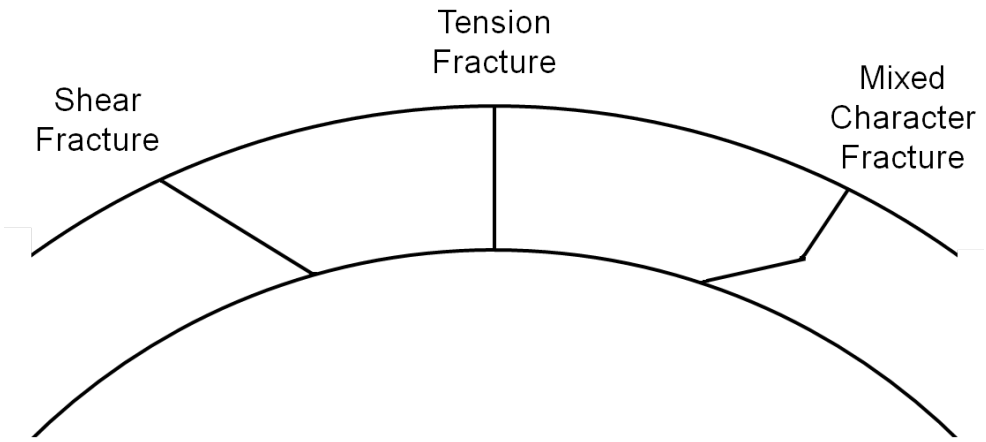

Figure 4.9: Classification schemes for fragment fracture surface profiles.

that show a microscopic brittle, tensile character. Figure 4.9 is a schematic which illustrates different failure types. Mott [4] and Mock and Holt [225] both developed much more sophisticated fragment failure classification schemes based on the presence of shear or tension fractures and to what extent fragments contained portions of the inner and/or outer surfaces. It was not felt practical in this case, as it was often impossible to say what the original orientation of fragments or their fracture surfaces were when fragments were smaller than 0.5 mm, and the majority of fragments were under this size. However, in the larger fragments, different macroscopic failure mechanisms were noted and the fracture surfaces do show different failure mechanisms at work which will be significant when fragment populations are discussed. In Figure 4.8, most of the Mott fractures do not have the angled surfaces typical of shear failures such as those shown in Figure 4.9. Rather, they show a brittle, tensile failure character.

Dramatic height variations of features on the fracture surface are evidence of multiple intersecting fractures, rather than a single dominant fracture. This is clearly evident in Figure 4.10a and Figure 4.10b. The presence of multiple fractures suggests that there were many different sights for fracture nucleation at a given load.

As seen in the plot of fragment number versus mass in Figure 4.11a and the

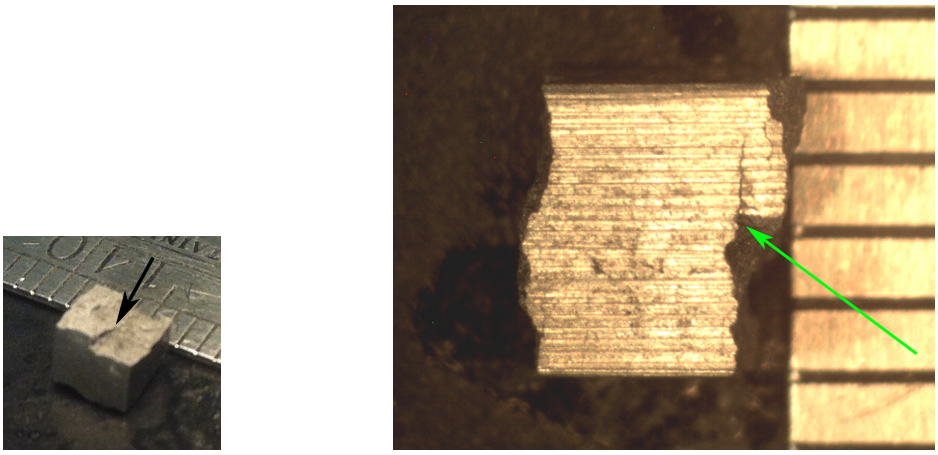

(a) (b)

Figure 4.10: Crack intersection on a fragment from Cambridge experiment E101020A on cold sprayed Ni+Al. The scale marker is in millimeters. (a) The topography of the fracture surface is evidence of multiple intersecting fractures. (a) A close up of the same fragment looking at the outside diameter. The intersecting crack faces are clearly evident.

plot of fragment mass fraction versus fragment mass in Figure 4.11b, the fragments initially formed an approximately bimodal distribution in test E101020A, the test with the smallest charge size in this series. One mode is concentrated at the lowest fragment sizes and is quite narrowly constrained. The other is much larger and spans the majority of the mass of the ring. As charge size was increased, the fragment size distribution begins to take on a unimodal character as the mode with the larger fragments moves closer to the mode with the small fragments. The total number of fragments as well as the mass in the smallest bins increases dramatically with strain rate as evident from Figure 4.11a and Figure 4.11b.

The multimodal character of the fragment distribution is a significant result because it implies the existence of different fragmentation mechanisms operating simultaneously. Bimodal fragment distributions have been observed by Odintsov [184] who studied fragmentation in steel cylinders with varying carbon contents. Odintsov found that the fragment populations from a low carbon steel showed a distinctly bimodal

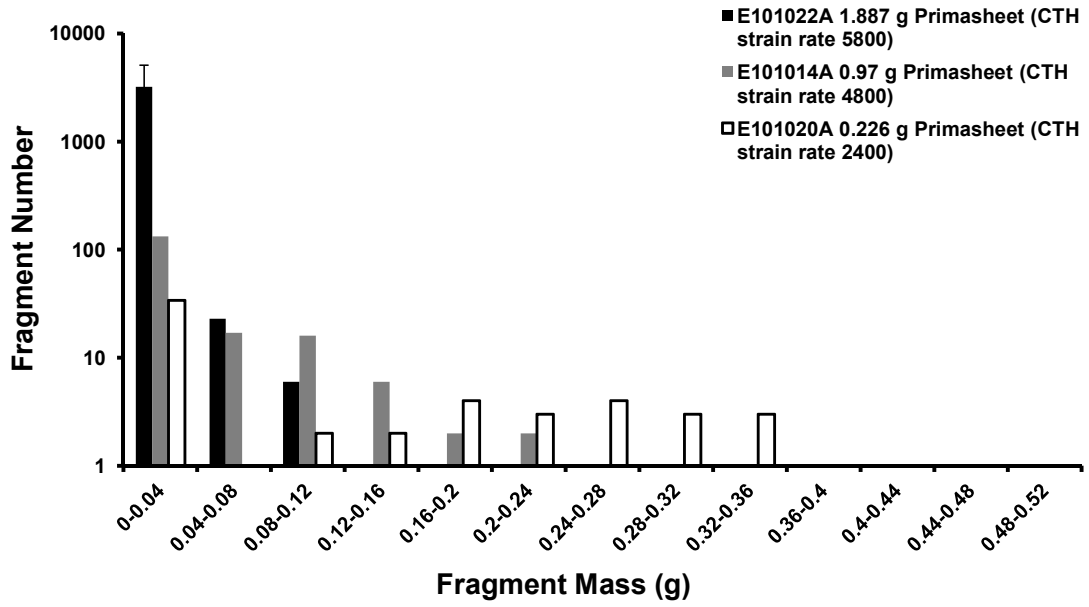

(a)

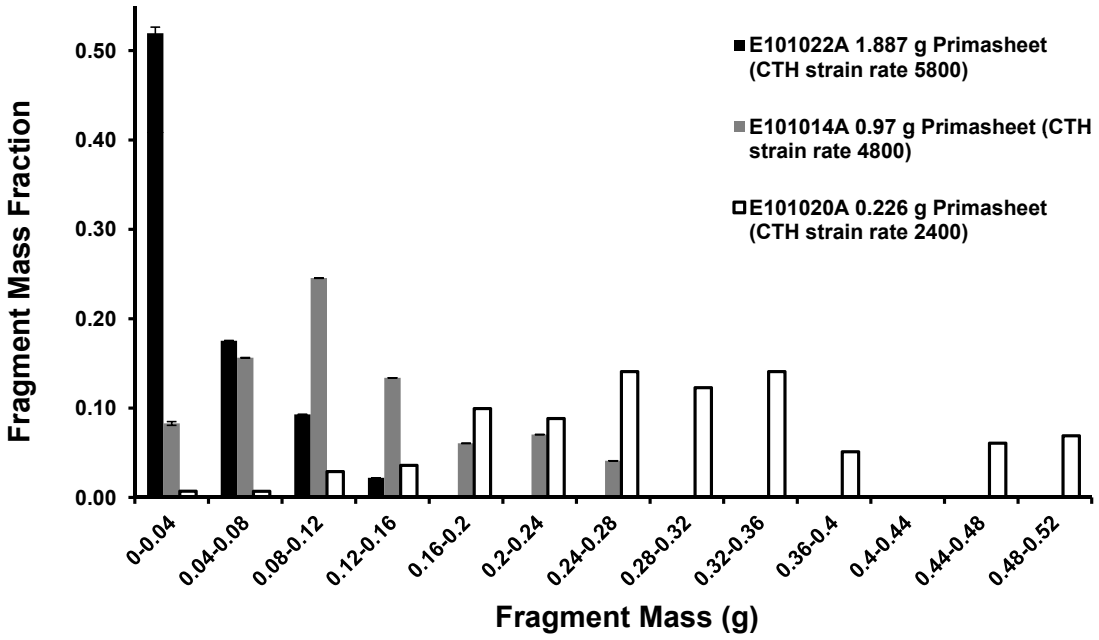

(b)

Figure 4.11: Fragment distributions of ring fragmentation experiments at Cambridge conducted on cold sprayed Ni+Al. (a) Fragment number distribution. (b) Fragment mass distribution. The presence of multiple modes in the fragment distributions strongly implies the existence of multiple fragmentation mechanisms. As strain rate increases, the modes in the distribution approach one another.

character, whereas the fragment population for the high carbon steel was unimodal in character [184]. Multi-modal fragment populations were observed by Hooper [185] in his study of fragmentation of pressed Al samples, though as a result of different impact velocities rather than different compositions. Hooper inferred the existence of bulk fracture and smaller scale crack branching leading to two different fragment populations. The same is true of the structural energetic materials tested here, different mechanisms are operative which provide different fragment populations.

Looking more carefully at fragments from a higher strain rate test, E101014A, we see that there are not only typical Mott radial fractures as shown in Figure 4.12a but that there is in fact another fragmentation mechanism giving rise to horizontal tensile fractures shown in Figure 4.12b. The horizontal fracture process is depicted schematically in Figure 4.13. As the fragments are loaded at increasing strain rates, the fragments split horizontally as well as through the typical Mott mechanism. A cross section view of a fragment from experiment E101014A, shown in Figure 4.14a, illustrates the effect of the impact of the tube against the inner surface of the sample ring. The tube is pushed outward against the ring by the high pressure gases within, but a gradient in the velocity along the tube axis gives rise to tensile loading in the ring apart from the hoop stress and produces horizontal fractures as illustrated in Figure 4.13. A clear view of the horizontal fractures are shown in Figure 4.14b. At low strain rates, only the Mott mechanism was operative because the tube expansion was slower and more uniform. At higher strain rates, the horizontal fracture mechanism also becomes operative.

Another feature that is evident in Figure 4.14b is extensive crack branching. Rather than a single dominant crack, a spiderweb of cracks is present forming many potential fragments. As the ring expands, work done on the ring leads to an increase in strain energy within the ring. Weak interfaces between phases in the cold sprayed material provide many possible crack paths. The application of large loads and the

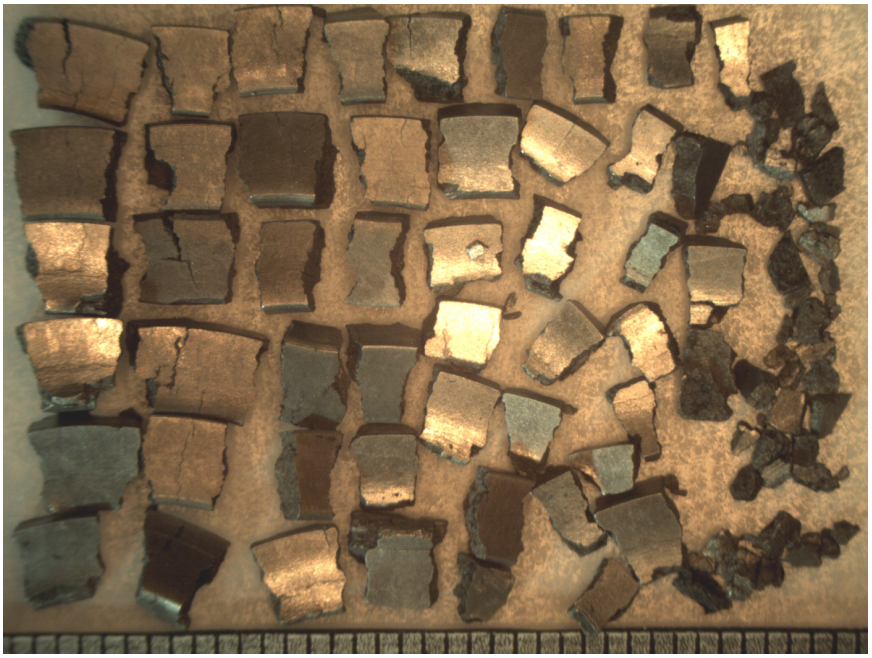

(a) Ring Top View

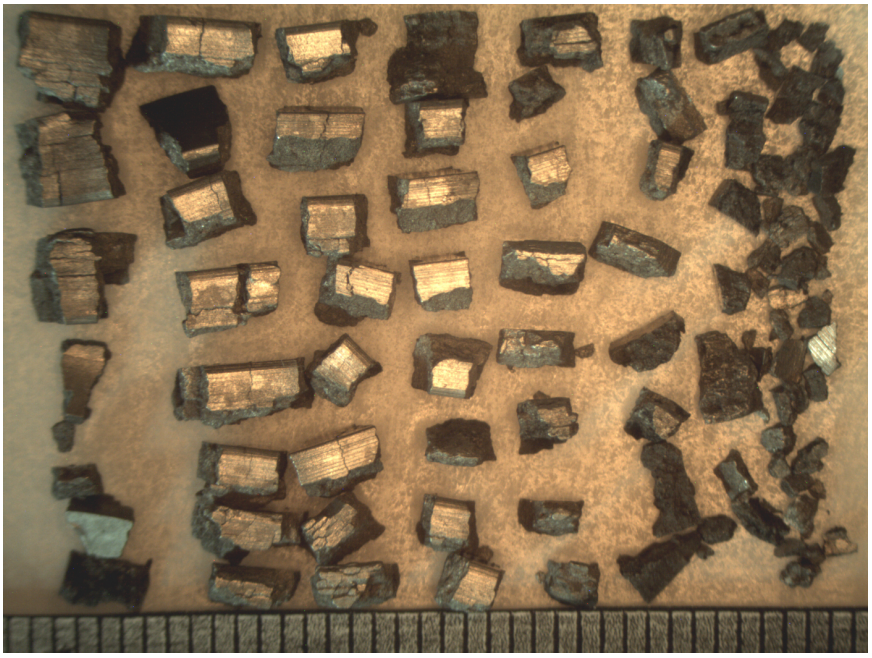

(b) Ring Inner Diameter View

Figure 4.12: A Selection of fragments from Cambridge ring fragmentation experiment E101014A. (a) The top of the ring is facing the viewer so that the profiles of the inner and outer ring diameter may be seen. Note that there are fewer incomplete cracks present than in Fig 4.8. This is consistent with Mott's theories on fragmentation. (b). The inner diameter surface of the ring is facing the camera. It is noted that many of the fragments have fractured horizontally as well as the usual radially oriented fractures consistent with Mott fragmentation. This is not a fragmentation mode predicted by Mott's idealized 1D fragmentation model. This additional fragmentation mode partially explains why the increase in fragment numbers is so precipitous. All scales are in mm.

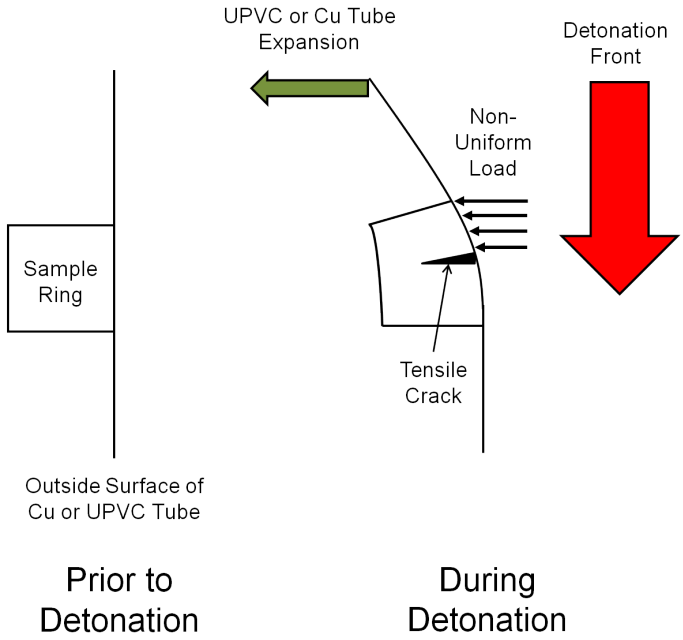

Figure 4.13: Non-uniform loading on the inner surface of the sample ring is caused by the finite transit time of the detonation front down the column of explosive. The non-uniform loading leads to tensile fractures in the horizontal plane of the ring which have been termed horizontal fractures in the present discussion.

weak interfaces lead to cracks branching to dissipate energy. These branches intersect each other and other fractures creating many fragments. In Figure 4.10b and Figure 4.14b, some of the fractures do follow machining marks left from fabrication. However, in both images, other fractures exist that ran perpendicular to the surface finish, suggesting that the fragmentation behavior was not dominated by the surface finish.

A Brazilian disk test conducted on a cold sprayed Ni+Al sample provides direct evidence of small fragments being produced at a much smaller scale than a macroscopic fracture. In Figure 4.15, the formation of a crack in the center of the test specimen is accompanied by plumes of fine particles being expelled from the crack. This effect couples with the horizontal and Mott fractures to provide a precipitous increase in fragment numbers with increases in strain rate and giving rise to a multimodal fragment distribution. With further increase in strain rate, the fragments from

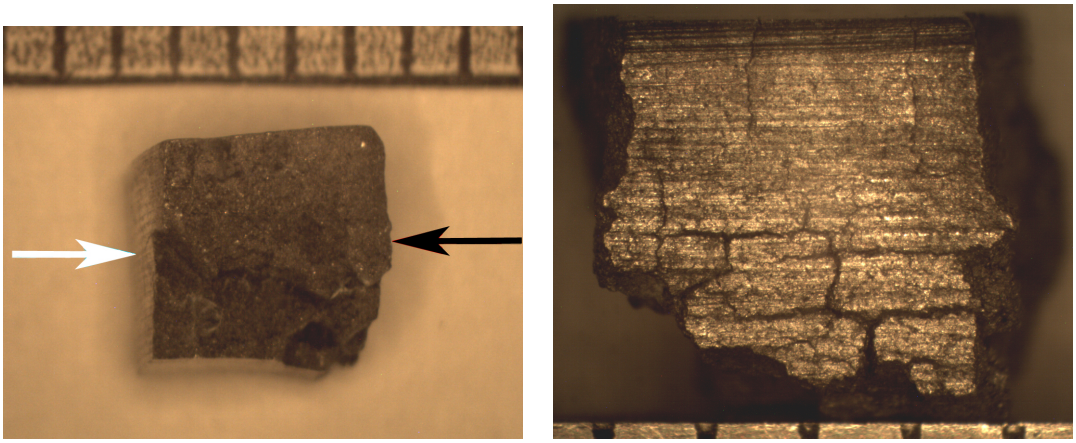

(a) (b)

Figure 4.14: (a) Cross section view of a fragment from Cambridge experiment E101014A. Note the height of the inner diameter surface, denoted by a black arrow, which is taller than the outer diameter surface, denoted by a white arrow, which is the original thickness. The motion of the UPVC tube leads to a tensile loading in the ring and horizontal fracture as observed in Figure 4.12b. (b) Nascent horizontal fractures in an intact fragment. It is readily apparent how quickly these fractures can increase the fragment numbers. All scales are in mm.

Mott fragmentation and the horizontal fragmentation process will get smaller and approach the small fragments produced by crack branching, converging to a single mode fragment distribution of small mean size. The effects of this process on the fragment size distribution are evident from the fragment number and mass distributions in Figure 4.11a and Figure 4.11b.

Given that the fundamental difference between the reactive material systems considered in this work and ordinary structural metals such as steel or high strength aluminum is the composite microstructure, it is important to know how the microstructure of the SEMs influences the fragmentation process. There are some clues to this already in Figure 4.15; the tiny fragments coming off of the fracture surfaces seem likely to be a product of the composite microstructure. Post mortem analysis fracture surface analysis was conducted to understand how fragments form and what microstructural features influence the fragmentation process.

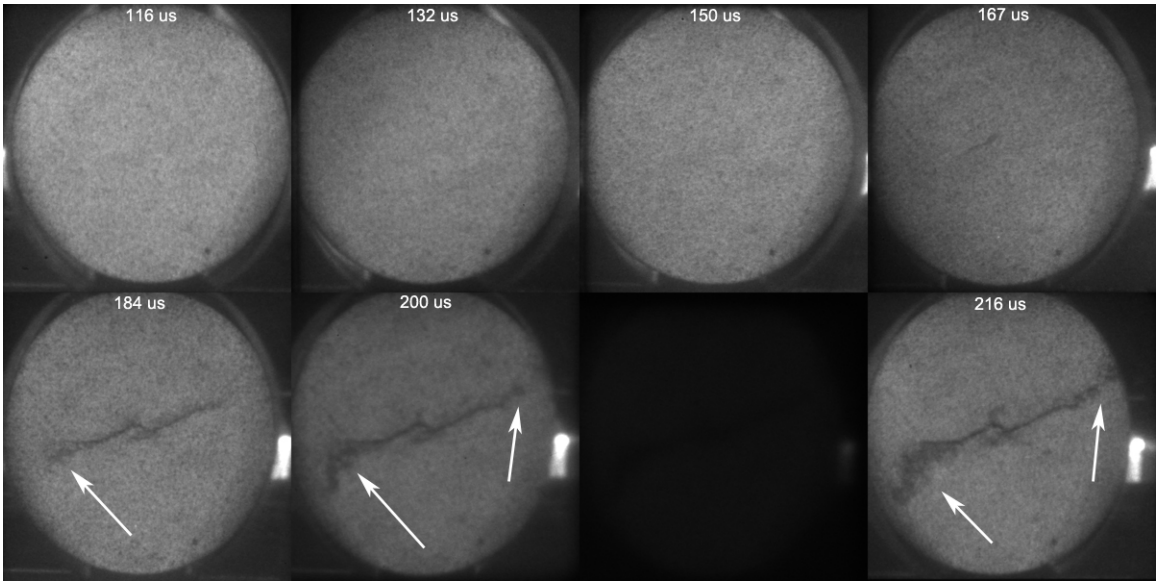

Figure 4.15: A Brazilian disk test on cold sprayed nickel+aluminum. Notice the plumes of fine dark fragments coming from the fracture as it grows as indicated by white arrows.

Post mortem analysis of fracture surfaces and individual fragments in the smallest size ranges were conducted on fragments generated in the explosively driven ring expansion experiments. Closer examination of a fragment seen in Figure 4.16, reveals the presence of limited macroscopic porosity. There is no evidence that any of the fractures observed nucleated at the pores, though it is difficult to completely discount them. There are no chevron marks or mirror-mist-hackel transitions that radiate from the regions around the pores. Rather, as seen in Figure 4.8, the fractures appear to nucleate at or near the surface of the samples. The stepped appearance of the fracture surface suggests multiple intersecting fractures.

Closer examination of the fracture surface also shows fracture and particulation of the nickel coatings on the aluminum particles. The crack surface lacks clearly defined features like chevrons or river marks at this length scale. Rather, individual particle fractures and failures are ubiquitous at this length scale. In Figure 4.17a as indicated by an orange arrow, almost an entire nickel coated aluminum particle pulled away from the surface, leaving part of its nickel coating behind. Looking at a

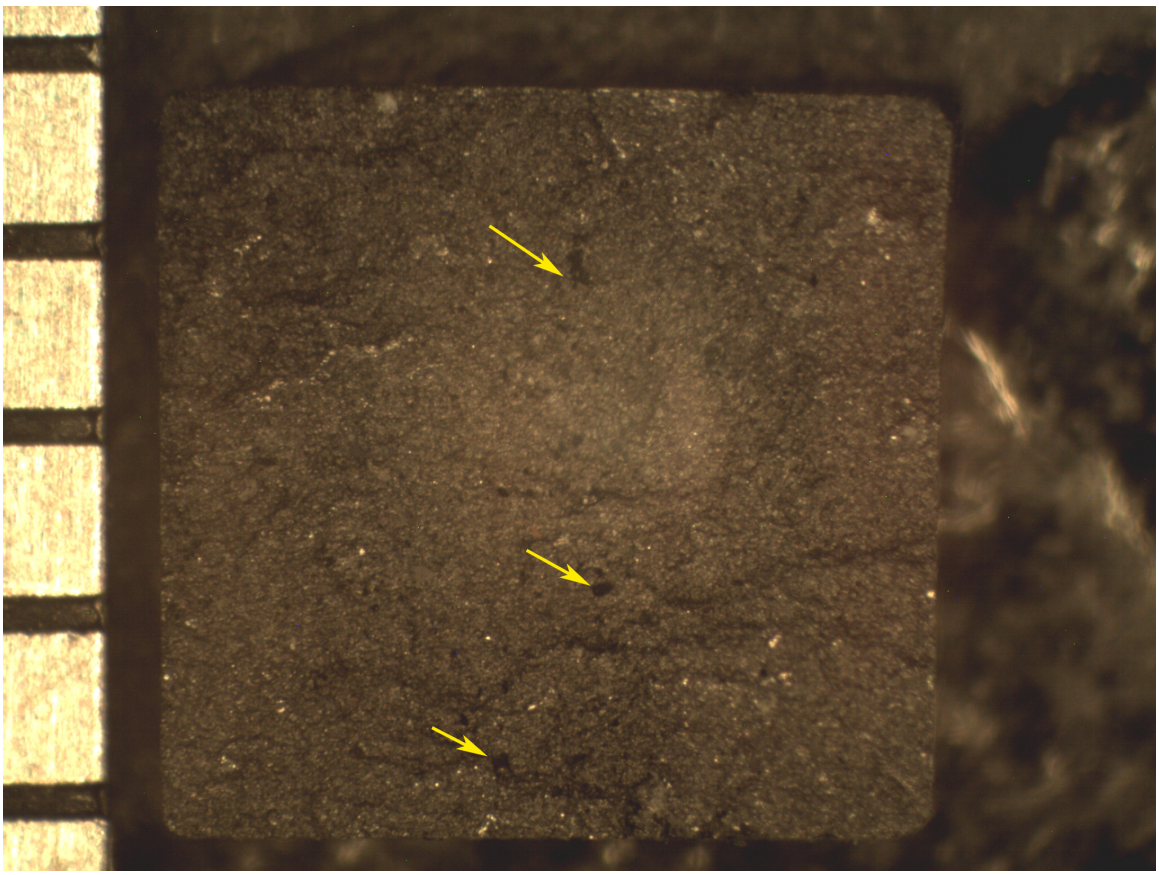

Figure 4.16: Fracture surface of fragments from Cambridge experiment E101020A on cold sprayed nickel+aluminum. Arrows denote porosity, which does not appear to have played a dominant role in the fragmentation process. Fracture surface topography suggests multiple intersecting fractures. The scale marker on the left is marked in millimeters.

backscattered electron image in the same region in Figure 4.17b, showing the brighter nickel and darker aluminum, a few instances of the breakup of the nickel and regions of necking of the aluminum are indicated with arrows labeled A and arrows labeled B respectively.

Some examples of similar behavior can be seen more clearly at higher magnification in Figure 4.18a. The nickel shows very little ductile necking, instead revealing debonding and fracture. Ductile failure of the aluminum where it has necked to a point can be seen in Figure 4.18b.

Mott type cracks in recovered Ni+Al fragments from the Cambridge Ni+Al ring tests demonstrated a distinct preference for the Ni phase of the Ni+Al material [17]. The global average V_V of Ni in the cold sprayed Ni+Al was found to be 0.51±0.02 Ni as shown in Table 3.3. The average fraction of the crack path in the Ni phase, was 0.63±0.08 [17]. Both Ni/Al and Ni/Ni interfaces fail, but Ni/Ni interfaces appear most frequently on the crack path as seen in Figure 4.19 [17]. Fracture surfaces of fragments from Cambridge experiment E101022a shown in Figure 4.20a and 4.20b, also reveal a preference for the cold sprayed Ni+Al material to fail along the interfaces. This is seen on the fracture surfaces of fragments from Cambridge experiment E101020A shown in Figure 4.18a and 4.18b as well. The weak interfaces within the cold sprayed Ni+Al provide many interfaces where failure may initiate and where cracks may propagate.

The apparent brittleness of the cold sprayed material is a result of the widespread debonding of the cold sprayed particles, along the Ni/Ni and Ni/Al interfaces. The high density of interfaces increases the probability of an unfavorably oriented interface initiating a fracture. The extensive work hardening of the Ni and Al during the cold spray process, and the phosphorous content in Ni (Figure 3.12b in Chapter 3) also play a role in the limited bulk plasticity evident in this material.

As previously indicated, small fragments from structural energetic materials may

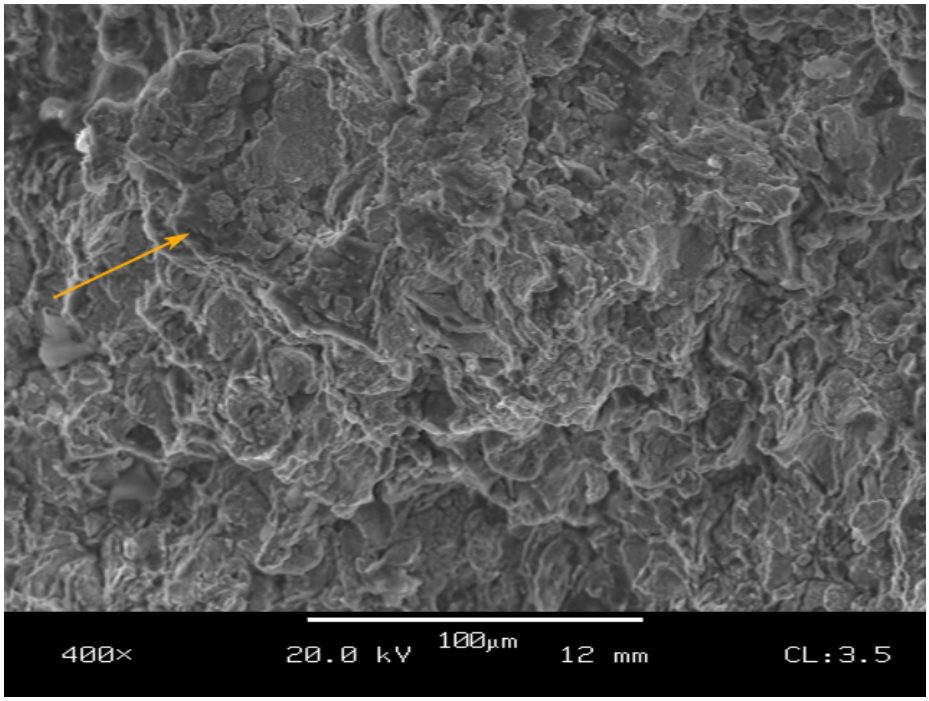

(a)

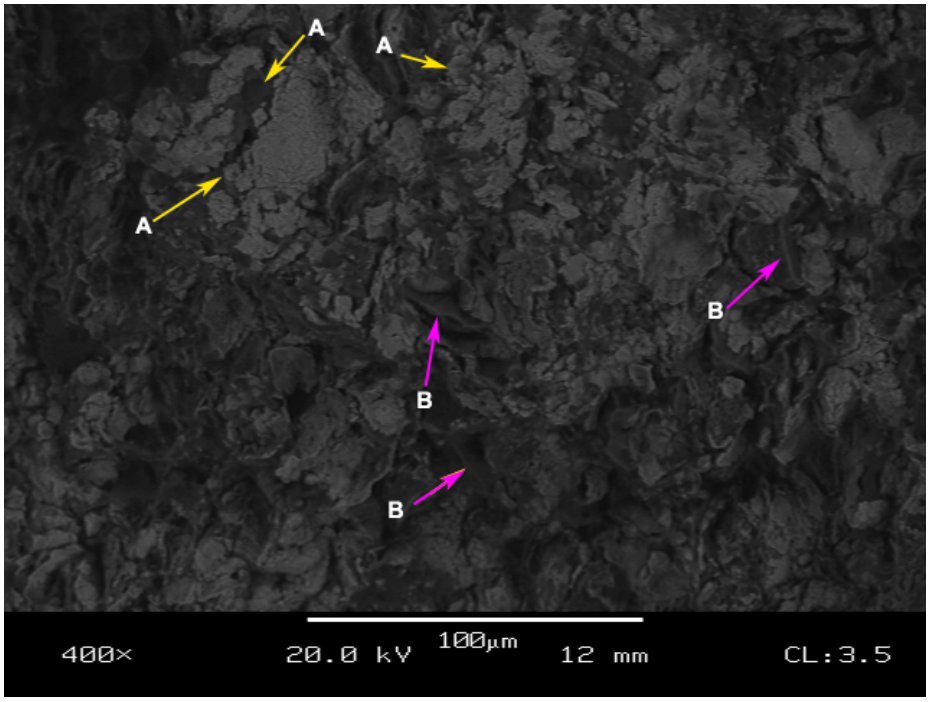

(b)

Figure 4.17: Nickel and aluminum on a fracture surface from Cambridge experiment E101020A on cold sprayed Ni+Al. (a) SEM image showing a region where almost an entire Ni coated Al particle pulled off of the surface, leaving a portion of the nickel coating behind, indicated by an arrow. (b) A backscattered SEM image of the same region. Nickel is the lighter phase. Break-up of the nickel is indicated by arrows labeled *A* and necking of the aluminum is indicated with arrows labeled *B*.

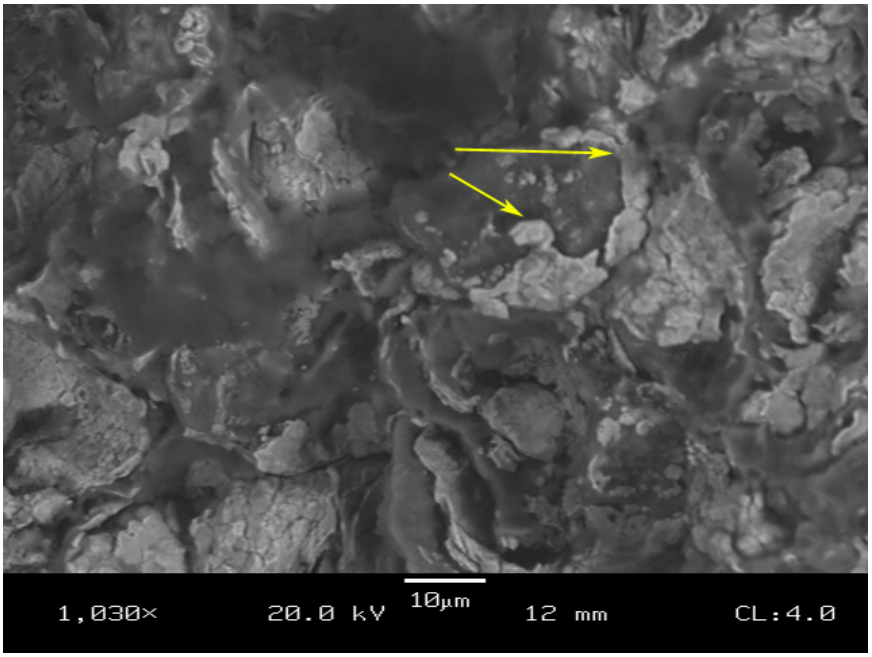

(a)

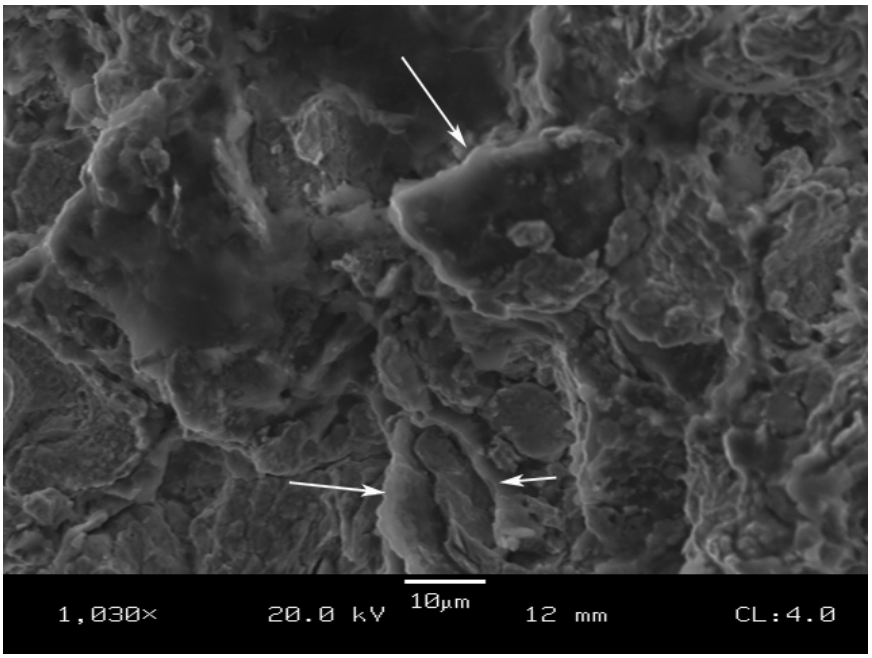

(b)

Figure 4.18: High magnification image of nickel and aluminum on a fracture surface from Cambridge experiment E101020A on cold sprayed Ni+Al. (a) A backscattered SEM image showing contrast between nickel (the lighter phase) and aluminum (the darker phase). Break-up of a nickel coated particle is indicated with arrows. (b). A secondary electron image of the same region as (a) showing ductile necking of aluminum as indicated with arrows.

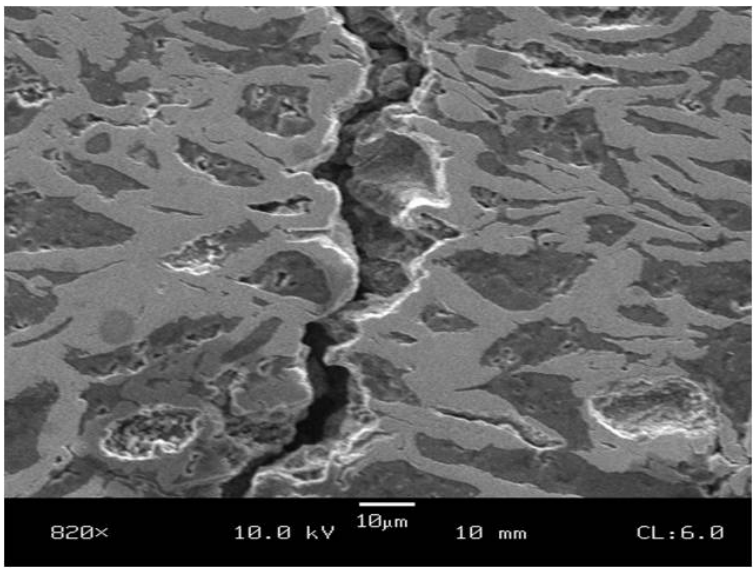

Figure 4.19: A crack in a fragment generated during Cambridge fragmentation test E101014A. The crack path favors the nickel phase [17]. Ni is the lighter phase and Al the darker phase.

combust, contributing useful energy. The composition and character of the fragments provide clues to the subsequent combustion behavior. Figure 4.20a and 4.20b show a backscattered electron image and secondary electron image of a fragment from experiment E101022A which sieved between 75 and 150 μm in size. The Ni and Al components of the fragment are clearly evident. Even very small fragments retain the composite nature of the bulk material. This fragment appears to be composed of pieces of several Ni coated Al particles. The composite nature means that both combustion and intermetallic formation reactions are possible avenues of energy release. If the fragment had failed principally on the Ni or Al interfaces, one might expect a largely intact oxide layer to exist. However, this fragment (which is typical) appears to have formed via fractures which cut through both Al and Ni, significantly disrupting any oxide layer.

4.3.1.2 ARL Tests on Cold Sprayed Ni+Al

The tests conducted at the Army Research Laboratory were, with the exception of 11207-3, done at much lower strain rates than those done on cold sprayed nickel+aluminum

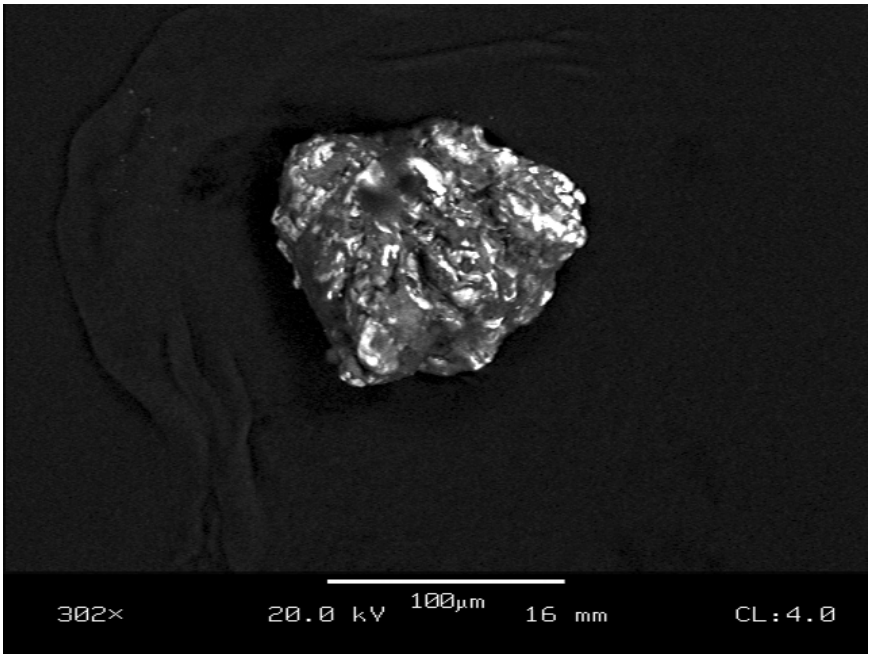

(a)

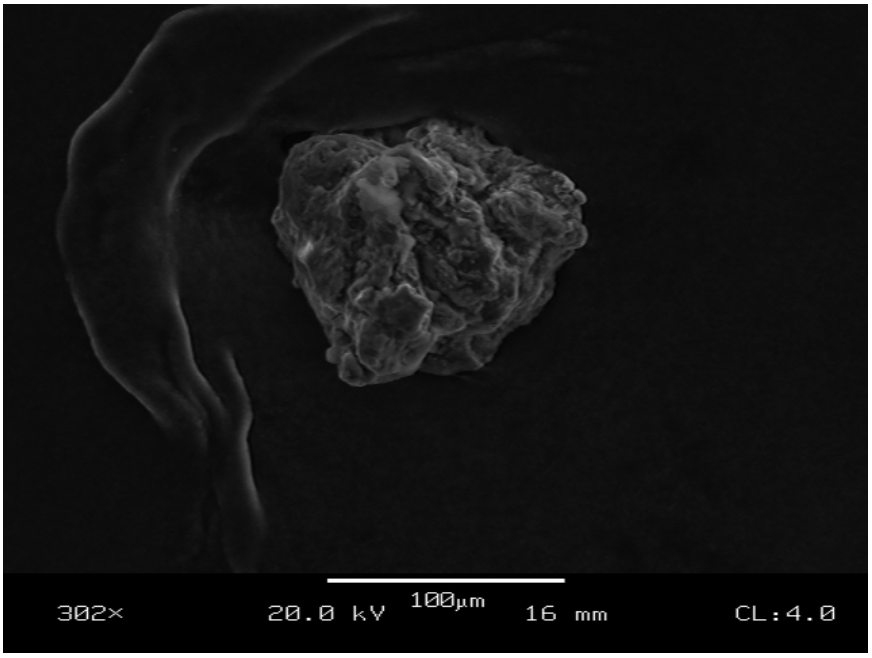

(b)

Figure 4.20: Fragment from Cambridge experiment E101022A on cold sprayed Ni+Al. (a) A backscattered SEM image showing contrast between nickel (the lighter phase) and aluminum (the darker phase). The shadow on the particle is a remnant of the wax used for soft capture. (b) A secondary electron image of the same fragment. This fragment sieved between 75 and 150 μm in size.

at Cambridge. A selection of the fragment distributions for three of the experiments-11203-1, 11209-2, and 11207-3-are displayed in Figure 4.21a. The lowest strain rate test, 11203-1, initially has a unimodal character with just three large fragments. There were no fine fragments recovered, though recovered mass was 75.3%; so it is possible that fine fragments were formed and simply not recovered.

As strain rate increases, multi-modal fragment size distributions form in the fragment populations, with the peaks of the distribution approaching each other more closely with increasing strain rate as seen in Figure 4.21a,b. Relatively few tiny fragments are produced at crack surfaces, due in part to the small number of fractures and the lower strain rates. Again it must be acknowledged that the total mass collection, shown in Table 4.2, was lower than in the Cambridge tests and that fine fragments are the least likely to be collected.

Looking closely at the fragments from ARL experiment 11209-1 in Figure 4.22, we see that there is evidence of shear and tensile failures in the rings, based on the definition illustrated in Figure 4.9. Portions of the fracture surfaces are normal to the ring radius; these are regions dominated by tensile failure. Other fracture surfaces formed at an angle to the ring tangent which failed in shear or some combination of shear and tension. There is no evidence of horizontal fracture in these specimens. The mixture of shear and tensile failures shown in Figure 4.22 are typical of behavior observed in other ARL tests. As suggested in Odintsov's [184] work on carbon steels, the mixture of shear and tensile failures, in addition to the crack branching observed, leads to the multimodal fragment distributions in Figure 4.21a and Figure 4.21b. Experiment E11203-1, taking place at a strain rate of 140, formed only a handful of fragments.

Mass recovery was lower on average in this series of experiments than in others. This was due in part to the use of the argon candle as a light source which did more damage to the experimental setup than the charge used for ring expansion.

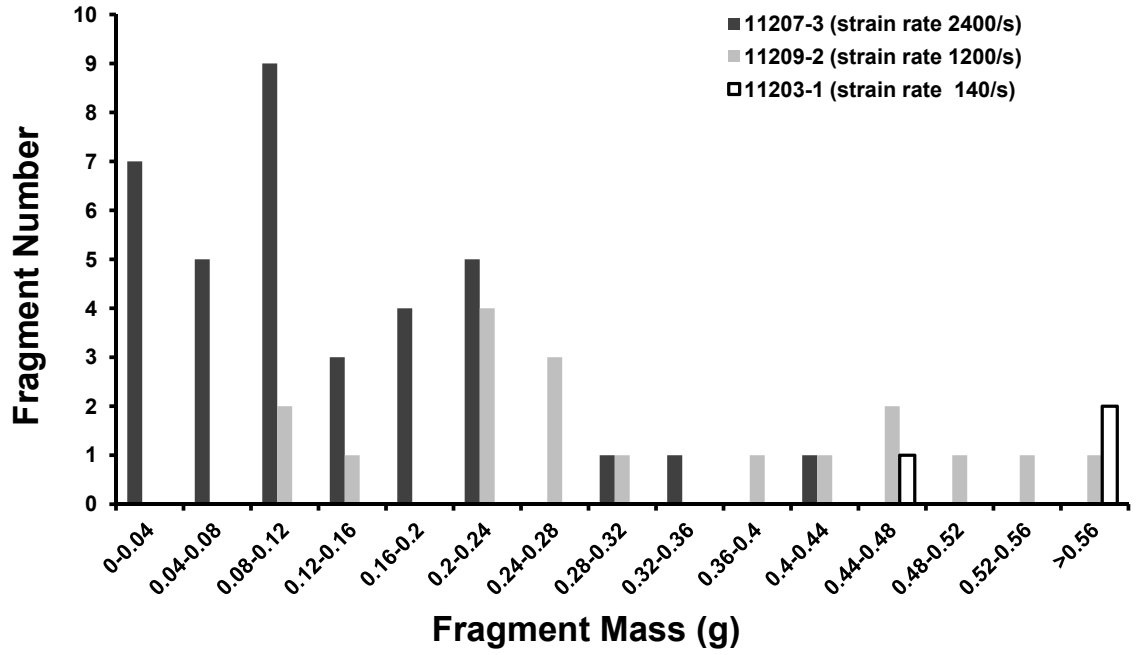

(a)

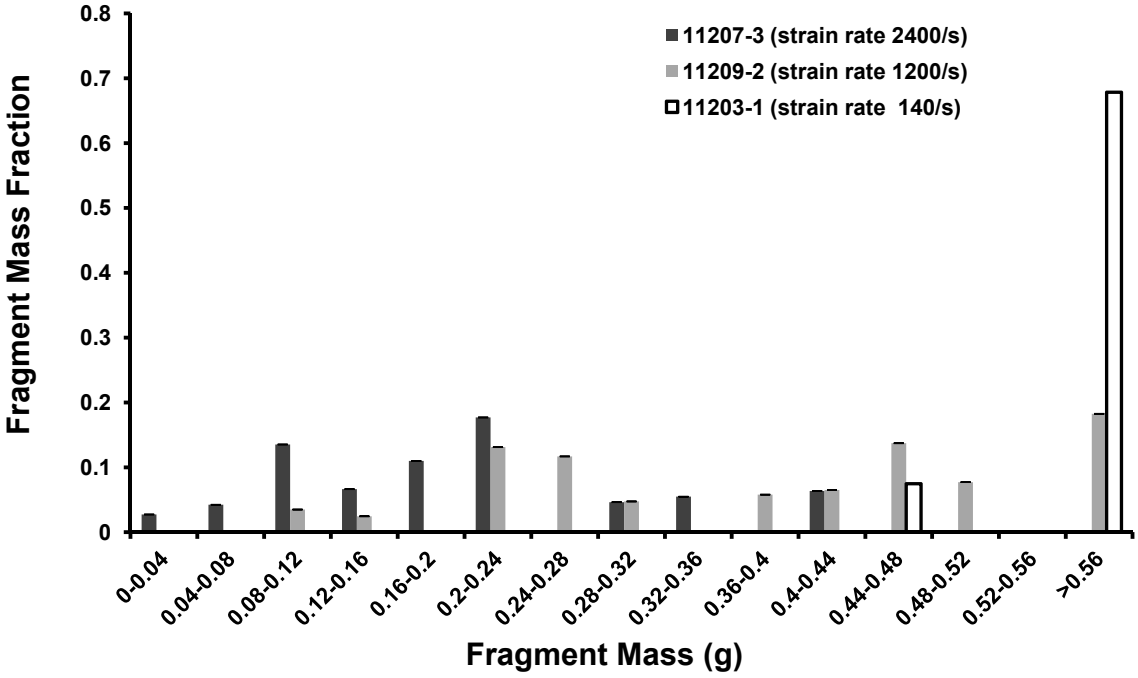

(b)

Figure 4.21: (a) Selected fragment distributions from ring expansion tests on cold sprayed nickel+aluminum rings. Notice the multimodal character that develops in the fragment distribution data. (b) The mass fraction of the fragments also shows a multimodal distribution effect due to the multiple fragment formation mechanisms, however, the absence of very small fragments indicates either a failure to collect such fragments or that the experiments took place at a strain rate sufficiently low that crack branching was not significant.

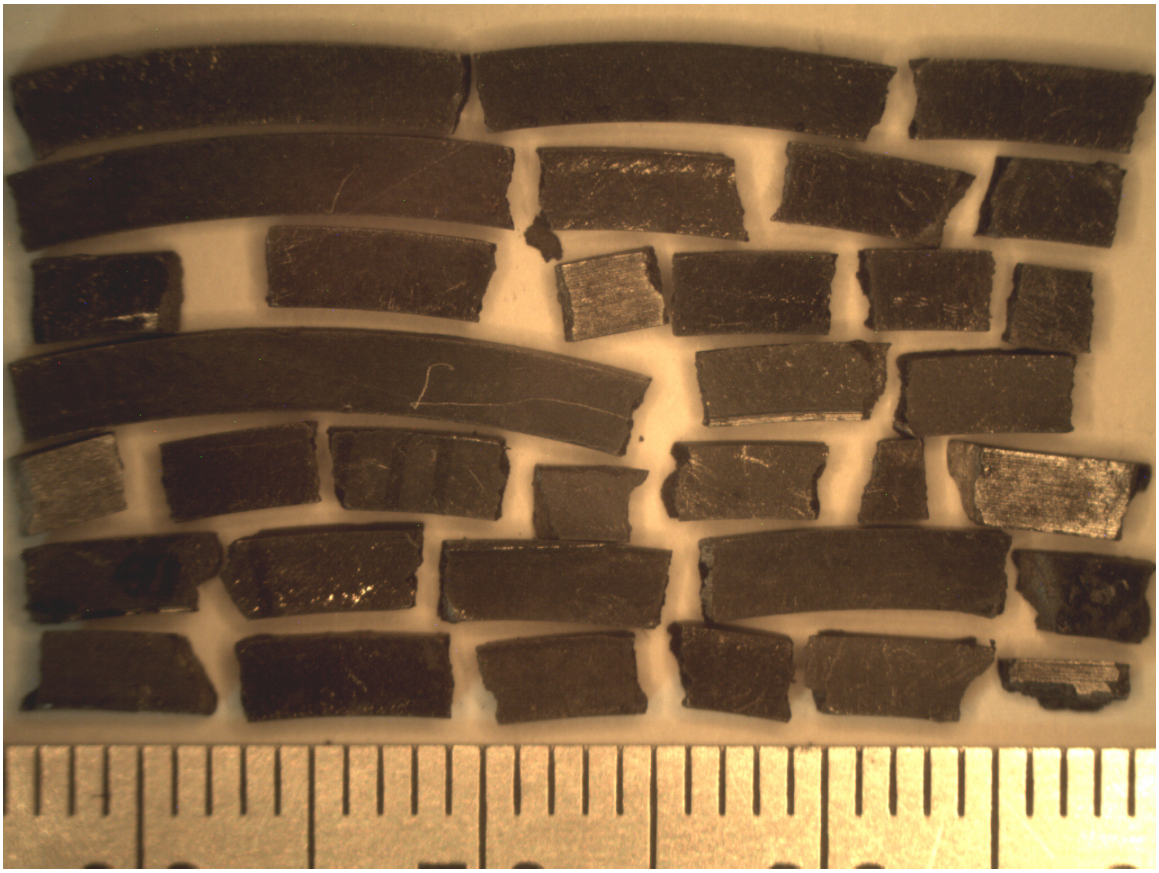

Figure 4.22: Fragments from ARL experiment 11209-1.

This made recovery of fragments in general more difficult. However, the overall features of multiple fragment formation mechanisms operating simultaneously appears to be qualitatively consistent with the results from the Cambridge experiments on CS Ni+Al. The absence of very fine fragments observed in other experiments may either reflect the relatively lower fragment mass recovery or the low strain rates were not sufficient to cause significant amounts of crack branching or both.

4.3.1.3 Results of the ARL Ni+Al Cased Charge Experiment

An enlarged image of the fragmenting cold sprayed case is shown in Figure 4.23a. Notice the very fine web of cracks that have formed across the surface. These finely spaced fractures form very small fragments. An Aermet 100 cylinder filled with LX-17 (92.5% TATB with 7.5% inert binder) and detonated is shown in Figure 4.23b [226]. Despite being exposed to a shock pressure of 26 GPa in the Aermet cylinder [226] versus 16 GPa (simulated) due to the more brisant explosive fill and higher impedance of the steel, the Aermet forms much larger fragments.

A number of fragments in flight are shown in Figure 4.24. These fragments are those which passed through the obturator and which struck the background at an oblique angle and then apparently burst into flame, most likely due to impact and subsequent shock heating of the photographic background materials (paper and expanded polystyrene) above their autoignition temperature. The fragment velocity tangential to the background was 1.99 km/s. The fragment images are significant because they do not show the long, shard-like fragments typical of top detonated cylinders or pipe bombs with casings formed from steel or other ductile metals. Rather, the fragments are much smaller, ranging from barely distinguishable to 6 mm in size.

[11]Reprinted from *International Journal of Impact Engineering*, vol 35., pp. 1547-1556, 2008, "Investigation of the fracture and fragmentation of explosively driven rings and cylinders,"' D.M. Goto, R. Becker, T.J. Orzechowski, H.K. Springer, A.J. Sunwoo, and C.K. Syn, Figure 9, Copyright 2008, with permission from Elsevier.

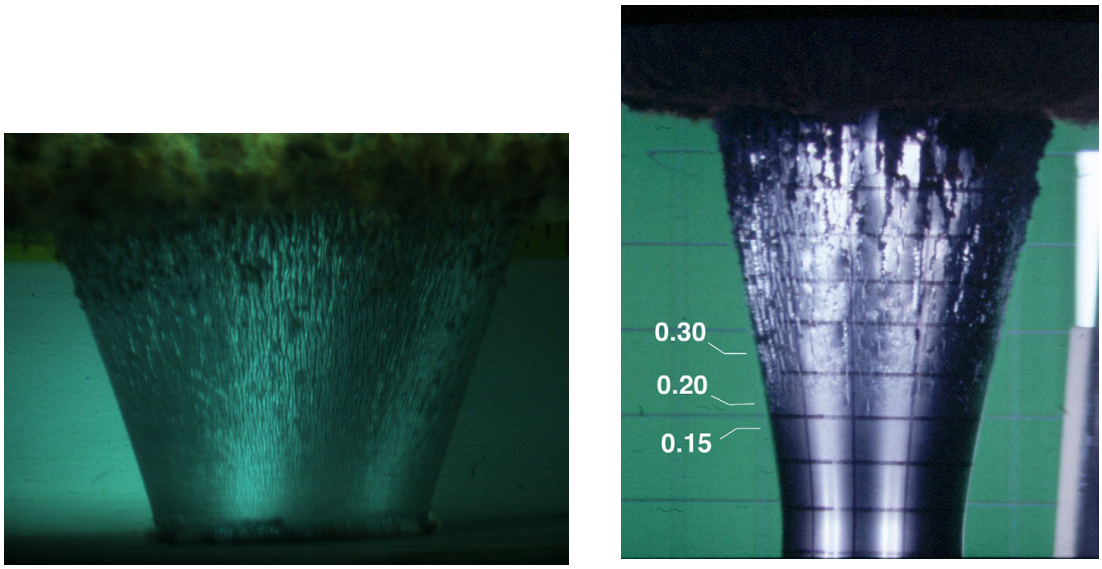

(a) (b)

Figure 4.23: Comparison of cold sprayed nickel+aluminum and Aermet 100 cases post detonation. (a) TNT filled cold sprayed nickel+aluminum case 12.921 μs post detonation. (b) An Aermet 100 case 25 μs post detonation [226] [11]. The numbers refer to strains in the casing. Notice the much larger fragments in the Aermet case despite a larger magnitude shock loading.

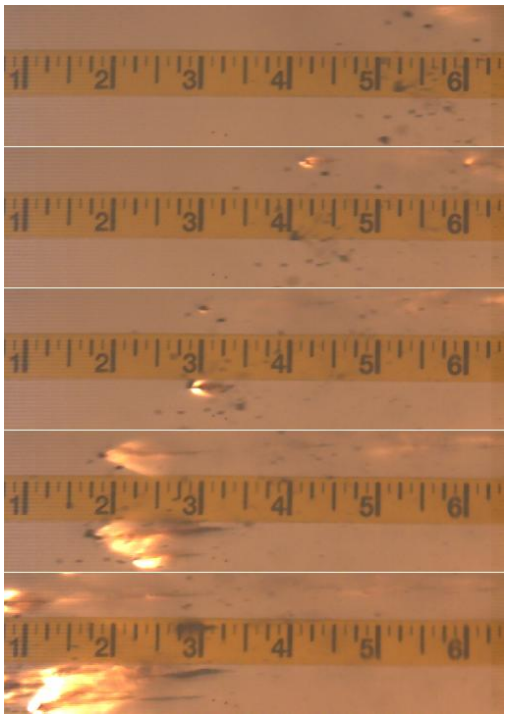

Figure 4.24: Sequential photographs of Ni+Al fragments striking the background. This sequence spans a time length of 79 μs.

These fragments are representative of the largest fragments produced during the experiment. Smaller fragments will have their velocities reduced more quickly by air resistance. The horizontal fracture mechanism which was observed in the Cambridge CS Ni+Al experiments may be operative here as well due to the velocity and subsequent strain gradient which is created by the propagation of the shock wave down the column of TNT in the case.

4.3.1.4 OSU Tests on Cold Sprayed Ni+Al

The experiments conducted at OSU also show similar results to those conducted on cold sprayed Ni+Al at Cambridge and ARL. Figure 4.25a shows that an initial multimodal distribution of fragment numbers develops, but as strain rate increases the distribution shifts toward a unimodal character with very small fragments. The fragment mass distribution evolves from very little mass in the smallest particles to a very substantial mass as seen in Figure 4.25b.

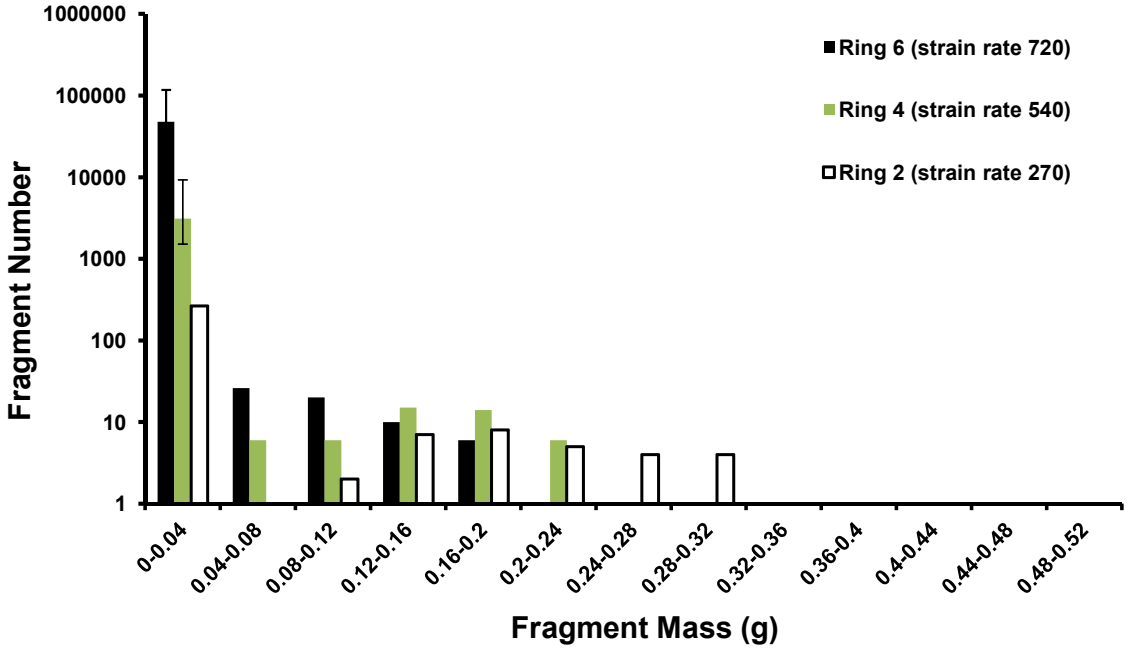

(a)

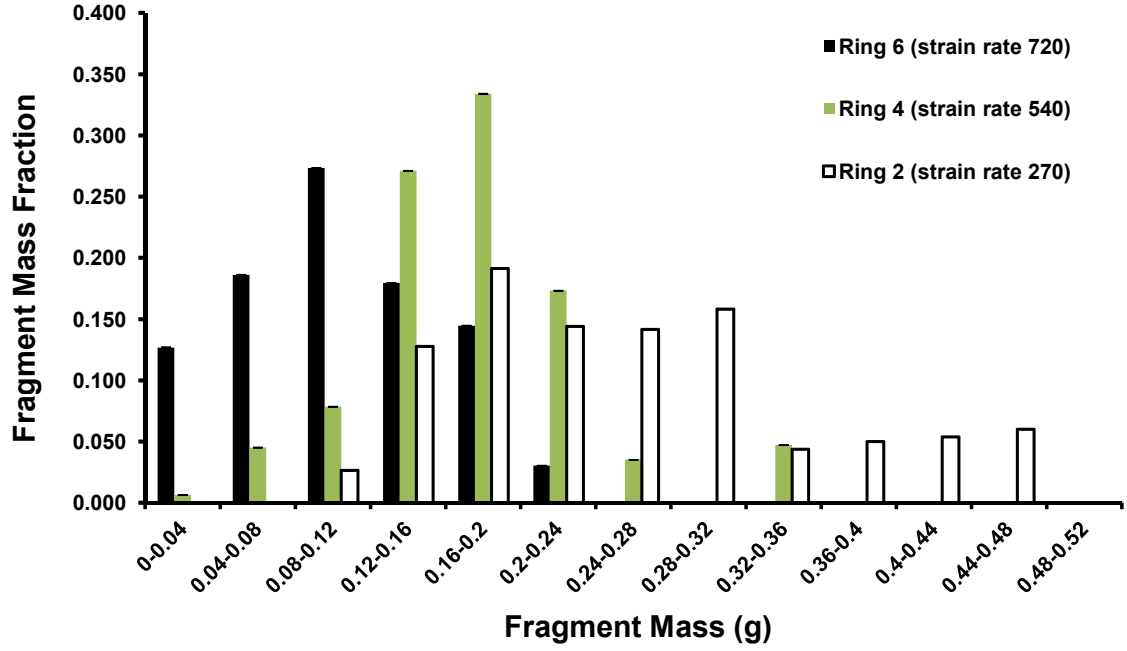

(b)

Figure 4.25: (a) Selected fragment distributions from ring expansion tests on cold sprayed nickel+aluminum rings. Notice the multimodal character that develops in the fragment distribution data that is very similar to that in Fig 4.21a and Fig 4.11a. (b) The fragment mass distribution of the same experiments as in (a). The apparent shifting of the fragment population to a unimodal distribution at higher strain rates is similar to that seen in Cambridge experiments on CS Ni+Al.

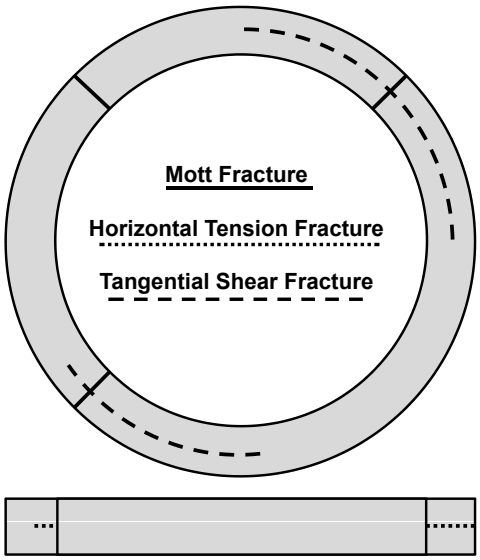

Figure 4.26: Different types of fractures are illustrated here. The Mott fractures are radially oriented. Additional fractures observed in the Cambridge experiments are oriented horizontally, and are termed horizontal fractures. The tangential shear fractures observed in the OSU experiments are oriented such that they lie between the inner diameter ring surface and the outer diameter ring surface.

Closer examination of fragments from OSU experiment Ring 2, shown in Fig 4.27a, reveals that the fracture surfaces have features similar to those observed in the ARL CS Ni+Al tests in Figure 4.22. There is what appears to be a mixture of shear failures (angled crack surfaces) and tensile failures (in a radial direction).

Looking more closely, something new is evident that has not been observed in any of the previous experiments. Figure 4.27b shows tangential shear cracks which have formed in the center of fragments from OSU Ring 2. These cracks are very different from the horizontal tension cracks that were observed in the Cambridge experiments. They appear in a different location on the ring and are generated via a different mechanism, as illustrated by the schematic in Figure 4.26.

Examining fragments from OSU Ring 3, it is evident that the increased strain rate leads to an increased amount of fragmentation, especially tangential shear fracture. Looking at Figure 4.28, we see a large number of fragments that have formed via tangential fracture. This mechanism, like the vertical fracture mechanism seen earlier,

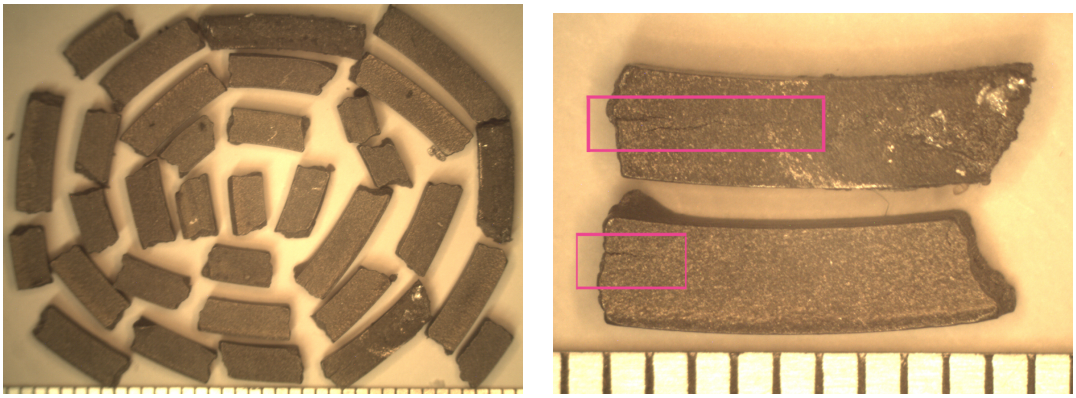

(a) (b)

Figure 4.27: Selected Fragments from OSU experiment Ring 2 (a) Fragments from OSU ring experiment Ring 2. Note similar tension and shear features on the fracture surfaces to those in Figure 4.22. (b) Tangential shear fractures, enclosed in a pink box, roughly in the center of select fragments of OSU Ring 2. All scales are in mm.

leads to a drastic increase in the number of fragments. The presence of both shear and Mott fractures and the crack branching taking place, lead to a large increase in the numbers of small fragments formed, as illustrated by the fragment distribution data.

The OSU fragment data is number averaged and plotted versus strain rate in Figure 4.29. The data shows significant scatter. For the 72 mm outer diameter rings, the most apparently inconsistent data point is OSU Ring 3 with an average strain rate of 500 and an average fragment mass of 0.06 grams. Ninety percent of the mass in that experiment was recovered. The smallest fragment masses are the hardest to recover experimentally. With higher fragment mass recovery, the average fragment mass would most likely fall to a lower average and fit into the experimental trend better.

The 26 mm outer diameter rings also appear not to fit the experimental trends for the OSU 72 mm outer diameter rings; the OSU experiments on 26 mm outer diameter rings showed much higher strain rates for comparable fragment sizes as shown in Figure 4.29 with the notable exception of OSU Small Ring 1 (average strain

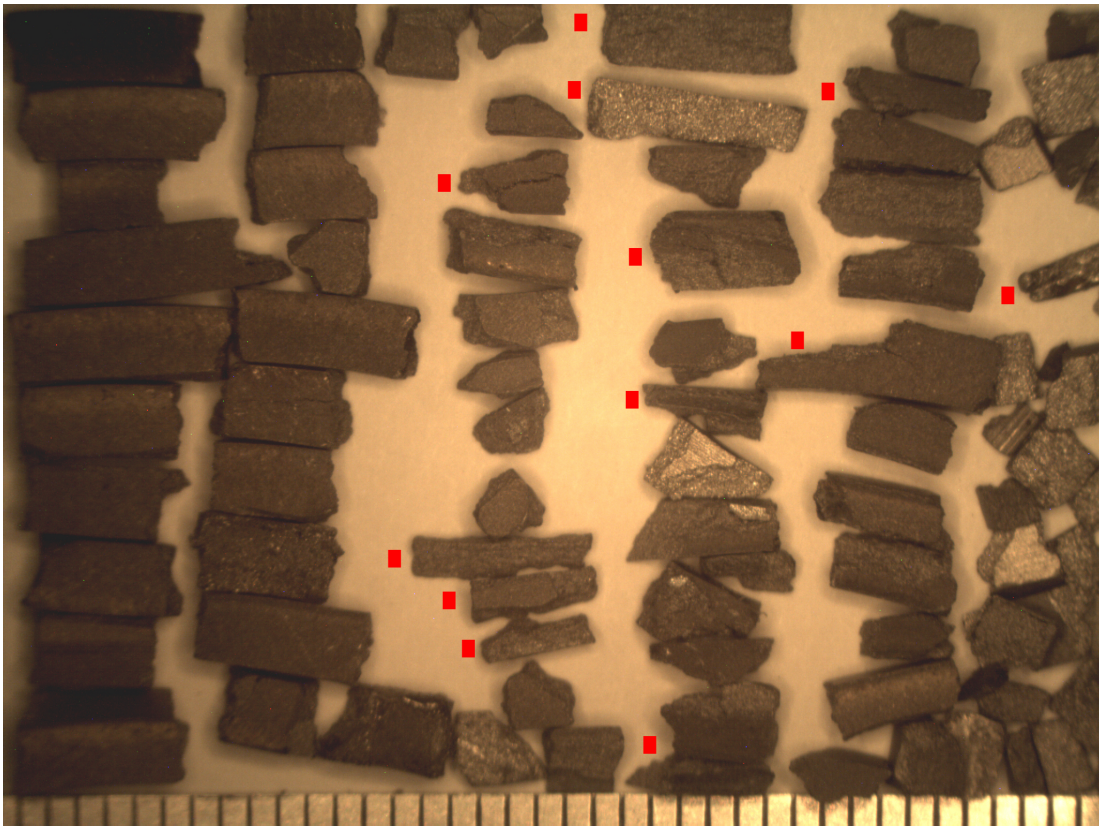

Figure 4.28: Top View of Fragments from OSU experiment Ring 3. Fragments that were shear cracked in half are indicated with a red rectangle. The scale is in mm.

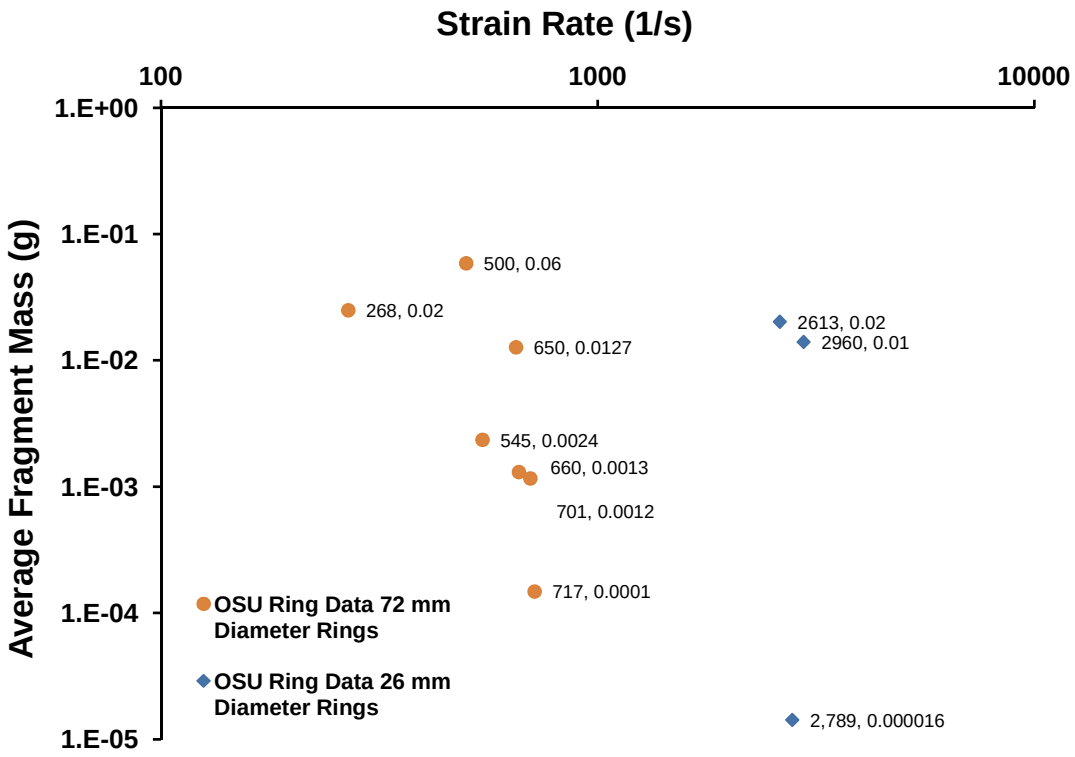

Figure 4.29: Average fragment size vs. strain rate for the OSU fragmentation experiments. The 26 mm outer diameter rings required much higher strain rates for comparable fragment sizes. Points are labeled with strain rate and average mass.

rate 2789). OSU Small Ring 1 demonstrated an average fragment size much smaller than those of OSU Small Ring 2 and 3, but not consistent with the OSU experiments on larger rings either. OSU experiments Small Ring 2 and Small Ring 3 do not show shear driven tangential fractures or tensile horizontal fractures as seen in Figure 4.30a. If fragments from OSU Small Ring experiments are examined carefully, there is no evidence of shear induced tangential fracture. However, OSU Small Ring 1 fragments are horizontally fractured as seen in Fig 4.30b. This mechanism, which is coupled with the tiny fragment forming potential of the fracture surfaces, leads to much smaller average fragment sizes than those in OSU Small Ring 2 and 3. It is not clear why this happened. It is possible that variations in the urethane coupling medium or the aluminum wire led to uneven loading on the inside surface of OSU Ring 1, causing the horizontal tension fractures. This chance occurrence points out that the potential for small fragment generation of the tensile horizontal cracks is apparently less than that of the shear loaded tangential fractures of the larger OSU rings. The OSU experiments on larger rings demonstrated much smaller fragment sizes for a given strain rate than any of the other experiments. The horizontal fractures in OSU experiment Small Ring 1, the Cambridge CS Ni+Al experiments, and the Cambridge experiments on Mixture A and Mixture B all showed a precipitous increase in fragment number but still required a higher strain rate for comparable fragment sizes.

Measurements of fragment heights along the inside and outside diameter surfaces, shown in Table 4.4, for each test revealed a surprising trend. The height of fragments from 72 mm outer diameter OSU large rings was consistently less at the inner diameter than at the outer diameter. The difference was not large, but it was quite consistent. The trend was the opposite for the 26 mm outer diameter OSU small rings, which were found to be taller at the inner surface than at the outer surface. Greater fragment height at the inner surface was also observed in the Cambridge experiments on cold sprayed Ni+Al fragments in Fig 4.14a and Figure 4.37c. In exploding wire

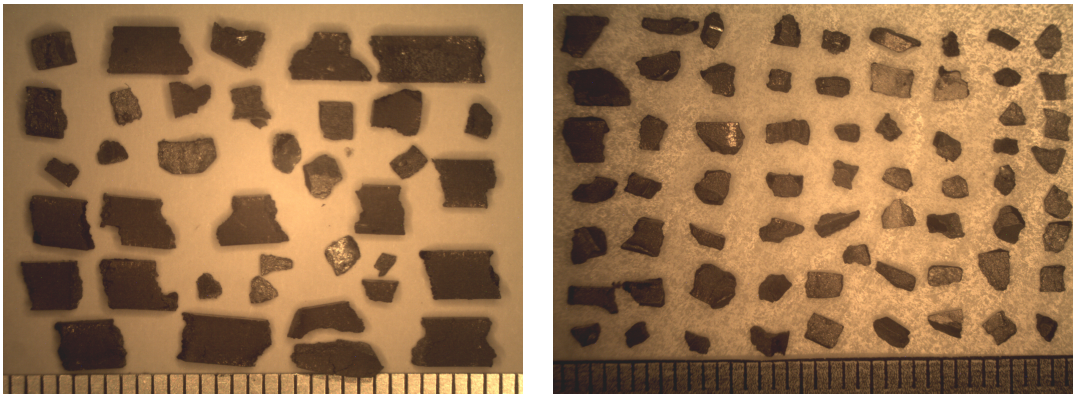

(a) (b)

Figure 4.30: (a) Side view of Fragments from OSU experiment Small Ring 2. Note similar tension and shear features on the fracture surfaces to those in Figure 4.22. No horizontal fracture or tangential shear fractures were noted in experiments Small Ring 2 or 3. (b) Side view of selected fragments larger than 1400 μm from OSU experiment Small Ring 1, which fractured horizontally in addition to Mott radial fractures, similar to the Cambridge experiments on CS Ni+Al. This is why OSU experiment Small Ring 1 yielded much smaller fragment sizes than Small Ring 2 and Small Ring 3.

experiments on aluminum wires confined in distilled water, it was observed that the Al plasma column diameter was very uniform vertically during expansion [227], rather unlike a high explosive where the explosive forms a Y shape with a varying diameter as the detonation front moves down the explosive column. Uniform expansion of the wire led to uniform loading of the urethane coupling medium and its uniform expansion. When the compliant urethane medium encountered the constraint of the ring, it wrapped around the top and bottom surfaces partially, providing a clamping effect that slightly deforms the ring, reducing the height of the inside edge. This pressure from the urethane led to significant friction between the urethane and the Ni+Al ring, causing a shear load on the ring which opposed the tensile deformation. As a result, the sample rings developed shear cracks. This mechanism is schematically illustrated in Figure 4.31.

The smaller size of the urethane driver for the 26 mm outer diameter rings provided less material to wrap around the edges of the smaller rings. The 26 mm outer diameter

Table 4.4: Selected fragment heights from OSU tested rings. Note the trend of the inner height being greater than the outer height in the samples from Small Rings 2 and Small Ring 3, and the opposite trend in rings 2-8.

Ring	Fragment Height at Inner Diameter (mm)	Fragment Height at Outer Diameter (mm)
Small Ring 1	–	–
Small Ring 2	2.973±0.009	2.967±0.003
	2.956±0.002	2.943±0.001
Small ring 3	3.035±0.001	3.024±0.001
	3.043±0.006	3.018±0.001
Ring 2	2.528±0.002	2.538±0.012
	2.517±0.002	2.548±0.004
Ring 3	2.516±0.001	2.553±0.004
	2.514±0.001	2.641±0.04
Ring 4	2.513±0.004	2.512±0.002
	2.525±0.003	2.560±0.005
	2.519±0.007	2.521±0.001
Ring 5	2.528±0	2.533±0.001
	2.541±0.004	2.558±0.006
	2.523±0.001	2.542±0.007
Ring 6	2.523±0.004	2.560±0.001
Ring 7	2.505±0.001	2.550±0
	2.487±0.001	2.516±0.001
Ring 8	–	–

rings were also thinner, nominally 2.0 mm thick, compared with the 2.5 mm thickness of the 72 mm outer diameter rings. This provided less purchase for the urethane and a smaller region over which a load from the urethane could act.

Fragments from two tests, OSU Ring 2 and OSU ring 3 were mounted in Emmerson and Cumming Stycast 1266 two-part, mounting epoxy mixed with about 25% by weight of nickel coated aluminum powder added for edge protection. The samples were cast so that the nickel coated aluminum powder settled thickly on and around the sample to provide maximum fracture edge retention. The samples were polished so that crack profiles were visible. Backscattered electron images of the crack paths were taken at 300x magnification and then the length of the crack profile bordering Nickel and Aluminum were measured as well as the total length of the crack profile. The ratio of these lengths provides a useful measure of which phase promotes failure. As in the Cambridge cold sprayed Ni+Al tension fractures, the fracture surface shows a definite preference for Nickel. In this case, the preference is even more marked with the fraction of fracture surface bordering Ni being 0.87±0.03, which is significantly

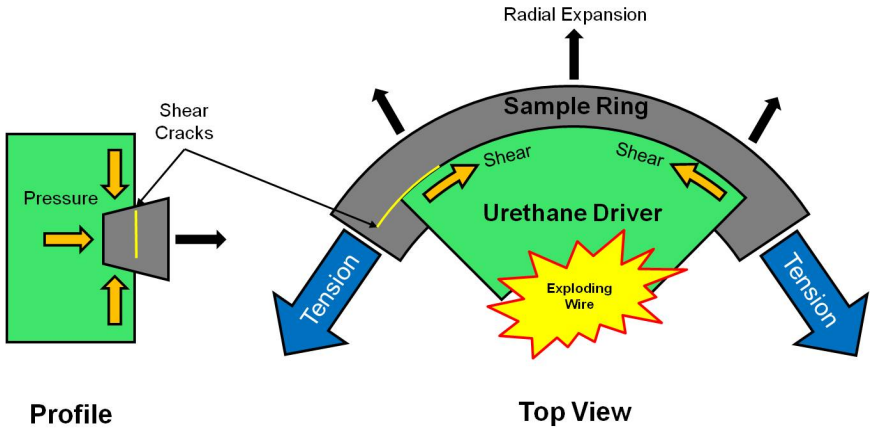

Figure 4.31: Tangential shear fracture mechanism. After the wire explodes, a compressive pulse is driven into the urethane and supported by high pressure plasma. The urethane wraps around the edge of the sample ring and compresses it. Friction between the urethane and the portion of the top and bottom ring surfaces that the urethane overlaps leads to a shear loading on a portion of the ring. The shear loading leads to the formation of tangential shear cracks and the ring expands.

Table 4.5: Line fraction of nickel on fracture surfaces in cold sprayed nickel+aluminum samples tested at Cambridge and OSU.

	CS Ni+Al
V_v	0.51±0.02 Ni
L_L Cambridge Crack	0.63±0.08 Ni
L_L OSU Shear Crack	0.87±0.03 Ni

greater than the average volume fraction of Ni which is 0.51±0.02; these results are shown in Table 4.5 for comparison. The preference of the crack for nickel can be seen in Figure 4.32. Thus, there is a quantitative difference between tensile and shear cracks in cold sprayed Ni+Al.

The results of the combined test data on cold sprayed Ni+Al provide several interesting insights. Mott fragmentation is present in all cases, but additional fragmentation mechanisms are also operative. The contrasting results of the Cambridge and ARL experiments on cold sprayed nickel+aluminum reveal the importance of horizontal fractures on the fragment population. Because of the coupled mechanism that generates small fragments from the fracture surfaces, horizontal fractures drastically

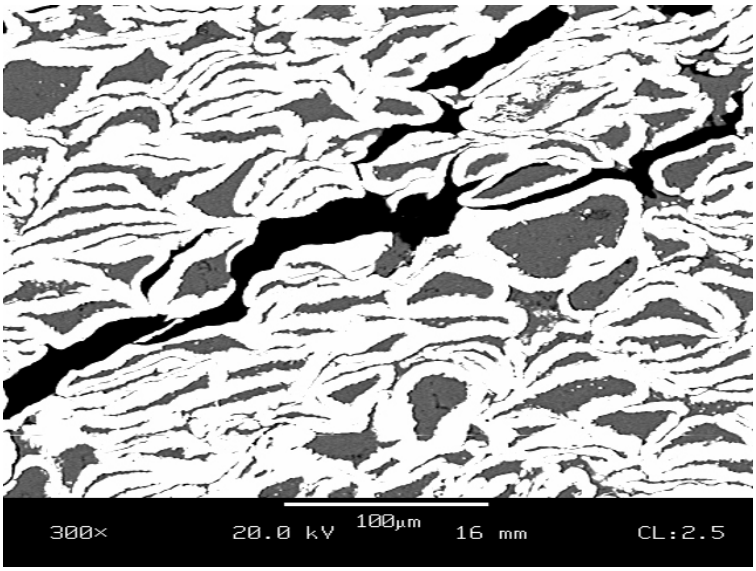

Figure 4.32: Shear crack profile from OSU Ring 2 fragment. Fragments with shear cracks from OSU Ring 2 and Ring 3 were carefully polished and then imaged. The crack path shows a distinct preference for Ni, as was seen in the Cambridge CS Ni+Al samples. However, in this case the preference is even more marked. The fraction of the crack bordering Nickel is 0.87±0.03.

reduce the average fragment size. The larger OSU rings showed Mott fragmentation, and an entirely different fragmentation mechanism was observed which resulted from the application of shear loads. Shear induced tangential fractures formed due to the clamping mechanism discussed earlier. This mechanism is an artifact of the test conditions, but provides insight into a unique secondary fracture mechanism that has not been previously reported in published literature to the best of the author's knowledge.

The fracture surfaces of the tangential cracks are much different than the tensile failures observed in the Cambridge CS Ni+Al experiments as is evident in Figure 4.17a, Figure 4.17b. As seen in Figure 4.33a, the topography of the fracture surface is much flatter, and far more Ni is visible as shown in Figure 4.33b. This surface topography suggests one or very few main cracks. The horizontal tension cracks that form have very rough topography and are clearly the result of many intersecting cracks. Figure 4.33b implies that the Ni/Ni interfaces between coated particles are

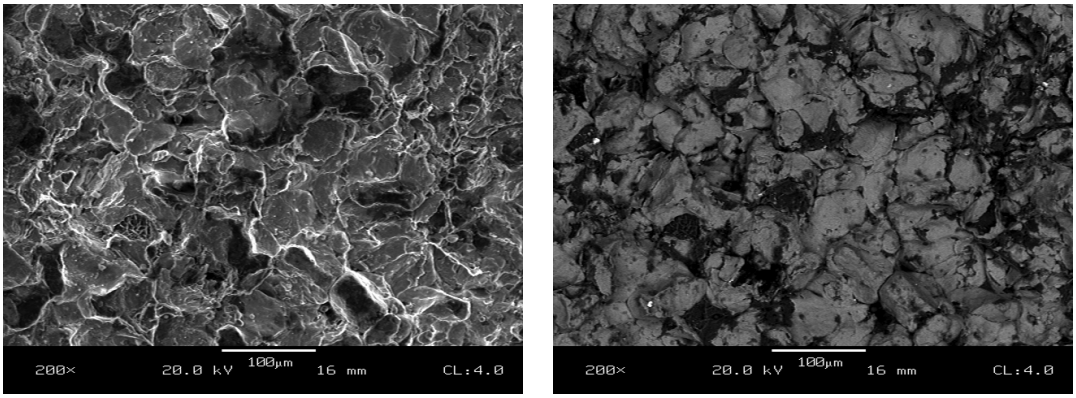

(a) (b)

Figure 4.33: Tangential shear fracture surface from OSU experiment Ring 8. (a) Secondary electron image showing the flatter topography of the tangential shear crack surface. (b) Backscattered electron image showing a preponderance of Ni on the fracture surface. When compared with the crack profile in Figure 4.32, the nickel on this fracture surface appears to be Ni from the outside of intact Ni coated Al particles from a failed Ni/Ni interface.

the interfaces most sensitive to failure. The OSU rings have much smaller average fragment sizes when compared with the ARL and Cambridge experiments on CS Ni+Al. The primary difference between those tests is the formation of tangential shear cracks. The shear cracks are evidently a more potent source of fragments than the tensile cracks. This suggests that the cold sprayed Ni coated Al particles are more prone to tear off when sheared.

There is virtually no bulk ductile necking to fracture in the OSU fragments as would be expected in a structural metal like aluminum, but there is limited and highly localized plasticity on the fracture surfaces. This is consistent with observations of the Cambridge and ARL experiments on cold sprayed Ni+Al samples.

Scrutiny of the smaller fragments formed reveals similar physical features to those observed in the larger fragments. Figure 4.34a and 4.34b are images of a fragment that sieved between 500 μm and 250 μm in size. This large particle shows extensive debonding between different constituent particles as well as between different phases

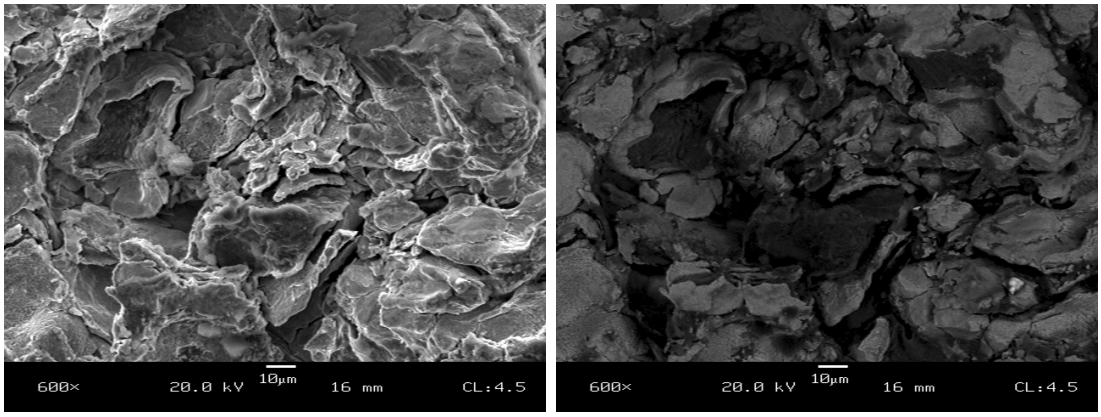

(a) (b)

Figure 4.34: Fragment fracture surface from OSU ring expansion experiment Small Ring 1 on cold sprayed Ni+Al. (a) Notice the debonding that has taken place on the fragment between particles and between nickel and aluminum. Branches from the main crack lead to the formation of small fragments. (b) A backscattered electron image of the same region as (a) showing ductile necking of aluminum. Notice the fracture of the Ni coating on the particles, exposing the aluminum.

in the particles, consistent with the physical picture seen in the earlier images. Figure 4.34b, a backscattered SEM image of the same region, shows the different phases. The extensive debonding leads to greatly enhanced surface area of the particle which may have important implications for possible combustion or reaction.

Figure 4.35a and 4.35b are backscattered SEM images of fragments that sieved between 38 μm and 75 μm in size. It is interesting to note that in each image, one fragment appears to be simply a nickel coated aluminum powder particle with a partially cracked or torn Ni coating. The other fragment is still a composite particle, but with more aluminum exposed. It may be that these particles are the aluminum cores of nickel coated particles with only a small remnant of the coating left. Or perhaps, portions of several particles fragmented off as one. In either case, the smallest cold sprayed nickel+aluminum fragments remain composite particles, capable of reacting to form intermetallic phases or combusting.

Comparison of small fragments from the OSU tests and the Cambridge tests is

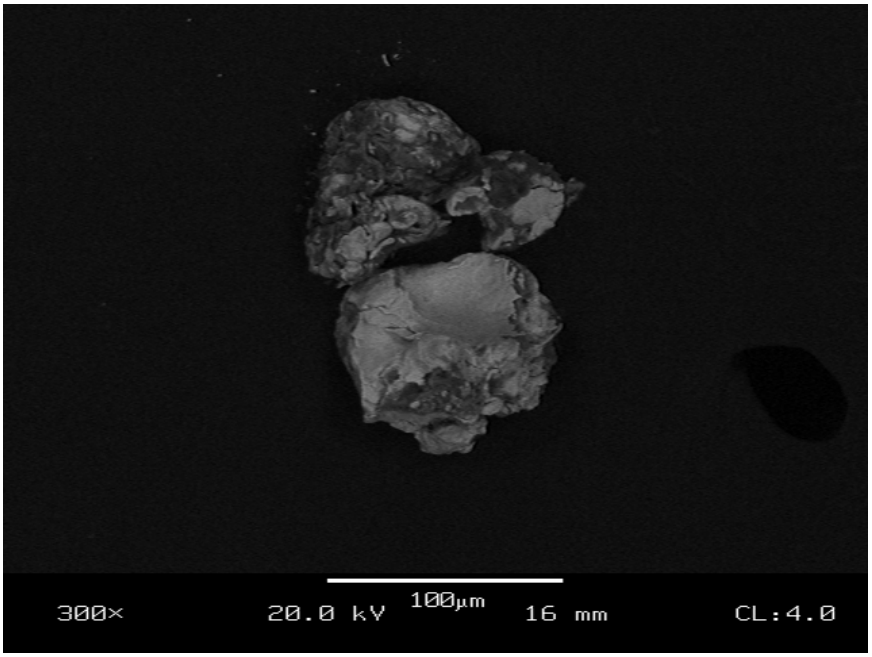

(a)

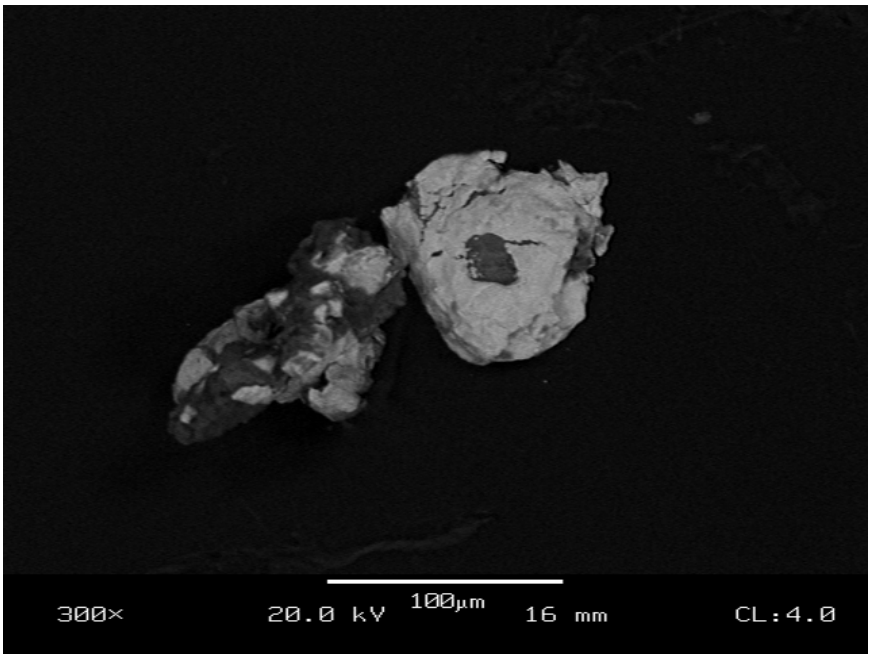

(b)

Figure 4.35: Cold sprayed Ni+Al fragments between 38 μm and 75 μm sieve sizes from OSU Ring 1. Notice that one of the fragments in each image appears to be a nickel coated aluminum powder particle. The other may be the aluminum core of such a particle or a fragment that contains portions of several such particles. All of the particles shown are composite particles with lighter colored Ni mixed with darker Al, capable of combustion or reaction to form an intermetallic phase.

worthwhile. A small fragment from Cambridge experiment E101022A is shown in Figure 4.20a. When compared with the fragments in Figure 4.34b, Figure 4.35a, and Figure 4.35b there seems to be more Ni on the surface of the fragments generated by the OSU experiments. This supports other observations about differences between the fragmentation mechanisms operative in the Cambridge and OSU fragmentation experiments. However, in both cases a composite fragment is what remains, which may strongly influence any subsequent combustion behavior.

4.3.2 Fragmentation Results For Explosively Compacted Mixture A and Mixture B

Sample rings fabricated from Mixture A and Mixture B were tested at Cambridge using the configuration depicted in Fig 4.3a. The sample rings were 25 mm outer diameter x 19 mm inner diameter x 3 mm tall. The explosively compacted Mixture A fragment distribution data is shown in Figure 4.36a and 4.36b. These are plots of the number and mass fraction distribution respectively, and they follow a similar trend to that seen in the Cambridge experiments on cold sprayed nickel+aluminum rings. A multimodal distribution of fragments forms at low strain rates and then converges at high strain rates to a unimodal distribution.

Scrutinizing recovered fragments provides evidence that the same fragmentation processes are taking place in the Mixture A fragments as were observed in the Cambridge experiments on cold sprayed nickel+aluminum. At lower strain rates, as seen in Figure 4.37a, the sample ring was not subject to horizontal splitting. At higher strain rates, we observe the horizontal fracture of the fragments (Figure 4.37a). This is due to the tensile loading which develops as a result of the velocity gradient in the copper tube on the inside surface of the ring, as can be seen in Figure 4.37c. A horizontal fracture is visible in Figure 4.38. Notice the branches of the horizontal fracture which will lead to additional fragments. The explosively compacted mixtures have interface densities within a factor of two of the cold sprayed Ni+Al (Mixture

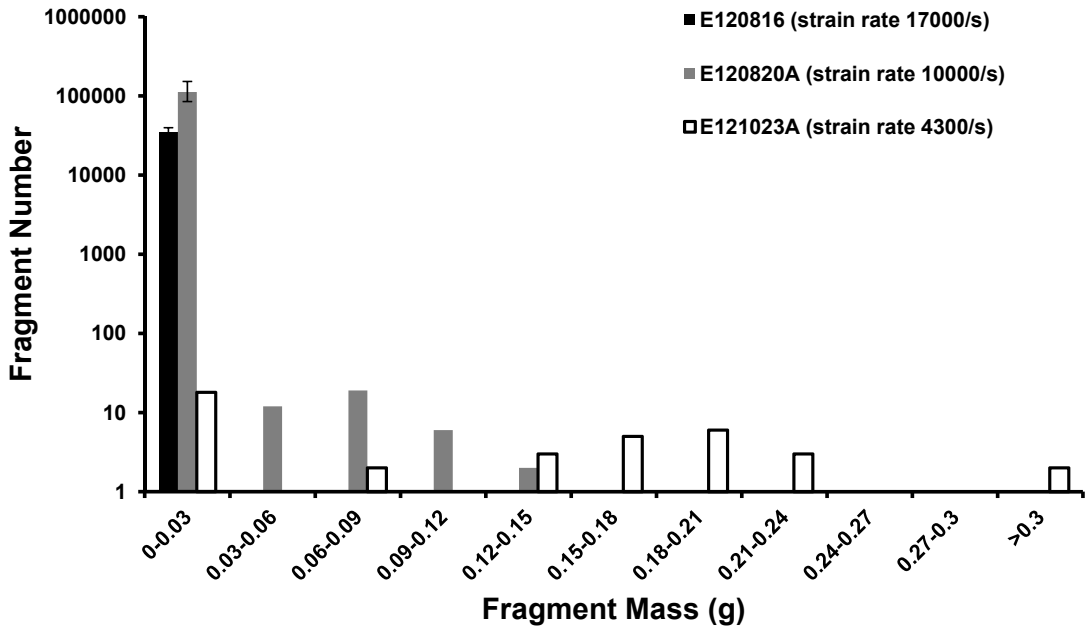

(a)

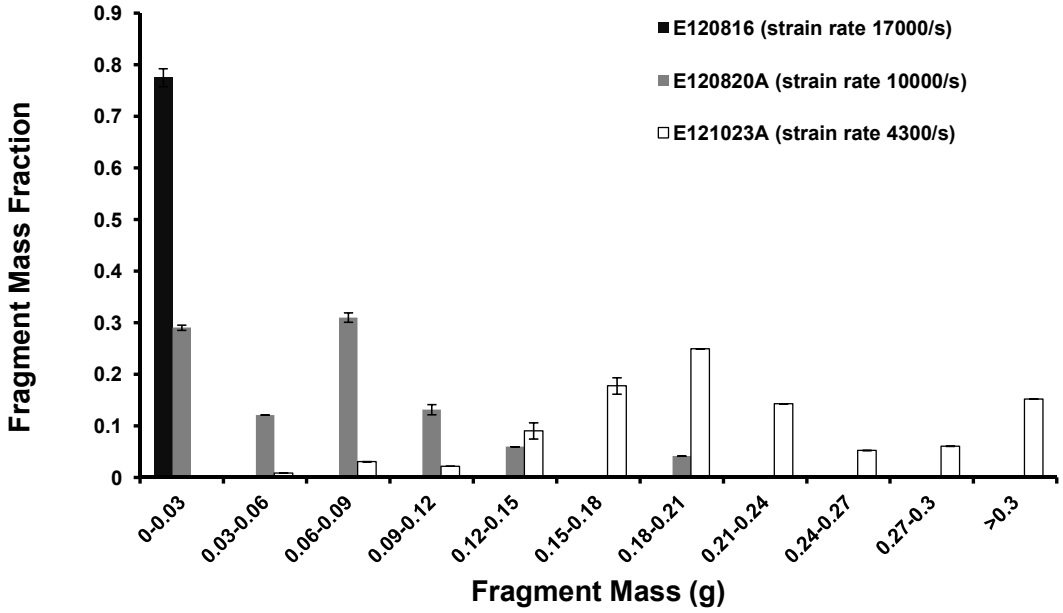

(b)

Figure 4.36: (a) The number distributions of fragments from ring fragmentation tests on Mixture A rings. For test E120816 77.5% of the fragment mass was recovered which may have skewed the number distribution. (b) The mass fraction distributions of fragments for Mixture A. Despite the relatively low fraction of recovered mass, the mass of the ring recovered from experiment E120816 is concentrated in the smallest fragments.

Table 4.6: Line fraction of each phase on fracture surfaces in Mixture A and Mixture B

	Mixture A	Mixture B
V_v	0.20 Ni 0.24 W 0.56 Al	0.08 Ni 0.25 W 0.13 Zr 0.55 Al
L_L	0.24±0.05 Ni 0.19±0.04 W 0.57±0.06 Al	0.07±0.05 Ni 0.24±0.05 W 0.05±0.05 Zr 0.65±0.05 Al

A:97±7 mm^{-1} and Mixture B:143±13 mm^{-1} versus CS Ni+Al:186±6 mm^{-1}). The high density of weak interfaces provide opportunities for crack initiation and crack propagation leading to the generation of many fine fragments.

The results from the fragmentation tests for Mixture B, seen in Figure 4.39a and 4.39b are very similar to those of Mixture A and by extension, to the cold sprayed Ni+Al results presented previously. At lower strain rates, the fragments form a multimodal distribution. As the strain rate of the expansion test increases, the distributions converge to a unimodal distribution with small fragment sizes. Exactly similar behaviors to those noted in Figure 4.37a, b, and c were observed in Mixture B.

To investigate the effect of the microstructure constituents on the fracture process, Mixture A fragments from experiment E121023A and Mixture B fragments from experiment E121023B were mounted in the Stycast two-part epoxy referenced earlier mixed with tungsten powder. The fragments were polished and the line fraction of each phase on the fracture profile was determined. The results are shown in Table 4.6 along with the original volume fractions for comparison.

Cracks measured in Mixture A fragments showed no statistically significant preference for any phase. A crack profile in Mixture A is shown in Figure 4.40. This was somewhat surprising because previous work by Wei et al. [132] had suggested that the

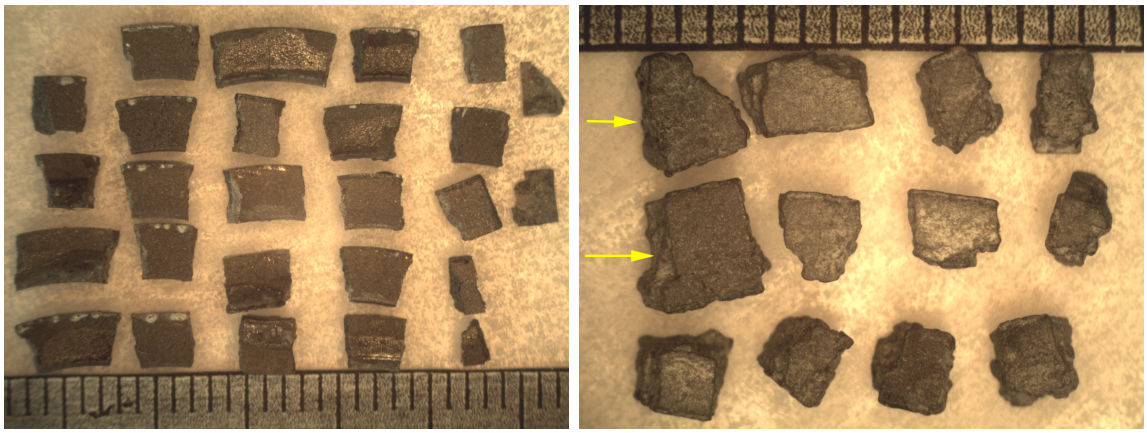

(a) (b)

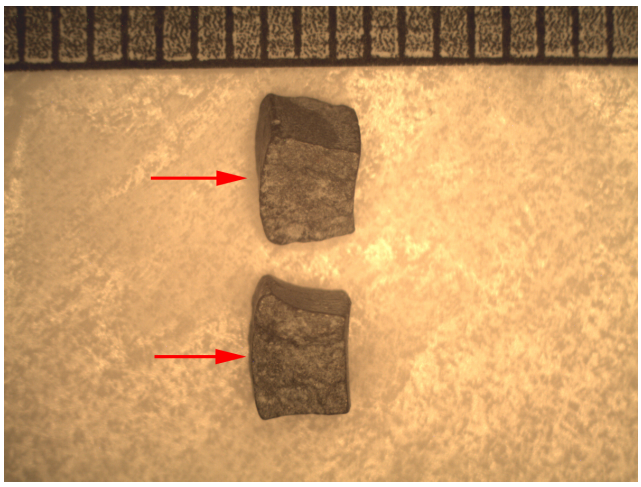

(c)

Figure 4.37: (a) Fragments from Cambridge experiment E121023A at $\dot{\epsilon} = 4300$. Note that the fragments are typical of Mott fragmentation with no other fragmentation mechanisms obviously active. Figure 4.22. (b) A selection of large fragments from experiment E120820A at $\dot{\epsilon} = 9800$. Fragments that have not been bisected by horizontal fractures are indicated by yellow arrows, though both have been cracked. The remaining fragments were bisected by horizontal fractures. (c) A profile picture of the intact fragments from E120820A. Note that the ring is taller next to the internal diameter surface, indicated by red arrows, and is close to the original original height next to the external diameter surface. The scales are all in mm.

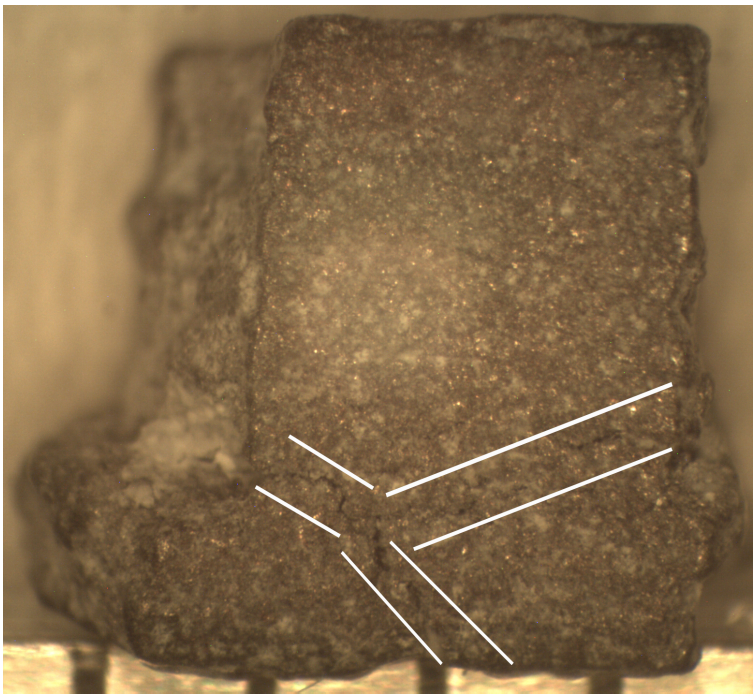

Figure 4.38: Tension fracture in Cambridge experiment E101020A on explosively compacted Mixture A, bounded by white lines for clarity. This type of fracture leads to horizontal bisection similar to that seen in Figure 4.37b. Notice also the branching of the horizontal crack, a mechanism which leads to the formation of fine fragments. The scale is in millimeters.

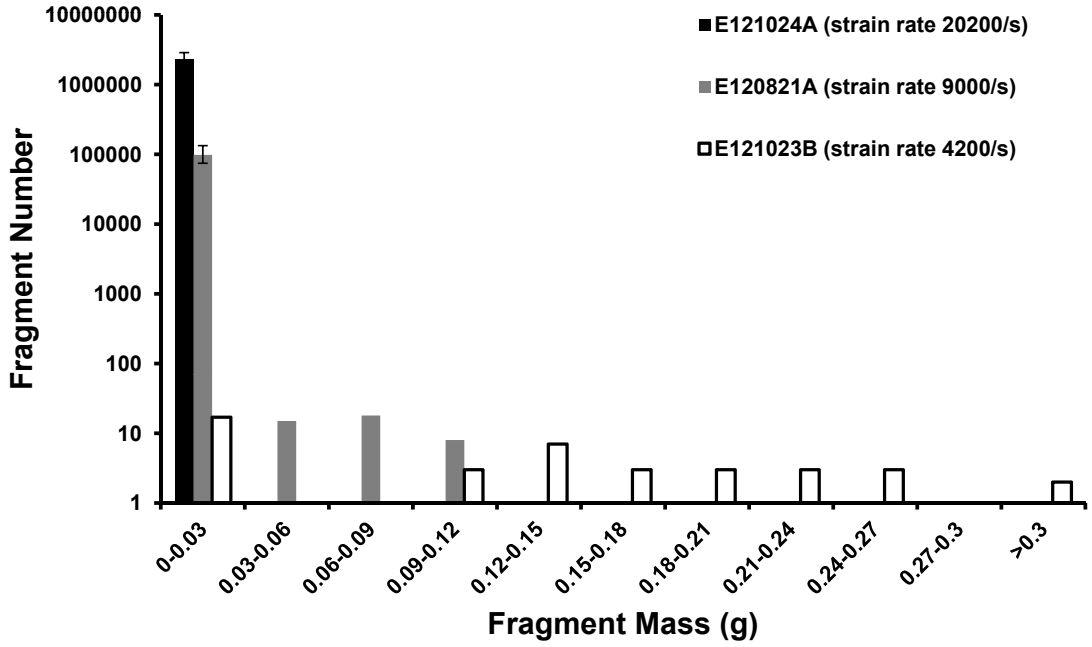

(a)

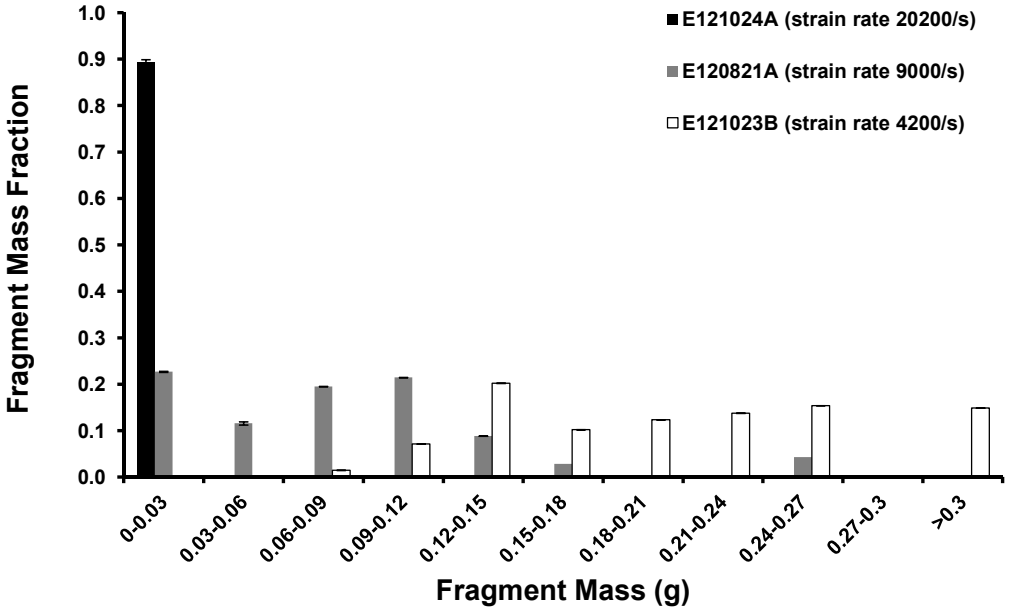

(b)

Figure 4.39: (a) The number distribution of fragments from ring fragmentation tests on Mixture B rings. (b) The mass fraction distribution of fragments for Mixture B. A high mass of recovered fragments at the lowest fragment sizes at the highest strain rates is evident here as well as in the tests in Mixture A samples.

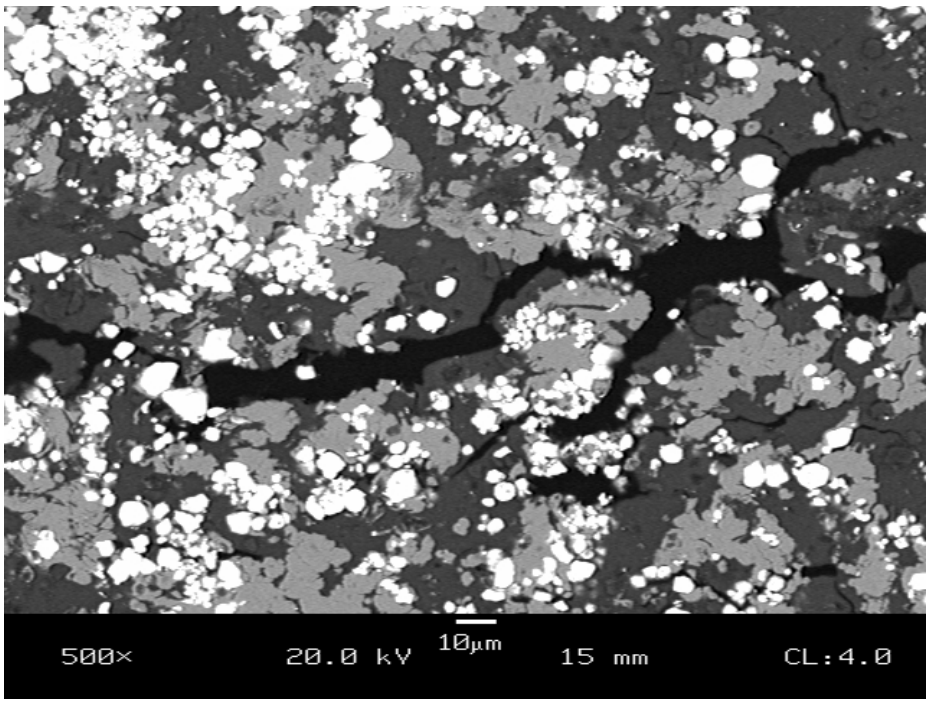

Figure 4.40: Cross section of fractures in a Mixture A fragment. Note the extensive crack branching.

Ni and W were not well bonded in binary explosively compacted mixtures Ni+Al and W+Al. Crack profiles in Mixture B also showed very little preference for any phase, except Al which appears slightly over represented on fracture surfaces on average. In both cases, the crack profiles revealed significant amounts of crack branching and microcracking apart from the main crack.

The character of the fracture surfaces are of interest because of their possible influence on reaction or combustion behavior. Figure 4.41a and 4.41b are electron microscope images of a fracture surface from a randomly selected fragment from Cambridge Experiment E121023A with an average strain rate of $\dot{\epsilon} = 4300$. Figure 4.41b is a backscattered electron microscope image which shows tungsten and nickel much brighter than the surrounding aluminum matrix. The presence of a large fraction of tungsten and nickel in Figure 4.41b is also noted.

Figure 4.41c and 4.41d are a set of images from a fracture surface of a randomly selected fragment from Cambridge Experiment E121023A with an average strain rate

of $\dot{\epsilon} = 10^4$. There are two major differences between these images and those of Figure 4.41a and 4.41b. As shown in Figure 4.41d, there is far less tungsten and nickel visible on the fragment surface. This does not seem to agree with the findings in Table 4.6. This is indirect evidence of interface failure. The discrepancy may be a result of the strain rates at which crack profiles were examined. Fragments from the lowest strain rate experiments for Mixture A and Mixture B were examined to determine the line fraction of phases on the crack path. At higher strain rates, it appears that the nickel or tungsten particles are pulled off of the fracture surfaces. This can be seen in Figure 4.43 wherein some nickel and tungsten particles which have separated from the larger composite particles are indicated with arrows. Tungsten or nickel particles coming off of the fracture surface during the fragmentation event would account for the porous appearance of the fracture surface in Figure 4.41c and 4.41d.

The explosively compacted mixtures shared similar fragment size distributions and so will be addressed together. Mixture A, an explosively compacted mixture of aluminum, nickel, and tungsten was found to produce small fragments, as seen in Figure 4.36a and Figure 4.36b.

Figure 4.41c shows a fracture surface more fissured than that in Figure 4.41a. This is evidence of additional crack branching and is expected at the higher strain rate ($\dot{\epsilon} = 10^4$ vs $\dot{\epsilon} = 4300$) because of greater energy dissipation. This is qualitatively consistent with the results of Jaeger, Englman, and Sprecher [182] and Aimone et al. [228] who reported the surface area added by incomplete cracks can be very significant in fragmentation events. Aimone et al. [228] further reported an increase in internal damage to fragments, increasing with strain rate, which is qualitatively consistent with the results observed in the present work.

The behavior of fragments from experiments on Mixture B is very similar to what has already been observed in Mixture A. Figure 4.42a and Figure 4.42b shows a

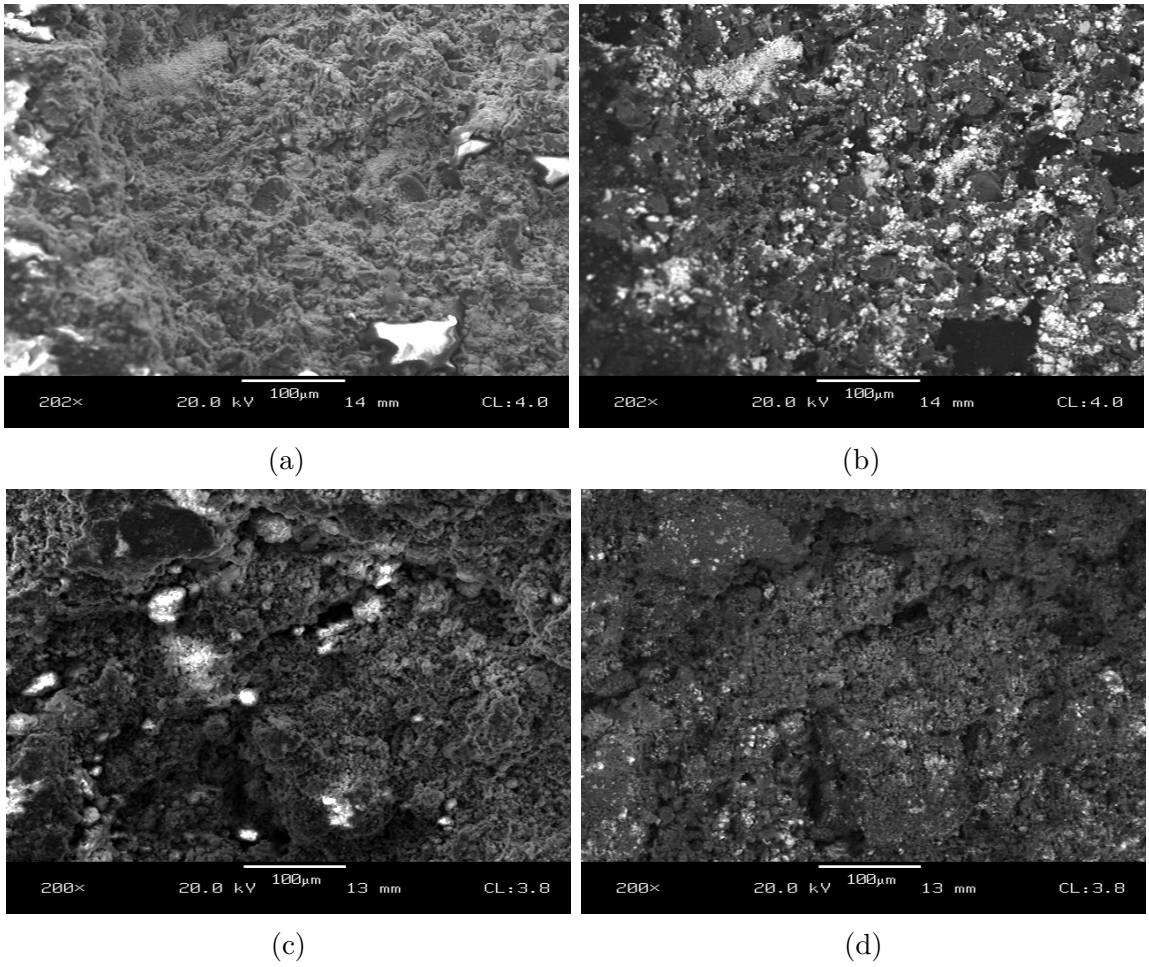

Figure 4.41: (a) Fracture surface from Mixture A experiment E121023A. The ring average strain rate was $\dot{\epsilon} = 4300$. The charging regions are wax deposits that remained after soft capture and cleaning. (b) A backscattered electron image of the same region as in (a). Notice the bright colored nickel and tungsten particles. (c) Fracture surface from Mixture A experiment E120820A. The ring average strain rate was $\dot{\epsilon} = 10^4$. Notice there are fissures and cracks on the surface that are not present on the surface depicted in (a). The charging regions are wax media that remained on the surface from the soft capture process. (d) A backscattered electron microscope image from the same region as (c). The bright particles are tungsten and aluminum and the wax coated regions are dark. Note that fewer bright tungsten and nickel particles are visible in this image than in (b), though the region is the same size. This is evidence of interface failure taking place.

fracture surface belonging to a fragment from Cambridge Experiment E121023B for which the average strain rate was $\dot{\epsilon} = 4200$. This can be compared with a fracture surface from Experiment E121021A, shown in Figure 4.42c,d with an average strain rate of $\dot{\epsilon} = 9000$. Again it is evident that the fracture surface of a fragment formed at higher strain rate has fewer reinforcement particles in it, in this case tungsten, nickel, and zirconium. This suggests that these particles were dislodged during the fragmentation process, contributing small fragments themselves. This again is indirect evidence of interface failure and the influence of the interfaces.

Figure 4.43 highlights the composition of a group of fragments between 75 μm and 150 μm in size (sieved). At this length scale, many of the small fragments still have a composite structure. They retain the ability to undergo an intermetallic formation reaction. The separation of some nickel and tungsten particles as noted above will expose more aluminum, which may have important implications for fragments undergoing combustion.

An examination of small fragments formed from Mixture B reveals similar features to those observed in Mixture A fragment samples. The Mixture B fragments remain composite particles even at the smallest sizes, with significant exposed aluminum surface area as seen in Figure 4.44b

4.4 The Results of Fragmentation Experiments on Structural Energetic Materials

A plot of average fragments size vs. fragment mass normalized by density is shown in Figure 4.45 for all of the fragment data generated in this work. As seen in Figure 4.45, there is a fair amount of data scatter. This naturally arises from natural stochastic variations in material, difficulties in the collection of fragments and the comparison of different fragmentation techniques.

However, there is an important source of variation apart from these natural sources that is an artifact of unanticipated experiment conditions. The OSU data diverges

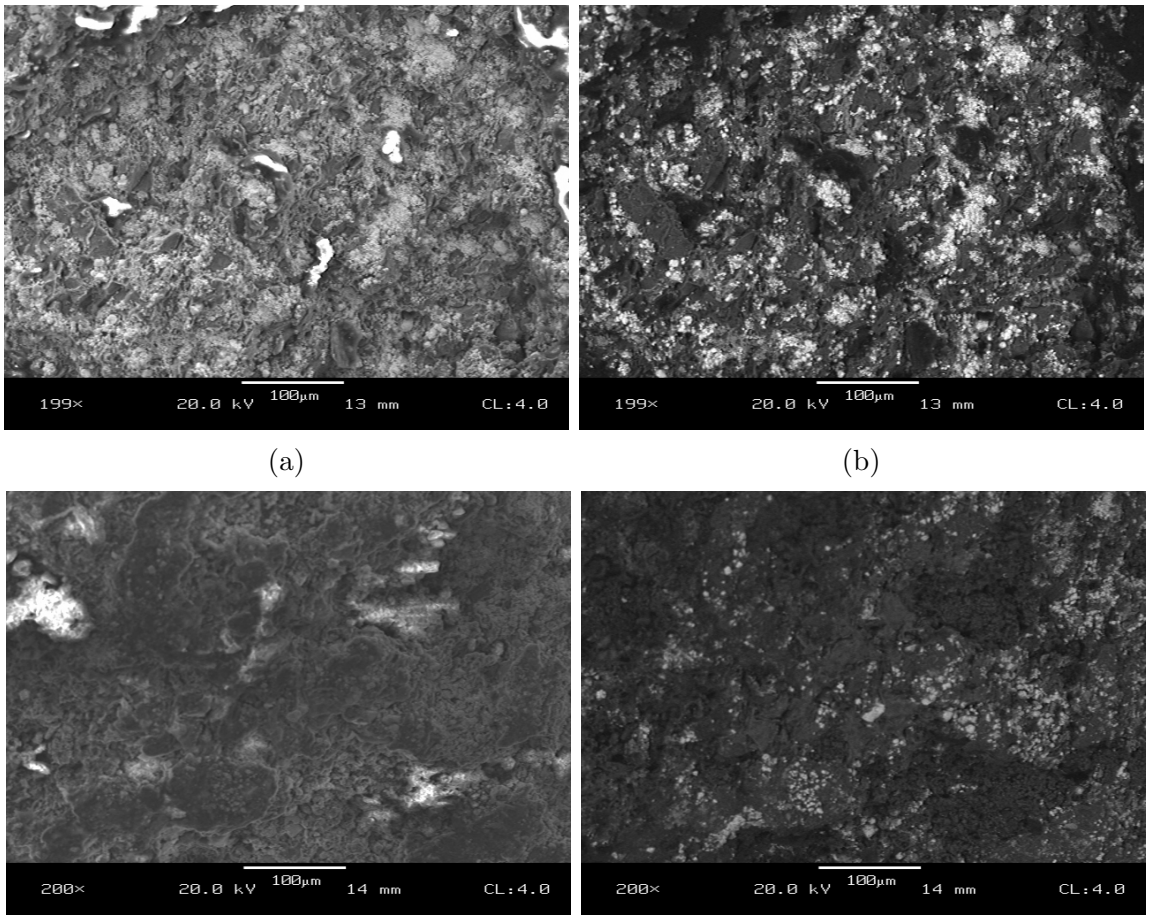

Figure 4.42: (a) Fracture surface from Mixture B experiment E121023B The ring average strain rate was $\dot{\epsilon} = 4200$. The charging regions are wax deposits that remained after soft capture and cleaning. (b) A backscattered electron image of the same region as in (a). Notice the bright colored nickel and tungsten particles. (c) Fracture surface from Mixture B, experiment E120820A. The ring average strain rate was $\dot{\epsilon} = 9000$. Notice there are fissures and cracks on the surface that are not present on the surface depicted in (a). The charging regions are wax media that remained on the surface from the soft capture process. (d) A backscattered electron microscope image from the same region as (c). The bright particles are tungsten and aluminum and the wax coated regions are dark. Note that fewer bright tungsten and nickel particles are visible in this image than in (b), though the region is very nearly the same size. It is apparent also that the difference in the amount of tungsten, nickel, and zirconium that remained on the surface is not so great as that in Figure 4.41b and 4.41d because of the smaller difference in strain rates.

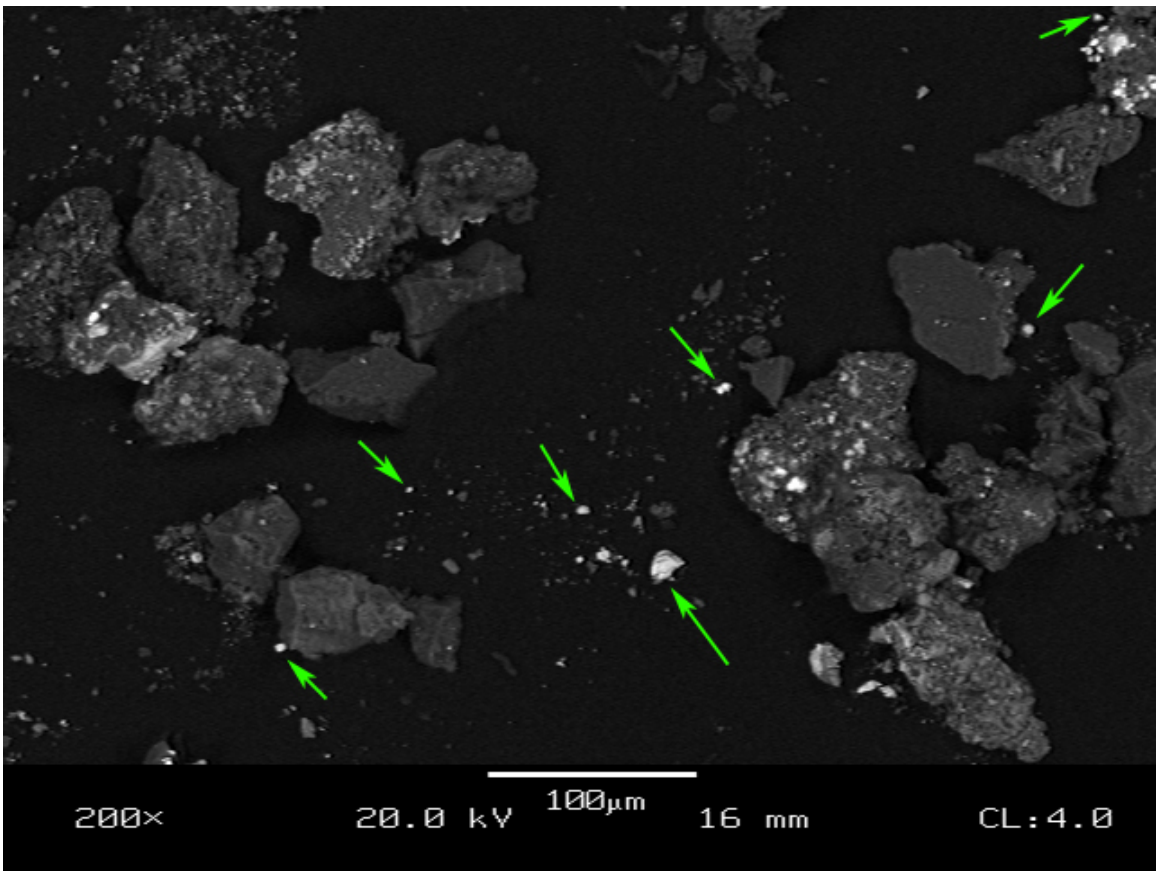

Figure 4.43: (a) Cambridge fragmentation experiment E121016A Mixture A fragments Between 75 μm and 150 μm sieve Sizes. Nickel and tungsten appear much brighter than aluminum in this backscattered electron microscope image. Tungsten and nickel particles that have separated from the larger particles are indicated with arrows.

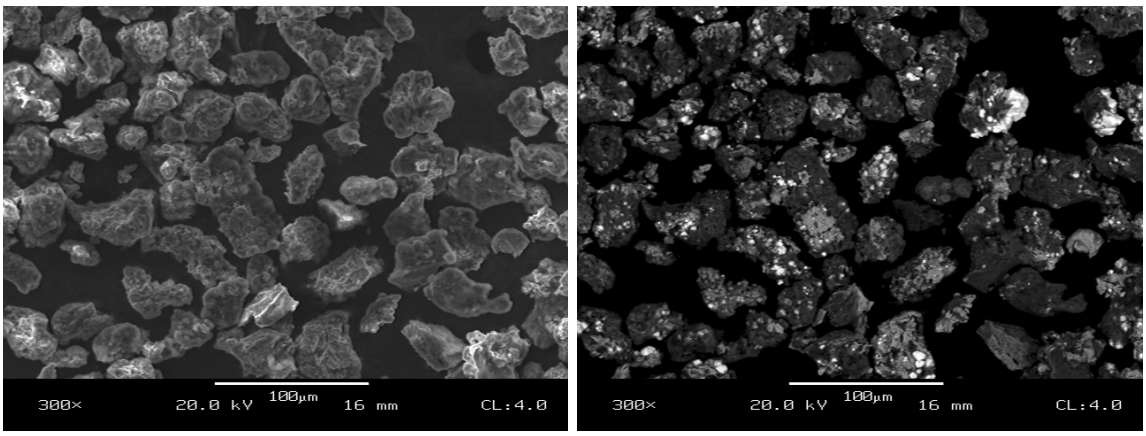

(a) (b)

Figure 4.44: Fracture surface of fragments from Cambridge experiment E121024A on Mixture B. These fragments sieved <38μm in size. (a) Secondary electron image of fragments. They have an irregular, blocky appearance. (b) The composite nature of the fragments is evident in the backscattered electron image. Many fragments retain a significant fraction of W, Ni, and/or Zr.

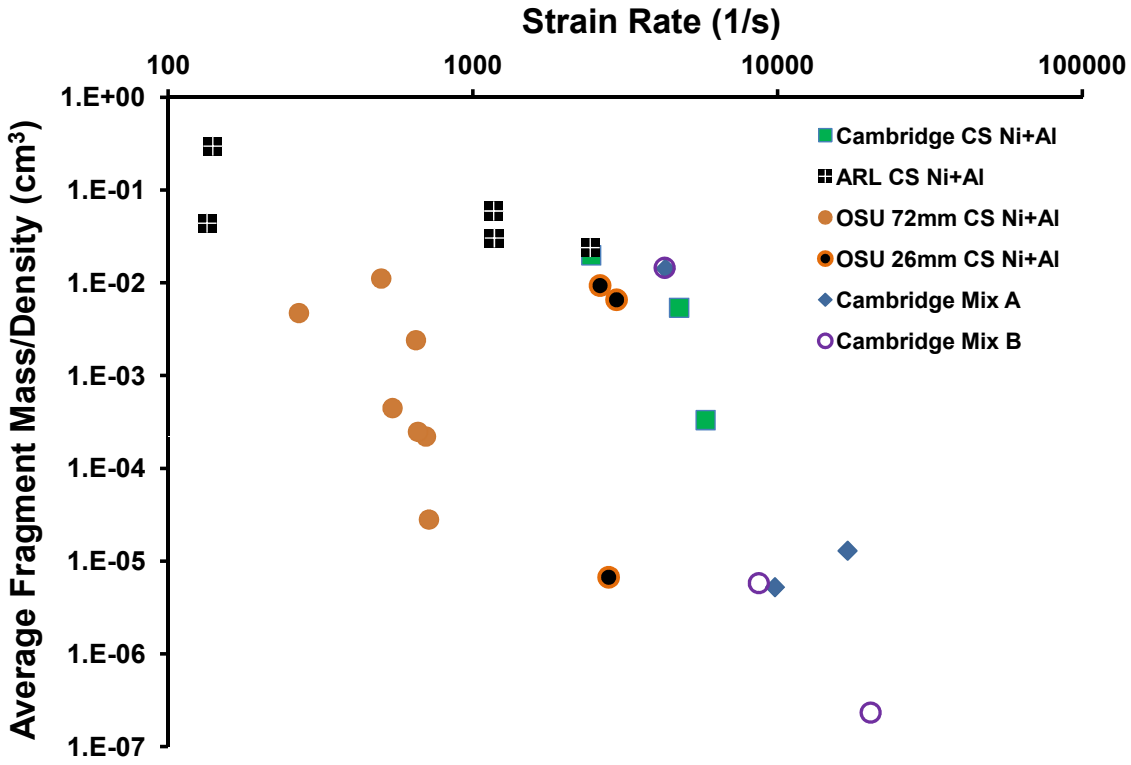

Figure 4.45: Average fragment size versus strain rate for all data. There is considerable scatter in the data due to different fracture mechanisms being operative, different sample sizes, and less than complete fragment collection.

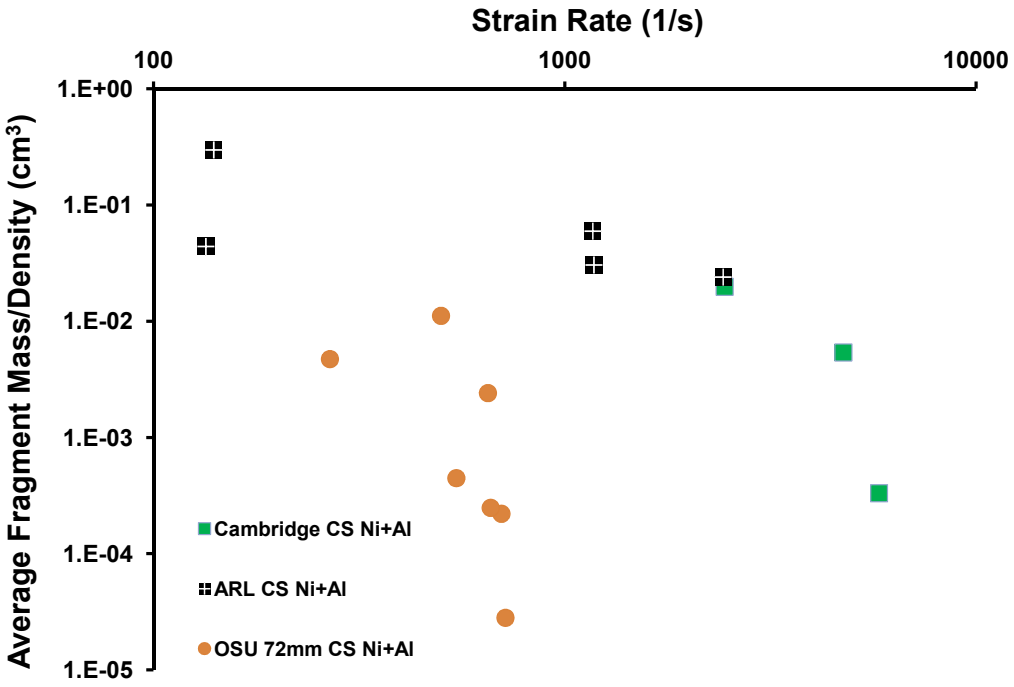

(a)

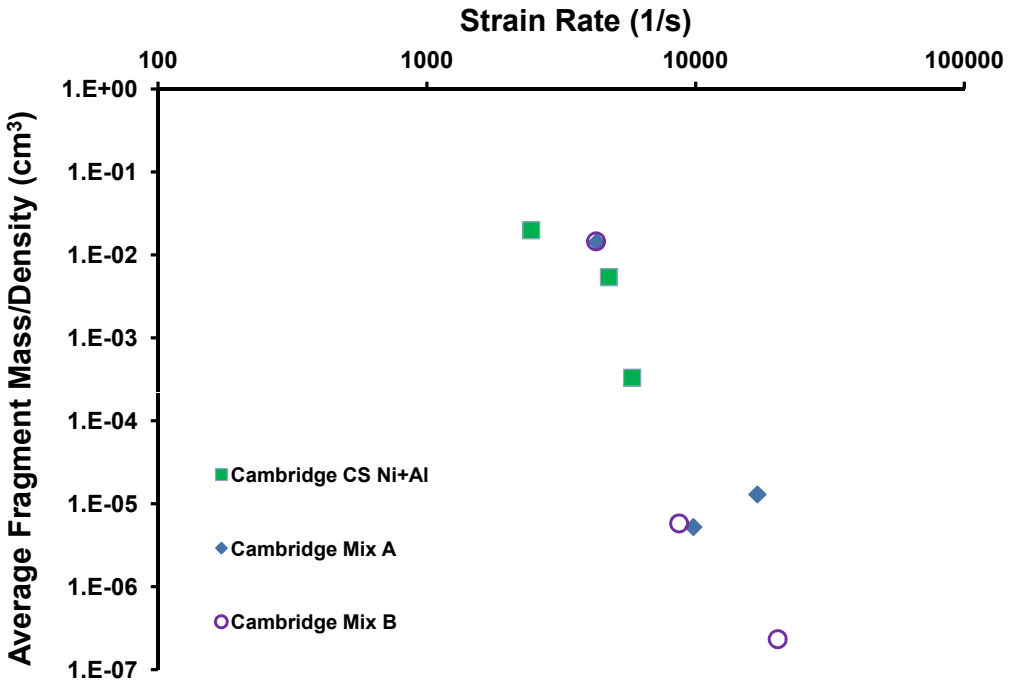

(b)

Figure 4.46: (a)Average fragment size versus strain rate for the OSU 72 mm OD, ARL, and Cambridge CS Ni+Al Data. Notice that the OSU 72 mm OD ring data doesn't follow the same trends as the ARL and Cambridge data sets. (b) Comparison of Cambridge CS Ni+Al, Mixture A, and Mixture B. Notice how consistent the results are.

from the ARL and Cambridge cold sprayed Ni+Al. This can be seen more clearly in Figure 4.46a which clearly shows the divergence of the OSU 72 mm ring data from the ARL data which was came from rings of the same size. This is a result of the tangential shear fracture mechanism that was discussed earlier. Presumably the shearing crack faces dislodge loosely attached particles. This would not occur in a tensile crack. This mechanism appears to be a very potent generator of small fragments and leads to smaller fragment sizes. In future analysis, the 72 mm OD data from OSU will be excluded. The Cambridge CS Ni+Al data, the ARL data, the OSU data from 26 mm outer diameter rings, and the Mixture A and Mixture B data will be shown to be in reasonable agreement.

The Cambridge data sets and the ARL data are quite consistent as seen in Figure 4.46a and Figure 4.46b. The Cambridge CS Ni+Al overlaps the ARL data set at the low end of its strain rate range and the Mix A and Mix B data sets at the other end of its strain rate range. This suggests that these data sets are all experiencing substantially similar fragmentation mechanisms and trends. This implies that it is not the different constituents that dominate the fragmentation behavior, but rather the interfaces within the materials.

It might have been expected that the higher strength of the cold sprayed material would have played a significant role; however, the consistency between the Cambridge CS Ni+Al, Mixture A, and Mixture B experimental data does not appear to bear this out. The cold sprayed Ni+Al is strong in compression because of its topology; the Nickel coatings are topologically connected and are the strongest part of the microstructure. The brittleness of the Ni coating and the high density of interfaces are less important in compression. The explosively compacted Mixture A and Mixture B samples have lower strength, but more ductility in compression. When subjected to tensile loads, the interfaces in the cold sprayed samples appear to fail readily. The poor adhesion between nickel and aluminum coated particles and the Ni/Al interfaces

seen in 4.3.1 lead to failures of these interfaces. The interfaces in the explosively compacted mixtures appear to be similarly brittle as both Ni and W particles were observed separated from the Al matrix (see for example Figure 4.43). The explosively compacted mixtures and the cold sprayed material have roughly comparable surface area per unit volume (compare Table 3.2 and Table 3.3); both have ample sites for failure.

4.5 Comparison of Structural Energetic Fragments with those of Common Structural Metals

One of the objectives of this work is to understand the fragmentation process in comparison with ordinary structural metals since structural energetic materials are seen as a replacement for more ordinary metal alloys in some applications. Perhaps the most widely circulated data set on structural metals was published by Grady and Benson [164]. They studied fragmentation in OFHC Cu and 1100-O Al rings 35 mm in diameter and 1 mm thick. These rings were subjected to expansion via a pulsed power supply which discharges into a coil which the sample ring is placed on. The resultant current which is induced in the ring repels the coil forcing it to expand. Expansion strain rates of 10^3 to 10^4 were observed.

Grady and Benson [164] collected and measured the total length of fragments which they recovered in a wax/Vaseline mixture. For the present work, this was not practical for most of the SEM rings as they were in too many pieces to easily measure. However, for experiments where a camera was utilized, the time at which failure took place was noted and the ring velocity profile was used to compute the average strain at the time of the failure. This measurement of failure strain is an average over incomplete fractures and is similar in principle to that used by Grady and Benson [164]. It should not be construed as the local strain of the material where failure occurs. The failure strain as it is used here and by Grady and Benson [164] reveals the effect of the increasing number of complete and partial failed regions with

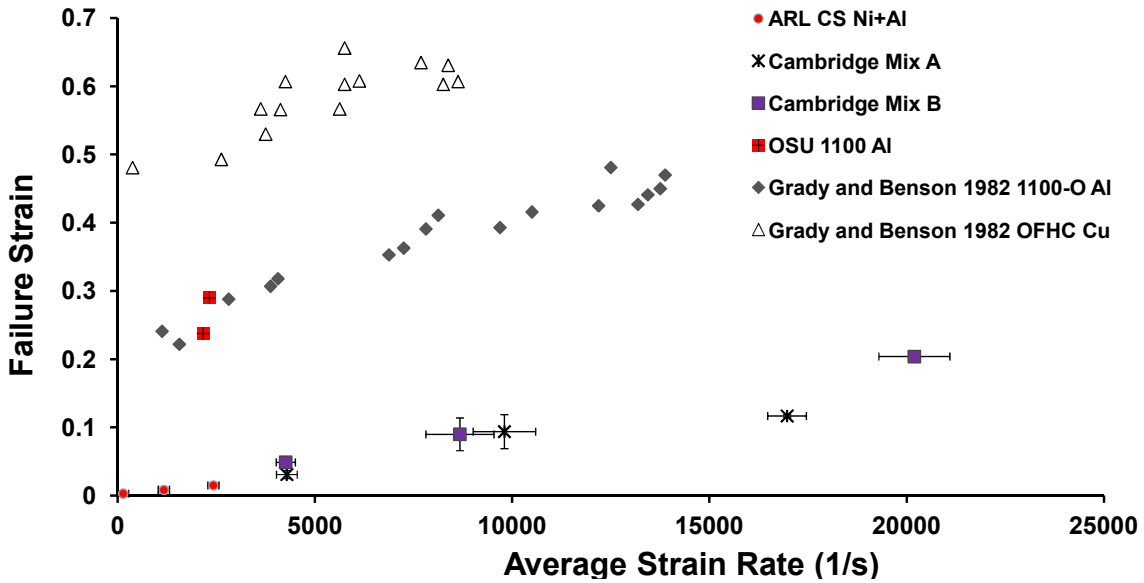

Figure 4.47: Comparison of failure strain in cold sprayed Ni+Al, Mixture A, and Mixture B rings with data published by Grady and Benson [164] on OFHC Cu and 1100-O Al. Note that Cu and Al rings had significantly higher average strains at failure.

strain rate. Failure strain values for the current SEM experiments along with Gray and Benson's [164] Al and Cu data are plotted in Figure 4.47. Note that the SEM rings have significantly lower failure strains than the ductile Cu and Al rings that Grady and Benson tested. This is indicative of the low ductility of these materials in tension.

Grady and Benson's data is also averaged and plotted versus strain rate in Figure 4.48. At low strain rates, the average fragment size versus strain rate is very comparable for Ni+Al, Mixture A, Mixture B and the Grady data on OFHC CU and 1100-Al. It is interesting to note that the OSU 1100 Al data and the Cambridge 6082 Al data both yielded fairly large fragment sizes, larger even than the Grady and Benson data. At higher strain rates, the average fragment sizes of the structural energetic materials sharply diverged from Cu and Al fragments. However, additional fragmentation mechanisms developed in the experiments on cold sprayed Ni+Al, Mixture A, and Mixture B due to the non-uniform loading in the Cambridge

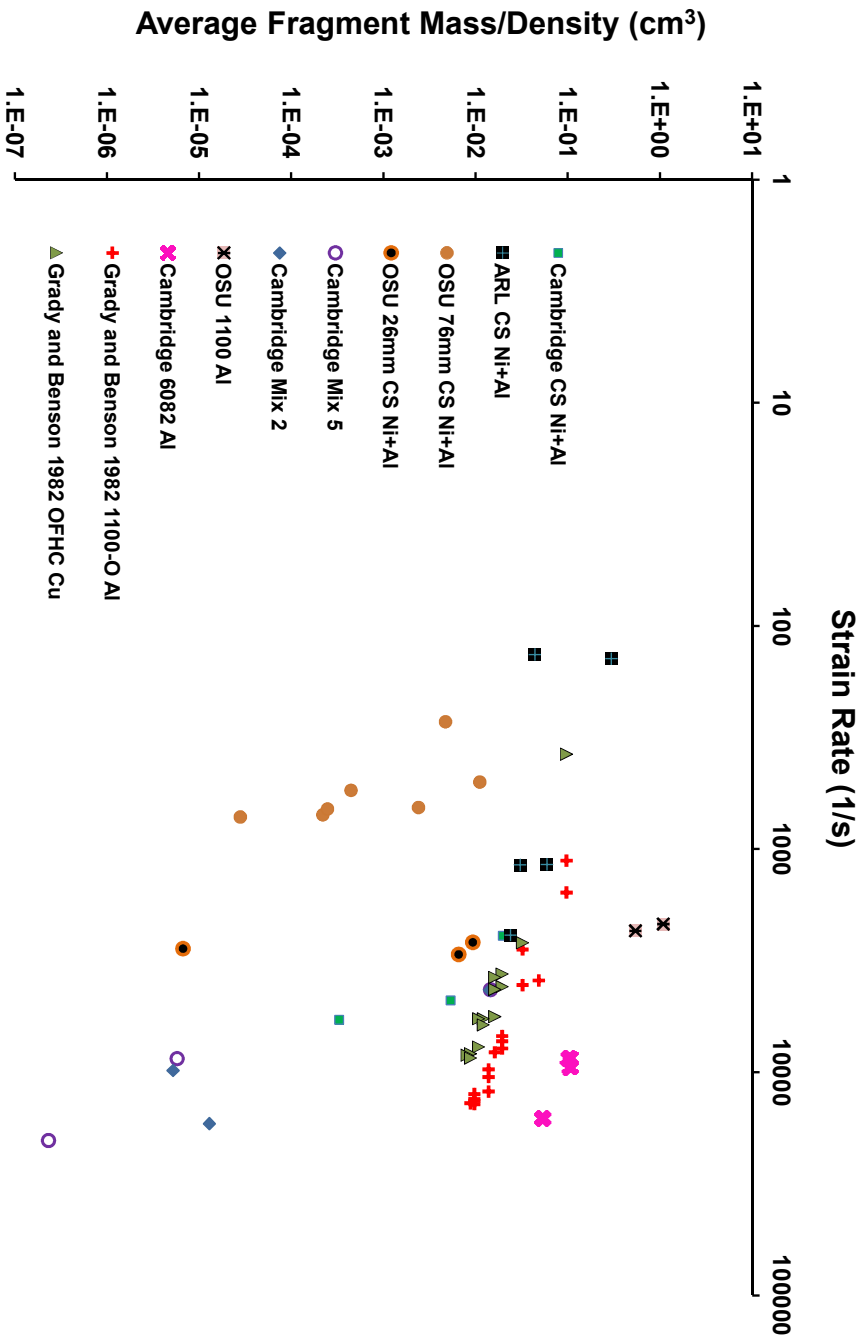

Figure 4.48: Comparison of average fragment sizes from cold sprayed Ni+Al, Mixture A, and Mixture B rings with data published by Grady and Benson [164] on OFHC Cu and 1100-O Al as well as 1100 Al rings tested by OSU and 6082 Al rings tested by Cambridge. The data is normalized by density.

experiments or the clamping effect seen in the exploding wire experiments. Due to the loading and the different sample size (32 mm diameter, 1 mm^2 cross section) the Grady and Benson data is not completely comparable. However, the OSU 1100 Al data and the Cambridge 6082 Al data was tested under the same conditions with the same experimental setups as the corresponding OSU cold sprayed Ni+Al data and the Cambridge cold sprayed Ni+Al data respectively. Hence, it is evident that the fragments produced by the structural energetic materials are far, far smaller than those produced by ordinary structural metals.

In Chapter 2, the fragmentation models of Mott [156] and Kipp and Grady [179] were discussed. It is of interest to compare these models to the fragment data on the structural energetic materials fabricated from cold sprayed Ni+Al, explosively compacted Mixture A, and explosively compacted Mixture B.

The fragment size estimate of Mott, $d = \frac{\kappa}{\dot{\epsilon}}\sqrt{\frac{2\sigma_y}{\rho\gamma}}$ (Eq. 2.21), and Kipp and Grady, $d = \left(\frac{\sqrt{12}K_f}{\rho c\dot{\epsilon}}\right)^R$ where $R = 2/3$ for uniaxial fragmentation and $R = 4/3$ for biaxial fragmentation (Eq. 2.22, 2.23) each scale with strain rate differently. A comparison of Grady and Benson's [164] data and the ARL, OSU 26 mm OD, and Cambridge data sets as well as Mott's [156] and Kipp and Grady's [179] models are shown in Figure 4.49. Mott's $d \propto \dot{\epsilon}^{-1}$ fragment scaling is a better fit to the Cu and Al data of Grady and Benson [164]. Excluding Grady and Benson's [164] data for the sake of clarity and replotting Mott's model to fit the structural energetic material data in Figure 4.50, it is evident that the Kipp-Grady model with $-\frac{2}{3}$ scaling is a better fit for the ARL CS Ni+Al data and the Cambridge CS Ni+Al, Mixture A, and Mixture B data at $\dot{\epsilon} \leq 4500$. Least squares fitting of an exponential function to the data yields an exponent of -0.6, close to the theoretical value of the Kipp-Grady model of $-\frac{2}{3}$; admittedly, there is enough scatter in the data that Mott's model may also be a reasonable fit. The agreement of the data when $\dot{\epsilon} \leq 4500$ and the Kipp and Grady [179] and Mott [156] models suggests that the fragmentation is well captured

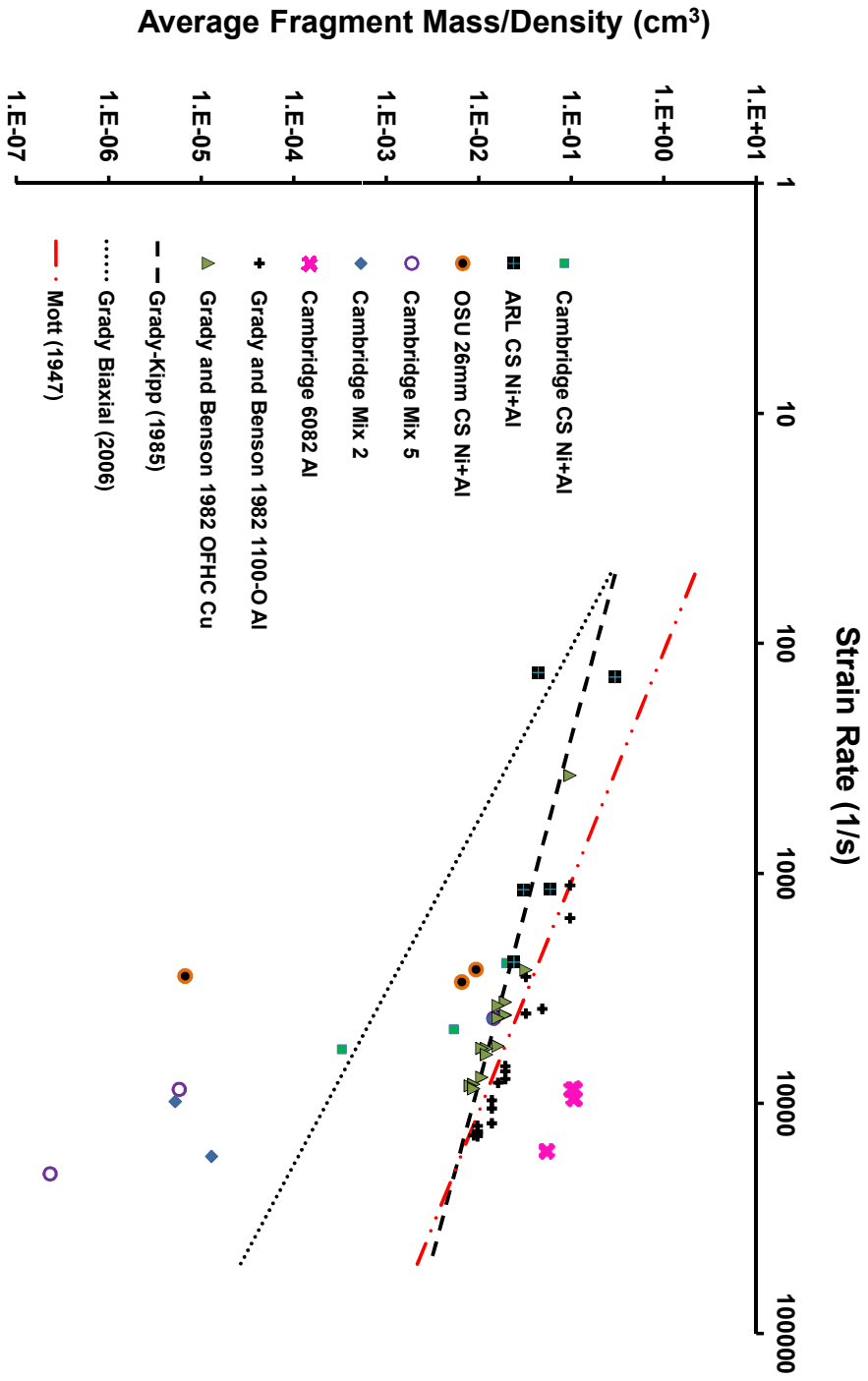

Figure 4.49: Comparison of Grady and Kipp and Mott fragmentation models with copper, aluminum, and reactive material fragment data. Mott's linear fragment scaling is a better fit to the Cu and Al data of Grady and Benson [164]. At $\dot{\epsilon} \geq 4500$, the OSU 26 mm OD and the Cambridge data sets change with strain rate at a much greater rate than predicted by even the Grady Biaxial $-\frac{4}{3}$ scaling.

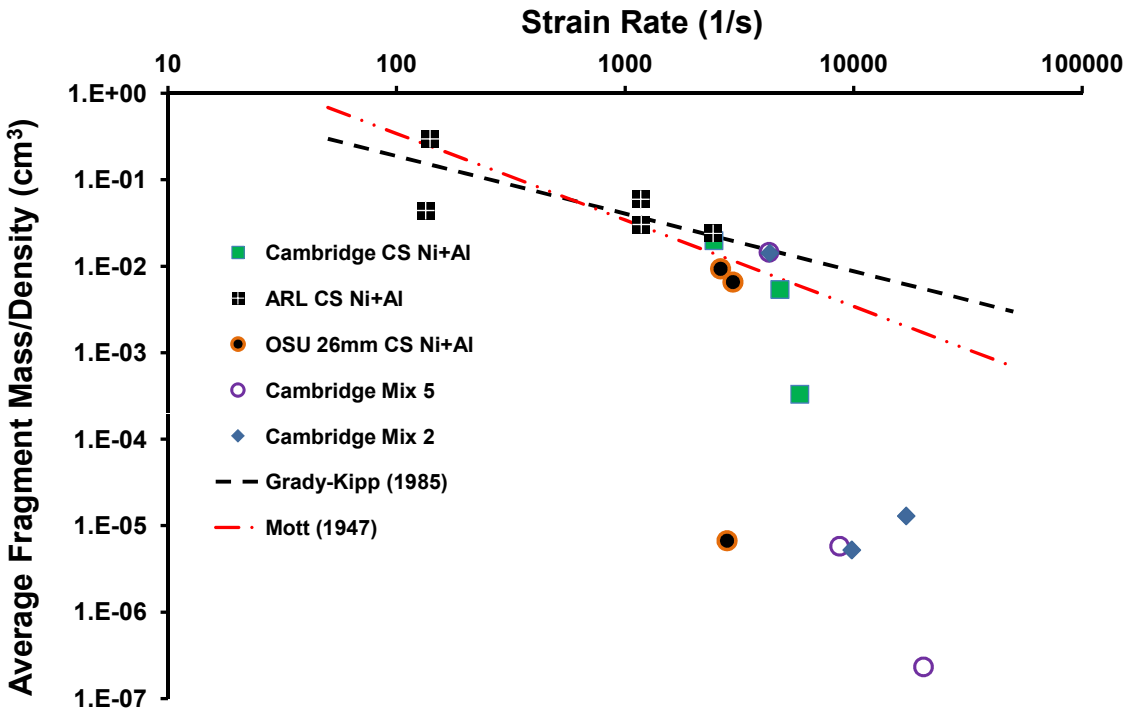

Figure 4.50: Comparison of Kipp and Grady and fragmentation models with reactive material fragment data. The Kipp-Grady model with $-\frac{2}{3}$ scaling is a reasonable fit for the ARL CS Ni+Al and Cambridge CS Ni+Al at $\dot{\epsilon} \leq 4500$. None of the models fit Mixture A and Mixture B fragment data.

where the mass of fragments produced by crack branching is relatively insignificant to the mass of fragments produced by ordinary Mott fragmentation.

The lack of model agreement with the Cambridge data sets at $\dot{\epsilon} \geq 4500$ suggests that these models do not contain any insight into fragmentation problems where fragment formation due to crack branching and intersection is significant. Horizontal fracture or shear fracture processes by themselves would only alter the average fragment size by a factor of two because these processes bisect the fragments that are produced. Crack branching provides a mechanism whereby fragment numbers increase by orders of magnitude as has been observed in the present work which leads to the lack of model agreement. This is because these materials lack significant capability for plastic deformation, thus, their primary mode of energy dissipation must be cracking. The energy that needs to be dissipated is the kinetic energy of the

ring, which is proportional to the velocity squared. Thus fragment number must also depend on kinetic energy at high strain rates.

A simple adjustment may be made to the Kipp-Grady model [179] to account for the kinetic energy dissipation due to crack network growth in these materials. Kinetic energy is defined as

$$KE = \frac{1}{2}mv^2 \tag{4.2}$$

where m is mass and v is velocity. Strain rate may be defined as

$$\dot{\epsilon} = \frac{v}{r} \tag{4.3}$$

where r is radius. Therefore,

$$KE = \frac{1}{2}m(\dot{\epsilon}r)^2. \tag{4.4}$$

It may reasonably be concluded then that fragment numbers due to growth of crack networks must increase with the square of strain rate, or conversely, that fragment size must decrease with the inverse of strain rate squared. This mechanism is coupled with the Mott fragmentation mechanism because macroscopic fractures will yield side branches which will grow and branch. Therefore at high strain rates

$$d \propto \dot{\epsilon}^{-\frac{2}{3}}\dot{\epsilon}^{-2} \tag{4.5}$$

or

$$d \propto \dot{\epsilon}^{-\frac{8}{3}}. \tag{4.6}$$

Writing out the kinetic energy modified Kipp-Grady model

$$d = C\left(\frac{\sqrt{12}K_f}{\rho c\dot{\epsilon}}\right)^{8/3} \tag{4.7}$$

where the terms all have the same meaning as previously described, except C which is a scaling constant.

Based on the Figure 4.50, the Kipp-Grady model with $-\frac{2}{3}$ fit the ARL data at low strain rates reasonably well. Therefore, it is presumed that there is some threshold level below which cracks do not branch or crack branching is insignificant. Therefore the following form of the fragment size estimate is introduced

$$d = \Gamma \left(\frac{\sqrt{12} K_f}{\rho c \dot{\epsilon}} \right)^{2/3} + (1 - \Gamma) C \left(\frac{\sqrt{12} K_f}{\rho c \dot{\epsilon}} \right)^{8/3} \tag{4.8}$$

with a normalization factor, Γ, which mediates the transition from Mott dominated fragmentation to fragmentation dominated by the growth of networks of cracks. The growth of the crack population at any one time depends on the current crack population, and it is sensible to conclude that the number density of cracks grows exponentially. It is convenient to consider that the normalization term decays exponentially from one to zero to capture the precipitous change from Mott fragmentation behavior to crack branch dominated behavior. Γ is defined as

$$\Gamma = exp \left(-\frac{\dot{\epsilon}}{\dot{\epsilon}_{ref}} \right) \tag{4.9}$$

where $\dot{\epsilon} = ln(2)\dot{\epsilon}_{ref}$ is the strain rate at which the fragment average size is equally influenced by Mott fragmentation and crack network driven fragmentation. In practice, this term behaves essentially as a fitting parameter. This semi-empirical adjustment extends the Kipp-Grady fragmentation model to work reasonably well on the structural energetic materials considered in this thesis as shown in Figure 4.51. It has some significant limitations, including its lack of ability to predict mean fragment size based on microstructural parameters. These are bound up in K_f, the fracture toughness, and possibly the reference strain rate $\dot{\epsilon}_{ref}$. However, this modified form of the Kipp-Grady model is convenient to use.

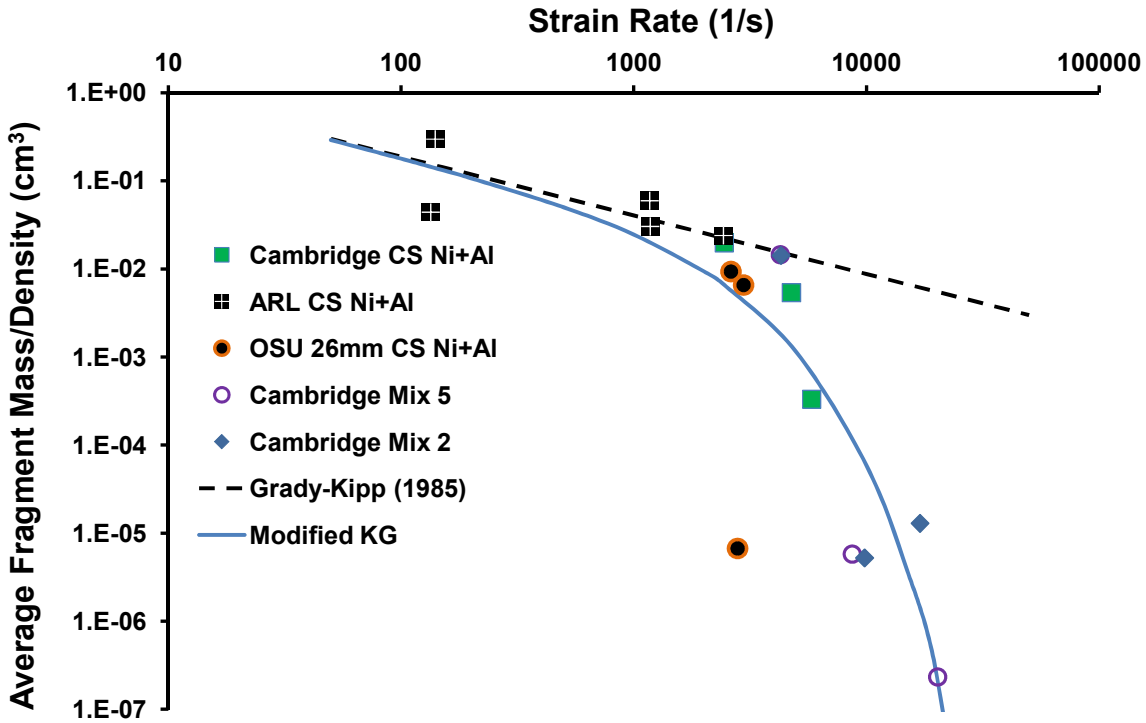

Figure 4.51: Comparison of Kipp and Grady and Kipp and Grady model modified to account for growth in crack population and its influence on the mean fragment size. The Kipp-Grady model with $-\frac{2}{3}$ scaling is a reasonable fit for the ARL CS Ni+Al and Cambridge CS Ni+Al at $\dot{\epsilon} \leq 4500$. None of the models fit Mixture A and Mixture B fragment data.

4.6 Summary of the Fragmentation Results

The fragmentation data reveals a few important trends and features of interest:

- Explosively compacted Mixture A, explosively compacted Mixture B, ARL CS Ni+Al, and the Cambridge CS Ni+Al data sets yield reasonably comparable results, which show that these structural energetic materials produce much smaller fragments than ordinary metals such as aluminum or copper at high strain rates. The ARL cased charge fragmentation experiment demonstrated that the small fragment sizes are not solely an artifact of the ring geometry (the geometry tested at OSU and Cambridge) but are typical of these materials.

- There is no evidence of a significant effect from topology of the CS Ni+Al versus the topology of Mixture A and Mixture B. Under compression, the Ni/Ni and Ni/Al interfaces are less likely to open up. In tension, these interfaces fail and the Ni phase does not behave as a continuous matrix. The nickel coating on each particle does not adhere perfectly to other nickel coated particles and some original particle boundaries are retained to serve as failure points and crack paths.

- Both the cold sprayed Ni+Al and the explosively compacted systems show evidence of interface failure, though in the case of Mixture A and Mixture B, this is much less certain. This suggests that the interface density is an important parameter in the fragmentation of composite reactive material systems.

- Existing fragmentation models do not capture the fragmentation behavior of the tested structural energetic materials with increasing strain rate because of crack branching behavior. The composite nature and large interface densities of these materials create a low toughness material with a large density of potential failure sites leading to many fragments for each macroscopic failure point. This

leads to large numbers of small fragments. This trend couples with the different failure mechanisms noted (horizontal or shear fractures) to create more rapid growth in fragment populations with strain rate than would be expected in homogeneous materials.

- A straightforward modification of the Kipp-Grady [179] fragmentation model to account for crack network dominated fragmentation can fit the existing mean fragment size data for the ARL CS Ni+Al, Cambridge CS Ni+Al, Mixture A, and Mixture B fragmentation data.

CHAPTER V

REACTION BEHAVIOR OF STRUCTURAL ENERGETIC MATERIALS

The value of structural energetic materials lies in their ability to replace inert structural components with components that are capable of releasing energy. When used as a casing, a structural energetic material will fragment into many pieces. Based on the size of the fragments, a structural energetic material may release energy either through (a) intermetallic forming reaction/combustion where small fragments which mix with explosive product gases and/or ambient atmosphere and react or (b) impact induced reaction when a fragment collides with a surface and the impact event initiates reaction. These processes are illustrated schematically in Figure 5.1. In this chapter, the intermetallic forming reaction/combustion and impact induced reaction behavior of structural energetic material fragments will be explored in detail.

5.1 Combustion of Composite Fragments

As indicated in Chapter 1, reaction of SEM fragments is a significant potential source of energy release. Reaction and/or combustion of fragments was observed by Homan et al. [23], Homan et al. [24], and Densmore et al. [135]. Based on what is now known about fragment sizes and composition, the combustion of fragments can be investigated with some confidence.

5.1.1 Combustion of Structural Energetic Material Fragments

In Chapter 2, a basic picture of Al combustion was established and augmented by limited work on Ni coated Al and Al+Ti. A few of the likely similarities and differences in the combustion behavior of composite fragments formed by the fragmentation of

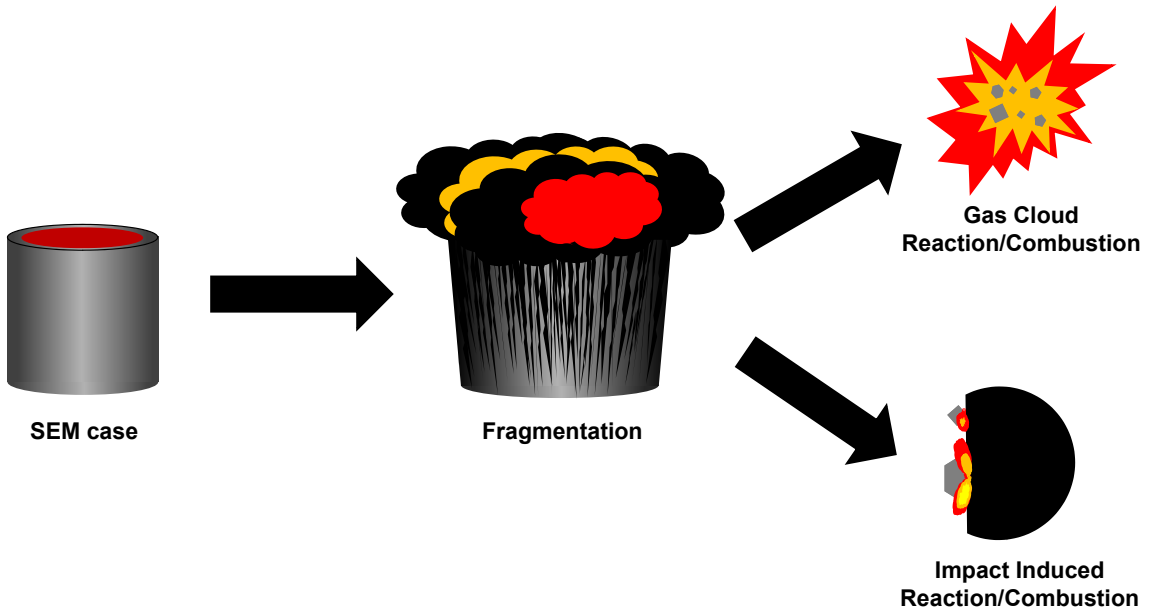

Figure 5.1: Energy release mechanisms of structural energetic materials. Fragments from a structural energetic material may undergo intermetallic reaction or combustion when they mix with hot gases from an explosive if they are small enough or they may undergo impact induced reactions.

various SEMs studied in this work (as seen in Chapter 4) can now be addressed.

In Al combustion, the oxide layer is the limiting obstacle in the combustion process. Al combustion cannot take place until the oxide shell has melted, volatilized, or fractured [140, 142]. Given the high volatilization temperature of alumina, 4000 K for the stoichiometric adiabatic combustion temperature [229], the destruction of the oxide coating, rather than melting or volatilization, is what precedes combustion [140, 142]. This destruction can apparently take place via thermal mismatch causing fracture in the alumina layer upon rapid heating of the particle or some external mechanical loading [140,142]. All of the structural energetic material fragments observed in this work have substantially disturbed oxide layers due to deformation and fracture processes. As seen in Figure 4.35a, 4.35b and Figure 4.43, fragments experience extensive, local deformation along fracture surfaces. This is expected to aid the combustion process significantly by exposing unoxidized surfaces for combustion.

The aluminum on the surface of the structural energetic particles is expected to

be in a highly reactive condition. Cold sprayed fragments show evidence of extensive cracking of the Ni coating and in many cases the coating is removed in large patches, exposing Al without an oxide layer. Based on the results of Yagodnikov and Voronetskii [147], Mukasyan et al. [149], and Shafirovich et al. [150], the latency period that is required for a coefficient of thermal expansion mismatch to lead to stress sufficient to break through the Ni coating would not be required in the case of SEMs studied in this work. The fragments are expected to be in a very reactive state, having fractured oxide layers and exposed unreacted surfaces, in addition to considerable aluminum being exposed on surfaces of fragments from cold sprayed Ni+Al. In the case of the explosively compacted Mixture A and Mixture B fragments, the Ni, W, and Zr particle boundaries are well defined, but no Al particle boundaries remain from the original powder. Thus, when the fragment is formed, the aluminum surface is formed without an intact oxide layer. The unoxidized Al surfaces on the structural energetic material fragments created by the fragmentation process are expected to combust readily because no energy would be consumed in breaking through an oxide layer or a coating. Yagodnikov and Voronetskii found combustion far more rapid for Ni coated Al powders once the Ni coating was removed by thermal expansion to expose bare, unoxidized nickel [147].

The structural energetic material fragments also have non-aluminum components which will participate in various ways in the reaction and combustion processes. Cold sprayed Ni+Al, EC Mixture A, and EC Mixture B fragments have exposed Ni components. Nickel is likely to react to form an intermetallic at the melting point of Al as seen by Mukasyan et al. [149] and Shafirovich et al. [150] in their studies of Ni coated Al particles. Nickel has also been observed to combust after aluminum is consumed [150]. Nickel is not as flammable as Aluminum; its oxide has a slightly lower melting point, but the vapor pressure of Ni is much lower than Al [150]. There is evidence that nickel particles can become separated from the aluminum matrix in

Mixture A and Mixture B fragments as seen in Figure 4.43. By themselves, nickel articles have not been found to be very combustible; in combustion tests on 6 μm particles, Ni did not ignite at any tested concentration [143].

Tungsten, present in explosively compacted Mixture A and Mixture B, is a refractory metal with high melting point and an extremely low vapor pressure. It is not likely to participate extensively in the combustion process, though it might react to form an intermetallic compound. When pure aluminum combusts, aluminum oxide often condenses on the surrounding Al, forming an unreactive cap that inhibits combustion [140]. Tungsten particles embedded in the surface of fragments are not likely to combust and may act as a cap, inhibiting combustion behavior and radiating heat away from the combusting particle, and it has been shown in tests by Cashdollar and Zlochower [143] that tungsten powder approximately 10 μm in size is unignitable.

Explosively compacted Mixture B also contains zirconium, which is very prone to combust when finely divided; When its oxide is disturbed by the violent fragmentation process it is expected to combust readily whether it is by itself or embedded in aluminum.

Frost et al. [145] studied the optimal size of aluminum particles in various nitromethane charges. One result of Frost et al.'s [145] work on mixtures of Al and sensitized nitromethane was that the optimal size of Al particles for charge detonation was 56 μm. This result is apparently inconsistent with the D^2 combustion time law. The optimal size for aluminum combustion should be the smallest size attainable, all things being equal. Frost et al. [145] does not explain this anomaly, but similar behavior was observed by Eapen et al. [230] who studied flake Al particles. Eapen et al. [230] compared the combustion of spherical and flake Ni with equivalent diameters calculated using gas adsorption behavior. The larger surface area of the flake Al should have provided better combustion behavior, but experimental data showed that spherical Al consistently outperformed it [230]. This effect was attributed to

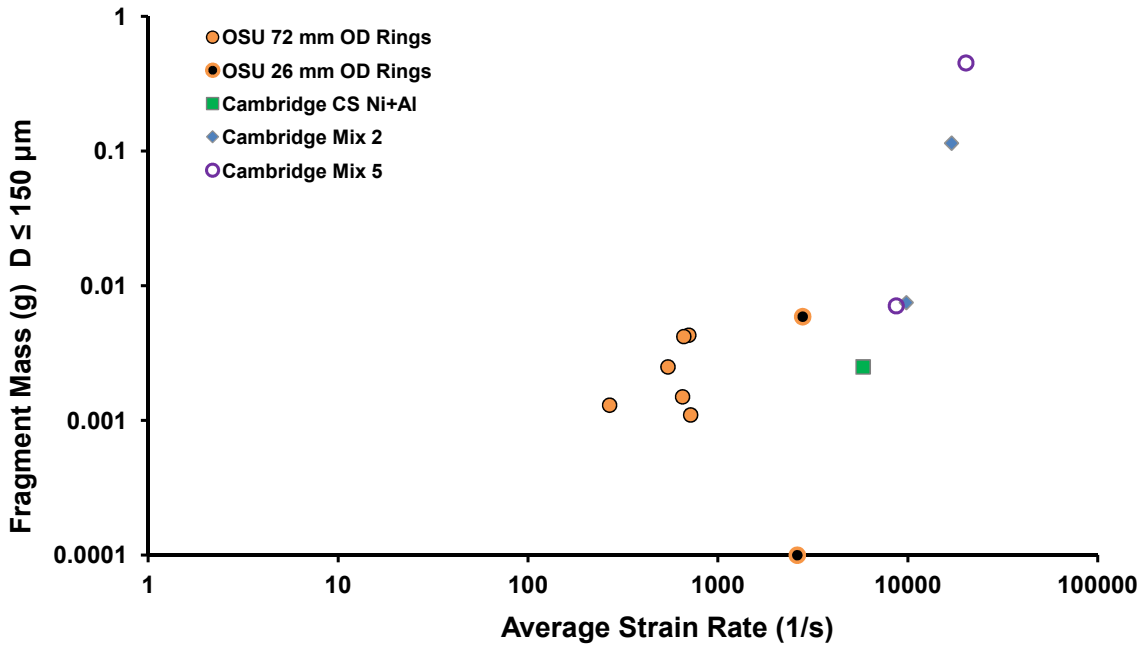

Figure 5.2: Fragment mass which sieved to D≤150μm for cold sprayed Ni+Al, Mixture A, and Mixture B.

agglomeration of the flakes. Mukayasyan et al. [149] and Breiter et al. [146] found that a Ni coating on Al particles inhibited agglomeration. It is expected that in the case of the cold sprayed Ni+Al fragments, the retention of some of the Ni coating will tend to reduce agglomeration and yield better combustion behavior as compared with pure Al particles. This would be true to a lesser extent for Mixture A and Mixture B fragments which appear to have retained less of the non-Al metallic phases on their surface than the cold sprayed Ni+Al fragments.

It is evident from Figure 5.2, that at low strain rates the reactive materials produce insignificant mass below 150 μm in size. Above strain rates of 10^3, the amount of mass below 150 μm produced by fragmentation increases rapidly. Above strain rates of 10^4, quantities from 0.1g to 0.5g of fragments smaller than 150 μm are available from the explosively compacted Mixture A and B rings. The original mass of these rings was ≈4.8g. This represents up to 10% of initial sample mass converted into fragments of 150 μm or less. If these trends remain consistent and are scalable, an

appreciable quantity of energy can be liberated from combustion of fragments. In this case, the charge size of Primasheet used in highest strain rate experiments on Mixture A and Mixture B is 4 grams, from Table 4.1. The Primasheet is 65% PETN, thus 2.6 grams of PETN were used. According to Table 2.1, PETN has a detonation enthalpy of 6.23 KJ/g or in this case a total detonation enthalpy of 16.2 KJ. The mass fraction of Al in Mixture B is about 0.20, yielding about 0.1 grams of Al. The combustion of this Al would yield 31.0 KJ/g of energy or a total energy of 3.1 KJ which is 20% of the total detonation enthalpy. It is readily apparent how significant the combustion of small fragments can be in the total energy output of an explosive device. Zhang and Wilson [26], studied reactive casings in a closed chamber with two different explosive fills. They measured the quasistatic overpressure which is related to the total energy output of the explosive and casing combustion/reaction. It is interesting to note that Zhang and Wilson [26] indicate for a reactive casing with a TBX explosive fill and a charge mass ratio of 0.75 that about 20% more quasistatic pressure is expected when compared with a bare charge of the same total mass [26]. The growth in potential combustion enthalpy with increasing fragment mass of size $d \leq 150\mu m$ is shown in Figure 5.3a which shows the percentage of ring mass converted into fragments less than 150 μm in size and Figure 5.3b which shows the growth in the combustion enthalpy of this fragment population

One topic that has not been addressed in the existing literature is the presence of phosphorous in the Nickel coating and its effects on combustion behavior; none of the cited papers reference a phosphorous content [146, 147, 150, 230]. It was noted in Chapter 3, that up to 0.5 atomic % of phosphorous had been detected in the Ni coated Al powder used in this work, probably as the result of the use of a sodium hyposphite reducing agent during the coating process [207]. As evident in the Ni-P phase diagram, seen in Figure 3.13, the addition of phosphorous in solution significantly reduces the melting point of Ni. It is also known that the addition of phosphorous increases

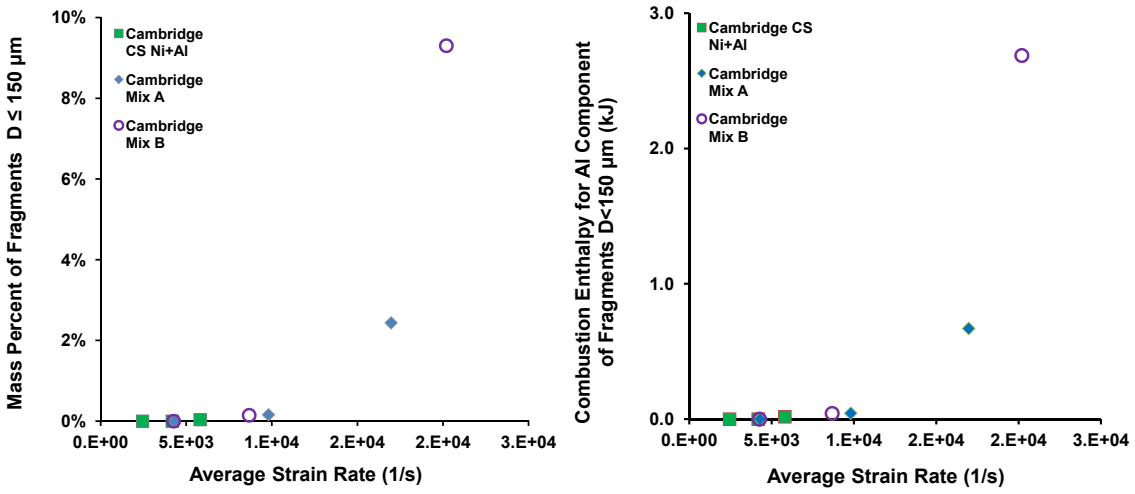

(a) (b)

Figure 5.3: Combustible fragment mass and enthalpy of structural energetic materials.(a) The percentage of the original sample mass which is potentially combustible, fragment sizes of $D \leq 150\mu m$, produced by Cambridge experiments on CS Ni+Al, Mixture A, and Mixture B fragments (b) The calculated combustion enthalpy of aluminum component of the fragments in (a).

the strength of Ni due to solid solution strengthening, but makes it very brittle [207]. Significant reductions in the melting point may tend to increase particle agglomeration based on the results of Breiter et al. [146], but the enhanced brittleness may lead to earlier failure of the Ni coating and result in better ignition behavior. It is not known at this time which of these effects is most significant, and it remains a fruitful area for future research.

5.1.2 Plastic Deformation Effects on the Thermal Behavior of Fragments

As discussed in Chapter 2, shock compression of materials leads to the creation of an extensive network of dislocations as well as significant mixing of powder constituents. This behavior was inferred by Hammetter et al. [108] and Thadhani et al. [109] in shocked powder mixtures based on differential thermal analysis data that showed the initiation of an intermetallic formation reaction and the release of energy below the melting point of Al. In comparison, unshocked material reacted at the melting point of Al as illustrated in differential thermal analysis (DTA) shown in Figure 2.6.

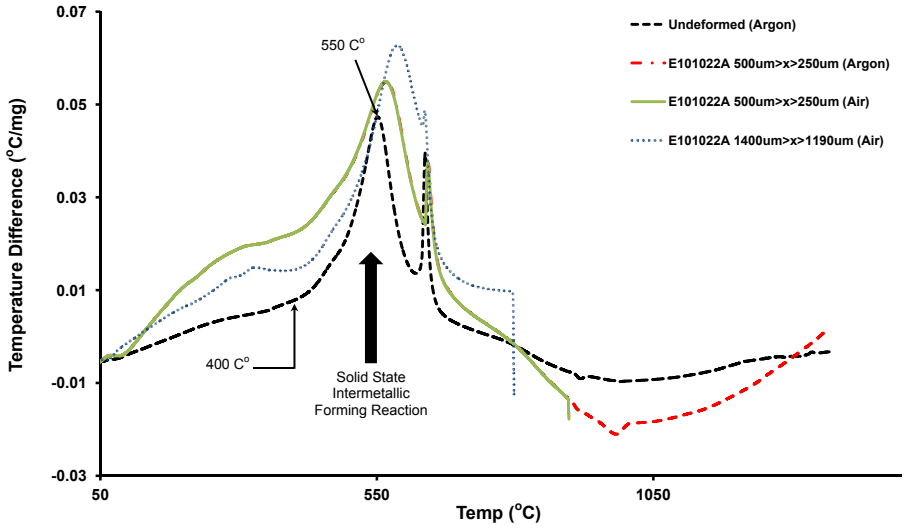

Figure 5.4: Differential thermal analysis data of cold sprayed nickel+aluminum fragments. Notice the solid state reactions that take place in all of the samples both undeformed and fragmented. The presence of oxygen has little impact on the DTA trace.

Undeformed and fragmented samples of cold sprayed Ni+Al from the Cambridge tests, Mixture A, and Mixture B were subjected to differential thermal analysis in argon and air at ambient pressure. A heating rate of 10 Kelvin per minute was used for all samples. Some salient features of each set are noted and discussed.

In the case of cold sprayed Ni+Al differential thermal analysis traces shown in Figure 5.4, similar pre-Al melt reaction exotherms were observed in undisturbed material as well as fragments. This suggests that the fragmentation process does not significantly alter the material; which is not unexpected. It was noted previously that there was very little macroscale plasticity, only localized deformation and failure on the fracture surfaces. Cold sprayed materials are formed by injecting the desired powder into a high pressure gas stream which passes through a converging diverging nozzle. The resulting high velocity gas stream carries the particles which are sprayed against a substrate where many adhere and the material is built up. Each high velocity powder particle impact is essentially its own shock loading event. The unconfined particles are free to deform extensively, the shock compacted powders

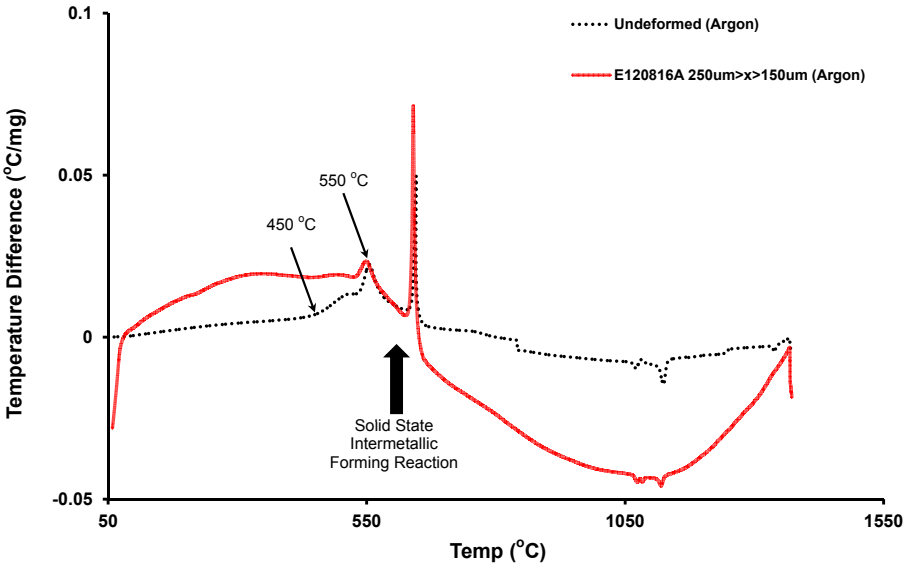

Figure 5.5: Differential thermal analysis data of explosively compacted Mixture A fragments. Notice the solid state reactions that take place in both the virgin compacted material and the fragmented material. The fragmentation process does not significantly alter the pre-melt exotherm. The presence of oxygen has little impact on the DTA trace.

studied by Hammetter [108] also deformed extensively, which leads to the same solid state reaction behavior. Such behavior stems from the same fine scale mixing and high dislocation densities; however, the fragmentation process does not contribute to mixing or plastic deformation significantly.

There is very little difference in the character of the DTA traces for unfragmented Mixture A and small Mixture A fragments which sieved between 150 μm and 250 μm in size as is evident in Figure 5.5. The size and shape of the exotherm below the melting point of aluminum is small relative to the main peak that is observed near the melting point. The features in both DTA traces are similar in shape and magnitude. This suggests that shock pressures were low enough during consolidation that very little intimate mixing took place between the Al, Ni, and W in Mixture A. Again, no significant effect from fragmentation is observed.

Mixture B DTA traces, shown in Figure 5.6, also demonstrate no significant difference between the undeformed sample and a fragmented sample. A highly exothermic

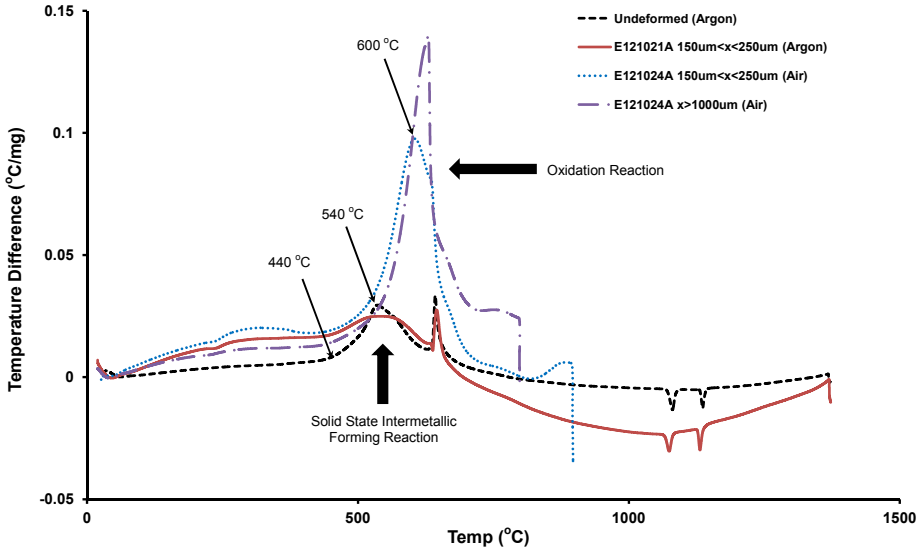

Figure 5.6: Differential thermal analysis data of explosively compacted Mixture B fragments. Notice the solid state reactions that take place in both the virgin compacted material and the different size fragments. The fragmentation process does not significantly alter the pre-melt exotherm. However, the presence of oxygen makes a significant difference. The exotherm in air is much larger than either of the main exotherms in argon.

reaction took place when these samples were tested in air. The shape of the curve of the traces tested in air below 540 ^{o}C is very similar to those tested in argon, implying that similar solid state reactions took place in both cases. The fragmented and virgin samples tested in air yielded similar results as shown in Figure 5.6, suggesting the fragmentation process has little bearing on the amount of deformation and constituent mixing that takes place in these materials, all of which takes place during fabrication. The peak in the fragmented sample is slightly lower; this might be a consequence of particles of W, Ni, and Zr being removed during the fragmentation process, illustrated for samples of Mixture A in Figure 4.43.

X-ray diffraction analysis (XRD) was conducted on Mixture B DTA samples tested in argon and air. The samples were mounted on the silicon wafer oriented to provide no measurable background in a thin layer of petroleum jelly, which was also found to provide negligible background. The XRD data was collected on a Panalytic X'Pert

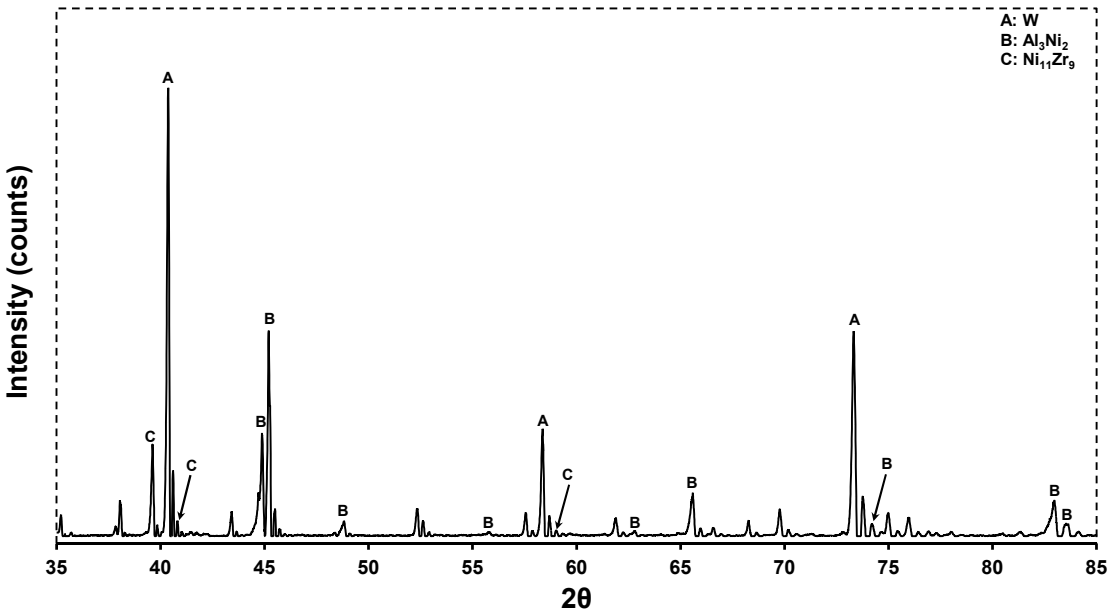

Figure 5.7: X-ray diffraction data for DTA samples of Mixture B tested in argon. The sample size was small and many different compounds were possible, therefore some peaks could not be identified. Those that could be identified with some confidence are indicated.

Pro MPD machine using a copper K-α_1 radiation source and a solid state scanning X'Celerator detector. Analysis was conducted using MDI Jade XRD analysis software. The XRD trace in argon is shown in Figure 5.7. Only three phases could be identified with confidence, though many peaks remained unidentified or could not be positively identified. Of the phases that could be identified with confidence, elemental tungsten was one. It did not appear to participate in any reaction and only functioned as a densifing agent. Al_3Ni_2 was identified as well as $Ni_{11}Zr_9$. No other reaction product phases could be confidently identified.

XRD results for the Mixture B sample tested in air are shown in Figure 5.8. Like the XRD trace for Mixture B in argon, this trace had many peaks that could not be identified. Those that could be identified were elemental tungsten, several binary Al_xNi_y intermetallics (x,y $\approx$ 1 in most cases), a ternary intermetallic with zirconium, and oxides of nickel and aluminum. Again tungsten evidently did not participate in any reactions, which implies that Mixture A and cold sprayed Ni+Al

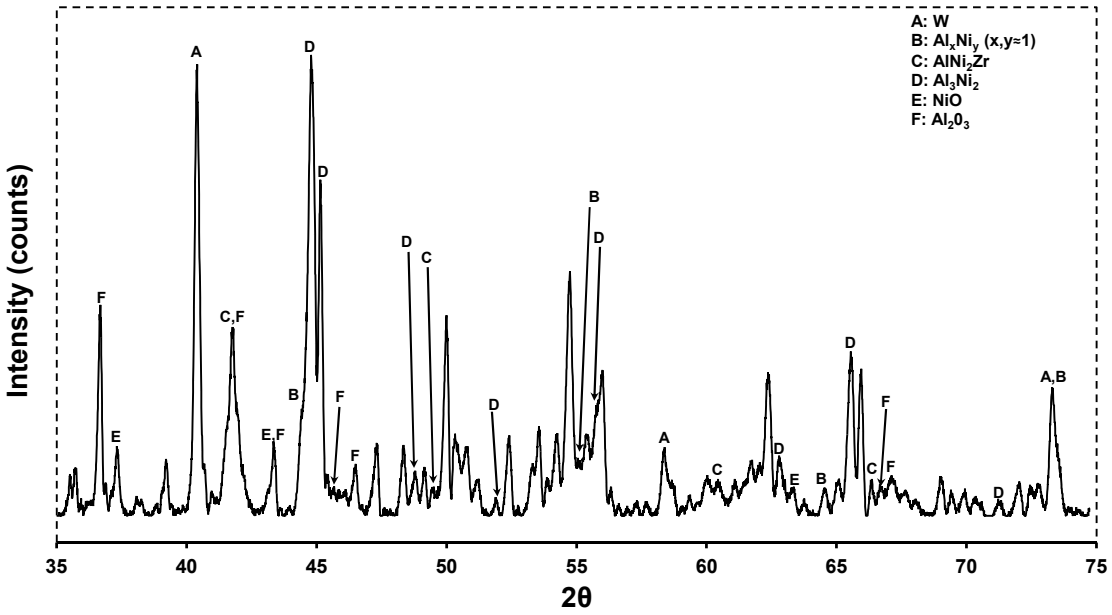

Figure 5.8: X-ray diffraction data for DTA samples of Mixture B in Air. The sample size was small and many different compounds were possible. Some peaks could not be identified.

would form similar phases, the familiar Al_xNi_y phases that occurred in both Mixture B samples. It is interesting to note that no zirconium oxides were detected, only a ternary intermetallic phase. The most significant difference between Mixture A and Mixture B is the presence of zirconium. DTA of CS Ni+Al and Mixture A showed no real sensitivity to the tested atmosphere and thus it is unlikely that a significant quantity of aluminum or nickel oxides were produced. Mixture B showed the most sensitivity to atmosphere and it is reasonable to conclude that the presence of zirconium is the reason. The reaction of zirconium, either the formation of an undetected oxide or the detected ternary intermetallic phase, provided the energy necessary to cause aluminum and nickel oxides to form.

5.1.3 Temperature of Cold Sprayed Ni+Al Fragments After Formation

As indicated in Chapter 2, shock compaction of porous materials can lead to significant changes in temperature. The structural energetic materials considered in

this work have between zero and five percent porosity. The Hugoniot of the cold sprayed Ni+Al was determined computationally and validated through parallel plate impact experiments; this was discussed in Chapter 3. The computationally determined Hugoniot of CS Ni+Al was applied to simulating the ARL cased charge experiment discussed in Section 4.2.3. A simple elastic-plastic constitutive model with a yield strength of 300 MPa was used to describe the deviatoric strength behavior. A strain based material failure criterion was used; when strain exceeded 0.01 in tension then material strength was set to zero and the failed material subsequently behaved as a fluid. The problem was assumed to be adequately described by 2D axisymmetry around the long axis of the cylinder. Both the TNT and Octol 78/22 explosive fills were simulated to yield different shock pressures using supplied CTH model constants. The casing density was varied between five percent porous and solid density to estimate the temperature change due to the porosity. CTH's adaptive mesh refinement was applied using indicators tied to the explosive density and the volume fraction of the casing with a maximum of four levels of refinement for a minimum cell size of 0.625 mm, which yielded a converged result. Temperature due to the shock wave at the casing center recorded and is plotted in Figure 5.9.

The small amount of porosity made a significant difference in the final temperature of the CS Ni+Al casing post shock. For TNT, the average post shock temperature change was 56 K for the solid density CS Ni+Al and 138 K for the 5% porous casing. For the Octol fill, the temperature changes for the solid density and porous casing were 95 K and 200 K. By itself, this temperature increase does not appear sufficient to cause reaction in the fragments, but temperature increases of a few hundred kelvin during the fragmentation process would further reduce the latency period of the fragments before subsequent combustion or lower the impact velocity required to initiate an impact induced reaction.

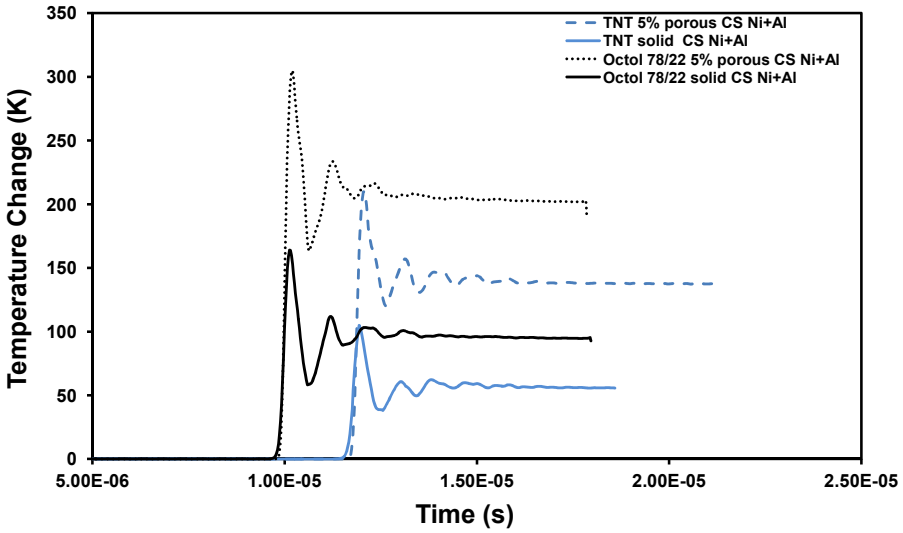

Figure 5.9: Simulated changes in CS Ni+Al casing temperature for different explosive fills and different porosities.

The DTA and XRD analysis as well as comparison with the literature on combustion of Al and composite materials provide important insights into the behavior of Cold Sprayed Ni+Al, Mixture A, and Mixture B fragments. Mixture B appears to be much more prone to oxidation than Mixture A or the CS Ni+Al. Cold sprayed Ni+Al and Mixture A are much less reactive than Mixture B, but they both show evidence of exothermic, solid-state reactions. The structural energetic materials studied here produce small fragment sizes, are composed of reactive mixtures, and are capable of undergoing exothermic reactions at temperatures below the melting point of aluminum. In addition to this, the fragmentation process is believed to significantly disrupt oxide coatings on the fragments as well as significantly increasing the temperature of fragments.. Taken together, the fragments from all of the tested structural energetic materials are likely to be more prone to reaction than pure Al or even undeformed Ni coated Al powders of similar size.

5.2 Impact Initiated Reactions in Structural Energetic Materials

As indicated by the fragment data in Chapter 4, large fragments may also form from structural energetic materials. These fragments, those that are too large to combust in any useful time frame, may react upon subsequent impact as shown by the experiments of Ames [15, 25], Ames and Waggener [16], Homan et al. [23], and Homan et al. [24]. It is desired to investigate how fragments behave during impact and what factors influence the impact induced deformation and reaction behavior. To that end, rod-on-anvil experiments and simulations were conducted in order to mimic fragment impact against a rigid surface.

The factors that contribute to the impact induced ignition of explosively compacted, approximately equivolumetric binary mixtures of Ni+Al, W+Al, and Ta+Al powders (hereafter Ni+Al, Ta+Al, or W+Al) were investigated [195]. The role of constituent behavior and microstructure properties, including topology, were explored [195].

5.2.1 Structural Energetic Materials Systems and Experimental Results

The systems considered here are binary intermetallic forming systems composed of mixtures of Ni+Al, W+Al, and Ta+Al which were made via explosive compaction. Fabrication was described in Section 3.2. The mechanical properties of these explosively compacted mixtures were recently studied by Wei et al. [132]. The current work focuses on the influence of mesoscale microstructure features and constituent properties on reaction initiation behavior, which is believed to be strongly influenced by deformation behavior in these same explosively compacted Ni+Al, W+Al, and Ta+Al mixtures. A few stereological properties are shown in Table 5.1. Thermal behavior, the method of manufacture, and the mechanical properties of these systems are discussed in Chapter 3.

Table 5.1: Properties of Explosively Compacted Ni+Al, W+Al, and Ta+Al including specific kinetic energy at impact corresponding to the lowest energy for reaction initiation, volume fraction, surface area per unit volume, integral mean curvature, and mean free path between Ni, W, or Ta and Al in Ni+Al, W+Al, and Ta+Al respectively. † Data from Du et al. [124].

	Ni+Al	W+Al	Ta+Al
V_v	0.51±0.018 Ni	0.54±0.02 W	0.61±0.02 Ta
S_v	68.5±1.8 mm^{-1}	56.0±1.8 mm^{-1}	117±2.7 mm^{-1}
M_v	0.00144±0.0004 $\mu m/\mu m^3$	0.00175±0.001 $\mu m/\mu m^3$	-0.0139±0.010 $\mu m/\mu m^3$
$\lambda = 4(1 - V_v)/S_v$	0.0287±0.001 mm	0.0325±0.002 mm	0.0133±0.0008 mm
Threshold V	no reaction †	502.0 m/s †	365.5 m/s †
Threshold KE	no reaction †	8.24x10^6 J/kg †	4.75x10^6 J/kg †

Small, cylindrical samples 3.0 ± 0.1 mm in diameter and 2 ± 0.1 mm thick were machined out of explosively compacted billets of Ni+Al, W+Al, and Ta+Al and mounted on 7.62 mm diameter copper projectiles. The projectiles were launched with a single stage gas gun at a hardened steel anvil contained within an experiment chamber from which the air can be evacuated, shown in Figure 5.10a and Figure 5.10b, at various velocities with the vacuum chamber evacuated to 50 mTorr to determine the impact velocity at which reaction takes place [124]. Velocities between 50 and 550 m/s are possible using commercially pure helium gas as a propellant. Copper projectile mass and vacuum levels within the experiment chamber were held constant for all experiments. An IMACON 200, a high-speed gated CCD camera, was used to film the impact and capture transient deformation. The velocity prior to impact was measured using a laser beam interruption system. It has been demonstrated that the highly exothermic reactions of metals [151, 231], thermites [15, 47, 232], and intermetallic forming mixtures [15, 33, 133, 192] produce brilliant light which has been utilized to detect reaction. Figure 5.11a shows a schematic of the rod-on-anvil experiment with a sample mounted on a copper rod, and Figure 5.11b shows an example of impact induced reaction recorded by the IMACON 200 during an experiment on Ta+Al after impact at 500 m/s.

The reaction thresholds of Ni+Al, W+Al, and Ta+Al are presented as minimum

(a) (b)

Figure 5.10: (a) The .30 caliber gas gun used for rod-on-anvil impact tests. Note the presence of the high speed Imacon 200 camera on the left of the image, and the experiment chamber on the right. The experiment chamber allows for testing to be done in a variety of atmospheres and pressures. (b) The experiment chamber contains a massive rigid steel anvil for conducting impact experiments.

impact energy leading to reaction in Table 5.1. It is evident that Ta+Al has a lower minimum specific kinetic energy (in joules per kilogram of sample mass) and impact velocity for reaction initiation than W+Al, and Ni+Al underwent no reaction at any tested velocity ($v_{impact} \leq 550$ m/s).

Samples of Ni+Al, W+Al, and Ta+Al, were sectioned, polished, and photographed to reveal their microstructures as seen in Figure 3.3. Between 25-50 images of the microstructures were taken of each sample in a uniform random manner. Volume fraction, V_v, and surface area per unit volume, S_v, were measured twice on each image. Mean free path, λ, between Ni, W, or Ta and Al, is calculated and tabulated along with V_v and S_v in Table 5.1 with 95% confidence. Additional contiguous images of each material microstructure were combined into a composite image covering an approximately 1 mm square area for the computational studies of deformation behavior discussed below.

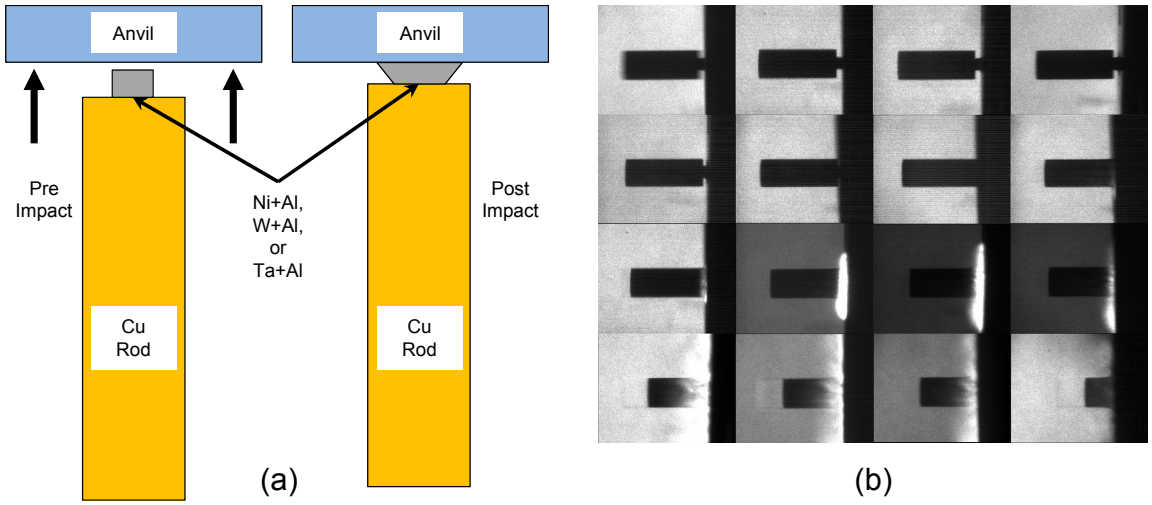

Figure 5.11: (a) A schematic of the rod-on-anvil impact test (b) Ta+Al impact at 500 m/s. The emission of bright light indicates reaction in Ta+Al. Total elapsed time for the 16 frames is 7.5 μs.

Prior work on composite Ni/Al foils has shown that reaction ignition energy is proportional to bilayer spacing for electrical [133, 192], mechanical [133, 192], or thermal [192, 193] ignition. Mean free path, λ, (analogous to bilayer spacing) compares the spacing of reactants in Ni+Al, W+Al, and Ta+Al. Table 5.1 illustrates that Ta+Al has both the lowest mean free path and the lowest minimum specific kinetic energy prior to reaction initiation. However, W+Al and Ni+Al do not follow the same trend in this case which suggests that other factors, notably differences in their deformation behavior, influence impact initiation of reaction. Computational studies of deformation behavior were performed to understand mesoscale features which influence impact induced reaction and are discussed next.

5.2.2 Computational Studies of Deformation Behavior

5.2.2.1 Computational Set-Up

Mesoscale CTH simulations of rod-on-anvil impacts (schematically illustrated in Figure 5.11a) were performed in 2D plane strain on each microstructure. The composite microstructure images of Ni+Al, Ta+Al, and W+Al were filtered and processed in MATLAB and then converted to a CTH diatom. The simulation setup consisted of

a 1 mm square microstructure, similar to, though larger than those shown in Figure 3.3, carried by a copper projectile and impacting into a rigid anvil at 350 m/s. The simulation emulates the experimental configuration, a reactive pellet on a copper rod, though reduced in size because of constraints on computational resources. The ratio of projectile to sample width was preserved.

The constitutive properties of the copper projectile were described using the Johnson-Cook strength model [233],

$$\sigma_y = \left[A + B\bar{\epsilon}_p^n\right]\left[1 + Cln\left(\frac{\dot{\epsilon}}{\dot{\epsilon}_0}\right)\right]\left[1 - T*^m\right].$$

Recall that $\dot{\epsilon} = \sqrt{\dot{\epsilon}_{ij}\dot{\epsilon}_{ij}}$ and $\bar{\epsilon} = \int \dot{\epsilon} dt$ with repeated indices indicating summation. A,B and C are fitting parameters. $T*$ is the homologous temperature, n is the work hardening constant, ϵ_0 is a reference strain rate, and m is the thermal softening parameter. For Ni and Al [216], the Steinberg-Cochran-Guinan strength model,

$$\sigma_y = \sigma_0\left[1 + \beta(\epsilon + \epsilon_i)\right]^n\left[1 + \frac{\sigma_p'}{\sigma_0}\frac{P}{\eta^{\frac{1}{3}}} + \frac{G_T'}{G_0}(T - 300)\right],$$

was used. Strain is defined in the same manner. ϵ_i is the initial plastic strain, $\eta = \frac{v_0}{v}$, P is pressure, G is the shear modulus, β and n are work hardening parameters, $(')$ denotes a derivative with respect to the subscript, and T is temperature. For Ta and W, the Zerilli-Armstrong [234] model for body centered cubic metals,

$$\sigma_y = \Delta\sigma_i + c_2\epsilon^{\frac{1}{2}}exp(-c_3T + c_4Tln\dot{\epsilon}) + kd^{-\frac{1}{2}},$$

was utilized. In this model, c_2 through c_4 are fitting parameters, $\Delta\sigma_i$ is the component of strength from solute or initial dislocation density, k is the Hall-Petch parameter, and d is the grain size. Model parameters were taken from the CTH model database. Following Wei et al. [132], the yield strengths of Al, Ni, Ta, and W were adjusted based on Tabor's Rule, $\sigma_y = H_v/3$.

The Johnson-Cook Fracture model was used for all the materials with values drawn from various sources [235, 236]. It has the form

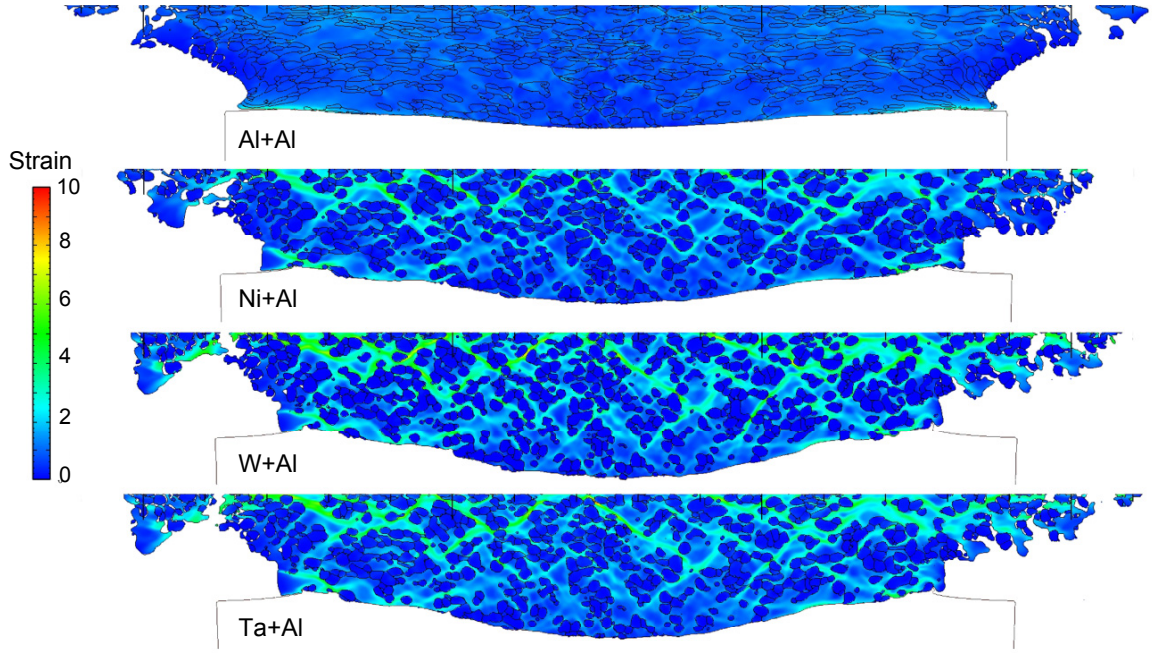

Figure 5.12: Contour plots of plastic strain in Al+Al, Ni+Al, W+Al and Ta+Al at 1.7 μs post impact at 350 m/s. The impact direction is toward the top of the page. Note the strain localization between the particles of Ni, W, or Ta.

$$\epsilon_f = [D_1 + D_2 exp(D_3 \sigma*)] \left[1 + D_4 ln\left(\frac{\dot{\epsilon}}{\dot{\epsilon}_0}\right)\right] [1 + D_5 T*]$$

$$D = \sum \frac{\Delta \epsilon_i}{\epsilon_f}.$$

When D=1 the material is no longer able to support a shear stress. In the above model ϵ_f is the failure strain, D_1 through D_5 are fitting parameters, $\sigma*$ is the hydrostatic stress, and the other parameters have the same meaning as above.

The fracture strength of each material was taken to be equivalent to the spall strength and typical values from the literature were used [237]. Interface strength between the nickel, tantalum, or tungsten and aluminum was varied between 0 and 400 MPa to explore the role of interface strength.

The Mie-Grüniesen equation of state was used to describe the pressure, volume, and temperature response for all of the constituents. Information about the implementation can be found by consulting the CTH documentation [238]. The focus of the present work is analysis of conditions prior to reaction rather than the formation of

product phases. No attempt was made to include a reaction model for the formation of intermetallic phases. The constants used for the equation of state and constitutive models were drawn from the CTH libraries.

A uniform mesh resolution of 2μm by 2μm was utilized. The maximum mesh resolution was dictated by the available computational power; mesh resolution studies indicated that the maximum strain values were not fully converged, however the patterns and relative amounts of strain described in the following sections were stable and consistent, differing only in the very highest value of strain predicted. The mesh was linearly graded from a cell size of 2 microns to 20 microns outside the area where the microstructure was deformed to conserve computational resources. The region of the mesh initially containing the copper rod was still more coarsely meshed with cells being graded up to 100 microns; this was also done to conserve computational resources.

The Ta+Al, Ni+Al, and W+Al samples were initially simulated using the same microstructure (that of the explosively compacted Ni+Al) with zero interface strength. The material properties, equations of state, and constitutive relations were changed to correspond with Ni+Al, W+Al, and Ta+Al which made it possible to study the effects of material properties on the deformation behavior and separate them from those of microstructure morphology. Simulations were then conducted on the actual Ni+Al, Ta+Al and W+Al microstructures while varying interface strengths. Lastly simulations were conducted wherein the components were switched, the matrix phase was the given the properties of the other phase and vice versa, to study the effect of topology on the material deformation response.

5.2.2.2 Computational Results

Figure 5.12 shows a series of contour plots of plastic strain, ϵ_p, for simulated impact on Al+Al, Ni+Al, W+Al, and Ta+Al using the same Ni+Al microstructure. The

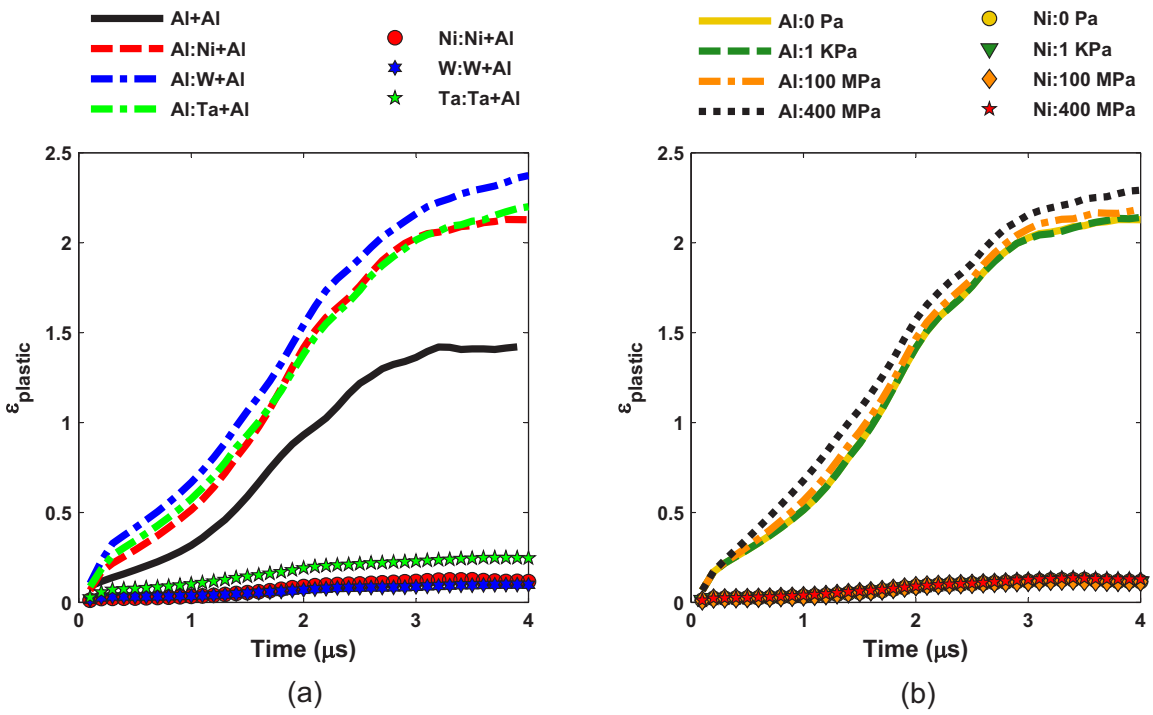

Figure 5.13: (a) ϵ_p vs. time for Al+Al, Ni+Al, W+Al, and Ta+Al. The Al matrix is plotted separately from the Ni, Ta, or W particles. The presence of Ni, W, or Ta particle increases deformation in the Al. This appears to be a function of both the density and strength of the particle in question. (b) Average plastic strain vs. time for Ni+Al for different interface strengths. Al and Ni are plotted separately. Increasing interface strength slightly increases deformation in the the Ni.

Al+Al data is included to show the effects of the Ni, W, or Ta particles on the extent of strain localization in the surrounding aluminum matrix. It can be seen that the deformation is localized into bands and enhanced by the presence of Ni, Ta or W particles.

Plastic strain data like that in Figure 5.12 is volume averaged and re-plotted as a function of time for the Al matrix and the Ni, Ta, and W particles separately in Figure 5.13a, for simulations where the same Ni+Al microstructure was used for all materials. The Al+Al material shows a much lower average plastic strain than Al in Ni+Al, W+Al, or Ta+Al. The higher densities and strengths of the Ni, W, and Ta relative to Al cause additional deformation in the Al matrix; the W particles cause the highest relative deformation in Al and the Ni particles the least. Ta was found

to plastically deform more than Ni and W particles.

Figure 5.13b and Figure 5.14a show the average strain versus time histories for Ni+Al and W+Al respectively; Plastic strain in the Al, Ni, and W is not very sensitive to interface strength. Both materials have similar morphologies, as shown in Figure 3.3a,c with convex Ni or W particles embedded in a continuous Al matrix. Due to the greater strength of the W and Ni particles and the connected nature of the Al matrix, the Al in Ni+Al and W+Al deforms preferentially in shear bands, allowing the Al to accommodate the majority of the deformation imposed by the copper rod during impact as shown in Figure 5.15a,b.

Figure 5.14b shows the strain history of Ta+Al, illustrating slightly greater sensitivity to interface strength and considerably more deformation in Ta than in the Ni or W. The Ta+Al material also demonstrates less deformation within the Al component. The morphology of this material, shown in Figure 3.3b, is quite different than that of the Ni+Al or W+Al. Ta forms a continuous phase and contains Al islands within it in a two dimensional view. This will be addressed in more detail below. Ta strains more as it is softer than either the W or the Ni and work hardens less that Ni. Furthermore, Al cannot deform around the Ta as easily as it does around the Ni or W as shown in Figure 5.15a,b. The Al regions link up and form shear bands during deformation, but those shear bands cannot propagate as far due to the unconnected nature of Al in Ta+Al as seen in Figure 5.15c. This limits the deformation of the Al and requires Ta to accommodate more deformation. In contrast, the localized deformation in Al circumvents Ni and W particles in Ni+Al and W+Al.

The interface strength sensitivity of the Ta deformation appears to be a result of the different microstructure morphology of Ta+Al. With high interface strengths, the aluminum is constrained to the Ni, W, or Ta. In Ni+Al and W+Al, the constraint does not change the strain history much because shear bands quickly form in the Al and most of the deformation is restricted to Al irrespective of interface strength. In

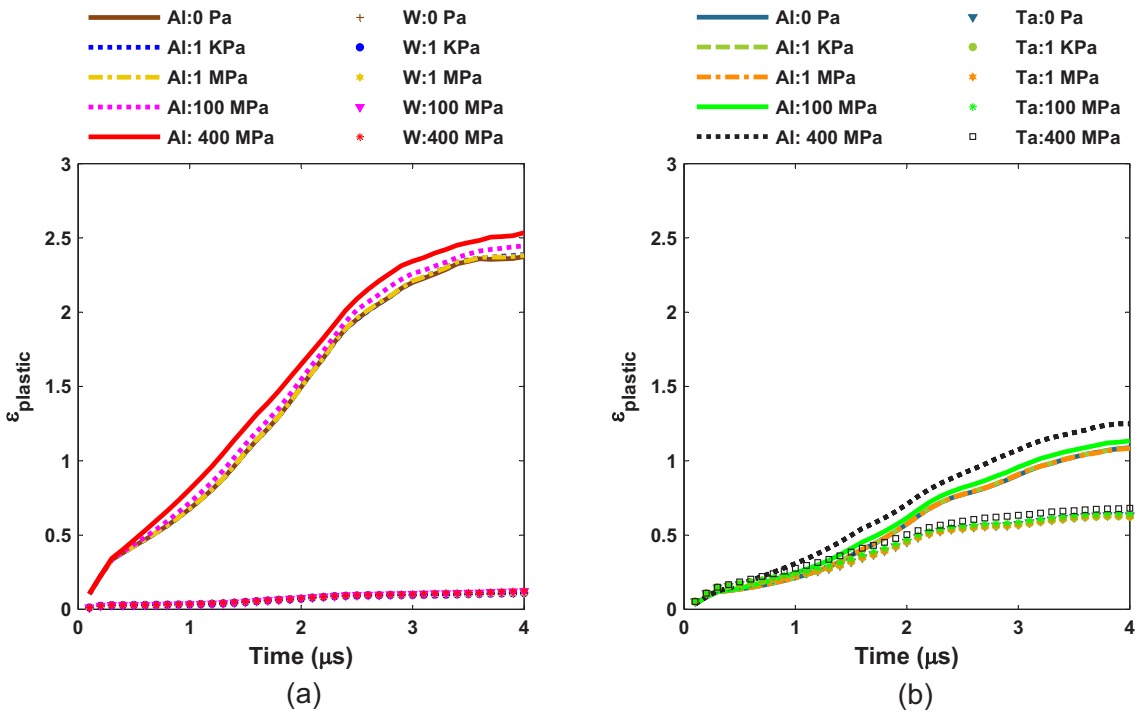

Figure 5.14: (a) ϵ_p vs. time for W+Al for different interface strengths. Al and W are plotted separately. (b) ϵ_p vs. time for Ta+Al for different interface strengths. Al and Ta are plotted separately. The Ta phase in Ta+Al deforms much more than W in W+Al, but the Al in Ta+Al deforms less than the Al in W+Al.

Ta+Al, shear stresses across the Al/Ta interfaces lead to earlier and more extensive formation of shear bands in the Al which then leads to greater deformation of the Ta. For lower strength interfaces, the Al/Ta interfaces fail more readily which accommodates the imposed deformation: shear bands do not form as quickly nor are they as extensive. The result is that Ta+Al has its highest average plastic strain values for high interface strengths.

Quasistatic and dynamic strength data obtained by Wei et al. [132] and SEM images of fracture surfaces provide clues about the interface strength in these material systems. Wei et al. [132] found that Ta+Al had much higher ultimate strengths than Ni+Al or W+Al, although a rule of mixtures approach would predict a different result. Using a finite element model in their analysis, they concluded that the Al/Ni interfaces in Ni+Al are of lower strength than the constituents. Wei et al. [132] were unable to deduce an Al/Ta interface strength for Ta+Al [132]. No analysis of interface strength was performed on W+Al.

In the present work, interface strength is found to influence the plastic deformation behavior in Ta+Al, hence it is important to have some sense of the relative strength of the Al/Ta interfaces. Fondse and Meyers [239] supplied fractured samples of W+Al, Ni+Al, and Ta+Al that were tested in a Split Hopkinson Pressure Bar. Comparison of fracture surfaces from Hopkinson bar compression samples of Ni+Al and W+Al, Figure 5.16a and 5.16b respectively, reveal extensive particle pull out and interfacial fracture, clear evidence of weak interfaces between Al and the other component. In contrast, SEM images of a Ta+Al fracture surface from a Hopkinson bar compression sample shown in Figure 5.17a and Figure 5.17b provide evidence that fracture in these samples is intergranular rather than interfacial. This suggests that adhesion between Ta and Al particles is much greater than adhesion between Ni and Al or W and Al. The higher level of adhesion promotes higher levels of plastic deformation in Ta+Al as shown in Figure 5.14b.

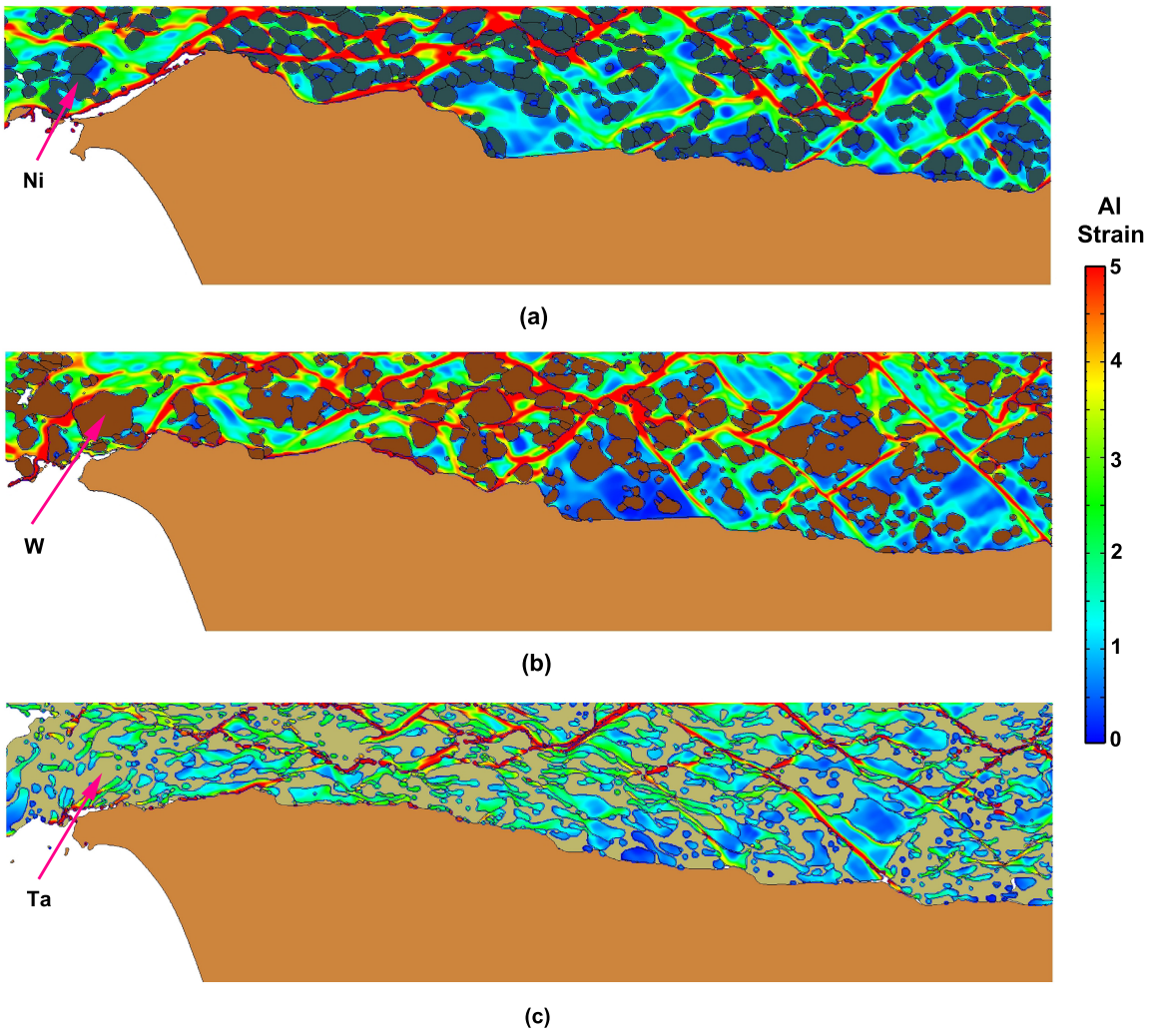

Figure 5.15: (a) Ni+Al microstructure 1.9 μs post impact. (b) W+Al microstructure 1.9 μs post impact. (c) Ta+Al microstructure 1.9 μs post impact. ϵ_p in Al in each material is depicted. Notice the smaller shear band like structures in Ta+Al. This reflects the reduced deformation in Al and the greater deformation in Ta.

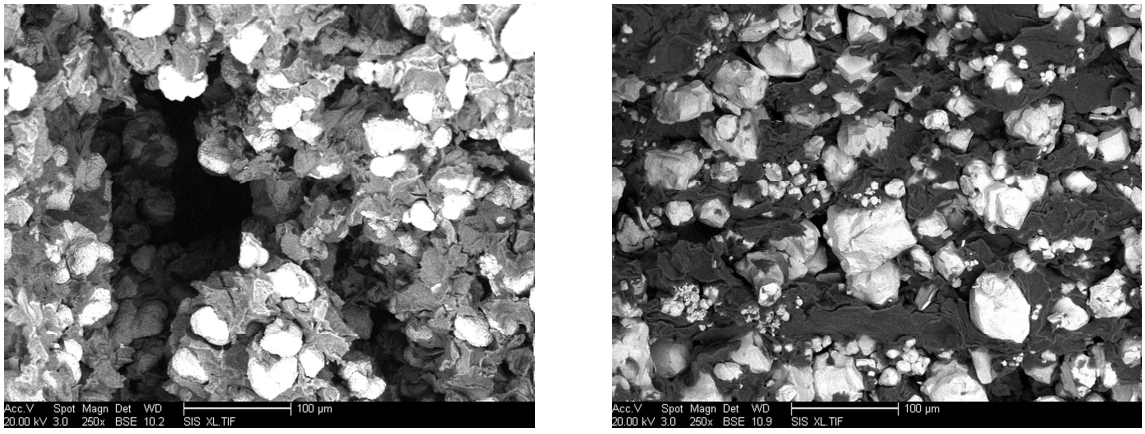

Figure 5.16: (a) Fracture surface from Ni+Al impacted in the Hopkinson bar showing interfacial fracture between phases. (b) Fracture surface from W+Al impacted in the Hopkinson bar also showing interfacial fracture between phases [239].

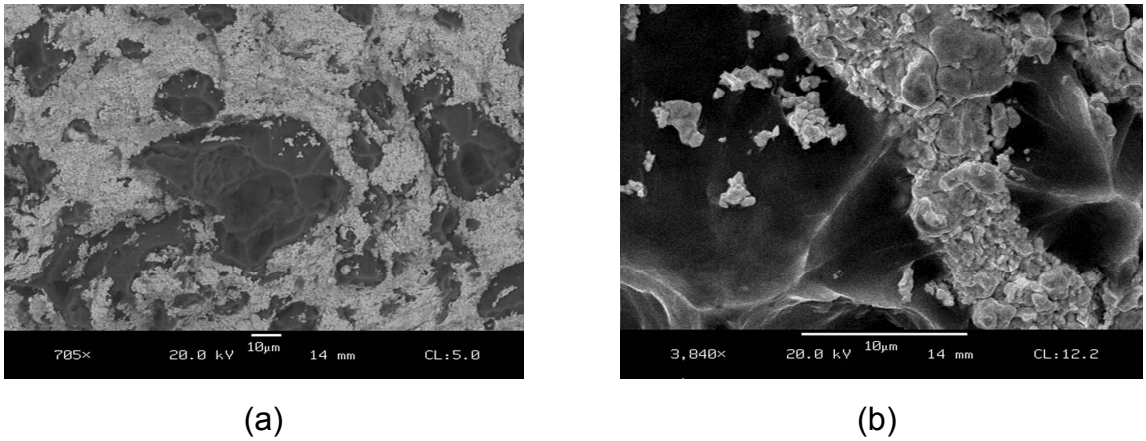

Figure 5.17: (a) Fracture surface from Ta+Al impacted in the Hopkinson bar at 705X. (b) Fracture surface from Ta+Al impacted in the Hopkinson bar at 3840x. Neither show evidence of interfacial fracture seen in Ni+Al and W+Al.

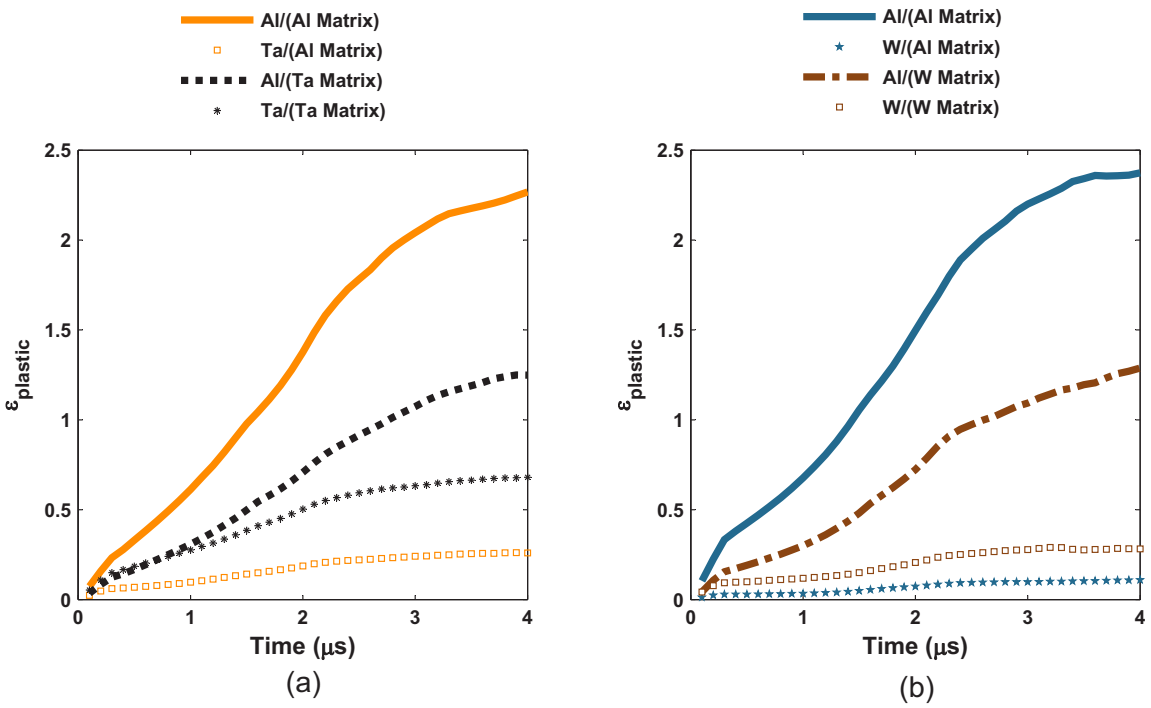

Figure 5.18: (a) ϵ_p vs. time for Ta+Al with 400 MPa interface strength for the experimentally derived and the reversed microstructures. Al and Ta are plotted separately. Reversing the microstructure such that Ta becomes embedded in Al leads to the same deformation trends seen in W+Al and Ni+Al. (b) ϵ_p vs. time for W+Al with 0 interface strength for the experimentally derived and the reversed microstructures. Al and W are plotted separately. Reversing the W+Al microstructure such that the W phase becomes the matrix leads to the same deformation trends seen in Ta+Al, e.g. the W deforms much more and the Al less.

If the same Ta+Al microstructure with a 400 MPa interface strength is altered by assigning the Ta phase the Al equation of state and constitutive properties and assigning the Al phase the Ta equation of state and constitutive properties and the simulation is rerun, the results are very similar to those observed for Ni+Al or W+Al. The amount of deformation in the Ta decreases drastically. The amount of deformation in the Al increases. The lower strength of the Ta relative to the W also concentrates less deformation in the Al. These results are shown graphically in Figure 5.18a, and they confirm that the topology of the tantalum phase plays a significant role in its deformation.

The same exercise of reversing the microstructures was performed on the W+Al

and Ni+Al microstructures, this time with zero strength interfaces because the interface strength was seen to be so low in these materials. The material properties were reversed such that W or Ni became the matrix phase and Al became the reinforcement phase. The results are very similar to those seen in Ta+Al as shown in Figure 5.18b and Figure 5.19. When W and Ni are the matrix, there is substantially more deformation in those phases. The reversed microstructure simulations show that having the stronger phase as the matrix increases the amount of deformation in that phase. This again shows the importance of the microstructure topology of these materials to their deformation behavior. When a hard material is made into the matrix, the topological connectivity is increased and that of the aluminum is decreased. Increasing the connectivity of a phase leads to additional deformation in that phase. These results also suggest that the deformation of these materials is influenced to a greater extent by the topology of constituents than by the interface density of the constituents.

5.2.3 Analysis of Simulation Data and Its Implication for Reaction Response

Mesoscale simulations predict that Ta+Al has the highest average plastic strain values in the non Al component when compared with Ni+Al and W+Al. Energy dissipated in plastic work will be dissipated principally as heat as discussed earlier; both phases need to undergo plastic deformation and associated heating to react. The Ta in Ta+Al plastically deforms more than the W in W+Al or the Ni in Ni+Al and thus has a higher deformation induced temperature increase. Having extensive deformation in both phases causes the Ta+Al to be more reactive than Ni+Al or W+Al. It was shown that this deformation relies on the mechanical properties of Ta and Al as well as the topology of the Ta+Al microstructure. When W+Al and Ni+Al were reversed, they showed more deformation in the hard phase which suggests that in that configuration they would be more reactive as well.

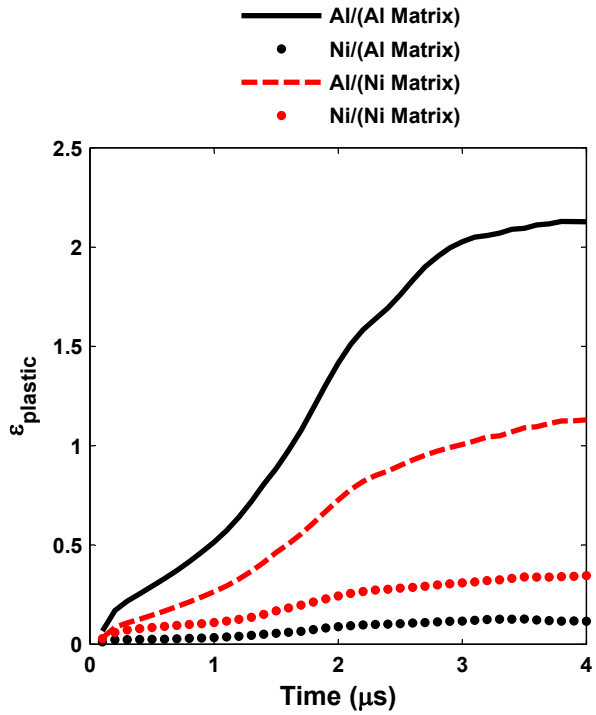

Figure 5.19: ϵ_p vs. time for Ni+Al with 0 interface strength for the experimentally derived and the reversed microstructures. Al and Ni are plotted separately. Reversing the Ni+Al microstructure such that the Ni phase becomes the matrix leads to the same deformation trends seen in Ta+Al and the reversed W+Al; the Ni deforms much more and the Al less.

The observed behavior points to the importance of the topology of each component in the material, particularly the hard phase. In general, it would be necessary to do 3D serial sectioning to determine topological properties in an arbitrary microstructure [240,241]. However, in the present case it is known that the Ta+Al, Ni+Al and W+Al materials were fabricated with 99.8% pure 325 mesh powders of Ta, Ni, W, and Al [124]. Images of the powder feedstock can be seen in Wei et al. [132]. The Ni and W particles are strong, essentially convex, simply connected powder particles. The Ta particles are spongy and appear to have non-zero connectivities. During explosive compaction Al could only flow around the Ni or W particles, which deformed to a lesser extent but their connectivity did not change. The Al was able to flow into the Ta holes and pores. This led to the microstructures shown in Figure 3.3 with convex Ni and W particles surrounded by a matrix of Al. The resulting Ta+Al microstructure is one in which Ta and Al are probably interpenetrating. It is likely not the case that the Al is entirely composed of isolated islands as perhaps implied by Figure 3.3. However, it is clearly the case that the connectivity of the Ta is much greater than that of the W or Ni. The 2D simulations, while not fully capturing the 3D topology of the material, do correctly capture the influence of having a more topologically connected hard phase on the deformation behavior of Ni+Al, Ta+Al, and W+Al. Taken with the experimental results, they also suggest that deformation and subsequent reaction behavior are more strongly influenced by the topology than interface density in this impact scenario.

It is also of interest to compare the roles of constituent strength and topology. In Figure 5.20, the integral mean curvature is plotted against the difference in constituent strength. The spot diameter is proportional to the maximum average plastic strain in the rod-on-anvil impact simulations. Data from the ordinary EC Ni+Al, EC W+Al, and EC Ta+Al and reversed Ni+Al, and reversed Ni+Al are plotted in Figure 5.20. It is evident that decreasing the difference between constituent strength increases the

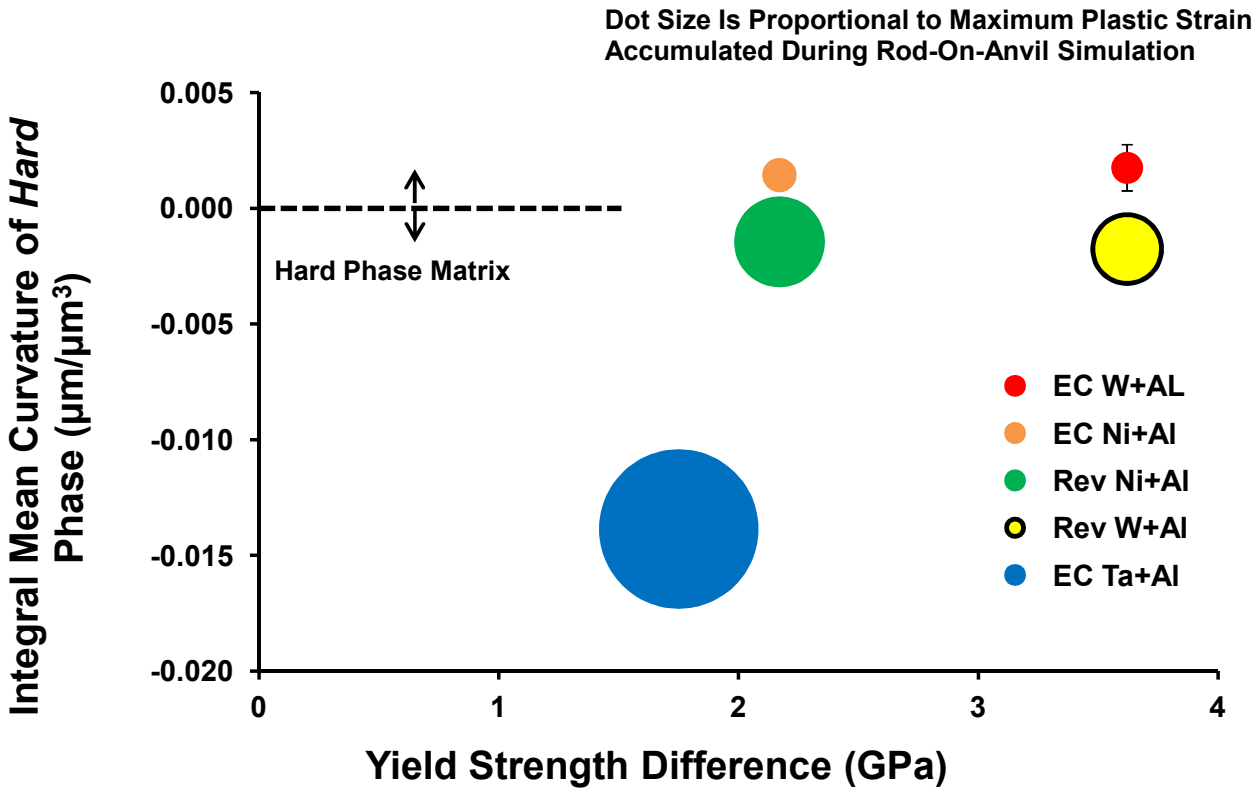

Figure 5.20: Effect of difference in constituent yield strength difference vs. integral mean curvature for maximum average plastic strain in the hard phase of EC Ni+Al, EC W+Al, and EC Ta+Al and reversed Ni+Al, and reversed Ni+Al. The spot diameter is proportional to the maximum average plastic strain in the hard phase. Notice that decreasing the difference between constituent strength increases the maximum average plastic strain. Increasing topological connectivity also increases the maximum average plastic strain, apparently more so than decreasing the difference between constituent strength.

maximum average plastic strain. Increasing topological connectivity also increases the maximum average plastic strain, apparently more so than decreasing the difference between constituent strength.

The simulation and experimental results on explosively compacted W+Al, Ni+Al, and Ta+Al suggest that the system that is most reactive when subjected to uni-axial stress impact is explosively compacted Ta+Al. The EC Ta+Al combines higher topological connectivity in the reinforcement phase, ductility in both constituents, reduced tendency to work harden in the reinforcement phase, high average density, good interface adhesion, and minimum separation between reactants.

5.3 Comparison of Cold Sprayed and Explosively Compacted Structural Energetic Materials

In explosively compacted Ta+Al, Ni+Al, and W+Al mixtures, it has been shown that large strains in both phases, but especially the stronger phase, are correlated with a lower impact velocity for reaction initiation [195]. Differences in plastic deformation that lead to impact induced reaction were found to be substantially a result of the topology of the material in question [195].

For explosively compacted Ni+Al and W+Al, the hard phase, Ni and W respectively, were found to be simply connected particles embedded in a more compliant Al matrix [195]. Mesoscale simulations reveal that the Al matrix rather than Ni or W particles deform to accommodate impact. Consequently, more energy is deposited in the Al matrix and its temperature is increased more than Ni or W. In contrast, the Ta in explosively compacted Ta+Al was found to be more topologically connected than the W or Ni particles. Al could not deform around the Ta which in turn was forced to accommodate more deformation, and therefore the Ta component's temperature will increase due to plastic deformation more than either the Ni in Ni+Al or the W in W+Al. This leads to the observed differences in sensitivity to impact and consequently the impact initiated reactions.

To gain a more complete understanding of this behavior, and in an attempt to remove constitutive behavior as a variable, two systems with the same constituents but different morphologies were studied to compare and contrast their differing performance with respect to impact induced reaction initiation [242].

5.3.1 Ni+Al Material Systems

The materials considered here consist of an explosively compacted Ni+Al mixture (EC Ni+Al) [124] and Ni+Al formed via gas dynamic cold spray (CS Ni+Al) [243] obtained from the Army Research Laboratory. The volume fractions and densities

Table 5.2: Physical parameters of interest for explosively compacted Ni+Al and cold sprayed Ni+Al used in impact experiments. † Data from Du et al. [32].

	EC Ni+Al	CS Ni+Al
V_V	0.51±0.02 Ni	0.52±0.01 Ni
S_V (mm^{-1})	68.5±1.8	186±6
$\lambda = 4(1 - V_V)/S_V$ (μm)	28±2	10.3±0.6
ρ (g/cm^3)	†5.64	5.27±0.02

of these materials are reasonably close as seen in Table 5.2. They differ primarily in their morphology.

The cold sprayed Ni+Al was formed from Ni coated Al particles which leads to a microstructure morphology where Ni forms a more topologically connected phase than the Al. The EC Ni+Al is nearly the opposite: Ni particles are essentially islands within a topologically connected Al matrix. These differences can be clearly seen in Figure 5.21 and 5.22. The differing microstructure morphologies allow closer examination of the unique effects of topology on reaction initiation. It is acknowledged the interface density, λ may influence reaction behavior as well by increasing the quantities of reactants in close proximity; however, it will be seen that the topology of the Ni plays a more dominant role in influencing deformation behavior and thus, the reaction initiation behavior.

5.3.2 Computational And Experimental Studies and Discussion

Relative reaction thresholds and other aspects of the deformation behavior of structural energetic materials can be studied via the rod-on-anvil impact test [33]. This test will be simulated for CS Ni+Al and EC Ni+Al and then compared with experimental data.

Following the approach discussed earlier, CTH, an Eulerian Hydrocode [215], was used to conduct 2D plane strain simulations of rod-on-anvil impacts on actual EC Ni+Al and CS Ni+Al microstructures 508 μm wide x 338 μm tall. The microstructure is driven by a copper projectile into a rigid anvil at 175 and 350 m/s. The simulation

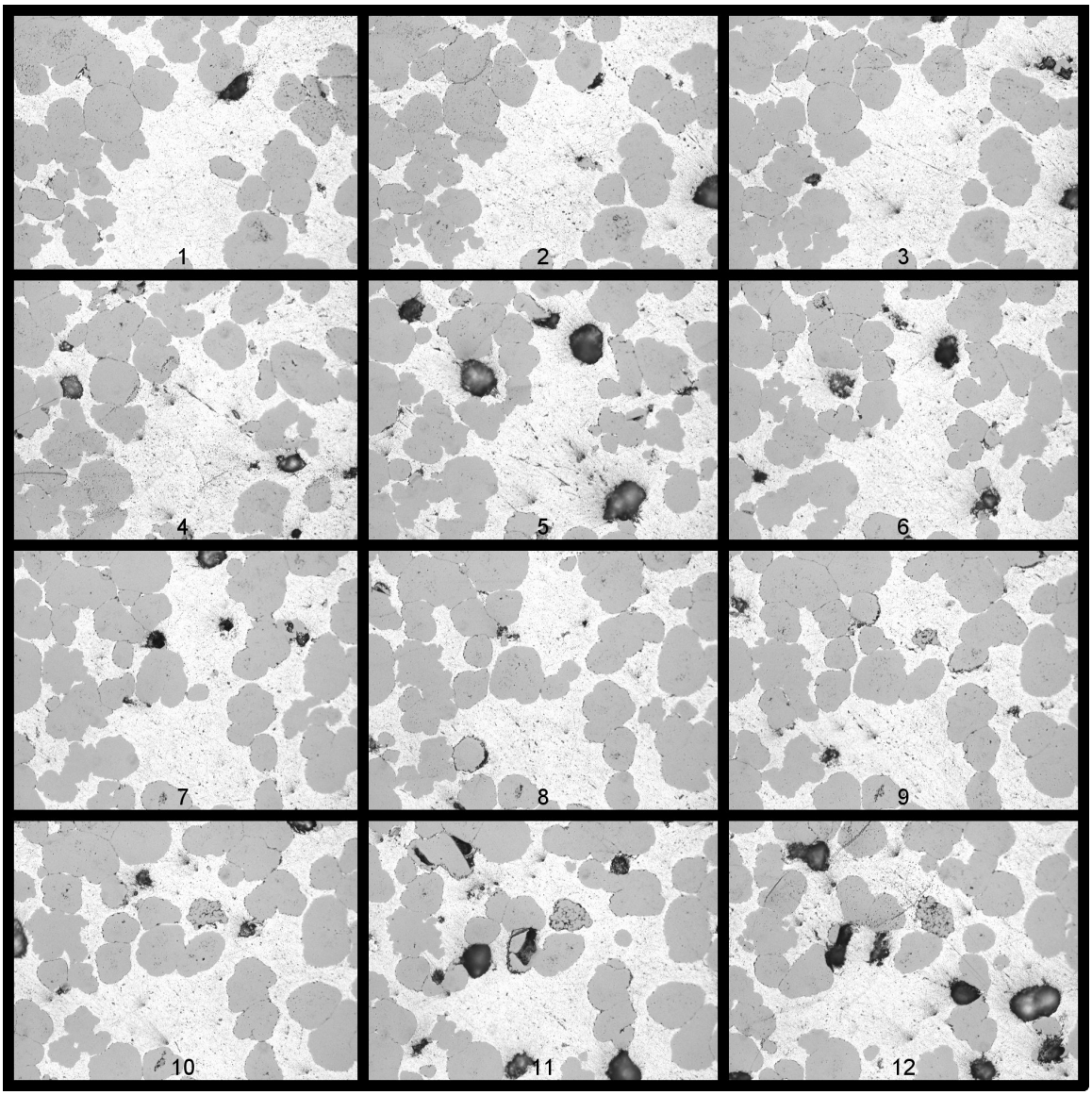

Figure 5.21: Explosively compacted Ni+Al serial sections with average vertical spacing of 3.7 μm. Each section is 269 μm wide and 201 μm tall. Notice that the lighter colored aluminum matrix surrounds the darker colored Ni particles which are simply connected. The black spots are regions where Ni particles pulled out during the polishing process.

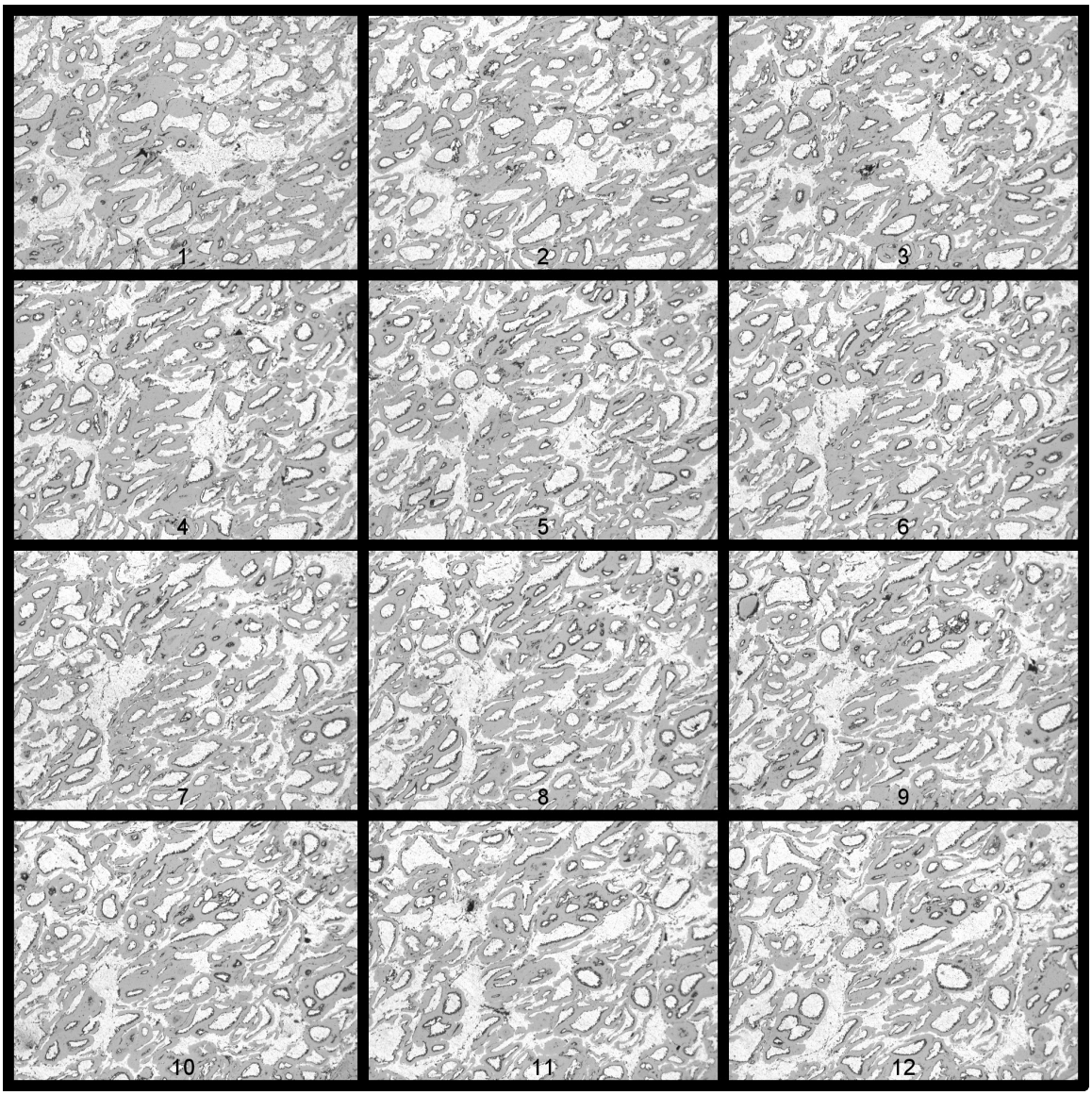

Figure 5.22: Cold Sprayed Ni+Al serial sections with average vertical spacing of 3.7 μm. Each section is 269 μm wide and 201 μm tall. Notice that the darker colored Ni now forms a network. The lighter colored aluminum is far less interconnected than in the explosively compacted Ni+Al material. The black spots are porosity and regions where Ni or Al pulled out during the polishing process.

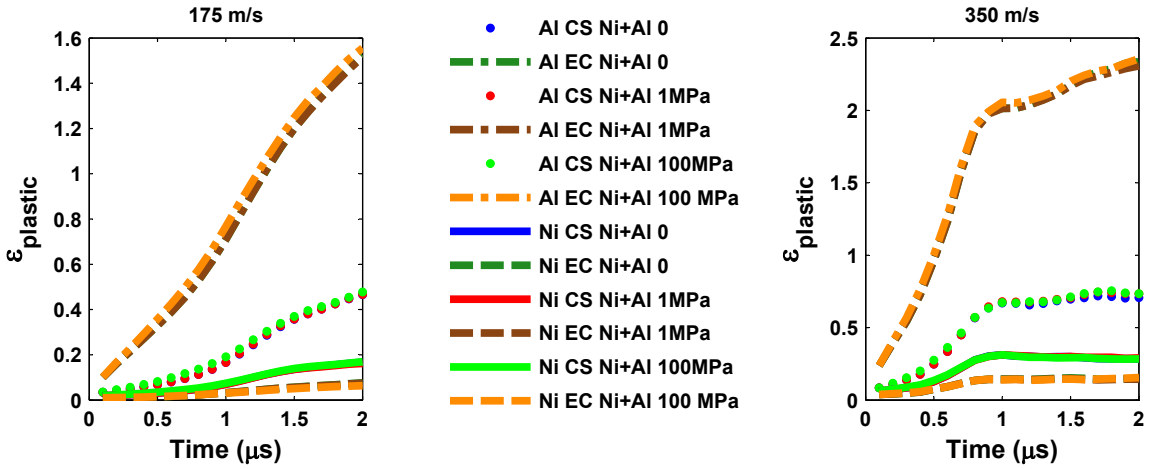

Figure 5.23: Averaged plastic strain in CS Ni+Al vs. EC Ni+Al compared for simulated rod-on-anvil impact at 175 m/s and 350 m/s. In CS Ni+Al, the Ni (the stronger phase) is the matrix. When Ni is the matrix, as in CS Ni+Al, it deforms to a much greater extent than when it is embedded as discrete particles in an Al matrix, as in EC Ni+Al. This aids in impact induced reaction initiation.

emulated the rod-on-anvil impact experimental configuration, though reduced in size. Constraints on computational resources make modeling a full size rod-on-anvil test sample while resolving its mesoscale features impractical. The mesh resolution used was 0.5 μm. The ratio of projectile to sample size was preserved. Interface strengths of 0, 1 MPa, and 100 MPa were simulated. The same yield strengths were used for the same materials in both CS Ni+Al and EC Ni+Al.

As shown in Figure 5.23a,b, the Al component of the EC Ni+Al deforms more than the Al component of the CS Ni+Al. The much softer Al matrix surrounds the harder Ni particles in EC Ni+Al and is deformed to a greater extent. This is illustrated in Figure 5.24 where it is evident that shear bands form in the Al and kink around the Ni particles, partially shielding them from deformation. Therefore, less strain develops in the Ni component of the EC Ni+Al. In CS Ni+Al, the shear bands in Al are much less extensive because the Ni is the more topologically connected phase; Ni is forced to accommodate more deformation. These trends proved quite

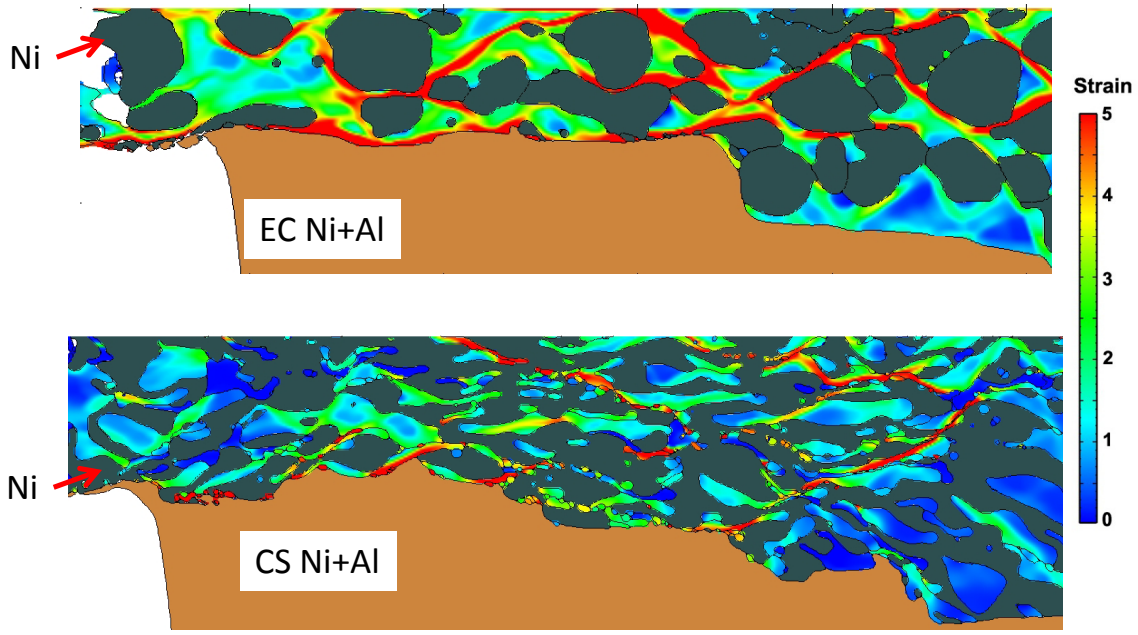

Figure 5.24: Plastic strain in CS Ni+Al and EC Ni+Al at 0.9 μs after impact compared for simulated rod-on-anvil impact at 350 m/s. Only plastic strain in the Al component in both CS Ni+Al and EC Ni+Al is shown for clarity.

consistent for different impact velocities and interface strengths. Increasing interface strength causes very modest increases in the plastic strain in both Ni+Al systems.

Rod-on-anvil tests were conducted on CS Ni+Al to compare with the simulation results and EC Ni+Al rod-on-anvil data [124]. OFHC copper rods 7.61 mm diameter x 30 mm length with the ends lapped flat were utilized as projectiles. CS Ni+Al pellets 2 mm length x 3 mm diameter were machined via wire EDM from a CS Ni+Al plate lapped flat. The pellets were center mounted on the copper rods with thin film epoxy. The projectiles were driven into hardened S7 steel anvils, ground and lapped flat, at velocities between 273 and 523 m/s in vacuum. Reaction was observed using an Imacon 200 framing camera and a NAC high speed video camera; a cold sprayed Ni+Al sample impacting at 494 m/s is shown in Figure 5.25. The results of the rod-on-anvil tests for CS Ni+Al and EC Ni+Al are shown in Figure 5.26. EC Ni+Al did not react when tested. The reaction threshold for CS Ni+Al was found to be 373 m/s.

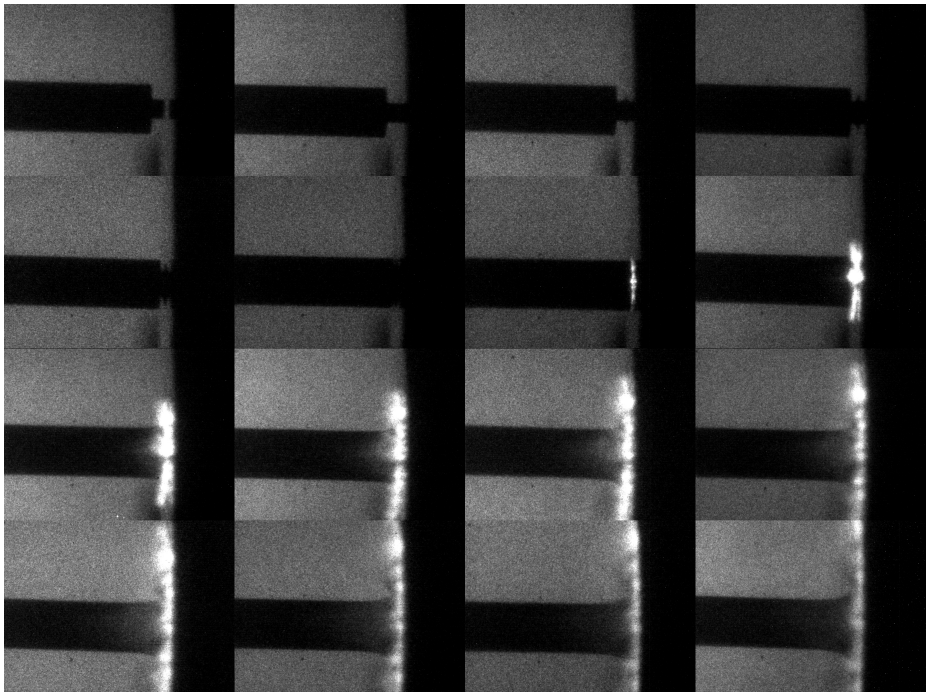

Figure 5.25: Rod-on-anvil impact At 494 m/s with a cold sprayed Ni+Al sample. The interframe time is 750 ns and the exposure time is 450 ns.

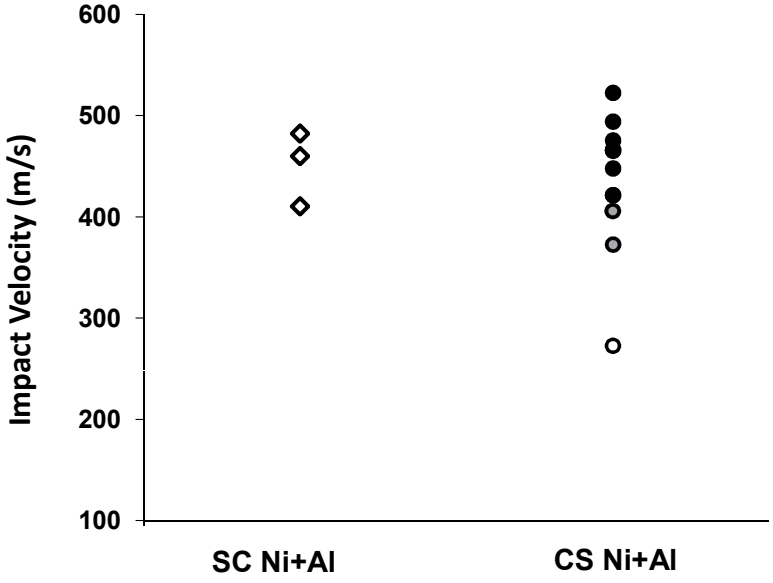

Figure 5.26: Rod-on-anvil experimental results for EC Ni+Al and CS Ni+Al in vacuum. Filled symbols indicate reaction. The reaction threshold of EC Ni+Al was determined to be 373 m/s.

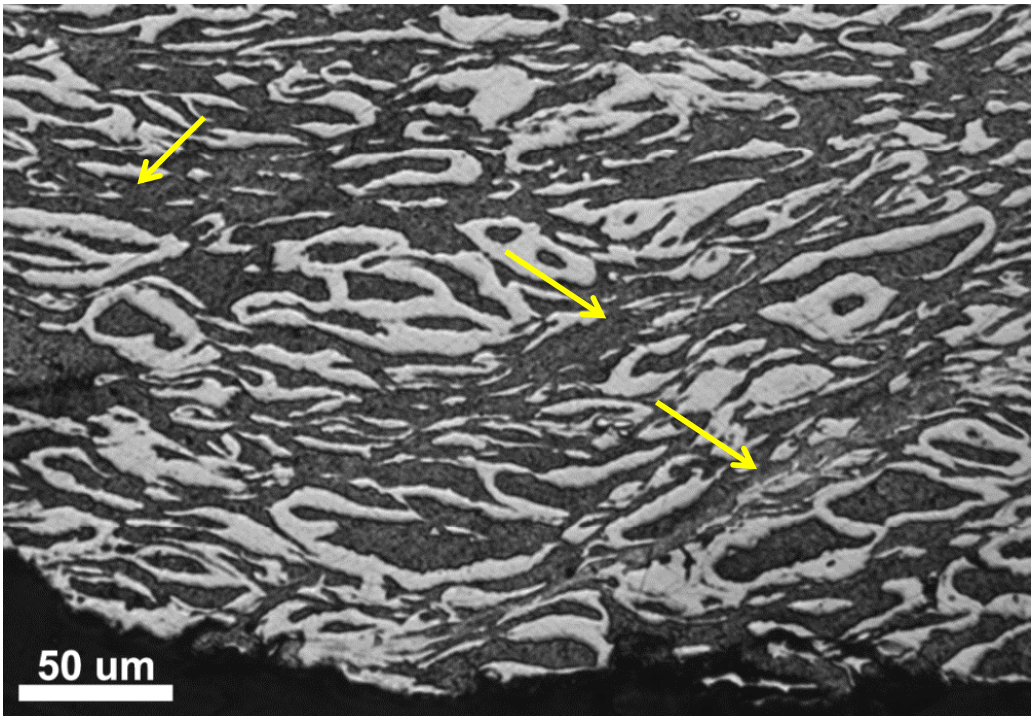

Figure 5.27: CS Ni+Al specimen recovered after impact at 354 m/s (in air) showing shear band formation (indicated by arrows) consistent with simulation results in Figure 5.24. The Ni is the lighter colored phase.

From Figure 5.26, it is evident that the CS Ni+Al is much more reactive than the EC Ni+Al when subjected to impact loading. This is due to the greater extent of deformation in the Ni component of the CS Ni+Al as shown in Figure 5.23 and Figure 5.24. As indicated, reaction initiation is very brief, $t \leq 5.5\mu$s. It is necessary to extensively deform and heat both constituents simultaneously in order to cause a reaction during the impact event. No doubt if both materials were subjected to the same extent of deformation and resulting temperature increase, the material with the higher interface density would react to a greater extent. However, the much greater deformations experienced by Ni in CS Ni+Al are dominated by its topology, not the interface density, which leads to increased deformation and enhanced reactivity.

A recovered sample of CS Ni+Al, shown in Figure 5.27 shows evidence of shear band formation similar to that predicted by the simulations in Figure 5.24. This provides a partial validation of the accuracy of the simulations. There is also evidence

of fine scale mass mixing within the shear bands which may play a role in the reactivity of these samples.

5.3.3 Conclusions Drawn from Comparison of Cold Sprayed and Explosively Compacted Ni+Al Systems

Cold sprayed Ni+Al and explosively compacted Ni+Al form a useful pair of structural energetic materials to study. With the same components, similar volume fractions but very different morphologies, the important role of topology is more fully explored. Simulations show that the highly connected nature of Ni in CS Ni+Al promotes plastic deformation and greater adiabatic heating of the Ni component of CS Ni+Al. The simply connected nature of Ni particles in the EC Ni+Al tends to reduce deformation in the Ni component leading to less adiabatic heating of Ni, suggesting that EC Ni+Al would be less reactive. Rod-on-anvil tests on CS Ni+Al and EC Ni+Al confirm that CS Ni+Al is indeed more reactive than EC Ni+Al.

5.4 Fragmentation and Reaction Map For Structural Energetic Materials

Structural energetic materials are designed to replace inert structural materials in munitions and augment the total energy output of such devices and/or reduce their hazard to innocent bystanders. Structural energetic materials based on metal-metal mixtures accomplish this task by fragmenting to form a distribution of fragments that has a mean size much lower than that of typical structural alloys used in munitions casings. Some fragments may react due to interactions with hot detonation products, and others may undergo impact induced reaction.

For the structural energetic materials considered in this work, it has been observed that the fragmentation behavior is governed by the tendency of these materials to crack profusely and form multicomponent fragments. The dominant factor influencing fragment size is the rate of loading. Growth of extensive networks of cracks occurring

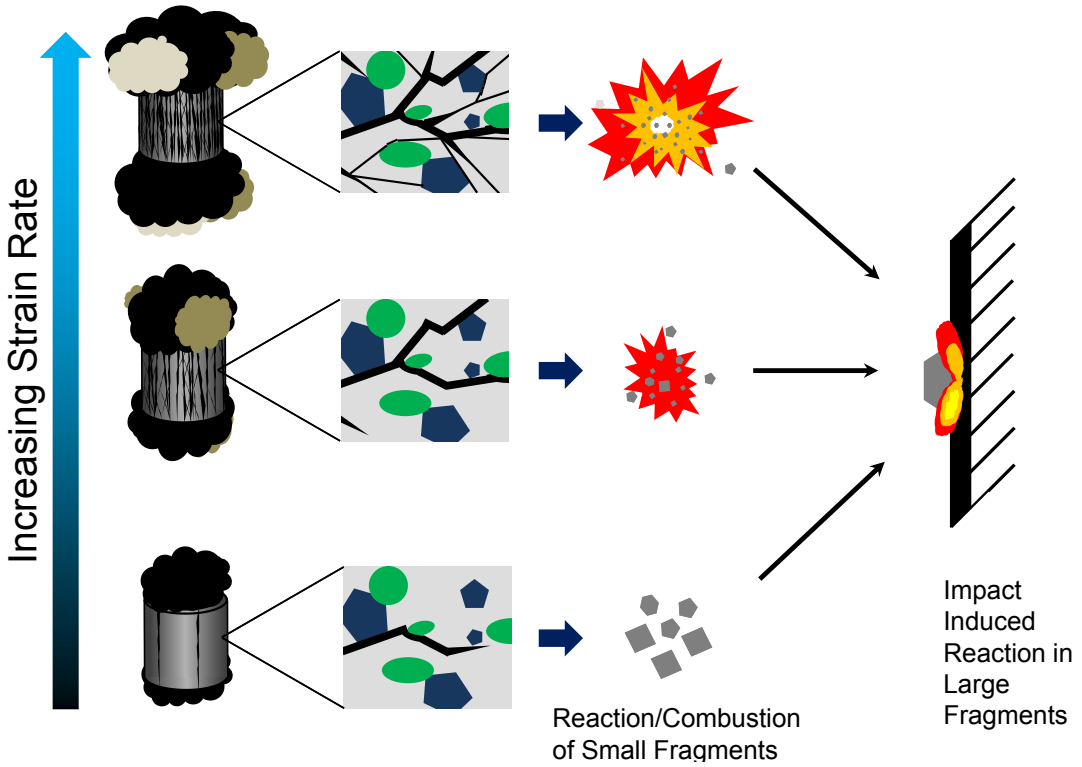

Figure 5.28: Fragmentation and reaction diagram for structural energetic materials composed of intermetallic forming mixtures. Fragments may react due to interactions with detonation products or due to impact. Which type of process leads to reaction is a function of fragment size which depends on fragment size. The cracking behavior within the material, which influences the fragment population, depends on the loading rate. Fragments around a hundred μm or less will react due to heat gain from detonation products, and will also enhance blast loading. Larger fragments will travel until they reach a solid surface and may react upon impact. Impact-initiated reaction depends on the loading condition and is strongly influenced by the fragment microstructure.

at high strain rates, apparently influenced in part by interfaces within the material, leads to the formation of small fragments. Fragments that are on the order of a hundred μm are prone to intermetallic formation reaction and combustion due to interactions with hot detonation products. This process, and its mediation by the development of networks of cracks, is shown schematically in Figure 5.28.

Larger fragments are will not react due to interactions with the detonation products, but may react upon impact with a solid surface. Impact induced reaction is found to be strongly influenced by microstructure topology. The propensity for reaction initiation upon impact increases with topological connectivity of the higher strength phase; e.g. Ni is the interconnected matrix in cold sprayed Ni+Al, and Ta is the interconnected matrix in explosively compacted Ta+Al. Impact induced reaction of larger fragments is also shown schematically in Figure 5.28.

5.5 Summary of the Fragment Combustion and Impact Induced Behavior

A number of significant features have emerged that relate to combustion and impact induced reaction of structural energetic material fragments.

- Multicomponent fragments formed from structural energetic materials have the capacity to react to form intermetallics as well as combust to form oxides.
- Disrupted oxide layers on newly formed fragments should provide a greatly reduced barrier to combustion.
- Fragment data from CS Ni+Al, Mixture A, and Mixture B show that at the highest tested strain rates, $\dot{\epsilon} = 10^5$, the structural energetic materials form a significant mass (up to 10% of the original sample ring mass) of fragments at sizes small enough for combustion. In one experiment on Mixture B fragments, the potential combustion enthalpy of these fragments was shown to be 20% of

the detonation enthalpy available from the charge used for the fragmentation experiment.

- Impact experiments on explosively compacted Ni+Al, Ta+Al, W+Al, and cold sprayed Ni+Al show the importance of topology to impact induced reactions. Materials in which the hard phase is topologically connected are more likely to react at a lower impact velocity. When Al surrounds simply connected Ni or W particles, Al accommodates nearly all of the deformation, which limits plastic deformation induced temperature increases in the Ni or W particles. In EC Ta+Al and CS Ni+Al, the topological connectivity of the hard phase ensures that Ta or Ni must deform much more, leading to a greater deformation induced temperature increase and more susceptibility to impact induced reaction.

CHAPTER VI

CONCLUSIONS AND FUTURE WORK

6.1 Summary of Results and Conclusions

Structural energetic materials were studied in detail to understand the underlying mechanisms leading to fragmentation and reaction. The systems investigated included aluminum, nickel, tantalum, tungsten, and zirconium and were fabricated via gas dynamic cold spraying (CS Ni+Al) and explosive compaction (binary mixtures composed of Ni+Al, W+Al, and Ta+Al; ternary mixture A composed of W+Ni+Al; and quaternary mixture B composed of W+Ni+Zr+Al). These materials were subjected to fragmentation experiments to determine fragment sizes and distributions. It was determined that fragments from explosively compacted Mixture A and Mixture B and cold sprayed Ni+Al yield comparable fragment sizes and distributions. Both the CS Ni+Al and the explosively compacted systems show evidence of interface failure. This suggests that the interface density is an important parameter in the fragmentation of composite reactive material systems. It was also shown that existing fragmentation models for ductile materials don't capture the fragmentation behavior of the structural energetic materials in question because of extensive crack branching, but a simple modification to the Grady-Kipp fragmentation model fits the average fragment size data reasonably well. The multicomponent nature and large interface densities of these materials create multiple fragments for each macroscopic fracture. This behavior results in large numbers of small fragments. The coupled nature of the fragmentation process means that the growth in fragment number is very rapid with increases in strain rate.

Fragment data from CS Ni+Al, EC Mixture A, and EC Mixture B demonstrate

that structural energetic material fragments can form a significant mass of combustion fuel for a post detonation after burn. The potential combustion energy of these fragments was shown to be a significant fraction of the detonation enthalpy available from the charges used for the fragmentation experiments.

Impact experiments and parametric simulations of impact experiments were conducted on explosively compacted Ni+Al, Ta+Al, W+Al, and cold sprayed Ni+Al. These studies show that the topology of the microstructure constituents, particularly the stronger phase, plays a significant role in regulating impact induced reactions. Materials where the hard phase is topologically connected are more likely to react at a lower impact velocity due to plastic deformation induced temperature increases. When a compliant matrix is used to surround stronger simply connected particles, the compliant matrix accommodates nearly all of the deformation, which limits plastic deformation induced heating in the stronger particles.

6.1.1 Significant Contributions

The following significant contributions have been made in this work:

- Shock compression data for cold sprayed nickel+aluminum with five percent porosity has been experimentally determined for the first time. A mesoscale model was utilized to predict the Hugoniot of cold sprayed Ni+Al, and the computationally derived Hugoniot was combined with a simple porosity model and validated with the shock compression data.

- Fragment data on various metal+Al based structural energetic materials has been collected. Comparison with Mott [156] and Kipp and Grady [179] fragmentation models indicate that the average fragment size of structural energetic materials is well predicted by these models, particularly that of Kipp and Grady, at or below strain rates on the order of 10^3. With increasing strain rate, the

growth of extensive networks of cracks leads to a more rapid increase in fragment number with strain rate. The Kipp and Grady model was modified to account for this increase at high strain rates and captures the trends of the experimental data reasonably well.

- It has been demonstrated that at strain rates above 10^5, for the studied structural energetic material systems, a sufficient quantity of fragments is generated to be an important source of energy via combustion or intermetallic reaction .

- It has been shown that the topology of the microstructure constituents plays a significant role in regulating the impact induced reaction behavior of metal+Al systems. This is particularly true of the topological properties of the less compliant phase(s) in metal+Al structural energetic systems.

6.2 Proposed Future Work on Structural Energetic Materials

As this work has progressed, a number of questions have developed which would require further experimental and computation efforts. These additional explorations should include different, and in some cases larger scale, fragmentation tests, an exploration of the effect of surface area per unit volume, an investigation of the optimal topology of a structural energetic material, and further study of the role of phosphorous in Ni coatings.

A careful study of the fragmentation results revealed that additional fracture mechanisms were taking place. In the case of the experimental set-up used by Cambridge, bending of the sample rings led to horizontal tension fractures. In the case of the Ohio State experiments, complex ring loading led to shear fractures developing within the ring. In both cases, fracture surfaces emitted small fragments due to crack branching. It is noted that in both experimental setups, structural metals were tested without developing these additional fragmentation mechanisms. However, it would

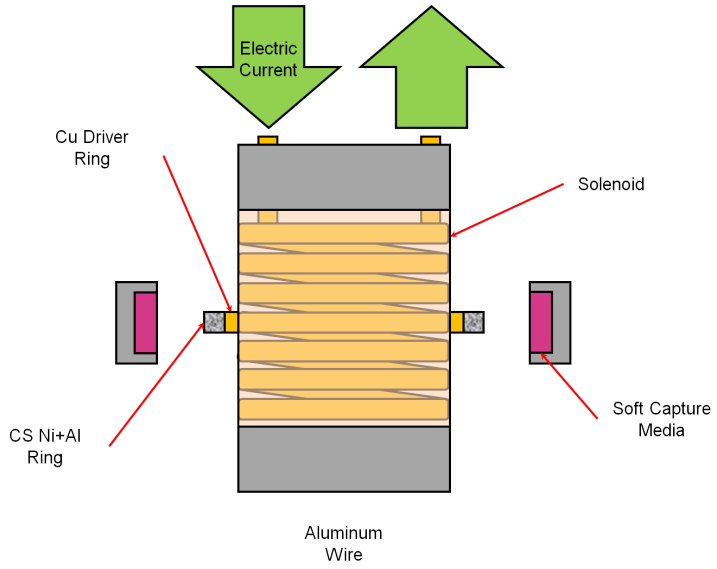

Figure 6.1: Expanding ring experiment with copper driver ring. The copper driver ring pushes the sample ring into fragmentation.

be desirable to determine how much the fragmentation behavior of the structural energetic materials would be altered if subjected to a more carefully controlled loading scenario. The crack branching that was observed doesn't result from geometry, but from low interface strength and high interface density. One possibility would be to use the same technique Grady and Benson used, but with a Cu driver ring as shown in Figure 6.1. The SEM rings would be mounted on the Cu driver ring which would then be mounted on the mandrel containing the solenoid. The Cu ring would drive the SEM ring outward and, as the more conductive element, contain most of the current. This would diminish the likelihood of electrical arcing setting off a reaction in the energetic samples and would provide a cleaner uniaxial stress loading to the sample rings which would avoid the bending and shear problems which developed in the other experimental setups.

Ultimately, higher strain rates are required in order to see how much mass ends up in a fragment size that may combust. The cased charge fragmentation test had measured fragment velocities of 2 Km/s. For a 72 mm initial diameter this leads to an initial strain rate of $\geq 6\text{x}10^4$. This was for TNT; more energetic explosives such

as RDX, HMX, and other newer formulations will achieve still higher strain rates. Experimental information about fragment behavior at these rarefied strain rates is entirely lacking, but essential for any practical application of structural energetic materials. In a laboratory setting, these strain rates are more likely to be achieved by changing the sample size to a minimum size and utilizing an exploding wire setup than by using powerful explosives. Proper scaling of sample ring sizes should ensure agreement with larger sample data; caution is required to avoid reducing sample size so much that size effects become an issue.

Extensive formation of fragments implied that branching of the main fracture led to the formation of many smaller fragments. It is clear that this process is influenced by the density of interfaces in the sample. The effect of interface density on fragment size and distribution was not studied systematically in this thesis and the relationship is not likely to be trivial. The Mixture A, Mixture B, and cold sprayed Ni+Al samples for which fragmentation properties were studied had roughly similar interface densities. However, there was strong evidence that the CS Ni+Al fractures were influenced by interface failure and some evidence that this was the case in Ni+Al, W+Al, Mixture A and Mixture B as well. The interface density essentially fixes one of the fragment distribution tails by dictating the smallest possible fragment size. However, the effect on the distribution shape and maximum fragment size are not necessarily dictated by the minimum spacing of interfaces. Surface area per unit volume may prove to be a useful variable in tailoring attributes of the fragment size distribution if its effect could be quantified. A reasonable approach would be to utilize samples formed from powders of radically different size. Samples formed from -325 mesh powder in and samples formed from +100 mesh powders, yielding size differences of about 1:3, would be a good place to start. It would also be of great interest to combine two different mesh sizes of powders to study the effect on fragment size distribution. This would lead to an improved understanding of the role

of interface density in fragment size and fragment distribution.

Topology of a structural energetic material influences the deformation and subsequent reaction behavior. Therefore a natural extension of this work would be to explore the optimal microstructure for impact induced reaction. It is not clear at this point if this microstructure would partition deformation such that both materials would change temperature equally for an increment of deformation or if this material would partition deformation such that the phase with the higher melting point would experience greater deformation induced temperature increase. In this work deformation has been taken as a surrogate for increases in temperature. This amounts to a tacit assumption of an equal volumetric heat capacity of all phases in a microstructure. Obviously, this is not correct, though the volumetric heat capacities of most solids lie between 1 and 4 $\frac{J}{cm^3K}$. An optimal microstructure would balance biasing the topological connectivity of the composite toward the material with the greater heat capacity with biasing the topological connectivity of the composite toward the material with greater strength. The effects and relative importances of these factors remain to be determined.

Another issue that has developed which would be of great interest is the role of phosphorous in the Ni coating on the Al particles. It has been established that a Ni coating inhibits agglomeration and enhances combustion behavior. The changes in melting point, strength, and strain to failure in thin Ni coatings would all play different and not necessarily complementary roles in the combustion process. A reduction in melting point tends to lead to agglomeration, an increase in strength may militate against thermal failure of the Ni coating. However, reducing the strain to failure may very well lead to earlier fracture of the Ni coating and further reduce the latency period before combustion begins. The mechanical properties of Ni-P coatings are also important to explore from the perspective of impact induced reaction. A brittle Ni coating would be less likely to undergo useful deformation induced heating than one

which is ductile, though it might mix more readily with the softer aluminum matrix after fracturing.

True understanding of any topic is like the horizon, it beckons and recedes before the inquiring mind, leading ever onward. This is certainly true in the case of structural energetic materials. Much work remains to fully understand the fragmentation behavior, the effects of topology and the influence of constituent behavior on the fragmentation and impact induced reaction of structural energetic materials.

REFERENCES

[1] W. G. Chace, "Exploding wires," *Physics Today*, vol. 17, no. 8, pp. 19–24, 1964. 1

[2] *Scientific Papers*. Cambridge University Press, 1910. 1

[3] C. Lineau, "Random fracture of a brittle solid," *Journal of the Franklin Institute*, pp. 221,485–494,674–686,769–787, 1936. 1

[4] N. F. Mott, "Fragmentation of H.E. shells: A theoretical formula for the distribution of weights of fragments," Tech. Rep. A.C. 3642, Ministry of Supply, 1943. 1, 43, 94, 108, 109

[5] R. Gurney, "The initial velocities of fragments from bombs, shell, grenades," Tech. Rep. BRL 405, US Army Ballistic Research Laboratory, Aberdeen Proving Ground, MD, 1943. 1, 43, 94

[6] G. Taylor, *Scientific Papers of G.I. Taylor [Vol III, No. 44]*. Cambridge University Press, 1 ed., 1963. 1

[7] R. E. Winter, "Measurement of fracture strain at high strain rates," in *Mechanical properties at high rates of strain, 1979: proceedings of the Second Conference on the Mechanical Properties of Materials at High Rates of Strain* (J. E. Harding, ed.), vol. 47, (Oxford, England), pp. 81–89, Bristol: Institute of Physics, Mar. 1979. 1, 50

[8] J. R. Asay and M. Shahinpoor, eds., *High-Pressure Shock Compression of Solids*. Springer, 1 ed., June 1993. 1

[9] D. A. Shockey, D. R. Curran, L. Seaman, J. T. Rosenberg, and C. F. Petersen, "Fragmentation of rock under dynamic loads," *International Journal of Rock Mechanics and Mining Sciences and Geomechanics Abstracts*, vol. 11, pp. 303–317, Aug 1974. 1

[10] D. Grady and M. Kipp, "The micromechanics of impact fracture of rock," *International Journal of Rock Mechanics and Mining Sciences & Geomechanics Abstracts*, vol. 16, pp. 293–302, Oct 1979. 1

[11] R. Moyes, "Explosive violence," Aug 2009. ISBN: 978-0-9551923-8-8. 2

[12] L. de Béjar, L. Simmons, and J. Davis, "Standoff-mortar fragment velocity characterization before and after perforating conventional building walls," *International Journal of Impact Engineering*, vol. 35, pp. 1043–1052, Sep 2008. 3

[13] P. Cooper, *Explosives Engineering*. Wiley-VCH, 1 ed., Nov. 1996. 3

[14] C. o. A. E. Materials and N. R. C. Manufacturing Technologies, *Advanced Energetic Materials*. The National Academies Press, 2004. 2, 4, 5, 6

[15] R. Ames, "Energy release characteristics of impact-initiated energetic materials," *MRS Proceedings*, vol. 896, 2006. 2, 5, 8, 9, 35, 55, 182, 183

[16] R. G. Ames and S. Waggener, "Reaction efficiences for impact initiated energetic materials," in *Proceedings 32nd International Pyrotechnics Seminar*, pp. 180–1–180–9, June 2005. 4, 5, 8, 9, 35, 55, 182

[17] B. Aydelotte, C. H. Braithwaite, K. McNesby, R. Benjamin, N. Thadhani, D. M. Williamson, and M. Trexler, "A study of fragmentation in a Ni+Al structural energetic material," *AIP Conference Proceedings*, vol. 1426, pp. 1097–1100, Mar. 2012. 4, 118, 121

[18] N. N. Thadhani, "Shock-induced and shock-assisted solid-state chemical reactions in powder mixtures," *Journal of Applied Physics*, vol. 76, pp. 2129–2138, Aug. 1994. 5, 20

[19] Y. Horie, R. Graham, and I. Simonsen, "Synthesis of nickel aluminides under high-pressure shock loading," *Materials Letters*, vol. 3, pp. 354–359, July 1985. 5, 20, 24

[20] E. Dunbar, N. N. Thadhani, and R. A. Graham, "High-pressure shock activation and mixing of nickel-aluminium powder mixtures," *Journal of Materials Science*, vol. 28, no. 11, pp. 2903–2914, 1993. 5, 24, 30, 66, 67

[21] D. Eakins and N. Thadhani, "Role of constituent configuration on shock-induced reactions in a Ni+Al powder mixture," *MRS Online Proceedings Library*, vol. 896, 2005. 5, 21, 27

[22] D. E. Eakins and N. N. Thadhani, "Investigation of Shock-Induced reactions in a Ni+Al powder mixture," *AIP Conference Proceedings*, vol. 845, pp. 1153–1156, July 2006. 5, 21, 27

[23] B. E. Homan, K. L. McNesby, J. Ritter, J. Colburn, A. Brant, and R. Pandey, "Investigations of the energy release mechanisms of aluminum-nickel reactive material system," (Orlando, FL), Dec. 2008. 5, 32, 35, 56, 74, 168, 182

[24] B. E. Homan, K. L. McNesby, J. Ritter, J. Colburn, and A. Brant, "Characterization of the combustion behavior of aluminum-nickel based reactive materials," Tech. Rep. ARL-TR-4917, Army Research Laboratory, Aberdeen Proving Ground, MD, Aug. 2009. 5, 35, 56, 168, 182

[25] R. Ames, "Vented chamber calorimetry for impact-initiated energetic materials," in *43rd AIAA Aerospace Sciences Meeting and Exhibit*, Aerospace Sciences Meetings, American Institute of Aeronautics and Astronautics, Jan. 2005. 0. 5, 9, 32, 35, 55, 182

[26] F. Zhang and W. H. Wilson, "The effect of charge reactive metal cases on air blast," *AIP Conference Proceedings*, vol. 1195, pp. 149–152, Dec. 2009. 6, 56, 173

[27] L. Ferranti and N. N. Thadhani, "Dynamic mechanical behavior characterization of epoxy-cast al + fe203 thermite mixture composites," *Metallurgical and Materials Transactions A*, vol. 38, no. 11, pp. 2697–2715, 2007. 8, 9

[28] C. Badiola, M. Schoenitz, X. Zhu, and E. L. Dreizin, "Nanocomposite thermite powders prepared by cryomilling," *J. Alloys Compd.*, vol. 488, pp. 386–391, Nov. 2009. 8, 9

[29] R. Russell, S. Bless, and M. Pantoya, "Impact-driven thermite reactions with iodine pentoxide and silver oxide," *Journal of Energetic Materials*, vol. 29, pp. 175–192, June 2011. 8, 9

[30] D. Eakins and N. N. Thadhani, "Discrete particle simulation of shock wave propagation in a binary Ni+Al powder mixture," *J. Appl. Phys.*, vol. 101, no. 4, pp. 043508–18, 2007. 8, 85

[31] D. Eakins and N. Thadhani, "Mesoscale simulation of the configuration-dependent shock-compression response of ni + al powder mixtures," *Acta Mater.*, vol. 56, pp. 1496–1510, Apr. 2008. 8, 85

[32] S. Du and N. Thadhani, "Impact initiation of pressed Al-Based Intermetallic-Forming powder mixture compacts," in *Proc., 16th APS Topical Conference on Shock Compression of Condensed Matter. American Physical Society* (M. Elert, M. D. Furnish, W. W. Anderson, W. G. Proud, and W. T. Butler, eds.), vol. 54, (Nashville, Tennessee), pp. 470–473, Woodbury, N.Y. : AIP Press, 2009. 8, 201

[33] E. B. Herbold, N. N. Thadhani, and J. L. Jordan, "Observation of a minimum reaction initiation threshold in ball-milled Ni+Al under high-rate mechanical loading," *J. Appl. Phys.*, vol. 109, p. 066108, 2011. 8, 183, 201

[34] S. H. Fischer and M. C. Grubelich, "A survey of combustible metals thermites and intermetallics for pyrotechnic applications," tech. rep., July 1996. 8

[35] X. Zhu, M. Schoenitz, V. K. Hoffmann, and E. L. Dreizin, "Reactive al-li powders prepared by mechanical alloying," *MRS Online Proceedings Library*, vol. 896, 2005. 9, 41

[36] Y. L. Shoshin, M. A. Trunov, X. Zhu, M. Schoenitz, and E. L. Dreizin, "Ignition of aluminum-rich al-ti mechanical alloys in air," *Combustion and Flame*, vol. 144, pp. 688–697, Mar. 2006. 9, 41

[37] W. Mock and W. H. Holt, "Impact initiation of rods of pressed polytetrafluoroethylene (PTFE) and aluminum powders," *AIP Conference Proceedings*, vol. 845, pp. 1097–1100, July 2006. 9

[38] J. Addiss, J. Cai, S. Walley, W. Proud, and V. Nesterenko, "High strain and strain-rate behaviour of PTFE/aluminuim/tungsten mixtures," in *Shock Compression of Condensed Matter - 2007, Pts 1 and 2* (M. Elert, M. D. Furnish, R. Chau, N. C. Holmes, and J. Nguyen, eds.), vol. 955, pp. 773–776, 2007. 9

[39] E. B. Herbold, J. Cai, D. J. Benson, and V. F. Nesterenko, "Simulation of particle size effect on dynamic properties and fracture of PTFE-W-Al composites," in *Shock Compression of Condensed Matter - 2007, Pts 1 and 2* (M. Elert, M. D. Furnish, R. Chau, N. C. Holmes, and J. Nguyen, eds.), vol. 955, pp. 785–788, 2007. 9

[40] W. Mock and J. T. Drotar, "Effect of aluminum particle size on the impact initiation of pressed PTFE-AL composite rods," *AIP Conference Proceedings*, vol. 955, pp. 971–974, Dec. 2007. 9

[41] J. Cai, V. F. Nesterenko, K. S. Vecchio, F. Jiang, E. B. Herbold, D. J. Benson, J. W. Addiss, S. M. Walley, and W. G. Proud, "The influence of metallic particle size on the mechanical properties of polytetraflouroethylene-al-w powder composites," *Applied Physics Letters*, vol. 92, Jan. 2008. 9

[42] E. B. Herbold, V. F. Nesterenko, D. J. Benson, J. Cai, K. S. Vecchio, F. Jiang, J. W. Addiss, S. M. Walley, and W. G. Proud, "Particle size effect on strength, failure, and shock behavior in polytetrafluoroethylene-al-w granular composite materials," *Journal of Applied Physics*, vol. 104, Nov. 2008. 9

[43] S. Xu, S. Yang, and W. Zhang, "The mechanical behaviors of polytetrafluorethylene/Al/W energetic composites," *Journal of Physics-Condensed Matter*, vol. 21, July 2009. 9

[44] K. Kappagantula, M. L. Pantoya, and E. M. Hunt, "Impact ignition of aluminum-teflon based energetic materials impregnated with nano-structured carbon additives," *Journal of Applied Physics*, vol. 112, pp. 024902–024902–7, July 2012. 9

[45] V. Subramanian and N. N. Thadhani, "Reaction behavior of shock compressed aluminum and iron-oxide powder mixtures," *AIP Conference Proceedings*, vol. 370, pp. 681–684, May 1996. 9

[46] N. N. Thadhani, K. S. Vandersall, R. T. Russell, R. A. Graham, G. T. Holman, and M. U. Anderson, "Shock compression of Al+Fe2O3 powder mixtures of different volumetric distributions," *AIP Conference Proceedings*, vol. 429, pp. 553–556, July 1998. 9

[47] S. M. Walley, J. E. Balzer, W. G. Proud, and J. E. Field, "Response of thermites to dynamic high pressure and shear," *Proceedings of the Royal Society of London. Series A: Mathematical, Physical and Engineering Sciences*, vol. 456, pp. 1483 –1503, June 2000. 9, 183

[48] N. R. Patel, *Intermediate Strain Rate Behavior of Two Structural Energetic Materials*. PhD thesis, Georgia Institute of Technology, Atlanta, GA, 2004. 9

[49] L. Ferranti and N. N. Thadhani, "Dynamic impact characterization of Al+Fe2O3+30% epoxy composites using time synchronized high-speed camera and VISAR measurements," *MRS Online Proceedings Library*, vol. 896, 2005. 9

[50] J. Nable, A. Mercado, and A. Sherman, "Novel energetic composite materials," *MRS Online Proceedings Library*, vol. 896, 2005. 9

[51] J. A. Puszynski, C. J. Bulian, and J. J. Swiatkiewicz, "The effect of nanopowder attributes on reaction mechanism and ignition sensitivity of nanothermites," *MRS Online Proceedings Library*, vol. 896, 2005. 9

[52] A. Rai, L. Zhou, A. Prakash, A. McCormick, and M. R. Zachariah, "Understanding and tuning the reactivity of nano-energetic materials," *MRS Online Proceedings Library*, vol. 896, 2005. 9

[53] S. F. Son, T. Foley, V. E. Sanders, A. Novak, D. Tasker, and B. W. Asay, "Overview of nanoscale energetic materials research at Los Alamos," *MRS Online Proceedings Library*, vol. 896, 2005. 9

[54] "Self-assembled ordered energetic composites of CuO nanorods and nanowells and Al nanoparticles with high burn rates," *MRS Online Proceedings Library*, vol. 896, 2005. 9

[55] V. Tomar and M. Zhou, "A study of shock-wave propagation in single crystalline fcc-Al and I-Fe2O3 and an interface between two such phases using MD simulations," *MRS Online Proceedings Library*, vol. 896, 2005. 9

[56] S. Umbrajkar, M. Schoenitz, and E. L. Dreizin, "Structural refinement in Al-MoO3 nanocomposites prepared by arrested reactive milling," *MRS Online Proceedings Library*, vol. 896, 2005. 9

[57] M. Schoenitz, T. S. Ward, and E. L. Dreizin, "Fully dense nano-composite energetic powders prepared by arrested reactive milling," *Proceedings of the Combustion Institute*, vol. 30, pp. 2071–2078, Jan. 2005. 9

[58] L. Ferranti, N. N. Thadhani, and J. W. House, "Dynamic mechanical behavior characterization of epoxy-cast Al+Fe2O3 mixtures," *AIP Conference Proceedings*, vol. 845, pp. 805–808, July 2006. 9

[59] L. Ferranti, J. L. Jordan, R. D. Dick, and N. N. Thadhani, "Shock hugoniot behavior of particle reinforced polymer composites," *AIP Conference Proceedings*, vol. 955, pp. 123–126, Dec. 2007. 9

[60] E. L. Dreizin, "Metal-based reactive nanomaterials," *Progress in Energy and Combustion Science*, vol. 35, pp. 141–167, Apr. 2009. 9

[61] E. M. Hunt, S. Malcolm, M. L. Pantoya, and F. Davis, "Impact ignition of nano and micron composite energetic materials," *International Journal of Impact Engineering*, vol. 36, pp. 842–846, June 2009. 9

[62] S. Bless, R. Russell, and M. Pantoya, "Advanced energetic materials for agent defeat: Impact driven reactions in biocidal reactive materials for WMD applications," Annual Progress Report 2008-2009 IAT.R 0589, Institute for Advanced Technology The University of Texas at Austin, Austin, TX, Sept. 2009. 9

[63] L. Dures, I. Plaksin, J. Antunes, J. Campos, and A. Portugal, "Radial combustion dynamics in Fe2O3/Al thermite: Variability of the flame propagation profiles," *AIP Conference Proceedings*, vol. 1195, pp. 428–431, Dec. 2009. 9

[64] A. Fraser, J. P. Borg, and J. L. Jordan, "The effect of nano-particles on the one-dimensional shock compaction of Al-MnO2 epoxy mixtures," *AIP Conference Proceedings*, vol. 1195, pp. 61–64, Dec. 2009. 9, 16

[65] C. Farley and M. Pantoya, "Reaction kinetics of nanometric aluminum and iodine pentoxide," *Journal of Thermal Analysis and Calorimetry*, vol. 102, pp. 609–613, June 2010. 9

[66] B. Dikici, M. L. Pantoya, and V. Levitas, "The effect of pre-heating on flame propagation in nanocomposite thermites," *Combustion and Flame*, vol. 157, pp. 1581–1585, Aug. 2010. 9

[67] K. S. Martirosyan, "Nanoenergetic gas-generators: principles and applications," *Journal of Materials Chemistry*, vol. 21, pp. 9400–9405, June 2011. 9

[68] R. Russell, S. Bless, A. Blinkova, and T. Chen, "Sporicidal effects of iodine-oxide thermite reaction products," *AIP Conference Proceedings*, vol. 1426, pp. 157–160, Mar. 2012. 9

[69] S. Meschel and O. Kleppa, "Standard enthalpies of formation of 5d aluminides by high-temperature direct synthesis calorimetry," *Journal of Alloys and Compounds*, vol. 197, pp. 75–81, June 1993. 9

[70] F. Chrifi-Alaoui, M. Nassik, K. Mahdouk, and J. Gachon, "Enthalpies of formation of the Al-Ni intermetallic compounds," *Journal of Alloys and Compounds*, vol. 364, pp. 121–126, Feb. 2004. 9

[71] B. M. Dobratz and P. Crawford, *LLNL Explosives Handbook: Properties of Chemical Explosives and Explosive Simulants.* Lawrence Livermore National Laboratory, University of California, 1985. 9

[72] J. R. Asay and M. Shahinpoor, eds., *High-Pressure Shock Compression of Solids.* Springer, 1 ed., June 1993. 10, 14, 19

[73] M. A. Meyers, *Dynamic Behavior of Materials.* Wiley-Interscience, 1 ed., Sept. 1994. 10, 11, 15, 16

[74] R. G. McQueen, S. P. Marsh, J. Taylor, J. Fritz, and W. Carter, *The Equation of State of Solids from Shock Wave Studies*, pp. 293–417. Academic, 1970. 15, 16

[75] Y. Alekseev, L. Altshuler, and V. Krupnikova, "Shock compression of two-component paraffin-tungsten mixtures," *Journal of Applied Mechanics and Technical Physics*, vol. 12, p. 624627, 1971. 15

[76] S. S. Batsanov, *Effects of Explosions on Materials: Modification and Synthesis Under High-Pressure Shock Compression*. Springer, Mar 1994. 15

[77] M. R. Baer, C. A. Hall, R. L. Gustavsen, D. E. Hooks, and S. A. Sheffield, "Isentropic loading experiments of a plastic bonded explosive and constituents," *Journal of Applied Physics*, vol. 101, p. 03490603490612, Feb 2007. 16

[78] J. L. Jordan, D. Dattelbaum, L. Ferranti, G. Sutherland, M. Baer, W. Richards, S. Sheffield, R. D. Dick, and N. N. Thadhani, "Shock equation of state of single constituent and multi-constituent epoxy-based particulate composites," *AIP Conference Proceedings*, vol. 1195, pp. 1253–1256, Dec 2009. 16

[79] D. E. Grady, N. A. Winfree, G. I. Kerley, L. T. Wilson, and L. D. Kuhns, "Computational modeling and wave propagation in media with inelastic deforming microstructure," *Le Journal de Physique IV*, vol. 10, p. 9.159.20, Sep 2000. 16, 19

[80] J. L. Jordan, L. Ferranti, R. A. Austin, R. D. Dick, J. R. Foley, N. N. Thadhani, D. L. McDowell, and D. J. Benson, "Equation of state of aluminum-iron oxide-epoxy composite," *Journal of Applied Physics*, vol. 101, pp. 093520–093520–9, May 2007. 16, 85

[81] R. R. Boade, "Compression of porous copper by shock waves," *Journal of Applied Physics*, vol. 39, pp. 5693–5702, Nov 1968. 17

[82] W. Herrmann, "Constitutive equation for the dynamic compaction of ductile porous materials," *Journal of Applied Physics*, vol. 40, pp. 2490–2499, May 1969. 19

[83] Y. Horiguchi, "The formation of tungsten and aluminum carbides by explosive shock," *Journal of the Less Common Metals*, vol. 11, pp. 378–380, Nov. 1966. 20

[84] Y. Horie, R. A. Graham, and I. Simonsen, "Observations on the shock synthesis of intermetallic compounds," in *Metallurgical Applications of Shock-Wave and High-Strain-Rate Phenomena* (L. E. Murr, K. Staudhammer, and M. A. Meyers, eds.), pp. 1023–1035, New York: Marcel Dekker, Inc., 1986. 20, 21

[85] L. H. Yu and M. A. Meyers, "Shock synthesis and synthesis-assisted shock consolidation of silicides," *Journal of Materials Science*, vol. 26, pp. 601–611, Feb. 1991. 21

[86] S. C. Kelly, S. Barron, N. Thadhani, and T. P. Weihs, "Laser-accelerated flyer system for investigating reactions in ni-al mixtures," *AIP Conference Proceedings*, vol. 1426, pp. 599–602, Mar. 2012. 21

[87] S. S. Batsanov, G. S. Doronin, S. V. Klochkov, and A. I. Teut, "Synthesis reactions behind shock fronts," *Combustion, Explosion and Shock Waves*, vol. 22, pp. 765–768, Nov. 1986. 21

[88] E. Dunbar, R. A. Graham, G. T. Holman, M. U. Anderson, and N. N. Thadhani, "Time-resolved pressure measurements in chemically reacting powder mixtures," *AIP Conference Proceedings*, vol. 309, pp. 1303–1306, July 1994. 21, 30

[89] N. Thadhani, R. Graham, T. Royal, E. Dunbar, M. Anderson, and G. Holman, "Shock-induced chemical reactions in ti-si powder mixtures: Time-resolved pressure measurements and materials analysis," *Journal of Applied Physics*, vol. 82, no. 3, pp. 1113–1128, 1997. 21, 28, 30

[90] M. Yoshida and N. N. Thadhani, "Study of shock induced solid state reactions by recovery experiments and measurements of hugoniot and sound velocity," in *Shock Waves in Condensed Matter-1991* (S. Schmidt, R. Dick, J. Forbes, and D. Tasker, eds.), pp. 585–592, Lausanne: Elsevier, 1992. 21, 28

[91] X. Xu and N. N. Thadhani, "Investigation of Shock-Induced chemical reactions in Ni-Ti powder mixtures using instrumented experiments," *AIP Conference Proceedings*, vol. 620, pp. 1123–1126, July 2002. 21, 27, 28

[92] X. Xu and N. N. Thadhani, "Investigation of shock-induced reaction behavior of as-blended and ball-milled Ni+Ti powder mixtures using time-resolved stress measurements," *Journal of Applied Physics*, vol. 96, pp. 2000–2009, Aug. 2004. 21, 27, 28

[93] M. B. Boslough, "Shock-induced chemical reactions in nickel-aluminum powder mixtures: Radiation pyrometer measurements," *Chemical Physics Letters*, vol. 160, pp. 618–622, Aug. 1989. 21

[94] M. B. Boslough, "A thermochemical model for shock-induced reactions (heat detonations) in solids," *The Journal of Chemical Physics*, vol. 92, pp. 1839–1848, Feb. 1990. 22

[95] F.-X. Jett, A. J. Higgins, S. Goroshin, D. L. Frost, Y. Charron-Tousignant, M. I. Radulescu, and J. J. Lee, "In-situ measurements of the onset of bulk exothermicity in shock initiation of reactive powder mixtures," *Journal of Applied Physics*, vol. 109, pp. 084905–084905–17, Apr. 2011. 22

[96] G. I. Taylor and H. Quinney, "The latent energy remaining in a metal after cold working," *Proceedings of the Royal Society of London. Series A*, vol. 143, pp. 307–326, Jan. 1934. 23

[97] L. Kator and P. Nyulas, "Method for determining the changes in the energy stored by a metal during plastic deformation," *Strength of Materials*, vol. 3, pp. 28–31, Jan. 1971. 23

[98] A. T. Zehnder, "A model for the heating due to plastic work," *Mechanics Research Communications*, vol. 18, no. 1, pp. 23–28, 1991. 23

[99] J. Mason, A. Rosakis, and G. Ravichandran, "On the strain and strain rate dependence of the fraction of plastic work converted to heat: an experimental study using high speed infrared detectors and the kolsky bar," *Mechanics of Materials*, vol. 17, pp. 135–145, Mar. 1994. 23

[100] P. Rosakis, A. J. Rosakis, G. Ravichandran, and J. Hodowany, "A thermodynamic internal variable model for the partition of plastic work into heat and stored energy in metals," *Journal of the Mechanics and Physics of Solids*, vol. 48, pp. 581–607, Mar. 2000. 23

[101] G. Ravichan, A. Rosakis, J. Hodowany, and P. Rosakis, "On the conversion of plastic work into heat during high strain rate deformation," in *SHOCK COMPRESSION OF CONDENSED MATTER - 2001: Proceedings of the Conference of the American Physical Society, Topical Group on Shock Compression of Condensed Matter*, (Atlanta, Georgia), pp. 557–562, American Institute of Physics, June 2001. 23

[102] A. T. Zehnder and A. J. Rosakis, "On the temperature distribution at the vicinity of dynamically propagating cracks in 4340 steel," *Journal of the Mechanics and Physics of Solids*, vol. 39, no. 3, pp. 385–415, 1991. 23

[103] V. F. Nesterenko, M. A. Meyers, H. C. Chen, and J. C. LaSalvia, "Controlled high-rate localized shear in porous reactive media," *Applied Physics Letters*, vol. 65, no. 24, pp. 3069–3071, 1994. 23, 29

[104] D. Eakins and N. N. Thadhani, "Discrete particle simulation of shock wave propagation in a binary Ni+Al powder mixture," *Journal of Applied Physics*, vol. 101, no. 4, pp. 043508–18, 2007. 23, 27

[105] D. Eakins and N. Thadhani, "Mesoscale simulation of the configuration-dependent shock-compression response of ni + al powder mixtures," *Acta Materialia*, vol. 56, pp. 1496–1510, Apr. 2008. 23, 27

[106] L. F. Trueb, "Electron microscope study of thermal recovery processes in explosion shocked nickel," *Journal of Applied Physics*, vol. 40, pp. 2976–2987, June 1969. 23

[107] B. Morosin and R. Graham, "X-ray diffraction line-broadening studies on shock-modified rutile and alumina," *Materials Science and Engineering*, vol. 66, pp. 73–87, Sept. 1984. 23

[108] W. Hammetter, R. Graham, B. Morosin, and Y. Horie, "Effects of shock modification on the self-propagating high temperature synthesis of nickel aluminides," in *Shock Waves in Condensed Matter 1987* (S. Schmidt and N. C. Holmes, eds.), pp. 431–434, Elsevier Science Publishers B.V., 1988. 23, 24, 25, 67, 79, 174, 176

[109] N. Thadhani, S. Work, R. Graham, and W. Hammetter, "Shock-induced reaction synthesis (SRS) of nickel aluminides," *Journal of Materials Research*, vol. 7, no. 05, pp. 1063–1075, 1992. 24, 30, 67, 174

[110] D. L. Frost, F.-X. Jetté, S. Goroshin, A. J. Higgins, and J. J. Lee, "Effect of particle morphology on critical conditions for shock-initiated reactions in titanium-silicon powder mixtures," *AIP Conference Proceedings*, vol. 1195, pp. 153–156, Dec. 2009. 24, 31, 67

[111] S. A. Namjoshi and N. N. Thadhani, "Reaction synthesis of shock densified titanium-silicon powder mixtures," *AIP Conference Proceedings*, vol. 429, pp. 659–662, July 1998. 26

[112] D. A. Porter, K. E. Easterling, and M. Sherif, *Phase Transformations in Metals and Alloys, Third Edition*. CRC Press, 3 ed., Feb 2009. 26

[113] I. Song and N. N. Thadhani, "Shock-induced chemical reactions and synthesis of nickel aluminides," *Metallurgical Transactions A*, vol. 23, pp. 41–48, Jan. 1992. 26, 29

[114] P. E. Specht, N. N. Thadhani, and T. P. Weihs, "Configurational effects on shock wave propagation in ni-al multilayer composites," *Journal of Applied Physics*, vol. 111, no. 7, pp. 073527–073527–12, 2012. 27, 85

[115] R. V. Reeves, J. D. E. White, A. M. Mukasyan, and S. F. Son, "Comparison of mechanical and thermal ignition characteristics for reactivity enhanced ni/al powders," *AIP Conference Proceedings*, vol. 1195, pp. 466–469, Dec. 2009. 28

[116] R. V. Reeves, A. S. Mukasyan, and S. Son, "Microstructural effects on ignition sensitivity in Ni/Al systems subjected to high strain rate impacts," *AIP Conference Proceedings*, vol. 1426, pp. 539–542, Mar. 2012. 28

[117] K. S. Vandersall and N. N. Thadhani, "Time-resolved measurements of the shock-compression response of Mo+2Si elemental powder mixtures," *Journal of Applied Physics*, vol. 94, pp. 1575–1583, Aug. 2003. 28

[118] S. Tamura and Y. Horie, "Discrete meso-dynamic simulation of thermal explosion in shear bands," *Journal of Applied Physics*, vol. 84, pp. 3574–3580, Oct. 1998. 28, 29

[119] V. F. Nesterenko, M. A. Meyers, H. C. Chen, and J. C. LaSalvia, "The structure of controlled shear bands in dynamically deformed reactive mixtures," *Metallurgical and Materials Transactions A*, vol. 26, pp. 2511–2519, Oct. 1995. 29

[120] K. Yano and Y. Horie, "A numerical study of shock-induced particle velocity dispersion in solid mixtures," *Journal of Applied Physics*, vol. 84, pp. 1292–1298, Aug. 1998. 29

[121] N. N. Thadhani, V. Subramanian, R. Russell, D. Savage, and Y. M. Gupta, "The effect of pulse duration on shock-induced chemical reaction in ti-si powder mixtures," *AIP Conference Proceedings*, vol. 370, pp. 709–712, May 1996. 29

[122] N. N. Thadhani, E. Dunbar, and R. A. Graham, "Characteristics of shock-compressed configuration of ti and si powder mixtures," *AIP Conference Proceedings*, vol. 309, pp. 1307–1310, July 1994. 30

[123] S. W. Du and N. N. Thadhani, "Impact initiation of pressed al-based intermetallic-forming powder mixture compacts," *AIP Conference Proceedings*, vol. 1195, pp. 470–473, Dec. 2009. 32

[124] S. W. Du, B. Aydelotte, D. Fondse, C.-T. Wei, F. Jiang, E. Herbold, K. Vecchio, M. A. Meyers, and N. N. Thadhani, "Explosive compaction of intermetallic-forming powder mixtures for fabricating structural energetic materials," *AIP Conference Proceedings*, vol. 1195, pp. 498–501, Dec. 2009. 32, 63, 65, 183, 198, 200, 205

[125] E. M. Hunt and M. L. Pantoya, "Impact sensitivity of intermetallic nanocomposites: A study on compositional and bulk density," *Intermetallics*, vol. 18, pp. 1612–1616, Aug. 2010. 33

[126] E. B. Herbold, N. N. Thadhani, and J. L. Jordan, "Observation of a minimum reaction initiation threshold in ball-milled Ni+Al under high-rate mechanical loading," *Journal of Applied Physics*, vol. 109, p. 066108, 2011. 33

[127] P.-H. Chiu and V. F. Nesterenko, "Dynamic behavior and fracture of granular composite al-w," in *DYMAT 2009 - 9th International Conferences on the Mechanical and Physical Behaviour of Materials under Dynamic Loading*, (Brussels, Belgium), pp. 947–953, EDP Sciences, 2009. WOS:000273128000003. 33

[128] P.-H. Chiu, S. Wang, E. Vitali, E. B. Herbold, D. J. Benson, and V. F. Nesterenko, "Particle size effect in granular composite aluminum/tungsten," in *Shock Compression of Condensed Matter - 2009, Pts 1 and 2* (M. L. Elert, W. T. Buttler, M. D. Furnish, W. W. Anderson, and W. G. Proud, eds.), vol. 1195, pp. 1345–1348, 2009. WOS:000276574100317. 33

[129] K. L. Olney, P. H. Chiu, C. W. Lee, V. F. Nesterenko, and D. J. Benson, "Role of material properties and mesostructure on dynamic deformation and shear instability in al-w granular composites," *Journal of Applied Physics*, vol. 110, pp. 114908–114908–9, Dec. 2011. 33

[130] P.-H. Chiu, C.-W. Lee, and V. F. Nesterenko, "Processing and dynamic testing of Al/W granular composites," *AIP Conference Proceedings*, vol. 1426, pp. 737–740, Mar. 2012. 33

[131] K. Olney, D. Benson, and V. F. Nesterenko, "Modeling shear instability and fracture in dynamically deformed Al/W granular composites," *AIP Conference Proceedings*, vol. 1426, pp. 729–732, Mar. 2012. 33

[132] C. Wei, E. Vitali, F. Jiang, S. Du, D. Benson, K. Vecchio, N. Thadhani, and M. Meyers, "Quasi-static and dynamic response of explosively consolidated metal-aluminum powder mixtures," *Acta Materialia*, vol. 60, pp. 1418–1432, Feb. 2012. 34, 71, 72, 81, 82, 144, 182, 186, 192, 198

[133] S. J. Spey, *Ignition properties of multilayer nanoscale reactive foils and the properties of metal-ceramic joints made with the same*. Ph.D., The Johns Hopkins University, United States – Maryland, 2006. 34, 66, 183, 185

[134] D. P. Adams, V. C. Hodges, M. M. Bai, E. Jones, M. A. Rodriguez, T. Buchheit, and J. J. Moore, "Exothermic reactions in Co/Al nanolaminates," *Journal of Applied Physics*, vol. 104, pp. 043502–043502–7, Aug. 2008. 34

[135] J. M. Densmore, M. M. Biss, B. E. Homan, and K. L. McNesby, "Thermal imaging of nickel-aluminum and aluminum-polytetrafluoroethylene impact initiated combustion," *Journal of Applied Physics*, vol. 112, pp. 084911–084911–5, Oct. 2012. 35, 168

[136] B. Rowland and W. B. Boyd, *U.S. Navy Bureau of Ordnance in World War II*. Bureau of Ordnance, Department of the Navy, 1953. 36

[137] J. Hunley, *The history of solid-propellant rocketry - What we do and do not know*. Joint Propulsion Conferences, American Institute of Aeronautics and Astronautics, Jun 1999. 36

[138] R. Pape and F. Schmidt, "Fires and explosions: Combustibility analysis of metals," *Advanced Materials & Processes*, vol. 167, pp. 41–44, Nov. 2009. 36

[139] R. Eckhoff, *Dust Explosions in the Process Industries, Second Edition*. Butterworth-Heinemann, 2 ed., 1997. 36, 37

[140] K. P. Brooks and M. W. Beckstead, "Dynamics of aluminum combustion," *Journal of Propulsion and Power*, vol. 11, pp. 769–780, Jul 1995. 36, 37, 169, 171

[141] Y. Huang, G. A. Risha, V. Yang, and R. A. Yetter, "Effect of particle size on combustion of aluminum particle dust in air," *Combustion and Flame*, vol. 156, no. 1, pp. 5–13, 2009. 36, 37

[142] M. W. Beckstead, "Correlating aluminum burning times," *Combustion, Explosion and Shock Waves*, vol. 41, pp. 533–546, Sept. 2005. 36, 37, 169

[143] K. L. Cashdollar and I. A. Zlochower, "Explosion temperatures and pressures of metals and other elemental dust clouds," *Journal of Loss Prevention in the Process Industries*, vol. 20, no. 4-6, pp. 337–348, 2007. 37, 41, 171

[144] B. Z. Eapen, V. K. Hoffmann, M. Schoenitz, and E. L. Dreizin, "Combustion of aerosolized spherical aluminum powders and flakes in air," *Combustion Science and Technology*, vol. 176, no. 7, p. 1055, 2004. 39

[145] D. L. Frost, S. Goroshin, J. Levine, R. Ripley, and F. Zhang, "Critical conditions for ignition of aluminum particles in cylindrical explosive charges," *AIP Conference Proceedings*, vol. 845, pp. 972–975, Jul 2006. 39, 171

[146] A. L. Breiter, V. M. Maltsev, and E. I. Popov, "Means of modifying metallic fuel in condensed systems," *Combustion, Explosion and Shock Waves*, vol. 26, pp. 86–92, Jan 1990. 39, 40, 172, 173, 174

[147] D. A. Yagodnikov and A. V. Voronetskii, "Experimental and theoretical study of the ignition and combustion of an aerosol of encapsulated aluminum particles," *Combustion, Explosion and Shock Waves*, vol. 33, pp. 49–55, Jan 1997. 40, 170, 173

[148] S. L. Vummidi, Y. Aly, M. Schoenitz, and E. L. Dreizin, "Characterization of fine nickel-coated powder as potential fuel additive," *Journal of Propulsion and Power*, vol. 26, pp. 454–460, May 2010. 40

[149] A. S. MUKASYAN, C. LAU, and A. VARMA, "Gasless combustion of aluminum particles clad by nickel," *Combustion Science and Technology*, vol. 170, no. 1, pp. 67–85, 2001. 40, 170, 172

[150] E. Shafirovich, A. Mukasyan, L. Thiers, A. Varma, B. Legrand, C. Chauveau, and I. Gökalp, "Ignition and combustion of al particles clad by ni," *Combustion Science and Technology*, vol. 174, no. 3, pp. 125–140, 2002. 40, 41, 170, 173

[151] Y. L. Shoshin, M. A. Trunov, X. Zhu, M. Schoenitz, and E. L. Dreizin, "Ignition of aluminum-rich Al-Ti mechanical alloys in air," *Combust. Flame*, vol. 144, pp. 688–697, Mar. 2006. 41, 183

[152] K. L. Cashdollar, "Overview of dust explosibility characteristics," *Journal of Loss Prevention in the Process Industries*, vol. 13, pp. 183–199, May 2000. 41

[153] B. R. Munson, D. F. Young, and T. H. Okiishi, *Fundamentals of Fluid Mechanics*. Wiley, 5 ed., May 2006. 42

[154] P. Cooper, *Explosives Engineering*. Wiley-VCH, 1 ed., Nov. 1996. 42, 43

[155] R. H. Bishop, "Maximum missile ranges from cased explosive charges," tech. rep., July 1958. 42, 43

[156] N. F. Mott, "Fragmentation of shell cases," *Proceedings of the Royal Society of London. Series A, Mathematical and Physical Sciences*, vol. 189, no. 1018, pp. 300–308, 1947. 43, 49, 50, 53, 94, 160, 213

[157] R. Gurney and J. Sarmousakis, "The mass distribution of fragments from bombs, shell, and grenades,," Tech. Rep. BRL 448, US Army Ballistic Research Laboratory, Aberdeen Proving Ground, MD, 1944. 43, 94

[158] N. Perrone, "On the use of the ring test for determining rate-sensitive material constants," *Experimental Mechanics*, vol. 8, pp. 232–236, May 1968. 43, 44, 94

[159] M. J. Forrestal, B. W. Duggin, and R. I. Butler, "An explosive loading technique for the uniform expansion of 304 stainless steel cylinders at high strain rates," *Journal of Applied Mechanics*, vol. 47, pp. 17–20, Mar. 1980. 44, 94

[160] T. Hiroe, K. Fujiwara, H. Hata, and H. Takahashi, "Deformation and fragmentation behaviour of exploded metal cylinders and the effects of wall materials, configuration, explosive energy and initiated locations," *International Journal of Impact Engineering*, vol. 35, pp. 1578–1586, Dec. 2008. 44, 94

[161] T. Hiroe, K. Fujiwara, H. Hata, M. Yamauchi, K. Tsutsumi, and T. Igawa, "Explosively driven expansion and fragmentation behavior for cylinders, spheres and rings of 304 stainless steel," *Materials Science Forum*, vol. 638-642, pp. 1035–1040, Jan. 2010. 44, 94

[162] F. I. Niordsen, "A unit for testing materials at high strain rates," *Experimental Mechanics*, vol. 5, pp. 23–32, 1965. 44, 53, 95

[163] H. Walling and M. J. Forrestal, "Elastic plastic expansion of 6061-t6 aluminum rings," *AIAA Journal*, vol. 11, no. 8, pp. 1196–1197, 1973. 44, 95

[164] D. Grady and D. Benson, "Fragmentation of metal rings by electromagnetic loading," *Experimental Mechanics*, vol. 12, pp. 393–400, 1983. 44, 45, 53, 95, 108, 157, 158, 159, 160, 161

[165] H. Zhang and K. Ravi-Chandar, "On the dynamics of necking and fragmentation–I. real-time and post-mortem observations in al 6061-O," *International Journal of Fracture*, vol. 142, no. 3, pp. 183–217, 2006. 45, 95

[166] H. Zhang and K. Ravi-Chandar, "On the dynamics of necking and fragmentation–II. effect of material properties, geometrical constraints and absolute size," *International Journal of Fracture*, vol. 150, no. 1, pp. 3–36, 2008. 45, 95

[167] H. Zhang and K. Ravi-Chandar, "Dynamic fragmentation of ductile materials," *Journal of Physics D: Applied Physics*, vol. 42, pp. 1–16, 2009. 45, 50, 95

[168] F. Zhou, J.-F. Molinari, and K. Ramesh, "Analysis of the brittle fragmentation of an expanding ring," *Computational Materials Science*, vol. 37, pp. 74–85, 2006. 45, 53

[169] F. Zhou, J.-F. Molinari, and K. Ramesh, "Effects of material properties on the fragmentation of brittle materials," *International Journal of Fracture*, vol. 139, no. 2, pp. 169–196, 2006. 45, 53

[170] R. E. Winter and H. G. Prestige, "A technique for the measurement of the high strain rate ductility of metals," *Journal of Materials Science Letters*, vol. 13, no. 8, pp. 1835–1837, 1979. 45, 46, 95

[171] T. J. Vogler, T. F. Thornhill, W. D. Reinhart, L. C. Chhabildas, D. E. Grady, L. T. Wilson, O. A. Hurricane, and A. Sunwoo, "Fragmentation of materials in expanding tube experiments," *International Journal of Impact Engineering*, vol. 29, pp. 735–746, Dec. 2003. 45, 46, 95

[172] D. E. Grady, "Local inertial effects in dynamic fragmentation," *Journal of Applied Physics*, vol. 53, no. 1, pp. 322–325, 1982. 46, 47, 48, 52, 53

[173] L. A. Glenn and A. Chudnovsky, "Strain-energy effects on dynamic fragmentation," *Journal of Applied Physics*, vol. 59, no. 4, pp. 1379–1380, 1986. 47, 49, 52, 53

[174] W. J. Drugan, "Dynamic fragmentation of brittle materials: analytical mechanics-based models," *Journal of the Mechanics and Physics of Solids*, vol. 49, no. 6, pp. 1181–1208, 2001. 49, 52, 53

[175] J. Lankford and C. R. Blanchard, "Fragmentation of brittle materials at high rates of loading," *Journal of Materials Science*, vol. 26, pp. 3067–3072, 1991. 49

[176] C. J. Shih, M. A. Meyers, V. F. Nesterenko, and S. J. Chen, "Damage evolution in dynamic deformation of silicon carbide," *Acta Materialia*, vol. 48, no. 9, pp. 2399–2420, 2000. 49

[177] D. A. Shockey, "Discussion of mechanisms of dynamic fragmentation: Factors governing fragment size," *Mechanics of Materials*, vol. 4, no. 3-4, pp. 321–324, 1985. 49

[178] E. H. Lee, W. Mueller, and M. Shaw, *The Continuum Mechanics Aspect of Material Properties Determination*, pp. 85–122. New York: Gordon and Breach, 1967. 51

[179] M. E. Kipp and D. E. Grady, "Dynamic fracture growth and interaction in one dimension," *Journal of the Mechanics and Physics of Solids*, vol. 33, no. 4, pp. 399–415, 1985. 52, 160, 163, 167, 213

[180] D. Grady, *Fragmentation of Rings and Shells: The Legacy of N.F. Mott*. Springer, 1 ed., 2006. 52, 53

[181] V. B. Shenoy and K. Kim, "Disorder effects in dynamic fragmentation of brittle materials," *Journal of the Mechanics and Physics of Solids*, vol. 51, pp. 2023–2035, 2003. 53

[182] Z. Jaeger, R. Englman, Y. Gur, and A. Sprecher, "Internal damage in fragments," *Journal of Materials Science Letters*, vol. 5, no. 5, pp. 577–579, 1986. 54, 149

[183] M. A. Meyers, *Dynamic Behavior of Materials*. Wiley-Interscience, 1 ed., 1994. 54

[184] V. Odintsov, "Hyperexponential spectra of exponential fracture," *Mechanics of Solids (Meckhanika Tverdogo Tela)*, vol. 27, no. 5, pp. 42–48, 1992. 55, 110, 112, 123

[185] J. P. Hooper, "Impact fragmentation of aluminum reactive materials," *Journal of Applied Physics*, vol. 112, p. 043508, Aug 2012. 55, 112

[186] V. F. Nesterenko, P.-H. Chiu, C. H. Braithwaite, A. Collins, D. M. Williamson, K. L. Olney, D. Benson, and F. McKenzie, "Dynamic behavior of particulate/porous energetic materials," *AIP Conference Proceedings*, vol. 1426, pp. 533–538, Mar. 2012. 57

[187] K. L. Olney, V. F. Nesterenko, and D. J. Benson, "Mechanisms of fragmentation of aluminum-tungsten granular composites under dynamic loading," *Applied Physics Letters*, vol. 100, pp. 191910–191910–4, May 2012. 57

[188] A. Dremin and O. Breusov, "Processes occuring in solids under the action of powerful shock waves," *Russian Chemical Reviews*, vol. 37, no. 5, pp. 392–402, 1968. 58

[189] R. A. Graham, "Issues in shock-induced solid state chemistry," Tech. Rep. SAND-89-0861C; CONF-890661-8, Sandia National Labs., Albuquerque, NM (USA), Jan. 1989. 58

[190] M. Meyers and S. Wang, "An improved method for shock consolidation of powders," *Acta Metall.*, vol. 36, pp. 925–936, Apr. 1988. 63

[191] L. M. Karlsson and A. M. Gokhale, "Stereological estimation of mean linear intercept length using the vertical sections and trisector methods," *Journal of Microscopy*, vol. 186, no. 2, pp. 143–152, 1997. 66

[192] G. M. Fritz, H. Joress, and T. P. Weihs, "Enabling and controlling slow reaction velocities in low-density compacts of multilayer reactive particles," *Combust. Flame*, vol. 158, pp. 1084–1088, June 2011. 66, 183, 185

[193] D. P. Adams, V. C. Hodges, M. M. Bai, E. Jones, M. A. Rodriguez, T. Buchheit, and J. J. Moore, "Exothermic reactions in Co/Al nanolaminates," *J. Appl. Phys.*, vol. 104, pp. 043502–043502–7, Aug. 2008. 66, 185

[194] J. C. Russ and R. T. Dehoff, *Practical Stereology (Second Edition)*. Kluwer Academic Publishing, 2nd edition ed., Aug 2000. 67

[195] B. Aydelotte and N. Thadhani, "Mechanistic aspects of impact initiated reactions in explosively consolidated Metal+Aluminum powder mixtures," *Materials Science and Engineering A*, vol. (accepted for publication), 2013. 71, 182, 200

[196] Y. Tamarin, *Atlas of Stress-Strain Curves, 2nd Edition*. ASM International, 2 ed., Nov 2002. 72

[197] Z. Horita, T. Fujinami, and T. G. Langdon, "The potential for scaling ecap: effect of sample size on grain refinement and mechanical properties," *Materials Science and Engineering: A*, vol. 318, no. 1, pp. 34–41, 2001. 72

[198] A. P. Alkhimov, V. F. Kosarev, and A. N. Papyrin, "A method of cold gas-dynamic deposition," *Doklady Akademii Nauk SSSR*, vol. 315, pp. 1062–65, 1990. 74

[199] A. P. Alkhimov, S. V. Klinkov, V. F. Kosarev, and A. N. Papyrin, "Gas-dynamic spraying study of a plane supersonic two-phase jet," *Journal of Applied Mechanics and Technical Physics*, vol. 38, pp. 324–330, Mar. 1997. 74

[200] A. P. Alkhimov, V. F. Kosarev, and A. N. Papyrin, "Gas-dynamic spraying. an experimental study of the spraying process," *Journal of Applied Mechanics and Technical Physics*, vol. 39, pp. 318–323, Mar. 1998. 74

[201] A. P. Alkhimov, A. N. Papyrin, V. F. Kosarev, N. I. Nesterovich, and M. M. Shushpanov, "Gas-dynamic spraying method for applying a coating," Apr. 1994. U.S. Classification: 427/192; 427/191; 427/195 International Classification: B05D 112. 74

[202] H. Assadi, F. Gärtner, T. Stoltenhoff, and H. Kreye, "Bonding mechanism in cold gas spraying," *Acta Materialia*, vol. 51, pp. 4379–4394, Sept. 2003. 74

[203] T. Novoselova, P. Fox, R. Morgan, and W. O'Neill, "Experimental study of titanium/aluminium deposits produced by cold gas dynamic spray," *Surface and Coatings Technology*, vol. 200, no. 8, pp. 2775–2783, 2006. 74

[204] V. K. Champagne, ed., *The Cold Spray Materials Deposition Process: Fundamentals and Applications*. CRC Press, Oct. 2007. 74

[205] P. Leyman and V. Champagne, "Cold spray process development for the reclamation of the apache helicopter mast support," Tech. Rep. ARL-TR-4922, Army Research Laboratory, Aberdeen Proving Ground, MD, Aug. 2009. 74

[206] A. Bacciochini, M. I. Radulescu, Y. Charron-Tousignant, J. Van Dyke, B. Jodoin, M. Nganbe, M. Yandouzi, and J. Lee, "Enhanced reactivity of mechanically-activated nano-scale gasless reactive materials consolidated via

the cold-spray technique," *AIP Conference Proceedings*, vol. 1426, pp. 543–546, Mar. 2012. 74

[207] R. Weil and K. Parker, "Chapter 4: The properties of electroless nickel," in *Electroless Plating: Fundamentals and Application* (G. O. Mallory and J. B. Hajdu, eds.), pp. 111–137, Cambridge University Press, 1990. 76, 77, 78, 173, 174

[208] B. Aydelotte, C. Braithwaite, P. Specht, N. Thadhani, and M. Trexler, "A study of fragmentation in a ni+al structural energetic material," in *Proceedings of The 58th JANNAF Propulsion Meeting / 44th Combustion / 32nd Airbreathing Propulsion / 32nd Exhaust Plume and Signatures / 26th Propulsion Systems Hazards Joint Subcommittee Meeting 2010, Crystal City, VA, April 18-21*, vol. JSC CD-66 (CD Rom) (April 2011), (Crystal City, VA), Apr. 2011. 78, 88, 96

[209] W. H. Gourdin, "Energy deposition and microstructural modification in dynamically consolidated metal powders," *Journal of Applied Physics*, vol. 55, pp. 172–181, Jan 1984. 79

[210] V. Champagne, P. Leyman, and D. Helfritch, *Magnesium Repair by Cold Spray.* No. ARL-TR-4438, May 2008. 79

[211] Z. Pan, W. Yin, and Q. Wei, "Mechanical testing of ni-al composites consolidated by hot-explosive-compaction: A technical report submitted to dr. laszlo kecskes army research laboratory, WMRD, aberdeen proving ground, maryland," technical, Department of Mechanical Engineering and Engineering Science, University of North Carolina, Charlotte, North Carolina, Jan. 2011. 82, 83, 84

[212] D. A. Crawford and M. E. Kipp, "Giant impact theory for origin of the moon: High resolution CTH simulations," in *Lunar and Planetary Institute Science Conference Abstracts*, vol. 41, p. 1405, Mar. 2010. 85

[213] S. Pappu and L. E. Murr, "Hydrocode and microstructural analysis of explosively formed penetrators," *Journal of Materials Science*, vol. 37, pp. 233–248, Jan. 2002. 85

[214] R. G. McQueen and S. P. Marsh, "Equation of state for nineteen metallic elements from shock-wave measurements to two megabars," *Journal of Applied Physics*, vol. 31, no. 7, p. 1253, 1960. 85

[215] J. McGlaun, S. Thompson, and M. Elrick, "CTH: a three-dimensional shock wave physics code," *Int. J. Impact Eng.*, vol. 10, no. 1-4, pp. 351–360, 1990. 88, 201

[216] D. J. Steinberg, S. G. Cochran, and M. W. Guinan, "A constitutive model for metals applicable at high-strain rate," *J. Appl. Phys.*, vol. 51, no. 3, pp. 1498–1504, 1980. 89, 186

[217] P. E. Specht, *Shock Compression Response of Aluminum-Based Intermetallic Forming Reactive Systems*. PhD thesis, Georgia Institute of Technology, May 2013. 89

[218] S. P. Marsh, ed., *LASL Shock Hugoniot Data*. University of California Press, 1980. 91

[219] I. Fyfe and A. Rajendran, "Dynamic pre-strain and inertia effects on the fracture of metals," *Journal of the Mechanics and Physics of Solids*, vol. 28, pp. 17–26, Feb. 1980. 95

[220] C. H. Braithwaite, B. Aydelotte, A. Collins, N. Thadhani, and D. M. Williamson, "Comparing cth simulations and experiments on explosively loaded rings," *AIP Conference Proceedings*, vol. 1426, p. 10491052, Mar 2012. 100

[221] K. McNesby, G. Sutherland, and R. Benjamin, "Color imaging of shock front emergence in TNT," Tech. Rep. ARL-TR-6181, Army Research Laboratory, Aberdeen Proving Ground, MD, Oct. 2012. 101

[222] R. Benjamin and T. Piehler, "Testing and evaluation of explosively filled steel reinforced fiber cases," Tech. Rep. ARL-RP-307, US Army Research Laboratory, 2010. 103, 104, 105

[223] A. Vivek, G. Taber, J. Johnson, H. Wang, S. Woodward, G. Fenton, and G. Daehn, "Electrically driven expanding plasma as a means to drive high velocity and high strain rate experiments," Mar. 2011. 105

[224] G. S. Daehn, J. R. Johnson, G. Taber, A. Vivek, Y. Zhuan, and G. K. Fenton, "Applications of PDV in electromagnetic forming," (Albuquerque, NM), 2008. Author Institution: The Ohio State University. 106

[225] W. Mock and W. H. Holt, "Fragmentation behavior of armco iron and HF-1 steel explosive-filled cylinders," *Journal of applied physics*, vol. 54, no. 5, pp. 2344–2351, 1983. 109

[226] D. Goto, R. Becker, T. Orzechowski, H. Springer, A. Sunwoo, and C. Syn, "Investigation of the fracture and fragmentation of explosively driven rings and cylinders," *International Journal of Impact Engineering*, vol. 35, p. 15471556, Dec 2008. 126, 127

[227] R. L. Doney, G. B. Vunni, and J. H. Niederhaus, "Experiments and simulations of exploding aluminum wires: Validation of ALEGRA-MHD," Tech. Rep. ARL-TR-5299, Army Research Laboratory, Aberdeen Proving Ground, MD, Sept. 2010. 135

[228] C. Aimone, M. A. Meyers, and N. Mojtabai, "Shock wave induced fragmentation of copper porphyries," in *Rock mechanics in productivity and protection: proceedings : Twenty-fifth Symposium on Rock Mechanics, Northwestern University, Evanston, Illinois, June 25-27, 1984* (D. Dowding and M. Singh, eds.),

Symposium on Rock Mechanics Series, (Northwestern University, Evanston, Illinois), pp. 979–995, Society of Mining Engineers of the American Institute of Mining, Metallurgical and Petroleum Engineers, Inc., 1984. 149

[229] I. Glassman and R. A. Yetter, *Combustion*. Academic Press, 2008. 169

[230] B. Z. Eapen, V. K. Hoffmann, M. Schoenitz, and E. L. Dreizin, "Combustion of aerosolized spherical aluminum powders and flakes in air," *Combustion Science and Technology*, vol. 176, no. 7, p. 1055, 2004. 171, 173

[231] B. Legrand, E. Shafirovich, M. Marion, C. Chauveau, and I. Gkalp, "Ignition and combustion of levitated magnesium particles in carbon dioxide," *Symposium (International) on Combustion*, vol. 27, pp. 2413–2419, 1998. 183

[232] M. Schoenitz, S. Umbrajkar, and E. L. Dreizin, "Kinetic analysis of thermite reactions in al-MoO_3 nanocomposites," *J. Propul. Power*, vol. 23, pp. 683–687, July 2007. 183

[233] G. R. Johnson and W. H. Cook, "A constitutive model and data for metals subjected to large strains, high strain rates, and high temperatures," in *Proceedings of the 7th International Symposium on Ballistics*, pp. 541–547, 1983. 186

[234] F. J. Zerilli and R. W. Armstrong, "Dislocation-mechanics-based constitutive relations for material dynamics calculations," *J. Appl. Phys.*, vol. 61, no. 5, pp. 1816–1825, 1987. 186

[235] G. R. Johnson and W. H. Cook, "Fracture characteristics of three metals subjected to various strains, strain rates, temperatures and pressures," *Eng. Fract. Mech.*, vol. 21, no. 1, pp. 31–48, 1985. 186

[236] G. R. Johnson and T. J. Holmquist, "Test data and computational strength and fracture model constants for 23 materials subjected to large strains, high strain rates, and high temperatures," Technical LA-11463-MS, Los Alamos National Lab, Los Alamos, NM, Aug. 1988. 186

[237] T. Antoun, L. Seaman, D. R. Curran, G. I. Kanel, S. V. Razorenov, and A. V. Utkin, *Spall Fracture*. Springer New York, Feb. 2010. 187

[238] D. Crawford, A. Brundage, E. Harstad, E. Hertel Jr., R. Schmitt, S. Schumacher, and J. Simmons, "CTH user's manual and input instructions version 10.0," Jan. 2011. 187

[239] D. Fondse and M. Meyers, "unpublished results." Oct. 2008. 192, 194

[240] R. T. DeHoff, E. H. Aigeltinger, and K. R. Craig, "Experimental determination of the topological properties of three-dimensional microstructures," *Journal of Microscopy*, vol. 95, no. 1, pp. 69–91, 1972. 198

[241] J. P. Kroustrup and H. J. G. Gundersen, "Estimating the number of complex particles using the ConnEulor principle," *Journal of Microscopy*, vol. 203, no. 3, pp. 314–320, 2001. 198

[242] B. Aydelotte and N. Thadhani, "A comparison of different ni+al structural energetic materials," *MRS Online Proceedings Library*, vol. 1521, 2013. 200

[243] V. K. Champagne, ed., *The Cold Spray Materials Deposition Process: Fundamentals and Applications*. CRC Press, Oct. 2007. 200